

Charged point defects in oxides – a case study of MgO bulk and surface F centers

vorgelegt von
Diplom-Physikerin
Norina Anna Richter
aus Ahlen

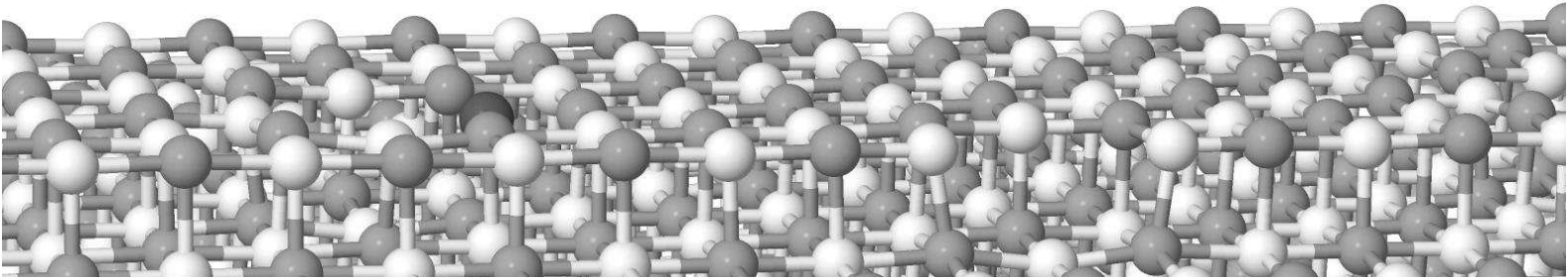
von der Fakultät II – Mathematik und Naturwissenschaften
der Technischen Universität Berlin
zur Erlangung des akademischen Grades
Doktorin der Naturwissenschaften
Dr. rer. nat.

vorgelegte Dissertation

Promotionsausschuss:

Vorsitzender	:	Prof. Dr. rer. nat. Mario Dähne, TU Berlin
1. Gutachter	:	Prof. Dr. rer. nat. Andreas Knorr, TU Berlin
2. Gutachter	:	Prof. Dr. rer. nat. Matthias Scheffler, FHI Berlin

Berlin 2013
D 83



Abstract

Metal oxides exhibit versatile chemical and physical properties. For example, they are used in gas-sensor technology, for solar cells, transparent conductors, and in catalysis. Oxygen vacancies, also termed F centers, change the electronic and geometric structure of the oxide and can appear in different charge states. F centers may enhance the performance of the material, or they may be undesirable. In both cases, a fundamental knowledge of these defects is essential.

Realistic metal oxides are typically doped, either intentionally or unintentionally, and this can affect defect concentrations and charge states. *Local* and *global* effects of doping can be distinguished. Global effects of doping include creation of a Fermi level, i.e., the chemical potential for electrons, formation of a space-charge region, and band bending at the surface. Local effects occur due to defect-induced localization of charge carriers at the dopant, and a local change in electronic structure and lattice relaxation around the dopant. Depending on the system specifics, either local or global or both doping effects can play an important role for the formation of F centers.

Experiments measuring defect concentrations *in situ* are extremely challenging and therefore scarce. Previous theoretical approaches to defect concentrations and formation energies have aimed at a description of isolated, non-interacting defects. In this work, bulk and surface F centers in metal oxides are studied using the example of MgO, which is widely used as a catalyst or catalyst support. It has been shown, that intentional *p*-type doping enhances the catalytic performance of MgO, and oxygen vacancies can play a decisive role in this context. However, charge states and concentration of these defects under realistic working conditions have so far not been analyzed.

In the present work, the standard methodology for calculating defect formation energies is extended to include defect-defect interaction, accounting for realistic temperature, pressure, electron chemical potential, and bulk doping concentrations. It is demonstrated how defect formation energies can be determined systematically and accurately, using *ab initio* atomistic thermodynamics in combination with hybrid density-functional theory (DFT) with parameters of the exchange-correlation functional optimized according to a consistency requirement on DFT and G_0W_0 ionization energies. Formation energies for neutral defects are validated by coupled-cluster calculations using embedded cluster models. The virtual-crystal approximation is used for a realistic modeling of doping to describe charged vacancies at the surface.

It is found that at catalytically relevant temperatures of \sim 400-1,000 K and oxygen partial pressures > 0.1 atm the concentration of charged F centers at surfaces of doped oxides is largely determined by two electrostatic effects, so far disregarded in literature: (i) charge transfer between surface defects and bulk dopants, leading to formation of a macroscopically extended space-charge region, bending of electronic bands, and an electric field that limits the formation of charged surface defects, and (ii) attraction between surface defects and the compensating charge, facilitating oxygen vacancy formation. The higher the concentration of charged defects, the larger are band bending and defect formation energy. Nevertheless, the concentration of F_s^{2+} centers at the (100) terrace of *p*-type MgO can be as high as 1% at realistic conditions, while F_s^+ and F_s^0 concentrations are negligible.

Zusammenfassung

So vielfältig wie ihre physikalischen und chemischen Eigenschaften sind auch die Anwendungsgebiete von Metalloxiden. Sie kommen z.B. als Gassensoren, Solarzellen, transparente, elektrische Leiter oder Katalysatoren zum Einsatz. Dabei verursachen Sauerstoff-Fehlstellen, die auch als F-Zentren bezeichnet werden, Veränderungen der elektronischen und atomaren Struktur, die für den technischen Einsatz des Materials teils unerwünscht, oft aber auch von essentieller Bedeutung sind. Ein Verständnis der Stabilität von F-Zentren unter realistischen äußeren Bedingungen ist in beiden Fällen unerlässlich. Dotieren des Oxids, durch gezieltes Einbringen von Fremdatomen oder unbeabsichtigte Verunreinigung, kann die Konzentration der Fehlstellen beeinflussen. Man kann dabei zwischen *globalen* und *lokalen* Dotierungseffekten unterscheiden. Global wirkt sich die Dotierung auf das Fermi-Niveau aus und kann zu einer Raumladungszone und Krümmung der elektronischen Bänder an der Kristalloberfläche führen. Lokale Effekte ergeben sich durch Änderungen der elektronischen Struktur und Gittergeometrie in unmittelbarer Umgebung der Fremdatome. Nur wenige experimentelle Studien wurden bisher zu Gleichgewichtskonzentrationen von F-Zentren durchgeführt, und theoretische Studien behandeln meist den Grenzfall nicht-wechselwirkender Defekte.

Die vorliegende Arbeit befasst sich mit der Berechnung von F-Zentren in Metalloxiden am Beispiel von Magnesiumoxid (MgO), das als Katalysator verwendet wird. Obwohl gezielte *p*-Dotierung die katalytischen Eigenschaften von MgO verbessert und Sauerstoff-Fehlstellen in diesem Zusammenhang eine entscheidende Rolle spielen können, wurden deren Ladungszustände und Konzentrationen in MgO bisher nicht unter realistischen Bedingungen analysiert. In dieser Arbeit wird das bestehende theoretische Modell zur Berechnung von Formationsenergien unter Berücksichtigung von Wechselwirkungen zwischen Defekten erweitert, so dass als thermodynamische Parameter Temperatur, Druck, Fermi-Niveau und auch Dotierungskonzentration eingehen. Formationsenergien werden mit Hilfe von *ab initio* Thermodynamik und Dichtefunktionaltheorie (DFT) systematisch und präzise berechnet. Dazu werden Hybrid-Funktional-Parameter, die das Austausch-Korrelations-Potential bestimmen, optimiert, so dass DFT- und G_0W_0 -Ionisationsenergien übereinstimmen. Formationsenergien für neutrale Sauerstoff-Fehlstellen werden durch coupled-cluster-Berechnungen von eingebetteten Cluster-Geometrien validiert. Für eine realistische Beschreibung geladener Oberflächen-Fehlstellen wird das dotierte Material als fiktiver Kristall (*virtual crystal*) behandelt.

Die Konzentrationen von geladenen Oberflächen-Fehlstellen in *p*-dotierten Oxiden unter katalytisch relevanten Bedingungen, Temperaturen von 400–1000 K und Sauerstoff-Partialdrucken >0.1 atm, werden von zwei elektrostatischen Effekten bestimmt: Ladungstransfer zwischen Oberflächen-Defekten und tiefer liegenden Dotierungs-Atomen führt zur Ausbildung einer Raumladungszone, Verbiegung der elektronischen Bänder und einem elektrischen Feld, wodurch die Konzentration von F-Zentren an der Oberfläche nach oben begrenzt wird. Andererseits erleichtert elektrostatische Anziehung zwischen geladenen Oberflächen-Defekten und Kompensationladung das Entstehen von F-Zentren. Die Konzentration von zweifach positiv geladenen F-Zentren an der (100)-Oberfläche von *p*-dotiertem MgO beträgt ca. 1 %, während Konzentrationen von neutralen und einfach positiv geladenen F-Zentren vernachlässigbar klein sind.

Contents

1. Introduction	1
I. Concepts to characterize charged point defects in oxides	4
2. <i>Ab initio</i> methods for electronic-structure calculations	5
2.1. The many-body problem	5
2.2. Hartree-Fock theory	8
2.3. Density-functional theory	9
2.3.1. Hohenberg-Kohn theorem	10
2.3.2. The Kohn-Sham equations	10
2.3.3. Exchange-correlation approximations and hybrid functionals	12
2.4. Beyond DFT and HF: MP2, RPA, <i>GW</i> , and coupled-cluster	15
2.5. Electronic-structure code of choice: FHI-aims	20
3. Computational models for defect calculations	23
3.1. Two well-established approaches: cluster and supercell	23
3.2. Modeling charged defects with supercell methods	26
3.2.1. Neutralizing background charge density	26
3.2.2. Compensating impurities	27
3.2.3. Doped material as a virtual crystal	29
3.3. Summary	32
4. Defect stability – formation energy and concentration	34
4.1. Stability of an isolated point defect	34
4.1.1. Fermi level position	36
4.1.2. <i>Ab initio</i> atomistic thermodynamics	37
4.1.3. Obtaining the dilute limit with supercell models	39
4.2. Stability of interacting surface defects in doped material	44
4.2.1. Space-charge effects due to surface defects	45
4.2.2. Concentration and formation energy of interacting defects	47
4.3. Experiments on point defect stabilities	50
4.4. Summary	52
II. Oxygen vacancies in MgO	53
5. MgO as a catalyst for methane oxidation	54

6. F centers in bulk MgO	56
6.1. Neutral oxygen vacancy in bulk MgO	56
6.2. Charged defects in bulk MgO	64
6.2.1. Geometric relaxation	64
6.2.2. Electronic structure	66
6.2.3. Opt-HSE for charge-transition levels and formation energies	70
6.2.4. Changes in lattice vibrations due to defect formation	76
6.2.5. vdW effects on defect formation energies	76
6.3. Summary	78
7. F centers at the MgO (100) surface	79
7.1. Geometric relaxation	79
7.2. Electronic structure	82
7.3. Formation energy of the neutral oxygen vacancy at MgO (100)	83
7.4. Charge-transition levels and formation energies in the dilute limit	85
7.5. Concentrations and formation energies of interacting F_s centers	87
7.6. Lattice-vibration effects on surface-defects energetics	91
7.7. Van der Walls effects on surface defect formation energies	92
7.8. Summary	94
8. Defect complexes in lithium-doped MgO	95
8.1. Experimental characterization of lithium-induced defects	96
8.2. Theoretical analysis of lithium-induced defect complexes	98
8.2.1. Hierarchy of defect stabilities	102
8.2.2. Position of defect levels	108
8.3. Summary	111
9. Concluding remarks	112
10. Outlook: F centers at low coordinated sites and polar surfaces	115
10.1. F centers at MgO (100) steps and corners	116
10.2. F centers at the MgO (111) surface	118
A. Appendix	121
A.1. Oxygen interstitials in MgO bulk	121
A.2. Convergence tests for periodic systems	123
A.3. MgO lattice-parameter optimization	126
A.4. Convergence tests and BSSE corrections for cluster calculations	126

1. Introduction

Due to their manifold, often tailorable chemical and physical properties, metal oxides are suitable for a wide range of applications. Gas sensors, for example for carbon monoxide detection, are often tin oxide based [1], while doped aluminum oxide in its mineral form is also known as sapphire or ruby, utilized to make jewellery but also for laser technology [2]. Furthermore, metal oxides are used in paints, in wallboards, for sunscreens, in electronic devices like capacitors, or for heat insulating material in mobile phones [3–6]. While all these areas may still be somehow specific, there is one class of metal-oxide applications that is of great general economic and ecologic interest: Metal-oxide catalysts can help us produce commodity chemicals like ethylene, as well as fuels and electricity in an efficient and economical way. Two prominent examples are titanium dioxide and magnesium oxide. Exploring the catalytic properties of titanium dioxide has led to valuable insights in the context of photocatalytic water splitting [7–10], which may make hydrogen available as an environmentally friendly fuel. And magnesium oxide (MgO) is a base material for promising methane conversion catalysts [11–21]. All applications mentioned above require very specific material properties. Point defects like vacancies, where an atom is missing from the regular crystal lattice, or dopants, where one atom has been substituted by a different species, induce unique features in the electronic and geometric structure of a metal oxide. While sometimes oxides of high purity are needed, often defects are indeed desirable. In some cases, oxygen vacancies, also termed F centers, can promote certain surface reactions or inhibit others and thus influence the selectivity of a catalyst. For example, Wu and van de Krol recently found a positive influence of oxygen vacancies on the selective photoreduction of nitric oxide to nitrogen over a TiO_2 photocatalyst [22]. Furthermore, dopants may be used to control electrical conductivity by providing free charge carriers. By doping, also the chemical potential for electrons, the Fermi level, can be fixed, which is important for charge transfer processes in the metal-oxide bulk or at interfaces with vacuum or other material. Understanding the defect physics of a metal oxide is a key to achieve an optimal performance in application. However, even the very first step is complex. Defect type, concentration, and charge state typically depend on outer conditions such as temperature and pressure, and furthermore, defects usually interact with each other in different ways that are sometimes not immediately obvious. Experiments on point-defect stabilities are challenging, since it is hard to establish thermodynamic equilibrium. In theoretical studies often only the limiting case of non-interacting defects is considered. For charged surface defects under realistic ambient conditions even a reliable theoretical framework has so far been lacking.

This work addresses the very basic and nevertheless very challenging question how stabilities of oxygen vacancies in different charge states at metal oxide surfaces can be described quantitatively within a self-contained *first-principles* theoretical approach. The goal is to understand how defect concentrations and charge states depend on temperature, pressure, electron reservoir (Fermi level) and doping concentration on the example of bulk and surface F centers in MgO .

Several distinct aspects need to be considered. Two different structure models are commonly

used to describe point defects within an electronic-structure approach. An embedded cluster model is a piece of material cut from the crystal lattice and surrounded by potentials that mimic the extended system. A periodic supercell model also uses a piece of material of the extended system, but repeats it periodically. In this work, the ambition is to survey advantages and disadvantages of both models, so that ideally the specific advantages of each model can be exploited for the system of interest.

In general, periodic models are more suitable to obtain information on the electronic energy bands of a solid, which is important specifically for charged defects. The challenge in periodic calculations of charged surface defects is to choose a suitable method of charge compensation. Due to the periodic repetition, the electrostatic potential in the calculation diverges, if it is not compensated. This reflects the physical fact that there is a significant energy associated with the long-range Coulomb interaction, which therefore must be mostly cancelled in realistic systems. The standard approach to overcome this issue is to apply a uniformly distributed background charge to the system [23]. However, this approach is somehow artificial and in a surface calculation, where two-dimensional slabs of host material are separated by vacuum, it is without doubt unphysical. Therefore, one necessary requirement for the computations of charged surface defects in this work and for future studies of similar systems is to find a physically meaningful way of charge compensation in supercell calculations.

To bridge the gap between microscopic and macroscopic effects, the energy gain or loss upon defect formation and resulting defect concentrations can be calculated using density-functional theory in combination with *ab initio* atomistic thermodynamics [24, 25]. This approach is commonly used for studies of bulk defects in semiconductors and oxides, accounting in the case of oxygen vacancies for three thermodynamic variables: Temperature, partial pressure of the surrounding oxygen atmosphere, and Fermi level. So far, theoretical approaches have been concerned to describe isolated, non-interacting defects by these means. This is justified for vanishing defect concentrations. However, usually interaction between defects can not be neglected. Specifically, this is true for charged defects, where electrostatic attraction or repulsion decays slowly with distance between charges. Furthermore, realistic metal oxides are typically doped, either with or without intent. It is important to identify and understand the electrostatic interactions that influence the stability and charge state of oxygen vacancies in metal oxides. And consequently, the existing thermodynamic framework for calculating defect concentrations and in particular the set of considered thermodynamic variables has to be extended, accordingly.

The quantity that determines the defect concentration is the Gibbs free energy needed to create the defect. When calculated with density-functional theory methods, the values of defect energy levels and total energies need to be tested carefully for their sensitivity to the employed approximate treatment of exchange and correlation of the many-electron system. All system characteristics that are important for the defect formation need to be identified. It must then be insured in a robust, self-contained theoretical approach that these characteristics are reproduced accurately by the optimal exchange-correlation functional.

Furthermore, there are specific challenges concerning oxygen vacancies in MgO. A long-standing discrepancy exists between the stability of a neutral bulk F center as measured in an optical-absorption experiment [26] and different published values of the formation energy calculated with electronic-structure methods [27–30]. With regard to the application of MgO in catalysis, it has been shown that *p*-type doping is a requirement for high selectivity of catalysts

for methane activation [31] and that *p*-type doping promotes the formation of oxygen vacancies in MgO [32]. Doping can affect defect formation in a local way, causing changes in electronic and geometric structure in the vicinity of a defect, and in a global way, determining the Fermi level position. Therefore, the aim is to acquire a detailed understanding of local and global effects of *p*-type doping on oxygen vacancy formation in MgO and to provide estimates for the equilibrium concentrations of surface oxygen vacancies, including these effects.

The thesis is structured in two parts, starting with a discussion of concepts to characterize charged point defects in oxides in general. For this purpose, first the theoretical background of electronic-structure calculations used in this work is summarized (Chapter 2). In the following, embedded cluster and periodic supercell models are discussed with an emphasis on charge compensation in periodic models of charged systems (Chapter 3). Next, it is explained how stabilities for isolated defects can be calculated, and a thermodynamic model for interacting surface oxygen vacancies is introduced that allows to calculate formation energies and concentrations of these defects taking into account their dependence on the concentrations of all other defects and dopants in the system (Chapter 4). Also, experimental methods are briefly sketched. In the second part of the thesis the outlined concepts are applied to point defects in MgO. The role of MgO in the context of methane activation is reviewed (Chapter 5) and the analysis of oxygen vacancies starts with defects in the bulk (Chapter 6). Geometric and electronic relaxation and charge transfer are examined and an optimal hybrid DFT functional is identified to be used for the calculations of neutral and charged F centers in MgO. Then, surface F centers in different charge states in doped MgO are investigated (Chapter 7). While the focus of this work is on global doping effects, finally also short-range effects of doping are studied, considering defect complexes formed in lithium-doped MgO (Chapter 8). At the end, the results of this work are summarized in the context of existing knowledge (Chapter 9) and an outlook on subsequent questions interesting with respect to future research is given (Chapter 10).

Part I.

Concepts to characterize charged point defects in oxides

2. *Ab initio* methods for electronic-structure calculations

The purpose of this work is to learn about the influence that point defects have on the electronic and geometric structure of a material and what this means for the properties of the solid. In the following, all non-adiabatic effects are neglected and electrons are considered as moving in a potential created by frozen nuclei. At atomic scale the corresponding electronic many-body problem is expressed by the electronic Schrödinger equation. The numerical cost for solving it scales exponentially with the number of electrons, making it impossible to compute the full solution for systems other than very small molecules. However, robust methods exist that allow for approximate solutions, in particular for ground-state properties. On the one hand there are techniques that make assumptions on the wave functions, namely Hartree-Fock (HF) theory and methods that are based on HF, such as Møller-Plesset perturbation theory, configuration interaction (CI), and coupled-cluster (CC). By construction, these methods allow to increase accuracy systematically, but this is at the cost of increasing computational effort. For example, high accuracy CC theory (in particular CCSD(T)) is still affordable only for molecules or small clusters, typically with less than 20 atoms. The most successful method for treating bulk and surface systems of up to several thousands of atoms, such that also long-range effects may be taken into account, is density-functional theory (DFT). Within this theory all uncertainty is folded into a density-dependent exchange-correlation potential, which is subsequently approximated. It is also possible to combine wave function and density-based approaches. Mixing a certain amount of HF non-local exchange, often called exact exchange, into a DFT local exchange potential, one can form a non-local hybrid functional. The underlying theoretical framework of the methods used in this work to solve the Schrödinger equation is reviewed in the following paragraphs.

2.1. The many-body problem

The key problem of finding the ground-state energy of an atomic system with electrons at \mathbf{r}_i and nuclei at \mathbf{R}_j is to solve the time-independent Schrödinger equation, which has the form of an eigenvalue problem

$$\hat{\mathcal{H}}|\Phi(\mathbf{R}_1, \dots, \mathbf{r}_1, \dots)\rangle = \mathcal{E}|\Phi(\mathbf{R}_1, \dots, \mathbf{r}_1, \dots)\rangle. \quad (2.1)$$

$\hat{\mathcal{H}}$ is the Hamilton operator and $\Phi(\mathbf{R}_1, \dots, \mathbf{r}_1, \dots)$ is the many-particle wave function and an element of the Hilbert space. Specifically, a variational principle can be written for the ground-state eigenvalue \mathcal{E}_0 and eigenvector Φ_0 of the Hamiltonian operator

$$\mathcal{E}_0 = \langle \Phi_0 | \hat{\mathcal{H}} | \Phi_0 \rangle \leq \langle \Phi | \hat{\mathcal{H}} | \Phi \rangle, \quad (2.2)$$

where Φ is an arbitrary element of the Hilbert space. The ground-state energy is for example needed to determine the system's ground-state geometric structure. Furthermore, by analyzing ground-state energy differences, observables like adsorption energies or defect formation energies may be estimated characterizing the system or process of interest.

Electrons and nuclei each carry charge which is responsible for Coulomb interaction between them. Neglecting relativistic effects, as for example spin-orbit coupling, the Hamiltonian operator for a system of N_{nuc} nuclei with atomic numbers Z_k located at \mathbf{R}_k and N_{el} electrons at \mathbf{r}_i , is

$$\hat{\mathcal{H}} = \hat{T}_{\text{n}} + \hat{T}_{\text{e}} + V_{\text{n-n}} + V_{\text{e-e}} + V_{\text{e-n}}. \quad (2.3)$$

The different contributions are (atomic units are used) the kinetic energy of the nuclei

$$\hat{T}_{\text{n}} = - \sum_{k=1}^{N_{\text{nuc}}} \frac{1}{2M_k} \Delta_{\mathbf{R}_k}, \quad (2.4)$$

where M_k is the ratio of the mass of nucleus k to the mass of an electron, the kinetic energy of the electrons

$$\hat{T}_{\text{e}} = - \sum_{i=1}^{N_{\text{el}}} \frac{1}{2} \Delta_{\mathbf{r}_i} = \sum_{i=1}^{N_{\text{el}}} \hat{t}_i^{\text{e}}, \quad (2.5)$$

the nuclear-nuclear interaction

$$V_{\text{n-n}} = \sum_{\substack{k, k'=1 \\ k \neq k'}}^{N_{\text{nuc}}} \frac{Z_k Z_{k'}}{|\mathbf{R}_k - \mathbf{R}_{k'}|}, \quad (2.6)$$

the electron-electron interaction

$$V_{\text{e-e}} = \sum_{\substack{i, i'=1 \\ i \neq i'}}^{N_{\text{el}}} \frac{1}{|\mathbf{r}_i - \mathbf{r}_{i'}|}, \quad (2.7)$$

and the electron-nuclear interaction

$$V_{\text{e-n}} = - \sum_{i=1}^{N_{\text{el}}} \sum_{k=1}^{N_{\text{nuc}}} \frac{Z_k}{|\mathbf{r}_i - \mathbf{R}_k|} = \sum_{i=1}^{N_{\text{el}}} v_i^{\text{ext}}. \quad (2.8)$$

Except for the two lightest elements, the mass of the nuclei is 10^4 - 10^5 times larger than the mass of the electrons, so that their motions are typically assumed to take place on different time scales, where the electrons adjust to the nuclear positions almost instantaneously. This means that the electronic energies can be approximated as only parametrically dependent on the nuclear coordinates, describing a potential energy surface for the motion of the nuclei. The assumption to neglect non-adiabatic coupling of the electronic and nuclear subsystems is known as the Born-Oppenheimer or adiabatic approximation [33]. The total electron-nuclear wave function is approximated by a product of the electronic and the nuclear wave functions $|\Phi\rangle = |\Psi\rangle|\chi\rangle$. This is valid for systems with well-separated adiabatic electronic states, in which electronic transition due to nuclear motion is not to be expected. The electronic problem for a set of nuclear positions $\mathbf{R} = [\mathbf{R}_1, \dots, \mathbf{R}_{N_{\text{nuc}}}]$ with electrons at $\mathbf{r} = [\mathbf{r}_1, \dots, \mathbf{r}_{N_{\text{el}}}]$ is then described by the electronic eigenvalue problem

$$\hat{H}|\Psi(\mathbf{R}, \mathbf{r})\rangle = E(\mathbf{R})|\Psi(\mathbf{R}, \mathbf{r})\rangle, \quad (2.9)$$

where $\hat{H} = \hat{T}_e + V_{e-e} + V_{e-n}$ is the many-electron Hamiltonian. The nuclear motion follows from the nuclear Schrödinger equation

$$\hat{H}_{\text{nuc}}|\chi(\mathbf{R})\rangle = [\hat{T}_n + V_{n-n} + E(\mathbf{R})]|\chi(\mathbf{R})\rangle = \mathcal{E}_{\text{BO}}|\chi(\mathbf{R})\rangle, \quad (2.10)$$

where the total energy $E_{\text{tot}}(\mathbf{R}) = V_{n-n} + E(\mathbf{R})$ provides a potential energy surface for the motion of the nuclei. \mathcal{E}_{BO} , including electronic, vibrational and translational contributions, is the Born-Oppenheimer approximation to the energy \mathcal{E} of the full coupled system in Eq. 2.1. Alternatively, the nuclear motion may be obtained from the classical equation of motion, neglecting quantum effects. According to the Hellmann-Feynman theorem [34], forces on a nucleus k , $\mathbf{F}_k(\mathbf{R})$, are given as

$$\mathbf{F}_k(\mathbf{R}) = -\nabla_{\mathbf{R}_k} E(\mathbf{R}) = \langle \Psi(\mathbf{R}, \mathbf{r}) | \nabla_{\mathbf{R}_k} \hat{H} | \Psi(\mathbf{R}, \mathbf{r}) \rangle. \quad (2.11)$$

The kinetic energy of the nuclei is usually $10^{-2} - 10^{-3}$ times smaller than the kinetic energy of the electrons. Within the Born-Oppenheimer approximation the contribution of nuclear-nuclear interaction to the total energy of the system depends only on the nuclei positions. What remains to be solved is the electronic many-particle problem (Eq. 2.9). One step that most methods for an approximate solution of the Schrödinger equation have in common is to first separate the interacting many-electron Hamiltonian \hat{H} into a mean-field, non-interacting Hamiltonian \hat{H}^{MF} and a remaining interaction Hamiltonian \hat{H}' ,

$$\hat{H} = \hat{H}^{\text{MF}} + \hat{H}'. \quad (2.12)$$

The mean-field Hamiltonian can be written as a sum of effective single-particle Hamiltonians \hat{h}_i^{MF} , according to

$$\hat{H}^{\text{MF}} = \sum_{i=1}^{N_{\text{el}}} \hat{h}_i^{\text{MF}} = \sum_{i=1}^{N_{\text{el}}} (\hat{t}_i^e + v_i^{\text{ext}} + v_i^{\text{MF}}), \quad (2.13)$$

with a corresponding set of effective single-particle Schrödinger equations

$$\hat{h}_i^{\text{MF}}|\varphi_i\rangle = \epsilon_i|\varphi_i\rangle, \quad (2.14)$$

where φ_i are single-particle wave functions and ϵ_i denote single-particle eigen energies. The mean-field ground state energy E_0^{MF} is

$$E_0^{\text{MF}} = \langle \Psi_0^{\text{MF}} | \hat{H}^{\text{MF}} | \Psi_0^{\text{MF}} \rangle, \quad (2.15)$$

where Ψ_0^{MF} is the mean-field ground state wave function. For example, in Hartree theory Ψ_0^{MF} is a product of single-particle wave functions, and in Hartree-Fock theory Ψ_0^{MF} is a single Slater determinant constructed of single-particle wave functions. This is discussed in more detail below. In different mean-field approaches, E_0^{MF} and Ψ_0^{MF} are either used directly to approximate the energy of the full electronic Hamiltonian or they are chosen as a reference, e.g. when perturbation theory is subsequently applied.

2.2. Hartree-Fock theory

In order to reduce the complexity of the $3N_{\text{el}}$ -dimensional electronic problem, different approximations have been suggested. Approaches based on the unknown many-particle wave function are for example the Hartree and Hartree-Fock approximations that were developed in the late 1920s [35].

Within the Hartree approximation each electron is moving in the average potential, or mean field, of all other electrons. The wave function is thus written as a product of single particle wave functions. Since the effective potential depends on the solution of the Hartree equation, this leads to the self-consistent field approach. An effective potential is guessed and used to obtain the solution of the equation that is subsequently used to build a new effective potential, and the procedure is repeated until self-consistency is reached. This concept is restored also in the practical implementations of density-functional theory.

Building up on the Hartree theory, the Hartree-Fock approximation additionally takes into account the fermionic character of the electrons. The many-electron ground-state wave function Ψ_0 is approximated by a single Slater determinant Ψ^{HF} of N_{el} spin orbitals φ_i that is antisymmetric upon interchanging the coordinates of two electrons and thus fulfills the Pauli principle

$$\Psi^{\text{HF}} = \frac{1}{\sqrt{N_{\text{el}}!}} \begin{vmatrix} \varphi_1(\mathbf{r}_1, \sigma_1) & \cdots & \varphi_{N_{\text{el}}}(\mathbf{r}_1, \sigma_1) \\ \vdots & \ddots & \vdots \\ \varphi_1(\mathbf{r}_{N_{\text{el}}}, \sigma_{N_{\text{el}}}) & \cdots & \varphi_{N_{\text{el}}}(\mathbf{r}_{N_{\text{el}}}, \sigma_{N_{\text{el}}}) \end{vmatrix}. \quad (2.16)$$

$\varphi_i(\mathbf{r}_j, \sigma_j)$ denotes the single-particle wave function of the j th electron, located at \mathbf{r}_j and with spin σ_j (spin up or spin down) in state i (comprising orbital and spin quantum numbers).

Applying the Rayleigh-Ritz variational principle [36], the expectation value of the electronic Hamiltonian \hat{H} evaluated at any state is always larger or equal to the exact ground-state energy E_0 . Considering the wave functions $\varphi_i^*(\mathbf{r})$ and $\varphi_i(\mathbf{r})$ as independent, E_0^{HF} can be minimized with respect to the choice of spin-orbitals under the constraint of normalization introduced with Lagrange multipliers ϵ_i . This results in the Hartree-Fock equations

$$\left\{ -\frac{1}{2} \Delta_{\mathbf{r}} + v_{\text{ext}}(\mathbf{r}) + v_{\text{H}}(\mathbf{r}) \right\} \varphi_i(\mathbf{r}) + \int d^3 r' v_{\text{xx}}(\mathbf{r}, \mathbf{r}') \varphi_i(\mathbf{r}') = \epsilon_i \varphi_i(\mathbf{r}). \quad (2.17)$$

The Hartree potential $v_{\text{H}}(\mathbf{r})$ is defined as

$$v_{\text{H}}(\mathbf{r}) = \int d^3 r' \frac{n(\mathbf{r}')}{|\mathbf{r} - \mathbf{r}'|}, \quad (2.18)$$

where

$$n(\mathbf{r}) = \sum_{i=1}^{N_{\text{el}}} |\varphi_i(\mathbf{r})|^2 \quad (2.19)$$

is the electron density. The non-local, exact exchange potential is

$$v_{\text{xx}}(\mathbf{r}, \mathbf{r}') = - \sum_{i=1}^{N_{\text{el}}} \frac{\varphi_i(\mathbf{r}) \varphi_i^*(\mathbf{r}')}{|\mathbf{r} - \mathbf{r}'|}. \quad (2.20)$$

Comparing the Hartree-Fock equations with Eq. 2.13 and Eq. 2.14, the exact exchange potential together with the Hartree potential can be identified with the Hartree-Fock mean-field potential v_i^{MF} . In general, the Hartree-Fock equations need to be solved numerically. Since the solutions $\varphi_i(\mathbf{r})$ have to be known already to solve the equations, a self-consistent scheme is applied, where the effective single-particle Hamiltonian is first obtained from an initial guess of the $\varphi_i(\mathbf{r})$. Solving the Hartree-Fock equations for this approximate Hamiltonian leads to a new set of solutions, that are compared to the previous ones. These steps are repeated until self-consistency is reached. The Hartree-Fock ground-state wave function Ψ_0^{HF} is then the Slater determinant of the N_{el} single-particle orbitals with lowest energies ϵ_i .

Accordingly, the Hartree-Fock total energy E_0^{HF} is

$$\begin{aligned} E_0^{\text{HF}} = \langle \Psi_0^{\text{HF}} | \hat{H} | \Psi_0^{\text{HF}} \rangle &= \sum_{i=1}^{N_{\text{el}}} \int d^3r \varphi_i^*(\mathbf{r}) \left(-\frac{1}{2} \Delta_{\mathbf{r}} + v_{\text{ext}}(\mathbf{r}) \right) \varphi_i(\mathbf{r}) \quad (2.21) \\ &+ \frac{1}{2} \sum_{i,j=1}^{N_{\text{el}}} \int d^3r d^3r' \frac{|\varphi_i(\mathbf{r})|^2 |\varphi_j(\mathbf{r}')|^2}{|\mathbf{r} - \mathbf{r}'|} \\ &- \frac{1}{2} \sum_{i,j=1}^{N_{\text{el}}} \int d^3r d^3r' \frac{\varphi_i^*(\mathbf{r}) \varphi_i(\mathbf{r}') \varphi_j^*(\mathbf{r}') \varphi_j(\mathbf{r})}{|\mathbf{r} - \mathbf{r}'|}. \end{aligned}$$

The second term in Eq. 2.21 is the Hartree energy E^{H} , the last term is the HF exchange energy E_{xx} that does not appear in the Hartree theory. The Hartree-Fock theory is self-interaction free, since the diagonal terms ($i = j$) of the HF exchange energy cancel exactly the self-interaction terms in the Hartree energy. The energy contributions that are not covered by the Hartree-Fock theory are called correlation energy. The correlation energy effects account for deviations from the mean-field (dynamic correlation) and the single-determinant (non-dynamic correlation) approximations. Determining very accurately the missing correlation energy, that typically makes up a small but still important $\approx 1\%$ contribution, is the subject of quantum-chemistry methods which are briefly discussed in Sec. 2.4. Density-functional theory, on the other hand, takes a different approach, reformulating the problem such that the explicit functional form of exchange and correlation energy with respect to electron density remains to be determined.

2.3. Density-functional theory

Both Hartree and Hartree-Fock theory result in effective single particle equations which are then solved numerically within the self-consistent field scheme. This also holds true for density-functional theory, reusing the techniques that were developed before. In contrast to the wave function based approaches, DFT focusses on the electron density, which was pointed out by Hohenberg and Kohn in 1964 to uniquely determine the physical properties of a system [37]. Even shortly before the Hartree theory became known, the electron density had already taken up an important role in the Thomas-Fermi theory (1927) that suggested an approximation of the kinetic energy of an atom as a functional of the electron density [38, 39].

2.3.1. Hohenberg-Kohn theorem

The first part of the Hohenberg-Kohn theorem states that for a system of electrons in an external potential, as the one due to electron-nuclear interaction, this potential is a unique functional of the ground-state electron density $n(\mathbf{r})$, which is related to the number of electrons in the system via the normalization

$$N_{\text{el}} = \int d^3r n(\mathbf{r}). \quad (2.22)$$

The external potential determines the electronic Hamilton operator (Eq. 2.9) which on the other hand leads to the electronic states holding the complete physical information on the system. Consequently, any ground-state physical property, in particular energy, can formally be written as a functional of the density

$$E_0 = \langle \Psi_0 | \hat{H} | \Psi_0 \rangle = E_0[n(\mathbf{r})]. \quad (2.23)$$

In its original form the Hohenberg-Kohn theorem can be proven via *reductio ad absurdum* (see for example Ref. [40]). An extension to also non-degenerate ground states was elaborated by Levy in 1979 [41].

While the energy contribution of the external electron-nuclear potential is straightforward to express as a functional of the density using Eq. 2.8 and 2.19, the more challenging part is to deal with the functional dependence of

$$F[n(\mathbf{r})] = \langle \Psi_0 | \hat{T}_e + V_{e-e} | \Psi_0 \rangle, \quad (2.24)$$

whose explicit form as a closed expression in terms of the density is unknown. $F[n(\mathbf{r})]$ is also referred to as the Hohenberg-Kohn functional.

The second part of the Hohenberg-Kohn theorem offers a way for practical calculations of the ground state energy. It states that the density that minimizes the total energy is the exact ground-state density. Any trial density, for which $n^{\text{trial}}(\mathbf{r}) \neq 0$ and $\int n^{\text{trial}}(\mathbf{r}) d^3r = N_{\text{el}}$, yields an energy greater or equal to the ground-state energy of the system $E[n_0^{\text{trial}}(\mathbf{r})] \geq E_0$, so that E_0 can be approached applying a variational principle. In orbital-free DFT one calculates the energy for a certain trial density and improves it iteratively in analogy with the self-consistent field method known from the Hartree theory. But a successful approximation to 2.24, especially for the kinetic energy functional, is rather difficult to find. Therefore, the approach that was undertaken by Kohn and Sham in 1965 achieved great approval [42].

2.3.2. The Kohn-Sham equations

Kohn and Sham suggested to choose a non-interacting reference system with the same electron density as the true interacting system. The respective normalized single-particle states $|\varphi_i\rangle$ (an index KS for the single-particle orbitals is not introduced for simplicity) are often referred to as Kohn-Sham orbitals. The single-particle orbitals are used to construct a Slater determinant Ψ^{KS} which corresponds to the many-electron wave function for the fermionic system, in analogy with the proceeding in Hartree-Fock theory (Eq. 2.16). The electron density of the true system $n(\mathbf{r})$

can then be expressed as that of the fictitious reference system $n^{\text{KS}}(\mathbf{r})$ according to

$$n(\mathbf{r}) = n^{\text{KS}}(\mathbf{r}) = \sum_i^{N_{\text{el}}} |\varphi_i(\mathbf{r})|^2. \quad (2.25)$$

In contrast to the kinetic energy functional of the interacting system, that of the non-interacting reference system is explicitly known as

$$E_{\text{kin}}^{\text{KS}} = -\frac{1}{2} \sum_{i=1}^{N_{\text{el}}} \int d^3r \varphi_i^*(\mathbf{r}) \nabla^2 \varphi_i(\mathbf{r}). \quad (2.26)$$

To simplify the unknown full electron-electron interaction term, it is split into the classical electrostatic energy of an electron gas with density $n(\mathbf{r})$, the Hartree energy E_{H} (compare Eq. 2.21),

$$E_{\text{H}}[n(\mathbf{r})] = \frac{1}{2} \int d^3r d^3r' \frac{n(\mathbf{r})n(\mathbf{r}')}{|\mathbf{r} - \mathbf{r}'|}, \quad (2.27)$$

and an unknown remaining term $E_{e-e}[n(\mathbf{r})] - E_{\text{H}}[n(\mathbf{r})]$. The Hohenberg-Kohn functional may then be written in terms of the energy quantities for the non-interacting reference system as

$$F[n(\mathbf{r})] = E_{\text{kin}}^{\text{KS}} + E_{\text{H}}[n(\mathbf{r})] + \underbrace{E_{\text{kin}} - E_{\text{kin}}^{\text{KS}} + E_{e-e}[n(\mathbf{r})] - E_{\text{H}}[n(\mathbf{r})]}_{E_{\text{xc}}[n(\mathbf{r})]}. \quad (2.28)$$

The unknown energy contributions for the true interacting system are thus substituted by those of the non-interacting reference system plus the thereby neglected terms which are summarized in the exchange-correlation energy functional $E_{\text{xc}}[n(\mathbf{r})]$. Solving the variational problem under the constraint 2.22, where ϵ_j enter as Lagrange parameters,

$$\partial_{\varphi_i^*} \left(E_{\text{H}}[n(\mathbf{r})] - \sum_{j=1}^{N_{\text{el}}} \epsilon_j \left(\int d^3r |\varphi_j(\mathbf{r})|^2 - 1 \right) \right) = 0, \quad (2.29)$$

leads to a set of effective single-particle Schrödinger equations, the Kohn-Sham equations

$$\left\{ -\frac{1}{2} \nabla_{\mathbf{r}}^2 + v_{\text{H}}(\mathbf{r}) + v_{\text{xc}}(\mathbf{r}) + v_{\text{ext}}(\mathbf{r}) \right\} \varphi_i(\mathbf{r}) = \epsilon_i \varphi_i(\mathbf{r}). \quad (2.30)$$

These describe non-interacting quasi-electrons moving in an effective, local, potential

$$v_{\text{eff}}(\mathbf{r}) = v_{\text{H}}(\mathbf{r}) + v_{\text{xc}}(\mathbf{r}) + v_{\text{ext}}(\mathbf{r}), \quad v_{\text{xc}}(\mathbf{r}) = \frac{\partial E_{\text{xc}}[n(\mathbf{r})]}{\partial n(\mathbf{r})}, \quad (2.31)$$

where the mean-field potential defined in Eq. 2.13 is the sum of the Hartree potential and the exchange-correlation potential. Reformulating the variational problem in terms of wave functions instead of densities partly spoils the beauty of the Hohenberg-Kohn theorem, but it is necessary, since they are needed for the kinetic energy of the non-interacting reference system. Strictly speaking, single-particle eigenstates $\varphi_i(\mathbf{r})$ of the KS reference system do not have a

physical meaning. Nevertheless, the corresponding eigen energies ϵ_i are often good approximations to the electronic single-particle ionization energies of the true interacting system. In specific, it can be shown that in exact DFT, the highest occupied energy level equals the exact first vertical ionization energy¹ [43, 44]. Furthermore, according to the Janak theorem [45] (the DFT analog of the Koopman theorem of HF theory [46]), the exact electron affinity of a system with N_{el} electrons is

$$E_{N_{\text{el}}+1} - E_{N_{\text{el}}} = \int_0^1 \varepsilon_l(n) dn, \quad (2.32)$$

where $\varepsilon_l(n)$ is the DFT eigenvalue for the lowest unoccupied orbital of the N_{el} system, and $0 \leq n \leq 1$ electrons are introduced into this orbital. Approximating this integral, for example in a lowest-order approximation by evaluating it only at the midpoint $n = \frac{1}{2}$, can in practice be used to calculate electron affinities or ionization energies [45, 47].

The Kohn-Sham equations must be solved self-consistently, since the effective potential depends on the final result for $n(\mathbf{r})$. For computational convenience the DFT total energy is typically calculated using the sum over the KS eigen energies

$$E_0^{\text{DFT}}[n] = \sum_{i=1}^{N_{\text{el}}} \epsilon_i - E_{\text{H}}[n] + E_{\text{xc}}[n] - \int d^3r v_{\text{xc}}([n(\mathbf{r})], \mathbf{r}) n(\mathbf{r}). \quad (2.33)$$

Since the exchange-correlation functional is not generally known, the consecutive step must be to find an approximate expression for $v_{\text{xc}}([n(\mathbf{r})])$. Opposed to quantum-chemical methods, which allow for successive improvement of accuracy, there is no obvious systematic way to do so for the exchange-correlation functional. Still, already rather crude approximations have proven to lead to good agreement with experimental observations and valuable physical insight.

2.3.3. Exchange-correlation approximations and hybrid functionals

A system, for which the exchange-correlation functional is known, is the homogeneous electron gas. For this model system, an analytic expression exists for the exchange energy density [48], while the correlation energy density can be determined numerically with extremely high precision [49]. In a jellium approach, the exchange-correlation energy is evaluated locally, at each point in space, using the exchange-correlation energy density $\epsilon_{\text{xc}}^{\text{HEG}}[n(\mathbf{r})]$ of the homogeneous electron gas,

$$E_{\text{xc}}[n] \approx E_{\text{xc}}^{\text{LDA}}[n] = \int d^3r n(\mathbf{r}) \epsilon_{\text{xc}}^{\text{HEG}}[n(\mathbf{r})]. \quad (2.34)$$

This became known as the local-density approximation (LDA) [42, 49, 50]. Using the local exchange-correlation energy of the homogeneous electron gas and therefore neglecting the true non-locality of $E_{\text{xc}}[n]$ works well for systems with slowly varying electron density, as for example for metallic solids or *sp*-bonded semiconductors [51]. Still, there are serious deficiencies,

¹The term *vertical* ionization energy refers to the energy required to remove one electron from the system, where possible changes in geometry that may result from the ionization are neglected. In a configuration coordinate diagram, which shows the total energy of a system as a function of configuration coordinate, this corresponds to the vertical distance between the energy minimum of the curve for N_{el} electrons and the curve for $N_{\text{el}} - 1$ electrons.

as LDA in general tends to an overbinding, which leads for example to overestimated cohesive energies. Especially for atoms and small molecules, with a strong variation of electron density in space, this is a severe drawback. Also, the local-density approximation introduces an electron self-interaction error, which means that Kohn-Sham orbitals that are highly localized may be destabilized.

An improvement in some points was achieved by semi-local generalized gradient approximations (GGA), which additionally take into account the dependence of the exchange-correlation energy on the gradient of the electron density

$$E_{\text{xc}}[n] \approx E_{\text{xc}}^{\text{GGA}}[n, |\nabla n|] = \int d^3r n(\mathbf{r}) \epsilon_{\text{xc}}^{\text{GGA}}[n, |\nabla n|]. \quad (2.35)$$

The exchange-correlation energy density $\epsilon_{\text{xc}}^{\text{GGA}}[n, |\nabla n|]$ can be separated into exchange and correlation contribution. The exchange energy density is expressed as that of the homogeneous electron gas multiplied with an enhancement factor $F_{\text{x}}[n, |\nabla n|]$,

$$\epsilon_{\text{x}}^{\text{GGA}}[n, |\nabla n|] = \epsilon_{\text{x}}^{\text{HEG}}[n] F_{\text{x}}[n, |\nabla n|]. \quad (2.36)$$

In the proximity of an electron the probability of finding another electron is reduced. This depletion of electrons (also called exchange-correlation hole) follows the electron density gradient and the result is an increased exchange energy density. The enhancement factor $F_{\text{x}}[n, |\nabla n|] \geq 0$ accounts for this effect. In the limit of a homogeneous system, where $|\nabla n| \rightarrow 0$, the local density approximation is recovered. However, it is not obvious how the exact functional form of $F_{\text{x}}[n, |\nabla n|]$ should be chosen. Different GGA flavors have been suggested, determining the enhancement factor in accordance with certain physical constraints or using parameters obtained by fitting certain properties of a class of systems to experimental results. The very successful Perdew-Burke-Ernzerhof (PBE) GGA, that was published in 1996 [52], obtains the exchange enhancement factor $F_{\text{x}}[n(\mathbf{r})]$ by using the form

$$F_{\text{x}}(s) = 1 + k_{\text{F}} - \frac{k_{\text{F}}}{1 + \frac{\mu s^2}{k_{\text{F}}}}, \quad (2.37)$$

where the reduced density gradient s is defined as

$$s := \frac{|\nabla n(\mathbf{r})|}{2k_{\text{F}}(\mathbf{r})n(\mathbf{r})}. \quad (2.38)$$

The functional form of $F_{\text{x}}(s)$ and the constants μ and k_{F} are determined by making the PBE exchange-correlation energy $E_{\text{xc}}^{\text{PBE}}$ reproduce the limit of known linear response for the uniform electron gas, and by making $E_{\text{xc}}^{\text{PBE}}$ obey the Lieb-Oxford criterium, which provides an upper bound for $F_{\text{x}}(s)$ [53].

In most cases, GGA functionals improve on bulk properties of solids like cohesive energies and lattice constants, as compared to LDA [54–56]. Considering molecules, atomization energies can be calculated more accurately using GGA than using LDA, while only small improvement is achieved for ionization energies and electron affinities (for details see Ref. [57] and references therein).

Still, a major drawback of the semi-local exchange-correlation functional is the incomplete self-interaction cancellation. For systems where localization plays an important role, e.g. for defects or surfaces, this deficiency can lead to large systematic errors.

On the contrary, Hartree-Fock theory does not suffer from the self-interaction error, but it lacks correlation energy, which leads to large errors in the description of chemical bonding. In order to partially cancel the self-interaction error in the semilocal GGA functional, combining GGA with HF exchange seems a promising solution. The idea was introduced by Becke in 1993 in the following form [58]:

$$E_{\text{xc}}^{\text{hyb}}[n] = \alpha \cdot E_{\text{xx}}[\varphi_i[n]] + (1 - \alpha) E_{\text{x}}^{\text{GGA}}[n] + E_{\text{c}}^{\text{GGA}}[n]. \quad (2.39)$$

So a fraction α of the exchange part of the GGA exchange-correlation functional is substituted by HF exchange. E_{xx} differs from the HF exchange energy (Eq. 2.21) in so far that it is not evaluated at the optimal HF Slater determinant as in HF theory, but instead at the orbitals of the non-interacting Kohn-Sham reference system. As a consequence of using the non-local E_{xx} , the exchange-correlation approximation is no longer local. The formal grounds for the derivation of this type of hybrid functional are within generalized DFT theory that incorporates KS-DFT as a special case, using an adiabatic connection between the noninteracting Kohn-Sham reference system and the fully interacting true system through a continuum of partially interacting systems, where all of those systems share a common density (see also Sec. 2.4). While the hybrid exchange-correlation energy expressed in Eq. 2.39 meets the expectations on reducing the self-interaction error and works well for molecules [59], it cannot be considered satisfying for metals and narrow-bandgap semiconductors, due to the long-range part of the exchange that should mostly cancel with the exact correlation [60–62]. Since only approximate correlation is used, remaining terms from the long-range part of the Hartree-Fock exchange introduce some error. For this reason it is desirable to include only a short-range part of Hartree-Fock exchange, and partition the Coulomb operator $\frac{1}{r} = \frac{1}{|r-r'|}$ in E_{xx} (Eq. 2.21) accordingly.

The Heyd-Scuseria-Ernzerhof functional HSE [63] introduces a screening parameter ω that partitions the Coulomb potential for exchange into a long-range (LR) and a short-range (SR) part using the computationally convenient error function

$$\frac{1}{r} = \underbrace{\frac{\text{erfc}(\omega r)}{r}}_{\text{SR}} + \underbrace{\frac{\text{erf}(\omega r)}{r}}_{\text{LR}}. \quad (2.40)$$

The exchange-correlation approximation then reads

$$E_{\text{xc}}^{\text{HSE}}(\alpha, \omega) = \alpha E_{\text{xx}}^{\text{SR}}(\omega) + (1 - \alpha) E_{\text{x}}^{\text{PBE,SR}}(\omega) + E_{\text{x}}^{\text{PBE,LR}}(\omega) + E_{\text{c}}^{\text{PBE}}. \quad (2.41)$$

There are two prominent limiting cases for $E_{\text{xc}}^{\text{HSE}}$. If ω is set to zero, a fraction α of the full exchange energy is replaced by exact exchange, and for $\alpha = 0.25$ the PBE0 exchange-correlation functional is recovered [64]. As ω approaches infinity or for $\alpha = 0$, $E_{\text{xc}}^{\text{HSE}}$ reduces to the pure GGA functional $E_{\text{xc}}^{\text{PBE}}$. In the HSE06 version of the functional [65], the exchange parameter is set to $\alpha = 0.25$, as optimized for atomization energies of molecules, based on perturbation theory arguments [64]. The range-separation parameter is selected empirically as 0.11 bohr^{-1} [65]. The value for ω was chosen from the performance of the functional for test sets of atoms,

molecules (G3/99 test set of 223 standard enthalpies of formation, 88 ionization potentials, and 58 electron affinities), and 29 solids covering insulators, semiconductors and metals. Within these tests it was shown that variation of the screening parameter strongly influences bandgaps of solids, while properties of molecular thermochemistry or lattice constants of solids are not so sensitive to its variation. Apart from the enhancement in modeling solid-systems properties, HSE06 is also easing the computational effort as compared to the earlier, not range-separated, hybrid functionals. The HF exchange interaction decays slowly with distance in metals and narrow-bandgap semiconductors, but it only needs to be evaluated for the short-range part and therefore computational costs are reduced, in particular for bulk and surface models of extended systems.

Hybrid functionals are sometimes regarded as not truly *ab initio*, because many of them involve parameters that are obtained by fitting to certain properties of materials. The B3LYP (Becke, three-parameter, Lee-Yang-Parr) hybrid functional for example owes its name to three parameters which determine, similar to α for the HSE functional, to what amount exact exchange and LDA as well as PBE exchange and correlation are mixed [66]. B3LYP was introduced in 1994, nine years before HSE. The three parameters were obtained from fitting to a set of atomization energies, ionization potentials, proton affinities, and total atomic energies, concentrating on good performance for molecular systems. Therefore, B3LYP has been widely and successfully used for calculations of molecules for the last 20 years.

Usually the predefined parameter sets have carefully been chosen to perform well at least for a large class of systems or materials and are therefore not intended to be changed. Still it is not uncommon that the parameters are fit to an individual system. This is assuming that a parameter set, performing well for a known property, will also yield valid predictions for the property of interest. However, if a hybrid functional's parameters are chosen to agree with a known value of property A, is this really the property relevant in order to obtain meaningful results also for property B? And are there ways to check the quality of the choice? In this thesis these questions will be addressed in detail on the example of defect formation energies calculated with HSE(α, ω).

2.4. Beyond DFT and HF: MP2, RPA, *GW*, and coupled-cluster

Validation with higher level methods is an option to reliably assess the performance of hybrid functionals. Therefore, also perturbative methods are used in this work to compare ground-state energy differences calculated with MP2, RPA, and coupled-cluster approaches, and electron-addition or ionization energies based on the *GW* approximation, with hybrid DFT results for specific MgO systems. Since these calculations are computationally expensive, they are, with the exception of non-self-consistent *GW*, usually applied to finite systems only, and the number of electrons that can be treated in practice is limited. The theoretical background of these methods is briefly reviewed in the following paragraphs.

Starting from the Slater determinant that solves the Hartree-Fock equations (Eq. 2.17), some methods aim to improve the model by introducing the missing correlation between electrons that is so far neglected. This can be done considering virtual excited states, by replacing occupied states in the Slater determinant with unoccupied states (virtual orbitals). Replacing one, two,

three,... states means to consider single, double, triple,... excitations.

One of the methods where excitations are introduced perturbatively is the Møller-Plesset perturbation theory [67]. The deviation between the true electronic Hamiltonian \hat{H} and the HF mean-field Hamiltonian \hat{H}^{HF} ,

$$\hat{H}' = \hat{H} - \hat{H}^{\text{HF}}, \quad (2.42)$$

can be expressed as a perturbative contribution to the unperturbed Hartree-Fock total energy. E_0^{HF} (Eq. 2.21) is already exact to first order, so that, following Rayleigh-Schrödinger perturbation theory, the ground-state energy in second-order perturbation (MP2) is

$$E_0 \approx E_0^{\text{HF}} + \sum_{l \neq 0} \frac{|\langle \Psi_l^{\text{HF}} | \hat{H}' | \Psi_0^{\text{HF}} \rangle|^2}{E_0^{\text{HF}} - E_l}. \quad (2.43)$$

Excited Slater determinants are denoted Ψ_l^{HF} , and E_l are the respective energy eigenvalues. According to the Brillouin theorem, singly excited HF states do not contribute in Eq. 2.43 (see for example Ref. [68] for derivation). Also, excitations of higher order than double excitations do not contribute, since \hat{H}' is a two-particle operator

$$\hat{H}' = \sum_{i < j}^{N_{\text{el}}} \frac{1}{|\mathbf{r}_i - \mathbf{r}_j|} - \sum_{i=1}^{N_{\text{el}}} v_i^{\text{HF}}. \quad (2.44)$$

Drawbacks of the MP2 method are divergence of the energy for metals and often an overestimation of the absolute value of the correlation energy due to the truncation of the expansion.

A method that overcomes these problems is the random-phase approximation (RPA). Originally it was used as an approximation in the description of the homogeneous electron gas by Bohm and Pines in the 1950s [69–71]. In an electron gas of high density the electron density fluctuates. On the one hand, long-range Coulomb interaction leads to collective oscillations termed plasma oscillations and screening of the individual electrons. On the other hand, when looking at a smaller length scale, there is a two-body screened Coulomb interaction between individual randomly moving electrons, interpreted as an individual quasi-particles component of the electron density fluctuations. Bohm and Pines state that the plasma component and the individual quasi-particles component of the electron density fluctuations can be regarded as decoupled. This means that random phase shifts in the collective oscillation, which may be caused by randomly distributed quasi-particles, are assumed to average to zero. In the form it is applied today, RPA can be derived in different ways, for example via Green-function-based many-body perturbation theory or in the framework of coupled-cluster theory, as reviewed by Ren *et al.* [72]. The derivation sketched here (details can be found in Ref. [72]) starts from the adiabatic connection [73–75], where a mean-field reference system is adiabatically connected to the many-body interacting system via a coupling strength $0 \leq \lambda \leq 1$. Within this framework, an exact expression for the DFT exchange-correlation energy can be deduced. The mean-field reference system is then the KS single-particle reference system. The exchange-correlation energy expression depends on the exchange-correlation hole which describes the fact that an electron located at \mathbf{r} reduces the probability of another electron being present in its vicinity at \mathbf{r}' . The exchange-correlation hole can be expressed in terms of density-density correlations which are formally

fluctuations of the density operator around its expectation value. According to the fluctuation-dissipation theorem [76], the response of a system in thermal equilibrium to a small external perturbation is equal to its response to a spontaneous internal fluctuation in the absence of a perturbation. This makes a link between the fluctuations and response properties of the system, shifting the challenge of finding a suitable approximation to the exchange-correlation energy (as discussed in the context of DFT) to the question of how to approximate the response functions of a series of fictitious systems along the adiabatic connection path. This is where RPA is applied – as an approximation to the response function $\chi^\lambda(\mathbf{r}, \mathbf{r}', i\omega)$. The exchange-correlation energy can be written as the sum of exact-exchange energy E_{xx} and RPA correlation energy E_c^{RPA} ,

$$\begin{aligned} E_c^{\text{RPA}} &= \frac{1}{2\pi} \int_0^\infty d\omega \text{Tr}[\ln(\epsilon(i\omega)) + (1 - \epsilon(i\omega))] \\ &= \frac{1}{2\pi} \int_0^\infty d\omega \text{Tr}[\ln(1 - \chi^0(i\omega)v) + \chi^0(i\omega)v] \\ &= -\frac{1}{2\pi} \int_0^\infty d\omega \sum_{n=2}^\infty \frac{1}{n} \text{Tr}[(\chi^0(i\omega)v)^n]. \end{aligned} \quad (2.45)$$

v is the unscreened Coulomb interaction, ϵ is the frequency-dependent RPA dielectric constant. The independent particle response function of the Kohn-Sham reference system $\chi^0(\mathbf{r}, \mathbf{r}', i\omega)$ is known according to

$$\chi^0(\mathbf{r}, \mathbf{r}', i\omega) = \sum_i^{\text{occ}} \sum_j^{\text{unocc}} \frac{\varphi_i^*(\mathbf{r}) \varphi_j(\mathbf{r}) \varphi_j^*(\mathbf{r}') \varphi_i(\mathbf{r}')}{\epsilon_i - \epsilon_j - i\omega} + \text{c.c.} \quad (2.46)$$

with single-particle orbitals $\varphi_i(\mathbf{r})$ and corresponding energies ϵ_i from the mean-field approach of choice. The same wave functions are also used to calculate E_{xx} . RPA is typically calculated non-self-consistently. The main improvement of RPA compared to MP2 is that it takes into account not the bare but the screened Coulomb interaction. The RPA correlation energy comprises the response of the non-perturbed system to a perturbation as well as the response of the response, etc., such that the contributions are summed up to infinite order in the perturbation. This makes it applicable also for zero-bandgap materials. Furthermore, the exact-exchange energy cancels the spurious self-interaction error in the Hartree energy, although there is still an RPA self-correlation error. The fully non-local RPA correlation energy also includes long-range van der Waals effects. Deficiencies of RPA are a systematic underestimation of binding energies [77–79] and insufficient description of short-range correlation [80].

The methods discussed so far have been developed to approximate the ground-state energy of a system. By taking the Hartree-Fock or DFT ground-state energy differences between systems of N and $N \pm 1$ electrons, also electron affinities or ionization energies can be calculated. This is known as the Δ -SCF method, since it uses the energy difference between two self-consistent-field (SCF) calculations [51]. An alternative way to compute excited states is to use a Green function formalism. The basic theory of Green functions can for example be found

in Ref. [81, 82]. The frequency-dependent Green function $G(\mathbf{r}, \mathbf{r}'; \omega)$ for a Hamiltonian with a time-independent external potential $v_{\text{ext}}(\mathbf{r})$ as introduced in Sec. 2.1 solves the Dyson equation according to

$$[\omega + \frac{1}{2}\delta - v_{\text{ext}}(\mathbf{r}) - v_{\text{H}}(\mathbf{r})]G(\mathbf{r}, \mathbf{r}'; \omega) - \int d^3r'' \Sigma(\mathbf{r}, \mathbf{r}''; \omega)G(\mathbf{r}'', \mathbf{r}'; \omega) = \delta(\mathbf{r} - \mathbf{r}'). \quad (2.47)$$

$v_{\text{H}}(\mathbf{r})$ is the Hartree potential (Eq. 2.18) and $\Sigma(\mathbf{r}, \mathbf{r}''; \omega)$ is the dynamical, non-local, complex self-energy, comprising all many-body exchange-correlation effects. The so-called GW approximation as introduced by Hedin in 1965 [83] expresses the self-energy as the leading term in an expansion in powers of the screened Coulomb potential according to

$$\Sigma^{GW}(\mathbf{r}, \mathbf{r}'; \omega) = \frac{i}{2\pi} \int d\omega' G(\mathbf{r}, \mathbf{r}'; \omega + \omega')W(\mathbf{r}, \mathbf{r}'; \omega')e^{i\omega\nu}. \quad (2.48)$$

The screened Coulomb potential W can be written as

$$W(\mathbf{r}, \mathbf{r}'; \omega) = \int d^3r'' \varepsilon^{-1}(\mathbf{r}, \mathbf{r}''; \omega)v(\mathbf{r}'', \mathbf{r}'), \quad (2.49)$$

where v is the bare Coulomb potential and ε is the dynamical dielectric function. The Hedin and Dyson equations require to be solved self-consistently, but in practice the non-self-consistent G_0W_0 method is often used, where from DFT single particle orbitals $\varphi_n(\mathbf{r})$ and energies ϵ_n a non-interacting Green function $G_0(\mathbf{r}, \mathbf{r}'; \omega)$ and an approximate W_0 are calculated. The non-interacting Green function is

$$G_0(\mathbf{r}, \mathbf{r}'; \omega) = \sum_n \frac{\varphi_n(\mathbf{r})\varphi_n^*(\mathbf{r}')}{\omega - \epsilon_n - i\nu \text{sgn}(\epsilon_{\text{F}} - \epsilon_n)}, \quad (2.50)$$

where the Fermi energy is denoted as ϵ_{F} and ν is a positive infinitesimal. G_0 and W_0 are used in Eq. 2.48 to obtain $\Sigma^{G_0W_0}$ and from this the G_0W_0 corrected eigen energies are calculated as

$$\epsilon_n^{G_0W_0} = \epsilon_n + \langle \phi_n | \Sigma^{G_0W_0}(\epsilon_n^{G_0W_0}) - v^{\text{xc}} | \phi_n \rangle. \quad (2.51)$$

In the correction term, the local DFT reference exchange-correlation potential is substituted by the non-local, energy-dependent GW self-energy. The GW method is very successful in the description of single-particle excitations in solids [84, 85]. Also total energies and structural properties can be extracted [86–88]. Compared to a self-consistent GW calculation, the G_0W_0 method is computationally much more efficient, but can suffer from starting-point dependence with respect to the DFT method chosen to compute the single-particle reference states and energies [89–91]. In this work, the consistency between ionization energies calculated with G_0W_0 and the reference DFT functional is used to identify optimal hybrid-functional parameters for defect calculations in MgO.

The method of choice for high-accuracy calculations of small molecules and clusters is the coupled-cluster method. In defect physics this method becomes practically interesting if a defect is so localized that it can already be described with a small cluster model. For example, for the neutral oxygen vacancies in MgO this is the case. The idea behind coupled-cluster theory is closely related to that of the configuration interaction method.

Rather than treating single, double or higher excitations perturbatively, as for example in MP2, it is also possible to directly use a modified wave function built from a linear combination of configuration state functions. In a configuration interaction model [92], symmetry-adapted linear combinations of the Hartree-Fock Slater determinant are used, where zero (Ψ_{HF}), one ($\Psi_i^{(1)}$) or two ($\Psi_i^{(2)}$) or more spin orbitals have been substituted with virtual orbitals (representing different electron configurations). For example, in case of configuration interaction with single and double excitations (CISD) the electronic ground state of the system can then be approximated according to

$$\Psi_0^{\text{CISD}} = \Psi_0^{\text{HF}} + \sum_i a_i^{(1)} \Psi_i^{(1)} + a_i^{(2)} \Psi_i^{(2)}. \quad (2.52)$$

The coefficients $a_i^{(1)}$ and $a_i^{(2)}$ are varied to find the optimal wave function. This means, interaction between different configurations is taken into account to obtain the desired ground-state wave function. If all possible configuration state functions are considered, meaning that all Slater determinants obtained by exciting all possible electrons to all possible virtual orbitals are included, full CI is recovered, which solves exactly the electronic Schrödinger equation within the space spanned by the orbital basis set. If not only the ground-state Hartree-Fock Slater determinant but also one or more excited configurations are used as a reference from which corresponding configuration state functions are built, this is referred to as multi-reference CI (MRCI). In general this should improve the correlation description, but the choice of reference Slater determinants must be made carefully in order to indeed include the dominant configurations. Opposed to Hartree-Fock theory, many-body perturbation theory, and full CI, the truncated CI and MRCI methods are not size-consistent, which means that, if obtained with truncated CI or MRCI, the sum of energies of two separate systems does not equal the energy of a system where both are included as non-interacting subsystems.

The coupled-cluster method is formally similar to CI, but fulfills size-consistency. It was first presented in the context of nuclear physics in 1960 [93] and six years later adapted to be used as an electronic-structure method [94]. Instead of including excitations linearly, an exponential approach is taken, where excitation operators $\hat{T}^{(j)}$ in the exponent act on the reference wave function, which is, as in CI, typically the Hartree-Fock Slater determinant. Again, states containing single, double, triple (...) excitations are generated. The single-excitation operator is most intuitively expressed in second quantization using the creation and annihilation operators \hat{a}^+ and \hat{a} as

$$\hat{T}^{(1)} = \sum_f \sum_i t_i^f \hat{a}_f^+ \hat{a}_i. \quad (2.53)$$

For $\hat{T}^{(1)}$ acting directly on the HF Slater determinant $\hat{T}^{(1)}|\Psi_0^{\text{HF}}\rangle$ this means that for each initially occupied state i a set of Slater determinants is created, where the state i is swapped for one of the available unoccupied states f . In the same fashion double ($j=2$), triple ($j=3$) and further excitation operators may be defined, making up the overall excitation operator $\hat{T} = \sum_j \hat{T}^{(j)}$ from which the coupled-cluster wave function is constructed with the overall excitation operator in the exponent, according to

$$|\Psi^{\text{CC}}\rangle = e^{\hat{T}}|\Psi_0^{\text{HF}}\rangle. \quad (2.54)$$

The coefficients t_i^f for all included excitations remain to be determined. In order to make this task feasible, usually only excitation operators generating up to double or triple excitations are included. Due to the exponential approach this does not keep higher excitations from contributing as well, since

$$e^{\hat{T}} = \sum_n \frac{\hat{T}^n}{n!}, \quad (2.55)$$

where the summation is restricted by the number of occupied and unoccupied states in the system. The coupled-cluster coefficients can be obtained by multiplying the CC Schrödinger equation

$$\hat{H} e^{\hat{T}} |\Psi_0^{\text{HF}}\rangle = E e^{\hat{T}} |\Psi_0^{\text{HF}}\rangle \quad (2.56)$$

by $e^{-\hat{T}}$ (resulting in a similarity transform of the Hamilton operator) and then projecting it to the set of the excited determinants that correspond to the sought coefficients. If all singly-excited determinants are denoted as $|\Psi_S^{\text{CC}}\rangle$, all doubly-excited as $|\Psi_D^{\text{CC}}\rangle$, etc., the CC coefficients are determined from the following system of equations

$$\begin{aligned} \langle \Psi_0^{\text{HF}} | e^{-\hat{T}} \hat{H} e^{\hat{T}} | \Psi_0^{\text{HF}} \rangle &= E \\ \langle \Psi_S^{\text{CC}} | e^{-\hat{T}} \hat{H} e^{\hat{T}} | \Psi_0^{\text{HF}} \rangle &= E \langle \Psi_S^{\text{CC}} | e^{-\hat{T}} e^{\hat{T}} | \Psi_0^{\text{HF}} \rangle = 0 \\ \langle \Psi_D^{\text{CC}} | e^{-\hat{T}} \hat{H} e^{\hat{T}} | \Psi_0^{\text{HF}} \rangle &= E \langle \Psi_D^{\text{CC}} | e^{-\hat{T}} e^{\hat{T}} | \Psi_0^{\text{HF}} \rangle = 0 \\ &\dots \end{aligned} \quad (2.57)$$

The highest excitation level is determined by that in the \hat{T} operator. The first equation yields the energy of the system after the coefficients have been obtained from iteratively solving the rest of them. In analogy with the CI nomenclature, CCS, CCSD, CCSDT may be performed including the excitation operators up to single, double or triple excitations, respectively. Because of the immense computational costs for including double or even triple excitations, it is also common to include for example triple excitations only perturbatively, denoted as CCSD(T). Again, including all possible excitations leads to the full CI solution, but the convergence to this limit with the highest level of excitation included in the excitation operator is known to be much faster than in the case of the CI expansion. In analogy to CI, also multi-reference CC methods exist, but computationally so demanding that today they can hardly be applied to systems other than small molecules.

2.5. Electronic-structure code of choice: FHI-aims

The usual strategy to solve the DFT effective single-particle equations is to expand the Kohn-Sham orbitals $\varphi_i(\mathbf{r})$ into a set of basis functions $\phi_j(\mathbf{r})$

$$\varphi_i(\mathbf{r}) = \sum_j c_{ij} \phi_j(\mathbf{r}). \quad (2.58)$$

These basis functions are for example plane waves, suiting well periodic boundary conditions, or atom-centered localized orbitals. The latter are often described by Gaussians, as for example

in the electronic-structure package NWChem [95] and TURBOMOLE [96] used for reference calculations in this work, or Slater-like orbitals. Also, numeric atom-centered orbital (NAO) basis functions can be used, as utilized in DMol [97, 98] and in the electronic-structure code employed for most of the calculations presented in this work, FHI-aims [99]. In FHI-aims, localized NAO basis functions of the form

$$\phi_i(\mathbf{r}) = \frac{u_i(r)}{r} Y_{lm}(\Theta, \Phi) \quad (2.59)$$

are employed, where $Y_{lm}(\Theta, \Phi)$ are spherical harmonics and $u_i(r)$ is the numerically tabulated and therefore flexible radial part. It is obtained by solving a radial Schrödinger-like equation on a logarithmic grid using a steep potential to spatially confine the basis functions. This makes a linear scaling with system size possible for large systems. Species-dependent basis sets are constructed in a hierarchical manner, such that the accuracy due to the used basis set in a calculation can be systematically increased. The minimal basis set is built from the core and valence functions of spherically symmetric free atoms. This is beneficial for the all-electron calculation, because the oscillatory behavior of the wave functions in the core-region is sufficiently accurately taken into account already at this level. A systematic hierarchy of basis sets for each atomic species is constructed by adding to the respective minimal basis set on the one hand radial functions of free ions mainly responsible for the description of chemical bonds, and on the other hand hydrogen-like functions which also improve the description of polarization and diffuse functions. These additional basis functions are arranged into tiers according to the improvement they induce for the total energy of a dimer of each element obtained with an LDA functional (see Ref. [99] for details on the basis construction process). Each tier contains several basis functions of different angular momenta, such as s, p, d, f, \dots functions.

In FHI-aims the three-dimensional integrations needed for the setup of the Hamiltonian and overlap matrices are performed on a real-space grid that includes all points from overlapping atom-centered grids. For localization of integrations needed to construct the Hamiltonian and overlap matrices, atom-centered partition functions are used. A Lebedev grid [100] of spherical integration shells around each atom is then employed for accurate integral evaluations.

To determine the Hartree potential, first the electrostatic potential associated with the initial superposition of free-atom densities is calculated. This main contribution of the Hartree potential is accurately interpolated with cubic spline functions on dense logarithmic grids. It is therefore convenient in each following scf cycle to only compute the electrostatic potential corresponding to the difference $\Delta n(\mathbf{r})$ between current electron density and superposition of free atoms. $\Delta n(\mathbf{r})$ is decomposed into a sum of partitioned, atom-centered charge multipoles and, according to the Green-function solution to the Poisson equation for multipoles from classical electrostatics, the respective Hartree potential components are calculated on a dense logarithmic grid, then numerically tabulated, and finally evaluated using cubic spline interpolation. For periodic boundary conditions, long-range contributions from distant unit cells of the difference density multipole components are accounted for by using the Ewald method [101, 102].

Hybrid density-functionals, RPA, MP2 and the *GW* method for finite and in the case of hybrid DFT also for periodic systems, which involve exact-exchange and/or non-local correlation terms, are implemented in FHI-aims using the resolution of identity technique. This is advantageous for calculating two-electron Coulomb repulsion integrals and the linear density-response function

(required for RPA and *GW*), based on NAO basis functions [103].

It is important to ensure that convergence with respect to the numeric and basis settings used to calculate a certain property for a specific system is reached. To ease the process of obtaining converged parameters, FHI-aims provides preconstructed default parameter options controlling the basis set (tiers), all integration grids (in particular the location-dependent grid density), and the accuracy of the Hartree potential (specifying the highest angular momentum for the multipole decomposition of the atom-center-partitioned charge density) for each species. These are called *light*, *tight*, and *really tight* (or *safe*), and allow to systematically increase the accuracy of a total energy or, more commonly desired, total energy differences. Within each default numeric parameter set the basis set tiers can orderly be increased or decreased. If not mentioned otherwise, for the calculations of defect formation energies performed in this work the *light* pre-defined settings have been used for geometry prerelaxations, and final, converged results for the ground-state structures and energies have been obtained using *tight* settings. Convergence tests for the parameter options used for the calculations in this work, as well as further computational details, can be found in the appendix.

Forces are needed in this work for structural relaxation and phonon computations via the finite displacement method. They are calculated by taking the negative analytic gradient of the total energy with respect to the nuclear coordinates including Hellmann-Feynman forces due to the embedding of each nucleus into the electrostatic field of the electron density and all other nuclei, as well as a correction term consisting of electrostatic multipole derivatives, and a further correction term, the Pulay forces [104], which is due to the dependence of the chosen atom-centered basis functions on the atomic coordinates. For GGA functionals, the variation of the density gradient with respect to the atomic coordinates has to be accounted for in addition (see also Ref. [105] and references therein).

3. Computational models for defect calculations

Different structure models can be employed to calculate point defects in the bulk or at the surface of a solid, applying the electronic-structure methods discussed above. Most common are the embedded cluster and the supercell model. Also, a cyclic cluster approach [106] or Green function methods [107–111] can be used, but are today rather scarce in application, due to their methodological complexity. In the following, embedded cluster and supercell method are described and the advantages and challenges of both approaches are discussed. A novel scheme for charge compensation in supercell calculations is introduced, since previous approaches are dissatisfying, in particular for charged surface systems. Charge compensation is necessary on the one hand, from a technical point of view, to avoid divergence of the electrostatic potential in a periodic calculation. On the other hand, it is shown that realistic charge compensation can make the theoretical model of defects in a metal oxide more realistic.

3.1. Two well-established approaches: cluster and supercell

For an embedded cluster calculation a part of the crystal structure containing the defect and surrounding atoms is chosen. This set of atoms is treated fully quantum-mechanically. The cluster is embedded in a set of point charges or a potential to account for long-range electrostatic interactions due to atoms of the crystal lattice outside the cluster region. For example, when modeling a defect in the strongly ionic material MgO, point charges 2+ for magnesium and 2– for oxygen ions are placed at the respective lattice positions, mimicking the further extended crystal lattice outside the cluster region. In addition to the point charges, the embedding can be improved by an intermediate region of pseudopotentials. In this work, pseudopotentials are placed at the first shell of embedding magnesium atoms of an MgO cluster to minimize non-physical polarization of peripheral oxygen anions by the embedding point charges. Alternatively, this intermediate region can be approximated using the shell model, as done for defects at the MgO surface by Sushko *et al.* [112]. Within this model an ion in the intermediate region is treated as a point core and shell connected by a spring simulating its dipole polarizability. The positions of the cores and shells in the intermediate region can be optimized with respect to the total energy of the system, in accordance with the relaxed geometric and electronic structure of the inner cluster. For materials with a more covalent bonding character pseudopotential and point charge embedding is also possible. In this case, point charges should be chosen according to the true ionicity of the crystal, which may not equal the formal charges of the atoms in the cluster. Oxidation numbers can for instance be determined by a population analysis of wavefunctions (e.g. Mulliken analysis [113]) or by partitioning the electron density (e.g. Hirshfeld analysis [114]). Another possibility for these materials is to saturate dangling bonds with hydrogen atoms or fractional hydrogen atoms. See for example the work by Rittner *et al.* and Stoldt *et al.* [115, 116] for a comparison of these techniques for the rutile (110) surface.

Choosing a suitable set of atoms in the cluster, as well as accurate embedding, and at the same time keeping the cluster size reasonable, is the challenge of the embedded cluster approach. Preferably, clusters for point-defect calculations should be geometrically symmetric with respect to the point defect they host and they should keep the stoichiometry of the original crystal. Also, the cluster must be large enough and embedded such that also long-range electrostatic effects are reproduced. A defect may then be in a state very similar to a defect in real, extended material. However, depending on the crystal lattice structure and the type of point defect it is sometimes impossible to create a cluster that fulfills all these criteria (Fig. 3.1). While neutral, localized defects, such as the neutral oxygen vacancy in MgO bulk or at an MgO surface, are nevertheless straightforward to calculate, the electronic and lattice polarizabilities around a charged defect is more difficult to reproduce with a cluster model. Cluster models have to be tested carefully for convergence of electronic structure as well as geometric relaxation with respect to cluster size and embedding. This is often difficult to achieve in a systematic way. On the other hand,

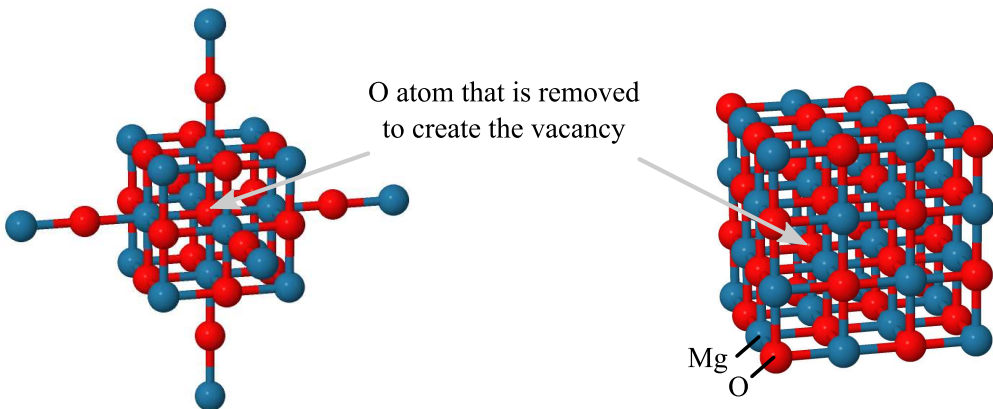


Figure 3.1.: Cluster models for an oxygen vacancy in bulk MgO. *Left:* $Mg_{20}O_{18}$, the cluster is symmetric with respect to the defect site, but the stoichiometry is not kept. *Right:* $Mg_{32}O_{32}$, the stoichiometry is as in natural MgO, but the defect can not be created in the center of the cluster.

the strong advantage of an embedded cluster calculation is that the cluster is typically small with respect to the number of atoms treated quantum-mechanically, allowing for the application of higher-level methods such as coupled-cluster. For supercell calculations that make use of periodic boundary conditions these methods are today not feasible for the system sizes typically needed to study defects in oxides.

In this work cluster calculations are employed for validation of hybrid density-functional theory with higher-level (*GW* and coupled-cluster) methods.

One advantage of using periodic boundary conditions over cluster models is that no assumptions on the effects of the cluster boundary are needed. This is especially important for charged defects, where the long-range Coulomb interaction can be strongly influenced in a cluster calculation, for example due to different polarization properties of atoms at the boundary, or due to induction of spurious multipole moments. Furthermore, the size of the supercell model used in a periodic calculation can be much larger than that of a cluster. In general, periodic boundary conditions offer a much more realistic way of modelling an extended system. However, care

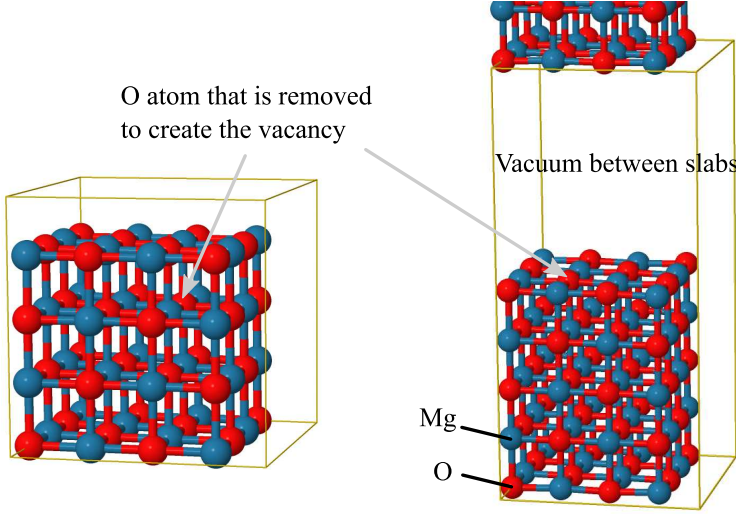


Figure 3.2.: Supercell models for an oxygen vacancy in MgO bulk and at the MgO (100) surface. The yellow boxes show the boundaries of the unit cell that is periodically repeated in three dimensions. *Left:* Model for a bulk defect. *Right:* Model for a surface defect. The vacuum region between repeating slabs has to be converged, so that the spurious interaction between slabs is minimal.

has to be taken, when charged systems are calculated within a periodic approach. The charge is periodically repeated, so that the corresponding electrostatic Coulomb energy v_{Cb} is

$$v_{Cb} = \sum_{i \neq j, \mathbf{R}} \frac{q_i q_j}{|\mathbf{r}_{ij} + \mathbf{R}|},$$

where i and j run over all atoms within the supercell and \mathbf{R} is a supercell lattice vector. Since the potentials of infinitely many image charges have to be summed up, the electrostatic energy diverges in the case of periodic systems with non-zero net charge per unit cell. Different ways to deal with this problem, providing charge compensation in the cell, are discussed in the following Sec. 3.2.

Furthermore, in addition to charge compensation, special care must be taken in supercell calculations to avoid errors due to interaction between images of the supercell generated by periodic boundary conditions. For example, constraints in geometric relaxation by the supercell size, or remaining electrostatic interactions have to be accounted for. Indeed, constraint in atomic relaxation is an important issue that occurs in both cluster and periodic calculations. The effects of the geometric relaxation around a defect on the electronic structure and formation energies can be quite significant, especially in case of charged defects. A sufficiently large number of host atom layers around the defect should lead to a reliable relaxation of the lattice. However, for some cases such as the vacancy in silicon in charge state 2+ important changes in the relaxation behavior will only be visible when going to very large cell sizes [117]. Also for charged oxygen vacancies in MgO large cell sizes are needed to obtain converged geometric relaxation and reproduce the lattice polarizability correctly.

3.2. Modeling charged defects with supercell methods

The main challenge when calculating charged defects in a periodic model is to find a suitable technique for charge compensation. The electrostatic potential for a charged, infinitely repeated system diverges. Therefore, in a periodic calculation of a charged system the charge must be compensated, so that the supercell is kept neutral. However, this is not a purely technical issue. In a real system with a non-vanishing concentration of charged defects for example, charge compensation typically occurs via dopants. A defect is charged by charge transfer between defect and dopants. The most common approach to address charge compensation in bulk calculations is to apply a uniform constant background charge density to the supercell. However, for surface systems, where the supercell contains not only atoms in a crystal lattice but also a vacuum region, the background method is not readily applicable [118]. In the following, the theoretical approach of the background method is briefly summarized. On the way to a more realistic description, introducing dopant atoms is discussed next. Finally, an alternative method for charge compensation, a variant of the virtual-crystal approximation (VCA) is tested and found to be the best approximation to reality. Opposed to the background method, applying the VCA has a physical meaning of modeling doped material and it can be used for both, bulk and surface systems. All periodic calculations of charged surface systems in this work were performed using the VCA.

3.2.1. Neutralizing background charge density

The electrostatic energy of a charged periodic system diverges, while this divergence is cancelled for neutral systems. Neglecting the divergent term in a charged periodic system, corresponds to implicitly introducing a constant background charge density, which cancels the divergence [101]. This standard approach of adding a neutralizing, uniformly distributed background charge is a very useful, although somehow artificial, concept for charged bulk systems. However, applied to a surface, the charge density would also spread through the vacuum region between repeating slabs. Confining the background to the slab could partly overcome the problem, but it is not obvious in what form the decay of the background at the slab surfaces should be defined.

Level alignment

Although the neutralizing background removes the divergence of the electrostatic energy and, therefore, allows to calculate the total energy of a charged system, difficulties occur when energy differences between systems in different charge states are required, as it is the case for charged-defect calculations.

Introducing the background potential not only cancels the divergent term in the Fourier sum but also introduces an additional arbitrary shift in the total energy of the charged system. The difference between the valence band maximum (VBM) of the charged and the neutral system has to be corrected in order to achieve consistent band edge energies. While for cluster calculations the vacuum can always be used as a reference energy zero, it is necessary to find a common reference energy level for the charged and the neutral periodic system to which the respective potentials can be aligned. Several ways of performing this potential alignment have

been suggested, e.g. aligning by the average electrostatic potential in the whole unit cell, or by the average difference of the atomic-site electrostatic potentials [119–121], where sometimes only atoms most distant from a charged defect are taken into account [122], taking the lowest energy level of the system as a reference [123], aligning to the core levels of most distant atoms, or correcting by the average core level shift excluding atoms close to the defect. However, there is no generally accepted scheme. This may be due to the fact that from different codes that apply for example pseudopotential versus full-potential concepts also different quantities are more easily accessible. In an all-electron approach, as taken for the FHI-aims code, the deep lying core states are readily available.

3.2.2. Compensating impurities

In a realistic material sample, compensating charges can be accommodated by impurities. In fact, metal oxides are often deliberately doped to modify their properties. A first approach to model this situation in a supercell calculation is to substitute a metal atom in the supercell by a dopant atom and consider this as the host system in which a vacancy is formed. Doping with low-valence (acceptor) or high-valence (donor) dopants, is possible, depending on the number of valence electrons of the dopant species with respect to the number of valence electrons of the host metal atoms. Low-valence dopants introduce holes as free charge carriers, which is referred to as *p*-type doping, while high-valence dopants provide electrons, termed *n*-type doping. Doping pins the Fermi level of the system, in case of *p*-type doping close to the VBM, in case of *n*-type doping to the CBM. Hence, the charge state of a vacancy in a metal oxide is determined by the concentration and type of the dopants and therefore by the availability of acceptor states or donor electrons and by the position and occupation of electronic levels introduced by the defect (defect levels). For example, oxygen vacancies in *p*-type MgO can be positively charged and at the same time have low formation energy, since there are dopant states near the valence band maximum that can accommodate the defect electrons.

On the other hand there are local effects of doping: depending on the atomic species and the distance between defect and dopant, geometric and electronic relaxation will be affected by the dopant. Therefore, these effects are important for formation of defect complexes.

When an explicit dopant is introduced in the supercell, the local and global effects of doping cannot be easily separated due to the limited size of the supercell. It is possible to obtain some information by studying the influence of a dopant on an oxygen atom close by in comparison with an oxygen atom further away from the dopant. For example, the local and global effects of doping on the formation of oxygen vacancies at La₂O₃ surfaces and in ceria have been studied in this way by Li and Metiu [124] and by Hu and Metiu [125]. However, very large supercells are needed to model far distances. Also, for surface defects it will typically make a difference, if the dopants are located at the surface, in the subsurface or deeper in the bulk.

To demonstrate the dependence of the local effect of doping on the position of dopants with respect to the defect, MgO with lithium dopants and an oxygen vacancy in the surface layer were calculated for two different supercell sizes, a 320-atom 5-layer slab, and a 500-atom 5-layer slab. Lithium has one valence electron, while magnesium has two valence electrons, so lithium is a low-valence, *p*-type dopant in MgO. As a global effect of lithium doping, electronic states are emptied near the VBM where as a consequence the Fermi level is pinned. A neutral oxygen

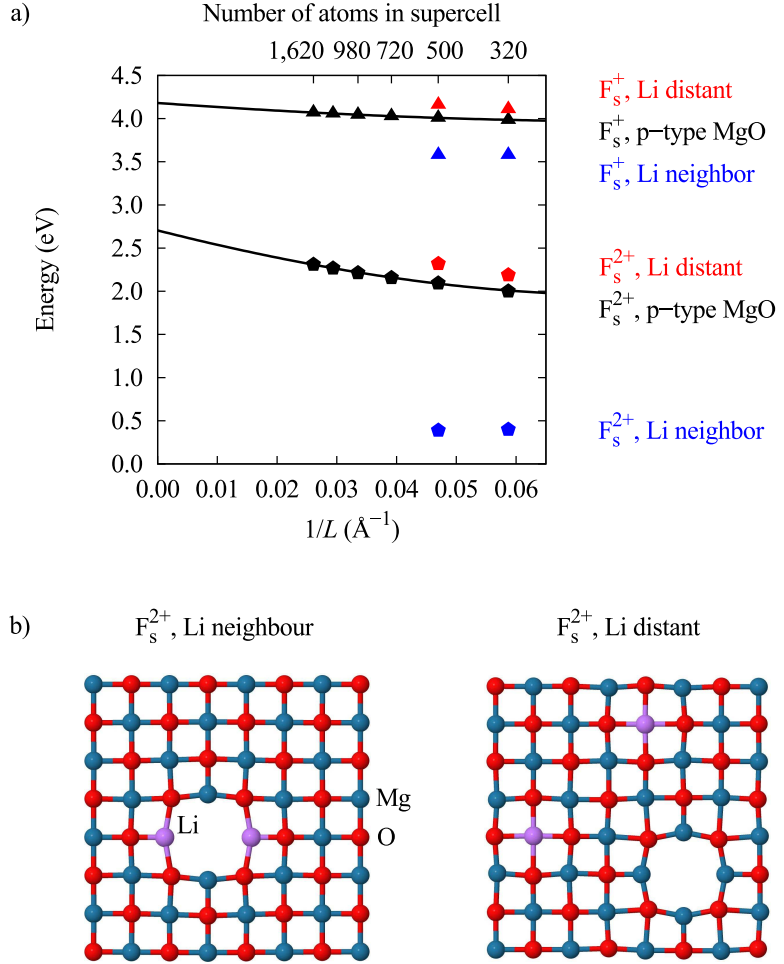


Figure 3.3.: a) Local and global effects of low-valence doping on the energy required to remove an oxygen atom from the MgO (100) surface, calculated according to Eq. 4.1 in an oxygen-rich environment ($\mu_O = 1/2E_{O_2}$) using PBE. The Fermi level is at the VBM. L is the supercell lattice constant. Oxygen vacancies in charge state 1+ and 2+ (F_s^+ and F_s^{2+}) compensated by one or two lithium dopants at the surface were calculated. Data points labeled *p*-type MgO, where long-range effects of doping dominate, are shown for comparison. They were calculated using a virtual-crystal approach, introduced in the following Sec. 3.2.3. Solid lines show the defect formation energy extrapolated to the dilute limit of a single defect in extended material ($L^{-1} \rightarrow 0$). The dilute limit, the extrapolation procedure, and finite-size correction schemes, suggested by Makov and Payne, and by Freysoldt *et al.*, are discussed in Sec. 4.1.3). b) Two different configurations were simulated, lithium dopants close by and further away at a distance of 8.8 Å, here shown in the top view of the 320-atom 5-layer surface slab for the doubly charged oxygen vacancy.

vacancy has two defect electrons occupying a defect level deep in the bandgap. To model a

singly positively charged oxygen vacancy, one magnesium atom is substituted by lithium in the supercell, so that one defect electron can transfer from the defect level to the dopant-induced states near VBM. For a doubly positively charged oxygen vacancy, two magnesium atoms are substituted to allow for transfer of two electrons. The energy needed to remove a surface oxygen atom (Eq. 4.1) can be used to show the influence of a dopant on the defect. It is lower when the lithium dopant is located adjacent to the vacancy, and higher when dopants and vacancy are at a larger distance (Fig. 3.3). This difference is due to different charge separation, and changes in local bonding and local electronic relaxation for the different configurations. For the adjacent dopant arrangements, defect complexes are formed, and the local effects of doping dominate. Since the defect complex is charge neutral, variation of the supercell size hardly has an effect, even when moderately large cells used. This is different when the dopant is situated at a larger distance from the defect. Long-range electrostatic interaction starts to dominate, and the Coulomb interaction with the charges in neighboring supercells is comparable in magnitude with the interaction within one unit cell. Thus, the interaction energy is affected globally by many unit cells, and the dependence on the supercell size becomes non-trivial. To examine the local and global effects of lithium doping on oxygen vacancies in MgO, dopants at various distances and in different layers would have to be studied, requiring very large supercells at high computational cost. In general, only unphysically high dopant concentrations can be calculated using the compensating impurity method.

3.2.3. Doped material as a virtual crystal

Besides explicit introduction of dopant species into the host material, doping can be modeled using the virtual-crystal approximation (VCA) [126–130]. In this approach, virtual atoms are constructed that interpolate between the native (A) and doping (B) atoms in the host material AC. The potential of the virtual atom modeling the doped material $(A_{1-x}B_x)C$ becomes

$$V_{\text{VCA}}(\mathbf{r}) = (1 - x)V_A(\mathbf{r}) + xV_B(\mathbf{r}). \quad (3.1)$$

So the real system is mimicked by constructing its potential from fractions of the potentials of the two different compounds. Pseudoatoms can for instance also be used in (embedded) cluster calculations to provide a realistic saturation of dangling bonds [131, 132].

In all-electron calculations, doping via the VCA is introduced by modifying the nuclear number of the atoms in the system, which determines the number of electrons from the condition of charge-neutrality. The dopant concentration N_D is controlled via the amount ΔZ by which the nuclear number Z is changed. A *p*-type doped metal oxide (MO) with a hole concentration of N_{holes} is modeled by changing the nuclear number Z_M of all n_M metal ions with a concentration of $N_M = n_M/\Omega$, where Ω is the supercell volume, according to

$$Z_M \rightarrow Z_M + \Delta Z_M, \quad (3.2)$$

where

$$\Delta Z_M = -N_{\text{holes}}/N_M. \quad (3.3)$$

In analogy, *n*-type doping can be modeled by changing the nuclear charges of the metal atoms by $\Delta Z = N_{\text{electrons}}/N_M$, where $N_{\text{electrons}}$ is the concentration of electrons. Opposed to the

compensating impurity method, in this approach also very small dopant concentrations can be simulated.

In this work, the concentration of *p*-type dopants in the simulation cell is chosen to allow for one or two defect electrons to transfer from the defect level to the VBM. This is obviously only possible, if a defect exhibits an occupied defect level in the bandgap. The nuclear number of all magnesium atoms in the supercell is changed by

$$\Delta Z_{\text{Mg}} = -q/n_{\text{Mg}}, \quad (3.4)$$

where q is the desired charge of the oxygen vacancy (+1 or +2), and n_{Mg} is the number of magnesium atoms in the supercell.

It is important to keep in mind the chemical and physical properties of a material, when applying the VCA for defect charge compensation. In principle, the nuclear charges can be modified in several different ways. One way is to distribute the charge of the defect among all nuclei according to their contribution to the overall nuclear charge, keeping the system neutral. Consider again the formation of an oxygen vacancy in MgO. For an MgO unit cell with n_{Mg} magnesium atoms and n_{O} oxygen atoms, not including the oxygen atom that is being removed, the changes in magnesium and oxygen atom charges are:

$$\Delta Z_{\text{Mg}} = -q \frac{Z_{\text{Mg}}}{n_{\text{Mg}} Z_{\text{Mg}} + n_{\text{O}} Z_{\text{O}}} \quad (3.5)$$

$$\Delta Z_{\text{O}} = -q \frac{Z_{\text{O}}}{n_{\text{Mg}} Z_{\text{Mg}} + n_{\text{O}} Z_{\text{O}}}. \quad (3.6)$$

However, this corresponds to simultaneous *p*- and *n*-type doping, since the reduction (in case $q > 0$) of the cation nuclear charge (Mg) reduces the number of electrons it can give away, while the reduction of the anion nuclear charge (O) reduces its ability to accept electrons. In reality, *p*-type doping of MgO is achieved by substituting magnesium atoms with atoms of lower valency like lithium. This situation is modeled by distributing the defect charge only among the cations. Thereby, delocalized states are emptied at the top of the valence band, which is composed mostly of oxygen 2p orbitals. As mentioned before, the formation of an oxygen vacancy creates a defect level occupied by two electrons in the bandgap, and therefore, electrons from this level transfer to the vacant states at the top of the valence band of the simulated *doped* material, which results in the electronic configuration of an F^+ or F^{2+} center (Fig. 3.4). The charge state of the defect can be tuned by the value by which the nuclear charge was modified, which is related to the concentration of the dopants.

The defect charge could also be distributed only among nuclei far away from the defect. This has the advantage that the immediate surrounding of the defect resembles the situation in the undoped material with the charged defect, at the expense of a more significant modification further away.

Contrary to the neutralizing background method, the reference system in the virtual crystal method should be the doped undefected system, not the perfect undoped system. Modification of the nuclear charges results in a large change in the total energy even if the modification is very small, due to the strong on-site electron-nuclear interaction. The change in the total energy

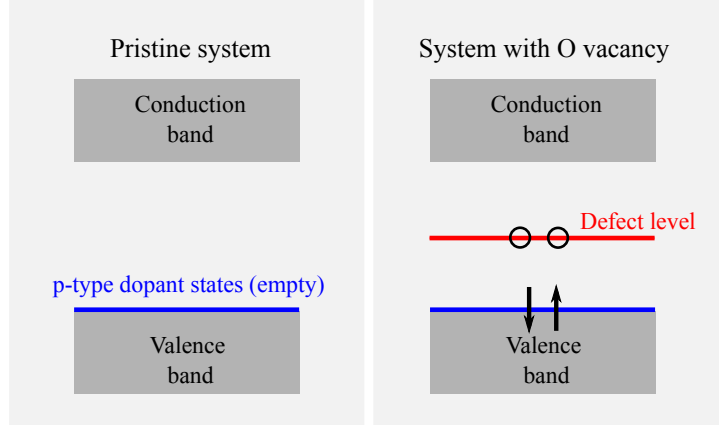


Figure 3.4.: F^{2+} center, modeled with the VCA. Schematic band structures of the pristine doped system (*left*) and the system with a defect (*right*)

can be written as:

$$E_{\text{el-nuc}}^{\text{VC}} \approx \sum_i \int \frac{(Z_i + \Delta Z_i)n(\mathbf{r})}{|\mathbf{r} - \mathbf{r}_i|} d^3r \quad (3.7)$$

$$= E_{\text{el-nuc}}^{\text{ref}} + \sum_i \Delta Z_i \int \frac{n(\mathbf{r})}{|\mathbf{r} - \mathbf{r}_i|} d^3r, \quad (3.8)$$

where $n(\mathbf{r})$ is the electron density. In fact, since the modification of the nuclear charges is inversely proportional to the number of the corresponding atoms in the supercell, the overall shift in energy is independent on the supercell size and it is quite large:

$$\Delta E = -q \cdot \sum_i \int \frac{n(\mathbf{r})}{|\mathbf{r} - \mathbf{r}_i|} d^3r. \quad (3.9)$$

As a proof of concept, the VCA method is tested for charged bulk F centers in MgO against the neutralizing background approach. The formation energies, neglecting vibrational effects, for the F^+ and F^{2+} centers were calculated for five different supercell sizes, once with the background method and once using distributed doping (Fig. 3.5), where the nuclear charge of all magnesium atoms in the system was modified. Both methods of charge compensation, constant background and VCA, yield the same total energy differences.

It becomes obvious from Fig. 3.5 that periodic models for charged defects can be used to study the defect concentration dependence for moderate to large concentrations. This is important, since studying isolated defects, as suitable for a cluster model, is not always justified, although it is a well-defined limiting case.

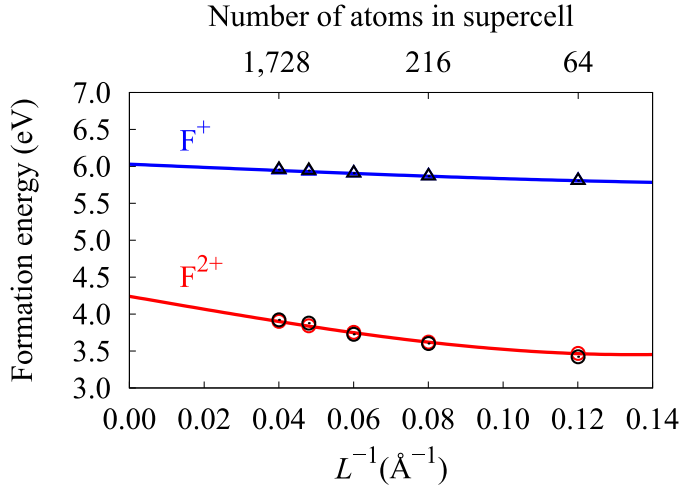


Figure 3.5.: Formation energy of F^+ and F^{2+} centers in MgO bulk, calculated with the neutralizing background method (blue and red symbols) and using the VCA (black symbols). The PW-LDA [50] exchange-correlation functional was used. The oxygen chemical potential is $1/2E_{\text{O}_2}$, and the Fermi energy is at the VBM. Solid lines show the defect formation energies of an F^+ and F^{2+} defect extrapolated to the dilute limit of a single defect in extended material ($L^{-1} \rightarrow 0$). The dilute limit, the extrapolation procedure, and finite-size correction schemes are discussed in Sec. 4.1.3).

3.3. Summary

In summary, embedded cluster models allow for efficient application of high-level methods like coupled-cluster, yet, embedding has to be tested carefully and the approach is restricted to small system sizes. Periodic models allow for simulations of higher defect concentrations, for a more reliable description of the electronic bands, and they incorporate long-range effects such as polarization. Hence, for defect studies, embedded-cluster models calculated with high-level methods can be very beneficial to identify a DFT functional providing the *best compromise* between accuracy and computational cost, using a small model system. The actual analysis of electronic and geometric structure of a defect in an extended material can then be performed with supercell models making use of the optimal DFT exchange-correlation treatment.

So far, for periodic calculations of charged surface systems, in particular of charged surface defects, it has been an unsolved issue how charge compensation could be provided in the supercell in a physically meaningful way. Here, an approach based on the VCA has been employed as a reliable compensation scheme for charged slab calculations. The VCA allows to model charged bulk or surface defects in doped metal oxides, incorporating global and also some local effects of doping as they can be observed in reality, providing a well-defined Fermi level and allowing for simulations of variable dopant concentrations. For the change in energy upon defect formation in bulk systems, the standard neutralizing constant-background approach and the VCA yield the same results. The difference is that with the VCA a realistic situation is modeled and can be interpreted as such. While the constant-background method is a technical trick,

that lacks any physical justification for surface systems, the VCA method, which can be used to model *p*- or *n*-doped material, is applicable for both, bulk and surface systems, in a physically meaningful way.

4. Defect stability – formation energy and concentration

Creating a point defect in the bulk or at the surface of a solid changes the free energy of the system. Depending on outer conditions, it may cost energy to introduce the defect or it may even be energetically favorable for the system. Therefore, the change in Gibbs free energy, when a defect is formed, termed the Gibbs free energy of formation, determines the equilibrium concentration of a defect for a given temperature, partial pressures of the involved atomic species, position of Fermi level, and dopant concentration.

A change in local bonding is one effect that contributes to the defect formation energy. For instance, removing an atom breaks bonds, while introducing an interstitial creates new bonds - but also weakens existing bonds. Also, geometric relaxation effects play a role. The atoms will take up new equilibrium coordinates, according to the changes in the Born-Oppenheimer potential energy surface. In addition, charging effects such as charge transfer from a defect level to the Fermi level, as well as defect-defect and defect-dopant interactions, will contribute to the formation energy. Changes in the vibrational energy and long-range dispersion interaction can also have a considerable effect.

In the literature, the term formation energy usually refers to the formation energy of a point defect in the dilute limit. This means, a single, non-interacting defect is hosted in extended material and it is not affected by other defects of the same or of a different type. For neutral defects, the formation energy in the dilute limit can be obtained already using moderate sizes of embedded clusters or supercells. For charged systems, long-range effects of electrostatic interaction and lattice polarization make the situation more complicated. Assuming very low defect concentrations, from the formation energy of a defect in the dilute limit, also its concentration can be calculated. The dependence of formation energies and concentrations on temperature and pressure is accounted for using *ab initio* atomistic thermodynamics.

However, considering defects as isolated is rather unrealistic, since due to long-range and short-range mutual interaction the formation energy for a certain type of defect will depend on its own concentration and also on the concentration of other defects. Thus, the most important part of this chapter discusses how formation energies and concentrations of interacting surface F centers in doped metal oxides can be obtained and how they are determined by different types of defect-defect interaction.

Since it would obviously be very interesting to compare theoretical predictions of defect stabilities with experimental measurements, an overview on experimental approaches to point defect concentrations is given at the end of this chapter.

4.1. Stability of an isolated point defect

The Gibbs free energy of formation $G_f^q(T,p)$ for an isolated point defect is given by the change in free energy of the system containing the defect with respect to the pristine system. It can be

written as

$$G_f^q(T, p) = E_{\text{def}}^q - E_{\text{host}} + \sum_i n_i \mu_i(T, p_i) + q\epsilon_F + \sum_i p_i \Delta V + \Delta F_{\text{vib}}^q(T). \quad (4.1)$$

n_i is the number of atoms of species i that have been removed ($n_i > 0$) and/or added ($n_i < 0$) upon defect creation. E_{def}^q and E_{host} are the total energies of the system with and without the defect in charge state q . The total energies can be obtained from electronic-structure calculations. $\mu_i(T, p_i)$ is the chemical potential of species i , which is a function of temperature T and partial pressure p_i . The chemical potential of electrons, the Fermi level ϵ_F , determines the electron reservoir for the formation of negatively and positively charged defects. ΔV is the change in volume of the crystal due to a defect, which is negligible for the defects in MgO discussed in this work. $\Delta F_{\text{vib}}(T)$ denotes the vibrational free energy contribution to the Gibbs free energy of formation. Using Eq. 4.1 the formation energy of an isolated defect can be calculated as a function of Fermi energy and atomic chemical potentials. Temperature and pressure dependence enter the formation energy via the atomic chemical potentials and the vibrational energy contribution.

The concentration in the dilute limit can be obtained by minimizing the change in Gibbs free energy of the system due to the defects. Gibbs free energy G , Helmholtz free energy F , and enthalpy H are related to each other via

$$G = H - TS = U + pV - TS = F + pV, \quad (4.2)$$

where U is the internal (total) energy, and S is the entropy of the system. In the following, the textbook expression for the concentration in the dilute limit will be derived.

The enthalpy of a system with n defects is $H = H_0 + nH_F$, where H_F is the formation enthalpy of the isolated defect. The total change in entropy of the system with a defect with respect to the pristine system $S - S_0 = S_d + nS_F$ can be separated into the entropy due to configurational disorder S_d , and a contribution due to disorder induced by lattice vibrations S_F . The total change in Gibbs free energy ΔG due to defect formation is then

$$\Delta G = G - G_0 = H - TS - (H_0 - TS_0) = n(H_F - TS_F) - TS_d. \quad (4.3)$$

In order to minimize ΔG , the derivative with respect to the number of defects is taken. In the dilute limit, the dependence of H_F and S_F on defect concentration can be neglected, so that

$$\frac{\partial \Delta G}{\partial n} = H_F - TS_F - T \frac{\partial S_d}{\partial n}, \quad (4.4)$$

where $G_f^q = H_F - TS_F$ is the free energy of formation of a single, isolated defect. According to Boltzmann's entropy formula, the configurational entropy is

$$S_d = k_B \ln \left(\frac{N!}{(N-n)!n!} \right), \quad (4.5)$$

where N is the number of possible defect sites, and k_B is the Boltzmann constant. Using Stirling's formula ($\ln x! \approx x(\ln x - 1)$), and assuming that the defects do not interact, leads to

$$\frac{\partial S_d}{\partial n} = k \left\{ \frac{\partial N}{\partial n} \ln \frac{N}{N-n} + \ln \frac{N-n}{n} \right\} \approx k \ln \frac{N-n}{n} \quad (4.6)$$

Using this expression in Eq. 4.4, and determining the minimum of ΔG , where the derivative is zero, yields the concentration of defects in the limit of low concentrations ρ_0 :

$$\rho_0 = \frac{n}{N} = \exp(-(G_f^q/k_B T + 1)). \quad (4.7)$$

According to Eq. 4.7, the equilibrium concentration of defects at $T = 1,000$ K is greater than 1 ppm only if $G_f^q \leq 1.1$ eV. The formation energy G_f^q as a function of defect concentration in the dilute limit is shown for two different temperatures in Fig. 4.1.

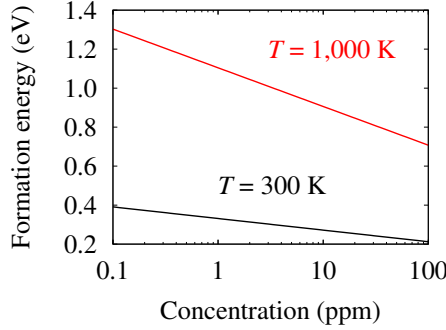


Figure 4.1.: Formation energy G_f^q as a function of concentration of defects in the dilute limit (Eq. 4.7) for temperatures $T = 300$ K and $T = 1,000$ K.

4.1.1. Fermi level position

According to Eq. 4.1, charged defects' formation energies depend on the position of the Fermi level, a reservoir for electrons and holes. Analyzing the formation energy dependence on the Fermi level in a region between valence band maximum (VBM) and conduction band minimum (CBm) usually covers the most realistic conditions. In an experimental setup, the position of the Fermi level is often hard to determine accurately. Doping, applying an electric field, or creating non-equilibrium populations of charge carriers by optical excitation can alter its position. However, this can also be used as an advantage in the context of defect engineering, where for example the charge state of a defect can be tuned by modifying the Fermi energy. In a theoretical approach, any position of the Fermi level can in principle be modeled. It is convenient to introduce a reference for the Fermi level, $\epsilon_F^{\text{ref}} = \epsilon_F - \Delta\epsilon_F$. The choice of reference will not affect any observables, but helps to identify a physically meaningful range of the electronic chemical potential. For practical reasons ϵ_F^{ref} is often set to the vacuum level in cluster calculations, since this is also the natural energy reference. Another possibility which is well-defined in both finite and infinite systems, is an easily identifiable electronic energy level, for example the lowest unoccupied or the highest occupied molecular orbital in a cluster, and the CBm or VBM in a crystal. In the dilute limit, the VBM and CBm of a system containing charged defects and of the host system, coincide. For finite defect concentrations (finite supercells), the Fermi level will shift. Therefore, care must be taken to identify a correct reference for the Fermi level, when using periodic models to calculate isolated charged defect formation energies.

4.1.2. *Ab initio* atomistic thermodynamics

The strength of DFT is to provide information about the electronic structure of a system as well as its total energy at zero temperature. Combining the DFT total energies with concepts known from thermodynamics can bridge the gap to higher temperatures and realistic pressures of the gaseous atmosphere, and to macroscopic properties of the system. This methodology is known as *ab initio* atomistic thermodynamics, and has been successfully used in defect and surface physics for the last 25 years [24, 133–135].

Calculating the Gibbs free energy of formation and the defect concentration, as described before, is already one example for applying this idea. The total energies of a system with a defect and the pristine system are used to calculate a thermodynamic potential function that is dependent on the ambient conditions - here, the Gibbs free energy. The concentration of defects, which is a macroscopic system property, can then be obtained using the standard methodology of thermodynamics. From the DFT total energies for different defect configurations and charge states, the corresponding defect formation energies can be obtained and used to find the most stable defect type for a certain set of chemical potentials.

The chemical potentials of the atoms involved depend on temperature and partial pressure. For an oxygen vacancy in a metal oxide, the chemical potential of oxygen has to be taken into account. It is determined by the condition of thermodynamic equilibrium with the surrounding gas-phase reservoir, which can be approximately treated as an ideal gas composed of N indistinguishable O_2 molecules. The chemical potential of oxygen at given temperature T and pressure p can be written as

$$\mu_{\text{O}}(T,p) = \frac{1}{2}\mu_{\text{O}_2}(T,p) = \frac{1}{2}(-k_{\text{B}}T \ln Z_{\text{O}_2}^{\text{tot}} + pV) / N, \quad (4.8)$$

where $Z_{\text{O}_2}^{\text{tot}}$ is the partition function of the ideal oxygen gas. Assuming, that the Born-Oppenheimer approximation holds, nuclear and electronic degrees of freedom are decoupled from vibrations and rotations. Taking place on different time scales, also vibrational and rotational motions are decoupled from each other, so that $Z_{\text{O}_2}^{\text{tot}}$ can be written as:

$$Z_{\text{O}_2}^{\text{tot}} = \frac{1}{N!}(z_{\text{O}_2})^N = \frac{1}{N!}(z^{\text{trans}} z^{\text{rot}} z^{\text{vib}} z^{\text{electr}} z^{\text{nucl}})^N. \quad (4.9)$$

Statistical mechanics can now be applied to calculate the individual contributions to the partition function. For details see the original work by Mc Quarrie *et al.* (1976) and the application of *ab initio* atomistic thermodynamics to surfaces by Rogal and Reuter (2007) [25, 136]. This leads to the following very convenient representation of Eq. 4.8

$$\mu_{\text{O}}(T,p) = \underbrace{\frac{1}{2}E_{\text{O}_2}^{\text{tot}}}_{\mu_{\text{O}}^{\text{ref}}} + \underbrace{\Delta\mu_{\text{O}}(T,p^0) + \frac{1}{2}k_{\text{B}}T \ln \left(\frac{p}{p^0} \right)}_{\Delta\mu_{\text{O}}(T,p)}, \quad (4.10)$$

where $E_{\text{O}_2}^{\text{tot}}$ is the total energy of the O_2 molecule, p is the partial pressure of oxygen, p^0 is the standard pressure $p^0 = 1$ atm, and $\Delta\mu_{\text{O}}(T,p)$ is the chemical potential of oxygen with respect to the reference chemical potential of oxygen $\mu_{\text{O}}^{\text{ref}}$. The total energy of the O_2 molecule,

can be calculated with DFT. However, the binding energy of the O_2 molecule, $E_{O_2}^{\text{bind}}$, is one of the big challenges for electronic-structure theory [50, 52, 137, 138]. The calculated binding energy is -6.23 eV at PBE level and -5.32 eV when HSE06 is used. To reduce the uncertainty due to this specific error, the experimental binding energy without zero-point energy $E_{O_2}^{\text{bind}} = -5.22$ eV [139] is used in this work, but the total energy of the free atom, E_O^{tot} , is calculated with the corresponding electronic-structure approach. This choice corresponds to a shift of the energy zero of the $\Delta\mu_O$ axis. $\Delta\mu_O(T,p^0)$ can be obtained from tabulated enthalpy and entropy values at standard pressure $p^0 = 1$ atm. (Values used in this work are taken from the JANAF Thermochemical Tables [140].)

The chemical potential of the metal can be deduced from the condition of thermodynamic stability of the bulk metal oxide. For the chemical potential of magnesium in MgO this means

$$\mu_{\text{Mg}} + \mu_O = E_{\text{MgO}}^{\text{bulk}}, \quad (4.11)$$

where the DFT total energy of an MgO unit cell $E_{\text{MgO}}^{\text{bulk}}$ approximates the corresponding Gibbs free energy. Choosing the chemical potential of magnesium in MgO bulk as a reference, $\mu_{\text{Mg}}^{\text{ref}} = E_{\text{MgO}}^{\text{bulk}} - \frac{1}{2}E_{O_2}^{\text{tot}}$, one can obtain $\Delta\mu_{\text{Mg}}(T,p) = -\Delta\mu_O(T,p)$ from Eq. 4.11.

Bounds for the chemical potentials are determined by limiting conditions for the system in thermodynamic equilibrium. One limit is the decomposition of the material into bulk metal and oxygen gas. For the chemical potential of magnesium this means $\max(\mu_{\text{Mg}}) = E_{\text{Mg}}^{\text{bulk}}(T,p)$. Again, the DFT total energy of a magnesium unit cell $E_{\text{Mg}}^{\text{bulk}}$ approximates the corresponding Gibbs free energy. Employing Eq. 4.11, the lower bound for the chemical potential of oxygen is thus given by

$$\min(\mu_O(T,p_O)) \approx E_{\text{MgO}}^{\text{bulk}} - E_{\text{Mg}}^{\text{bulk}} \quad (4.12)$$

Since the ionic bonds in MgO are strong, its melting and boiling temperatures at standard pressure are quite high (3,125 K and 3,873 K, respectively). Therefore, experimental conditions of interest for this work are usually far from the oxygen-poor limit.

A well-defined, reasonable estimate of the oxygen-rich limit is half the total energy of a free, isolated O_2 molecule at $T = 0$ K,

$$\max(\mu_O(T,p_O)) = \frac{1}{2}E_{O_2}^{\text{tot}}, \quad (4.13)$$

corresponding to $\Delta\mu_O = 0$. This highest possible value for the oxygen chemical potential may be identified with the liquid O_2 phase. In summary, the range of interest for the relative chemical potential of oxygen is

$$E_{\text{MgO}}^{\text{bulk}}(T = 0, p_O^0, p_{\text{Mg}}^0) - E_{\text{Mg}}^{\text{bulk}}(T = 0, p_O^0, p_{\text{Mg}}^0) - \frac{1}{2}E_{O_2}^{\text{tot}} < \Delta\mu_O(T,p_O) < 0. \quad (4.14)$$

Sometimes information on the chemical potentials of extrinsic species is needed, too. For example, in order to study the local interaction between defects and dopants, also lithium substitutional and interstitial defects in the vicinity or far away from oxygen vacancies in MgO have been calculated in this work. To explore a wide range of possible experimental situations, the chemical potential of lithium has been varied between the free energy of the lithium atom and that of a lithium atom in Li_2O , corresponding to fully oxidized lithium.

The remaining T -dependent contribution to the Gibbs free energy of formation of a defect is the difference in vibrational energy between the system with a defect and without a defect $\Delta F_{\text{vib}}(T)$. Within the harmonic approximation, the vibrational energy contribution to the Gibbs free energy can be written as an integral over the frequencies ω

$$F_{\text{vib}}(T) = \int d\omega F_{\text{vib}}(T, \omega) \sigma(\omega), \quad (4.15)$$

where $\sigma(\omega)$ is the phonon density of states (DOS). This expression can be derived by separating $F_{\text{vib}}(T)$ into vibrational energy

$$E_{\text{vib}}(T) = -\frac{\partial}{\partial \beta} \ln Z, \quad (4.16)$$

and vibrational entropy

$$S_{\text{vib}}(T) = k_B(\ln Z + \beta E_{\text{vib}}(T)), \quad (4.17)$$

where $\beta = \frac{1}{k_B T}$. Z is the partition function of an N -atomic system [141]

$$Z = \sum_{i=1}^{3N} \int \frac{d\mathbf{k}}{(2\pi)^3} \sum_{n=0}^{\infty} e^{-(n+\frac{1}{2})\beta\hbar\omega_i(\mathbf{k})}. \quad (4.18)$$

This yields Eq. 4.15 with

$$F_{\text{vib}}(T, \omega) = \frac{\hbar\omega}{2} + k_B T \ln \left(1 - e^{\beta\hbar\omega} \right). \quad (4.19)$$

The information needed to obtain the phonon density of states $\sigma(\omega)$ is contained in the potential energy surface and can therefore be calculated using DFT. The phonon properties in this work are calculated via the finite displacement method as implemented in Phonopy [142]. By displacing each atom in a supercell by a small amount from its equilibrium position and calculating the respective forces (using FHI-aims), the dynamical matrix for the system is constructed, and the corresponding eigenvalue equation yields the dispersion relation for the phonon frequencies. From this, the phonon density of states can be obtained and the vibrational energy is computed.

4.1.3. Obtaining the dilute limit with supercell models

Before considering interacting surface defects, the dilute limit (a single bulk or surface defect in extended material) is discussed. When the formation energy for an isolated, charged defect in a periodic model is calculated applying Eq. 4.1, the result will depend on the supercell size and shape. Even for very large supercell sizes, electrostatic interaction between defect and compensating charge, as well as Coulomb interaction between the defect and its periodic images will contribute to the computed formation energy. In accordance with a simple electrostatic model of point charges immersed into the jellium of opposite charge, these interactions scale as $\frac{1}{\epsilon L}$, due to Coulomb interaction between defects and compensating charge, for a cubic unit cell with the supercell lattice constant L corresponding to the distance between the defect and its closest images. In the limit of an infinitely large supercell the Coulomb interaction vanishes and the isolated, non-interacting defect is described. If the dilute limit of an isolated defect

is desired from the calculation of a realistic supercell size (100-1,000 atoms), the effects of Coulomb interaction between defect and compensating charge need to be removed, either by extrapolation or by correction schemes as discussed below, especially in systems with small static dielectric constant.

Makov-Payne correction scheme

Various post-processing corrections have been suggested to obtain the dilute limit in supercell calculations. The most widely used and discussed method for bulk defects is the correction scheme derived by Makov and Payne in 1995 [23] that builds on the work by Leslie and Gillan [143]. They considered an array of point charges compensated by a constant background charge within a structureless dielectric medium with dielectric constant ε . The Makov-Payne correction is

$$\Delta E^{\text{corr}} = \frac{q^2 \alpha}{2\varepsilon L} + \frac{2\pi q Q_r}{3\varepsilon L^3} + O(L^{-5}), \quad (4.20)$$

where $L = \Omega^{\frac{1}{3}}$ is the length of a cubic supercell of volume Ω , α is the Madelung constant that depends on the crystal structure (simple cubic, face-centered cubic, or body-centered cubic) and on the number of basis atoms, and Q_r is the second radial moment of the defect charge density

$$Q_r = \int_{\Omega} d^3 r \rho_p(\mathbf{r}) r^2. \quad (4.21)$$

The leading term in Eq. 4.20 is the screened Madelung lattice energy of point charges [143]. By decomposing the total charge density of a crystal containing a point defect into a periodic (net neutral) contribution of the underlying crystal ρ_p and the charge density of the aperiodic defect, Makov and Payne reproduced this first-order term, and additionally obtained a third-order correction term representing the interaction between the periodic density and the defect images.

The Makov-Payne correction scheme has been analyzed in numerous studies [119, 122, 144–149]. It has been shown that in most cases it leads to improved convergence to the dilute limit, but there are also shortcomings of the method. Lento *et al.* pointed out that Q_r is not necessarily independent on the supercell size, because the change in the charge density introduced by the defect need not be well localized as assumed by Makov and Payne [144]. Furthermore, Segev and Wei found that there may be situations for which the lattice relaxations lead to a symmetry breaking, and, as a consequence, a net dipole can appear, that would have to be taken into account [145]. Shim *et al.* showed that strongly localized charges are far better described by the Makov-Payne scheme than delocalized ones, by calculating vacancies and interstitials in diamond [122].

Freysoldt *et al.* correction scheme

Another correction scheme for bulk defects was suggested in 2009 by Freysoldt *et al* [150, 151]. The electrostatics in a system containing a charged point defect are analyzed and formulated in terms of the electrostatic potential in this approach.

The basic idea is to distinguish between two parts E^{inter} and E^{intra} of the correction term to the charged defect formation energy calculated for a finite cell size.

$$\Delta E^{\text{corr}} = E^{\text{inter}} + E^{\text{intra}} \quad (4.22)$$

E^{inter} is the interaction energy of the defect charge density $q_d(\mathbf{r})$ and the compensating charge density with the artificial potential due to periodic repetition, and E^{intra} is the interaction energy of the defect charge density and the background charge density in the reference cell.

To derive the corresponding terms, the creation of charged defects is divided into three steps, starting from a neutral defect. First, electrons are added to (or removed from) the defect state. An unscreened defect charge density $q_d(\mathbf{r})$ is introduced. Second, electrons are allowed to screen the introduced charge. This leads to a change in electrostatic potential with respect to the neutral defect $V_{q/0}(\mathbf{r}) = V_{\text{defect},q}(\mathbf{r}) - V_{\text{defect},0}(\mathbf{r})$. Third, artificial periodicity and a compensating homogeneous background charge density $n = -\frac{q}{\Omega}$ is introduced, leading to a periodic defect potential $\tilde{V}_{q/0}(\mathbf{r})$. All spurious interactions can be expressed through these quantities, according to

$$E^{\text{inter}} = \frac{1}{2} \int_{\Omega} d^3r [q_d(\mathbf{r}) + n][\tilde{V}_{q/0}(\mathbf{r}) - V_{q/0}(\mathbf{r})] \quad (4.23)$$

and

$$E^{\text{intra}} = \int_{\Omega} d^3r n V_{q/0}(\mathbf{r}). \quad (4.24)$$

The change in potential with respect to the neutral defect is then split into a long-range and a short-range part $V_{q/0}(\mathbf{r}) = V_q^{\text{lr}}(\mathbf{r}) + V_q^{\text{sr}}(\mathbf{r})$. The long-range part

$$V_q^{\text{lr}}(\mathbf{r}) = \frac{1}{\epsilon} \int_{\Omega} d^3r' \frac{q_d(\mathbf{r}')}{|\mathbf{r} - \mathbf{r}'|} \quad (4.25)$$

can be calculated analytically using a model charge density for $q_d(\mathbf{r})$, for example assuming a gaussian shape. $E^{\text{inter}} + E^{\text{intra}}$ is rewritten as a sum of two terms, where the first summand only contains long-range, and the second only comprises short-range contributions

$$\Delta E^{\text{corr}} = E_q^{\text{lat}} - q \cdot \Delta_{q/0}. \quad (4.26)$$

The term $\Delta_{q/0}$ is an alignment term, that suggests potential alignment between systems in different charge states based on the Hartree potential. It can be obtained by calculating $V_q^{\text{lr}}(\mathbf{r})$ analytically using Eq. 4.25 and demanding that $V_q^{\text{sr}}(\mathbf{r}) = V_{q/0}(\mathbf{r}) - V_q^{\text{lr}}(\mathbf{r})$ must approach zero far from the defect. Depending on the infrastructure of the applied electronic structure code this type of level alignment can be convenient.

If the lattice sum

$$E_q^{\text{lat}} = \int_{\Omega} d^3r \left[\frac{1}{2} [q_d(\mathbf{r}) + n][\tilde{V}_q^{\text{lr}}(\mathbf{r}) - V_q^{\text{lr}}(\mathbf{r})] + n V_q^{\text{lr}}(\mathbf{r}) \right] \quad (4.27)$$

is evaluated using a point charge model distribution, the linear term of the Makov Payne correction is recovered. In most cases E_q^{lat} only weakly depends on the choice of model charge distribution. This is shown on the example of charged F centers in MgO bulk, for which the Freysoldt corrections to the formation energies have been calculated using a gaussian charge distribution for different widths (Table 4.1). Up to a gaussian width of 2.0 the Freysoldt correction yields the same value as the first order Makov-Payne correction to within 0.03 eV.

Table 4.1.: Freysoldt finite-size correction (in eV) to the formation energies of an F^+ and F^{2+} center in a 64-atom bulk MgO supercell. The corresponding Makov-Payne first-order corrections for this example are 0.25 eV and 0.98 eV, respectively. The static dielectric constant of 9.8 and Madelung constant of 2.8373 were used.

Gaussian width	F^+	F^{2+}
0.1	0.25	0.98
0.8	0.25	0.98
2.0	0.25	0.95

Extrapolation to dilute limit

Although the correction pre-factors of the Makov-Payne scheme have been questioned, it is generally accepted that the leading contributions to the bulk defect formation energy dependence on the supercell size are the terms $\sim 1/L$ and $\sim 1/L^3$, where L is the supercell lattice constant. This implies that finite-size scaling according to

$$G_f^{\text{bulk},q}(L, \epsilon_F, \mu_O) = G_f^{\text{bulk},q}(L \rightarrow \infty, \epsilon_F, \mu_O) + \frac{a_1^q}{L} + \frac{a_3^q}{L^3} \quad (4.28)$$

leads to the correct formation energy in the dilute limit $G_f^{\text{bulk},q}(L \rightarrow \infty)$ [152–154]. Different variations of this scaling method have been proposed to improve the accuracy of the extrapolated energy [122, 145, 155–158].

In Fig. 4.2 the formation energies for the F^0 , F^+ , and F^{2+} center in MgO bulk are shown as a function of reciprocal supercell length in the oxygen-rich limit for the Fermi level at the VBM. All cells are fully relaxed, so that all elastic effects are taken into account for the calculated values.

The formation energy of a neutral F center is already converged for a small supercell of 64 atoms, while the formation energies of the F^+ and the F^{2+} center show a strong dependence on L , the higher the charge state the more pronounced is the effect. The difference in formation energy for a 1,728-atom supercell compared to a 1,000-atom supercell is still 50 meV for the F^{2+} center. Finite size scaling is performed by fitting each set of data (for F^+ and F^{2+}) to Eq. 4.28. The extrapolation procedure correctly incorporates the effects of atomic relaxation. When supercells containing up to 1,728 atoms are calculated for the doubly charged vacancies,

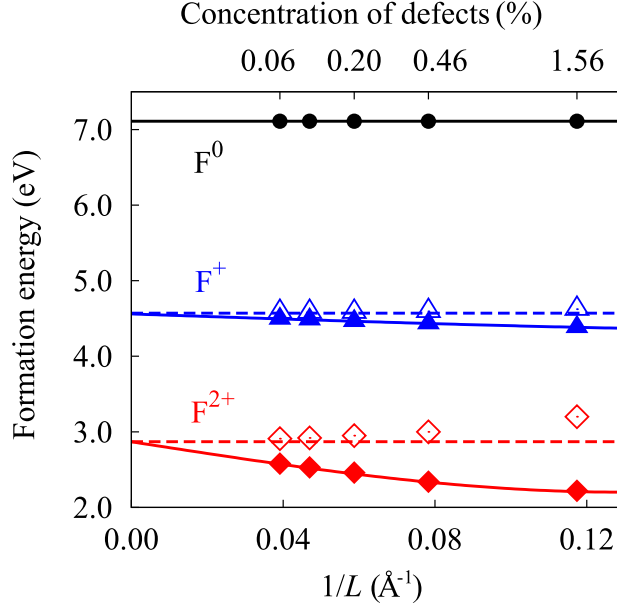


Figure 4.2.: Calculated formation energies of bulk F centers (filled symbols) as a function of the reciprocal supercell length L^{-1} at PBE level, neglecting vibrations. Formation energies including the first-order Makov-Payne correction are depicted by open symbols. Solid lines show finite-size scaling, where supercells of 64 to 1,728 atoms were calculated. Dashed lines mark the extrapolated formation energies.

using PBE exchange-correlation treatment, the accuracy of the least-square fits is ≤ 0.05 eV for the extrapolated values of the formation energies in the dilute limit.

The first-order Makov-Payne correction using the experimental value for the static dielectric constant of MgO ($\epsilon = 9.8$ [159]) improves the convergence, but still the computations for large cells are unavoidable to obtain converged results. By comparing the fitting parameters from the extrapolation procedure to the Makov-Payne formula, the static dielectric constant of MgO can be estimated. For DFT-PBE it is 10.70 with electronic and lattice components of 4.88 and 5.82. The corresponding experimental values are 9.34, 3.01, and 6.33 [160]. The PBE self-interaction error leads to a stronger deviation for the electronic component.

For charged surface defects, modeled using the VCA, the extrapolation is slightly different due to the broken symmetry at the surface. While for bulk supercells, the formation energies were fit to Eq. 4.28, where a term proportional to $\frac{1}{L^2}$ is zero due to symmetry, for the surface defects this term has to be included. The fitting function used is therefore

$$G_f^{\text{VCA},q}(L, \epsilon_F, \mu_O) = G_f^{\text{VCA},q}(L \rightarrow \infty, \epsilon_F, \mu_O) + \frac{a_1^q}{L} + \frac{a_2^q}{L^2} + \frac{a_3^q}{L^3}. \quad (4.29)$$

The periodicity of the surface calculations performed in this work is three-dimensional. Slabs are separated by a vacuum region, and this must be chosen large enough to remove undesired interactions between repeating slabs. In calculations for different L , only the lateral dimensions of the cell are changed, while the vacuum layer thickness is fixed. Since FHI-aims uses local-

ized basis functions, there is no extra computational cost when the vacuum region is large. The smallest distance between a defect and its closest atom from the slab image in z -direction, perpendicular to the surface, was chosen as 200 Å in this work. Using a slab to model a defect in the dilute limit in a semi-infinite system, is only meaningful if convergence of the desired property can be reached with respect to the number of layers N_L in the slab. The formation energies for an isolated F_s^{2+} center at the MgO (100) surface, extrapolated to the dilute limit, as obtained for 4-, 5-, and 6-layer slabs, are shown in Fig. 4.3. Full relaxation has been performed for all slab systems (using PBE), since also the convergence of geometric relaxation and lattice polarizability may vary with N_L . While a 4-layer slab is not sufficient to obtain an accurate result for the extrapolated formation energy in the dilute limit, where $1/L \rightarrow 0$, the 5-layer and 6-layer slab models yield the same value within 0.05 eV.

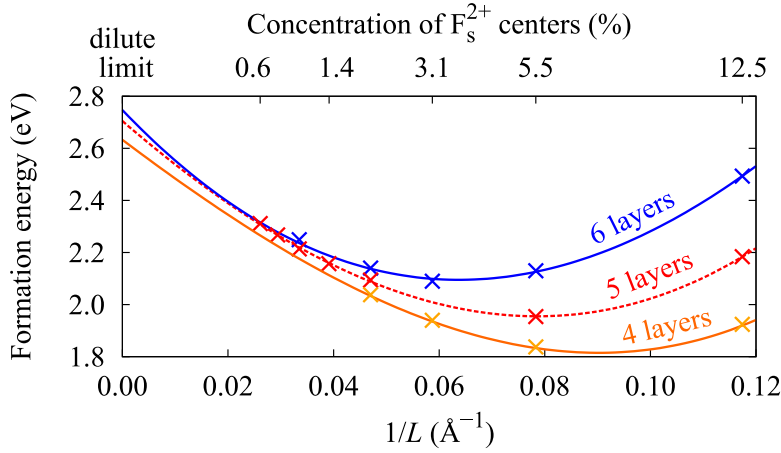


Figure 4.3.: Extrapolation of the F_s^{2+} formation energies $G_f^{VCA,q}(L)$, calculated with PBE according to Eq. 4.1 (vibrations neglected) for different lateral sizes of supercells and different numbers of layers in the slab, to infinite supercell size $L \rightarrow \infty$, using Eq. 4.29. The Fermi level is at the VBM and the chemical potential of oxygen is $\mu_O = 1/2 E_{O_2}^{\text{tot}}$.

Although computationally demanding, using the virtual-crystal approximation in combination with extrapolation is the most reliable method for calculating formation energies of charged bulk and surface defects in the dilute limit. The extrapolation procedure correctly incorporates polarization and geometric relaxation effects and can be applied to both bulk and surface systems.

4.2. Stability of interacting surface defects in doped material

It is not always realistic to assume that the defect concentration is small enough for the interaction between the defects to be neglected. In particular, charged defects and compensating electrons (or holes) cannot be considered non-interacting even at very low concentrations, because of the long-range nature of Coulomb interaction.

It is well known that charge transfer at dielectric materials interfaces can lead to spacially

confined depletion and accumulation of mobile charge carriers, so that a space-charge region is built up. The space-charge region is overall charge neutral, since the two oppositely charged material layers compensate each other. The effect is for example utilized in *p-n* junctions. In a similar way, charge transfer between surface defects and the host material can cause space-charge effects. These, in turn, have an influence on the charge state and stability of surface defects, affecting the defect formation energies and concentrations. For different reasons, the effect of space-charge layer formation on the energetics of defects (or adsorbates) at surfaces or interfaces has been disregarded in the literature. First of all, space-charge layer formation due to charge transfer between surface defects and the host material can only take place, if mobile charge carriers are present. In theoretical studies typically intrinsic material is considered instead of the more realistic situation, where the host material is intentionally or unintentionally doped. The technical problem, that in DFT calculations no reliable way of modelling charged surface defects in doped material existed, has certainly contributed to this restriction. Therefore, previous theoretical studies often only aimed at a description of neutral defects and excluded the possibility of defect charging, or else charged surface defects were calculated in the dilute limit using embedded cluster models, where space-charge effects were neglected. Yet another important aspect explored and accounted for in the following is, that the spacial extent of a space charge layer due to charged surface defects typically covers many more layers than the number of layers in a DFT surface slab model.

In a realistic situation, surface defects are charged by accommodating charge carriers from dopants in the subsurface layers. This results in depletion of the charge carriers and creation of a space-charge layer in the subsurface region. The resulting electrostatic potential causes band bending and increases the energy cost per defect. As a result, there are two leading electrostatic contributions to the formation energy of charged defects: attraction to the compensating charge and band bending. In the following, it is shown how the standard methodology for calculating defect formation energies can be extended to include the two electrostatic types of defect-defect interaction. Equilibrium surface defect concentrations are obtained by minimizing the free energy of the system with respect to the concentrations of surface oxygen vacancies in all possible charge states. Thereby, it is considered that the concentration of oxygen vacancies in a particular charge state depends on the concentrations of vacancies in all other charge states, on the bulk dopant concentration, on the position of the Fermi level, on temperature, and on partial oxygen pressure of the surrounding atmosphere.

4.2.1. Space-charge effects due to surface defects

The formation of a space-charge region due to charged surface defects will be explained qualitatively on the example of positively charged surface oxygen vacancies in *p*-type MgO with surface termination (100). First, consider the intrinsic material (Fig. 4.4, *left panel*), where oxygen vacancies have been introduced at the surface. They exhibit defect donor states deep in the bandgap that are each occupied by two defect electrons. The defects are neutral. Next, *p*-type dopants with a concentration N_D are introduced, but the system is not equilibrated (Fig. 4.4, *middle panel*). Empty acceptor levels pin the bulk Fermi level to the VBM, meaning that small variations in dopant concentration have a minor effect on the Fermi level position. In thermodynamic equilibrium (Fig. 4.4, *right panel*), charge carriers (holes) from the bulk have transferred

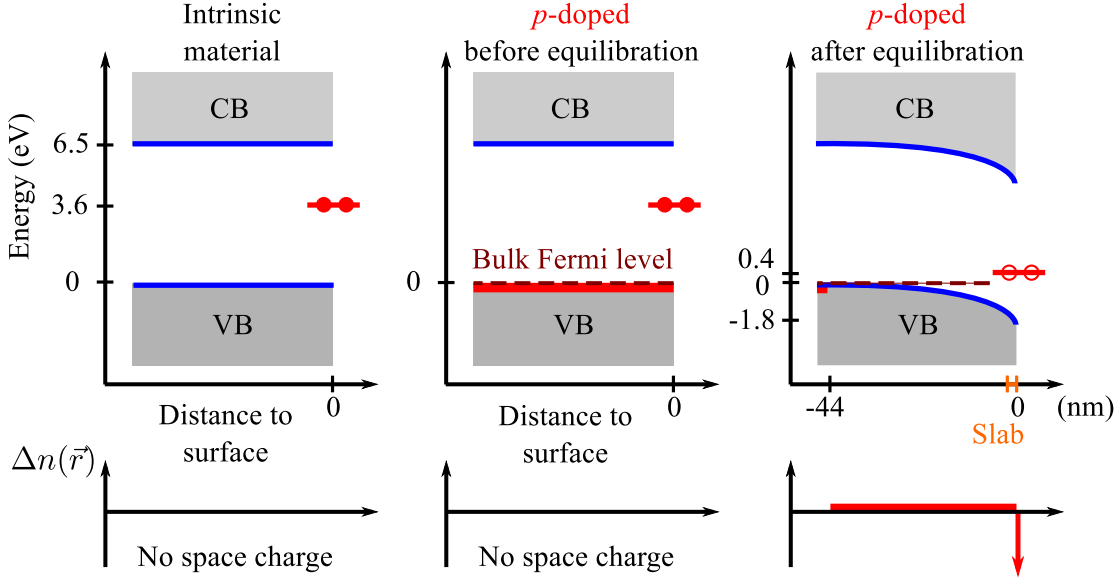


Figure 4.4.: Illustration of space-charge formation and band bending due to surface defects in p-type MgO. *Left:* Intrinsic material with a neutral surface defect. *Middle:* p-type dopants were introduced. The system is out of equilibrium. *Right:* In equilibrium, an electric field due to depletion of electrons at the surface and accumulation of compensating charge within a space-charge region $0 < z < z^{\text{SC}}$ causes band bending and limits the formation of charged surface defects. The calculated values (see text for details) are shown for a dopant concentration of $N_D = 10^{18} \text{ cm}^{-3}$ and surface charge density of $\sigma = 2.2 \cdot 10^{12} \text{ e/cm}^2$.

to the surface defects. A surface charge density σ due to the positively charged vacancies builds up (represented by the arrow), and is compensated by a macroscopically extended, yet localized negative charge density within a bulk space-charge region of thickness z^{SC} . The thickness depends on the doping profile, and may be limited by the thickness of the material. Assuming a uniform dopant distribution and semi-infinite bulk, the extent of the space-charge region is proportional to the space-charge density,

$$z^{\text{SC}} = \frac{\sigma}{eN_D}, \quad (4.30)$$

where e is the absolute value of the electron charge. Surface charge and space charge lead to an electrostatic potential that causes band bending within the space-charge layer. The corresponding electric field along the surface normal e_z is

$$E_z = \frac{\sigma}{\epsilon_r \epsilon_0} \left(1 - \frac{z}{z^{\text{SC}}} \right) e_z. \quad (4.31)$$

The potential difference $\Delta\phi$ due to band bending,

$$\Delta\phi = -\frac{\sigma}{2\epsilon_r \epsilon_0} z^{\text{SC}}, \quad (4.32)$$

can be calculated by integrating Eq. 4.31.

The energy $\sigma E^{\text{SC}}(\sigma, z^{\text{SC}})$ required to take electrons from the surface and distribute them uniformly over the thickness z^{SC} , increases with the surface charge density:

$$\sigma E^{\text{SC}}(\sigma, z^{\text{SC}}) = \frac{1}{2} \int_0^{z^{\text{SC}}} E_z^2 dz = \sigma \frac{\sigma}{6\epsilon_r \epsilon_0} z^{\text{SC}}. \quad (4.33)$$

The temperature dependence of z^{SC} and $E^{\text{SC}}(\sigma, z^{\text{SC}})$ at fixed σ is neglected. The more charged defects are formed, the higher becomes the energy cost per defect, since the energy gain due to charge transfer is reduced. In Fig. 4.4 this is reflected in the reduced energy difference between defect level and Fermi level.

In periodic calculations, the extent of the space-charge layer is usually artificially restricted to the slab thickness. In Fig. 4.4 (right panel) a slab thickness of 5 MgO layers is indicated for comparison. Therefore, when formation energies for interacting defects are calculated, the energy contribution due to band bending constrained to the thin thickness of the slab should be replaced by the energy contribution due to the correct band bending in the semi-infinite material.

In addition to band bending, the second important effect is electrostatic attraction between the localized defect charge and the compensating charge density. The two electrostatic contributions have opposite effects on the formation of charged surface defects. The band bending effect limits the concentration of charged surface defects, increasing their formation energies, while the electrostatic attraction facilitates charged defect formation, decreasing the formation energy. Both effects must be accounted for in order to calculate formation energies for interacting surface defects in metal oxides.

In analogy to the space-charge effects in *p*-type material with positively charged surface defects discussed above, band bending occurs in *n*-type systems with negatively charged surface defects. Furthermore, depending on the surface termination and the particular type of material, surface states can be situated in the bandgap, so that a space-charge layer due to surface states is formed. In this case, the Fermi level may be pinned to the surface band energy. For example, while the MgO (100) surface does not exhibit surface states in the bandgap, the MgO (111) oxygen octopolar termination is characterized by occupied states approx. 0.5 eV above the VBM (calculated with PBE). Therefore, for a *p*-type doped MgO (111) system a space-charge layer due to surface states will form and influence surface defect concentration (see also outlook in Chapter 10). The space-charge and band-bending effects due to surface-induced states are well-known in semiconductor physics. Yet, accounting for these effects in the context of oxide surface defect stability has so far been disregarded.

4.2.2. Concentration and formation energy of interacting defects

To obtain equilibrium concentrations for interacting surface defects, as a first step, formation energies of charged defects as a function of surface charge density σ are calculated. In Sec. 4.1.3 formation energies for isolated charged defects were extrapolated to the dilute limit and in this context the formation energy of one type of defect was calculated for decreasing concentrations of this defect (Fig. 4.3). The corresponding fitting function (Eq. 4.29) can be generalized to the case when defects in different charge states (for simplicity, these are assumed to be 1+ or 2+)

coexist at the surface. Eq. 4.29 is rewritten in terms of surface charge density σ_q for $q = 1, 2$ using $\sigma_q = qe/L^2$:

$$G_f^{\text{VCA},q}(\sigma_q, d) = G_f^{\text{VCA},q}(\sigma_q \rightarrow 0) + a_1^q \left(\frac{\sigma_q}{qe} \right)^{\frac{1}{2}} + a_2^q(d) \left(\frac{\sigma_q}{qe} \right) + a_3^q(d) \left(\frac{\sigma_q}{qe} \right)^{\frac{3}{2}}. \quad (4.34)$$

When defects in both charge states are present at the surface simultaneously, the surface charge density is $\sigma = \sigma_1 + \sigma_2$. Since the nature of the second and third term is purely electrostatic, a mean-field approximation is applied and σ_q is replaced with σ in these terms. The fourth term is more complicated, since in addition to higher-order electrostatic effects it also includes geometric relaxation effects. However, also in this term σ_q is replaced with σ . This corresponds to averaging the relaxation effects over different defect charge states. This averaging may give a noticeable error only in the specific case of comparable and at the same time not small concentrations of defects in charge states 1+ and 2+ ($> 3\%$ for F centers in MgO). Thus, the dependence of the formation energies on the overall surface charge density σ is given by:

$$G_f^{\text{VCA},q}(\sigma, d, \epsilon_F, \mu_O) = G_f^{\text{VCA},q}(\sigma \rightarrow 0, \epsilon_F, \mu_O) + a_1^q \left(\frac{\sigma}{qe} \right)^{\frac{1}{2}} + a_2^q(d) \left(\frac{\sigma}{qe} \right) + a_3^q(d) \left(\frac{\sigma}{qe} \right)^{\frac{3}{2}}. \quad (4.35)$$

Note, that $G_f^{\text{VCA},q}(\sigma, d, \epsilon_F, \mu_O)$ still depends on the slab thickness d . The electrostatic energy that causes the formation energy of charged defects to increase with slab thickness d is the band bending. According to Eq. 4.33, this contribution is

$$qE^{\text{SC}} = \frac{q^2 e}{6\epsilon_r \epsilon_0} \frac{d}{L^2}. \quad (4.36)$$

Subtracting qE^{SC} from the formation energies at every cell size $G_f^{\text{VCA},q}(L)$, removes the term $\propto 1/L^2$ in the finite-size scaling curve for each slab thickness. This is shown for the example of the F_s^{2+} center ($q = 2$) at the MgO (100) terrace in Fig. 4.5.

The term $\propto 1/L^3$ plays a role only for small L , so that the remaining linear dependence coincides for slabs with a number of layers $N_L = 4, 5, 6$ and 7 for all calculated surface charge densities $\sigma = 2e/L^2$. The solid black line shows a linear fit, incorporating all calculated formation energies. This linear fit yields the same value for the formation energy of the isolated defect as obtained before for the 5-, 6-, and 7-layer slabs using Eq. 4.29. The linear term is present due to the electrostatic attraction between the defects and the compensating charge.

Thus, formation energies of charged defects as a function of surface charge density $G_f^{\text{VCA},q}(\sigma, z^{\text{SC}}(\sigma))$ for an arbitrary space-charge thickness z^{SC} can be obtained by calculating $G_f^{\text{VCA},q}(\sigma, d)$, subtracting the band bending in the slab, $qE^{\text{SC}}(\sigma, d)$, and adding the band bending $qE^{\text{SC}}(\sigma, z^{\text{SC}})$:

$$G_f^{\text{VCA},q}(\sigma, z^{\text{SC}}(\sigma)) = G_f^{\text{VCA},q}(\sigma, d) - qE^{\text{SC}}(\sigma, d) + qE^{\text{SC}}(\sigma, z^{\text{SC}}). \quad (4.37)$$

Next, the change in Gibbs free energy per unit area upon defect formation can be expressed as

$$G(\eta_0, \eta_1, \eta_2, T, p_{\text{O}_2}, N_D) = \eta_0 G_f^0 + \sum_{q=1}^2 \eta_q G_f^{\text{VCA},q}(\sigma, z^{\text{SC}}(\sigma, N_D)) - T \sum_{q=0}^2 s_{\text{conf}}^q(\eta_0, \eta_1, \eta_2), \quad (4.38)$$

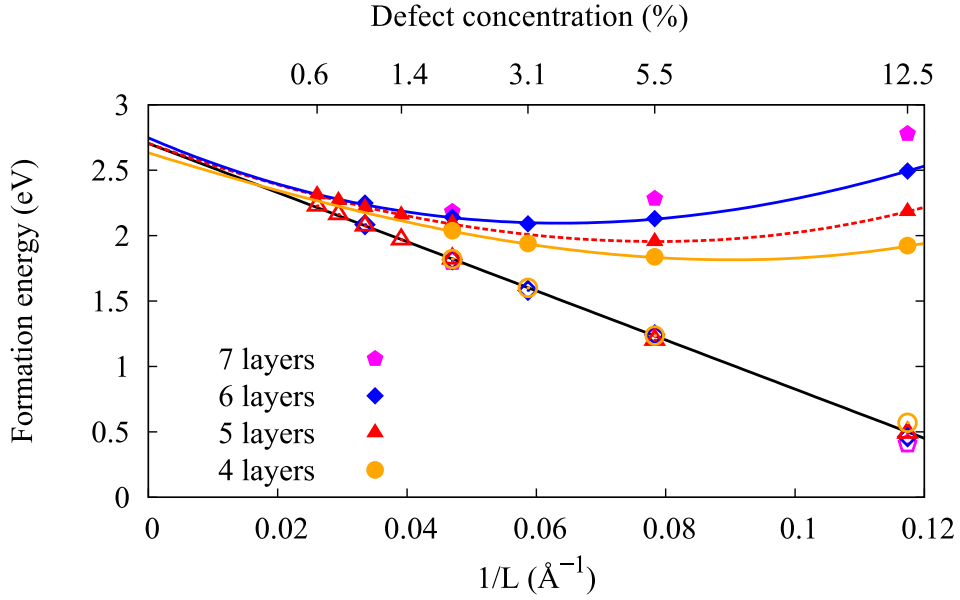


Figure 4.5.: Extrapolation of the F_s^{2+} formation energies $G_f^{\text{VCA},q}(L)$ (filled symbols, vibrations neglected), calculated with PBE according to Eq. 4.1 for different sizes of supercells, to infinite supercell size $L \rightarrow \infty$, using Eq. 4.29. The Fermi level is at the VBM and the chemical potential of oxygen is $\mu_{\text{O}} = 1/2 E_{\text{O}_2}^{\text{tot}}$. Open symbols and linear fit (black line) are obtained by subtracting the band bending contribution (Eq. 4.36).

where η_0 , η_1 , and η_2 are concentrations of surface defects in charge state 0, 1+, and 2+, respectively. The total surface charge density is determined by the concentrations of charged defects $\sigma = e\eta_1 + 2e\eta_2$. The configurational entropy per unit area $s_{\text{conf}}^q(\eta_0, \eta_1, \eta_2)$ accounts for energetically degenerate surface defect arrangements. Due to the screening of the charged defects by the compensating charge, the number of defect arrangements that have significantly different energy relative to the total number of possible arrangements at the surface for fixed η_0 , η_1 , and η_2 is expected to be small, and is vanishing for small defect concentrations. In analogy with Eq. 4.5, the configurational entropy for each type of defect can therefore be expressed as:

$$s_{\text{conf}}^q = k_{\text{B}} (\eta_q^{\text{sites}} \ln \eta_q^{\text{sites}} - \eta_q \ln \eta_q - (\eta_q^{\text{sites}} - \eta_q) \ln (\eta_q^{\text{sites}} - \eta_q)), \quad (4.39)$$

where η_q^{sites} is the surface density of available sites for the given type of defect:

$$\eta_q^{\text{sites}} = \eta^{\text{sites}} - \sum_{i \neq q} \eta_i. \quad (4.40)$$

For example, at the MgO (100) surface, the surface density of oxygen atoms is $\eta^{\text{sites}} = 0.11 \cdot 10^{16} \text{ cm}^{-2}$.

Finally, equilibrium defect concentrations η_0 , η_1 , and η_2 can be found by minimizing G with

respect to these concentrations:

$$\frac{\partial G}{\partial \eta_q} = G_f^q(\sigma, T, p_{O_2}, N_D, \epsilon_F) - T \frac{\partial \sum_{r=0}^2 s_{\text{conf}}^r(\eta_0, \eta_1, \eta_2)}{\partial \eta_q} = 0. \quad (4.41)$$

Here,

$$G_f^q(\sigma, T, p_{O_2}, N_D, \epsilon_F) = \frac{\partial}{\partial \eta_q} \sum_{r=0}^2 \eta_r G_f^{\text{VCA}, r}(\sigma, T, p_{O_2}, N_D, \epsilon_F) \quad (4.42)$$

is the formation energy of a defect in charge state q in the presence of other defects. The formation energy of an isolated charged defect ($q \neq 0$), as introduced in Sec. 4.1, is a limiting case of the formation energy of an interacting charged defect, approached when defect and dopant concentrations are vanishingly small. Since for a neutral defect ($q = 0$) there is no electrostatic interaction, its formation energy is close to the formation energy of the isolated defect also for larger defect concentrations. Disregarding the global electrostatic effects due to charge transfer between surface and bulk can result in an error of several orders of magnitude in defect concentration, as shown for F centers at the MgO (100) surface in the second part of this work.

4.3. Experiments on point defect stabilities

Different experimental techniques for measuring defect concentrations are known, but each of them is only applicable to a specific class of defects and materials.

A straightforward way to obtain point defect concentrations experimentally is to use the differential thermal expansion method as introduced by Simmons and Balluffi in 1960 [161]. It is assumed that for each vacancy in the crystal an atom is added at the surface, increasing its volume. The change in volume of a crystal sample as a function of temperature is then due to regular thermal expansion of the lattice as well as the dimensional change from point defects, especially vacancies. The temperature-dependent change in *microscopic* average lattice constant $\frac{\Delta a}{a_0}$, as determined in x-ray lattice parameter measurements, with respect to the lattice constant a_0 when the material is defect-free, and the change in "macroscopic" linear dilatation $\frac{\Delta L}{L_0}$ of a crystal, also with respect to the length L_0 for the defect-free system, can be measured simultaneously. The vacancy concentration is then obtained from the difference between the two. In general, unambiguous measurements for application of the thermal-expansion method can only be performed, if only one type of defect is present that changes the volume of the crystal sample. However, even if this is the case, some atoms that were originally occupying the vacancy site, may have taken up interstitial sites in the lattice and therefore no volume is added to the crystal. In particular, Frenkel defects in ionic crystals, consisting of a vacancy and an interstitial, cannot be measured by this method. Also, for metals it is usually a valid assumption that desorption of metal atoms into gas phase is energetically unfavorable. For oxygen vacancy formation in metal oxides on the other hand it is well possible that oxygen atoms at the surface react with atoms or molecules from the surrounding gas phase and leave the crystal sample. To limit oxygen fugacity, strongly oxidizing conditions have to be provided, but then also the oxygen vacancy concentration in the metal oxide will be very small. Furthermore, in ionic crystals

it is much harder to insure thermal equilibrium at each temperature measuring point. Since the defect concentration is small, but obtained from the difference of two large quantities $\frac{\Delta a}{a_0}$ and $\frac{\Delta L}{L_0}$ that are sensitive to small temperature changes, high accuracy in measuring $\frac{\Delta a}{a_0}$ and $\frac{\Delta L}{L_0}$ must be reached. Then, the thermal expansion method is in principle also applicable for oxygen vacancies in MgO [162]. For metals as for example lead, aluminum, and silver many successful measurements using the thermal expansion method of defect concentrations have been reported (see review by Seeger and references therein [163]).

Another possibility to measure the concentrations of vacancies is via the time constant for positron annihilation as a function of temperature [163, 164]. This method allows for measurements of even very small concentrations of the order of 10^{-7} vacancies per possible occupation site. Positrons can be generated by radioactive decay events, emitting a *start* radiation signal. They are shot into the sample, and after a certain lifetime annihilate with electrons, again emitting a certain type of radiation, providing a *stop* signal. Detecting these radiations the mean lifetime of the positrons can be determined, and from this the average electron concentration available for annihilation can be deduced. Many types of vacancies are able to trap the positrons. Therefore, the concentration of vacancies is related to the amount of positrons being trapped which is related to the measured mean lifetime. If the trapping probability, or the cross-section for positron capture, is known, the vacancy concentration can be determined. The positron annihilation method was for example applied to study vacancy formation in Cu and Si [165, 166]. Applications to MgO also exist, but are of minor relevance for this work, since only neutral and negatively charged magnesium vacancies readily trap the positrons. Also, the systems were not studied under thermal equilibrium conditions [167, 168].

An indirect method to measure defect concentrations is via optical absorption spectra, if these are accessible. This is also the method used in the only published experiment measuring the formation energy of a (neutral) F center in MgO bulk, that was performed by Kappers *et al.* in 1970 [26]. The experiment is discussed in detail in the context of the theoretical analysis of the F^0 defect in Sec. 6.1.

Other methods, that can in principle be used to study the formation of point defects in ionic crystals, are measuring the resistivity, if ionic conductivity is mediated by point defects, or, specifically for surface defects, the crystal sample can be exposed to atoms or molecules that adsorb preferentially at the defect sites and can be readily detected. It has also been suggested to obtain a surface vacancy concentration by simply counting the defects visualized in atomic resolution STM images [169]. However, for small defect concentrations the error in this method is rather large, and the conditions are usually far from realistic.

In summary, all of the methods mentioned are based on one or more assumptions critically important for the reliability of the deduced value of the formation energy. The general, main challenge for the temperature-dependent measurement of equilibrium defect concentrations or formation energies in ionic crystals is to establish precisely this thermodynamic equilibrium at each temperature.

4.4. Summary

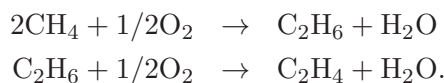
In this chapter, the standard approach of calculating formation energies and concentrations of neutral and charged F centers, assuming non-interacting, isolated defects, has been reviewed, and an extension to describe interacting surface defects has been introduced. In general, the concentration of one type of defect depends on the concentrations of all other types of defects. This has been taken into account by introducing concentration-dependent formation energies and minimizing the free energy of the system with respect to all surface-defect concentrations. In particular, global electrostatic effects due to defect-compensating charge interaction – effects that have so far been disregarded – have been considered. Charge transfer between surface defects and dopants in the bulk leads to formation of a space-charge region, band bending and an electric field. This limits the concentration of charged surface defects, competing with the second important electrostatic effect, attraction between surface defects and the compensating charge, which facilitates formation of charged F centers. Following the methodology suggested in this chapter, equilibrium concentrations of interacting surface defects for given temperature, pressure, Fermi level position, and dopant concentration can be calculated.

Part II.

Oxygen vacancies in MgO

5. MgO as a catalyst for methane oxidation

Today, high-value commodity chemicals used in industry are for the most part produced in a cost-intensive and environmentally unfriendly way from fossil resources by cracking and reforming. On the way to more sustainable energy conversion, as long as renewable feedstocks can not be utilized on a sufficiently large scale, efficient catalytic processes for production of base chemicals and fuels from methane are highly desirable. Methane (CH_4) is the main component of natural gas, and can also be produced from biomass. At present, methane is often used to generate electric power or heating by full combustion with emission of carbon dioxide. Methane conversion in the presence of oxygen is known as oxidative coupling of methane (OCM), where methane can react with oxygen to produce ethane (C_2H_6) and ethylene (C_2H_4),



However, to direct the reaction towards C_2 hydrocarbons rather than carbon monoxide or carbon dioxide, a suitable catalyst is needed. Already in 1982 different oxides, among them magnesium oxide (MgO), were tested for their activity as OCM catalysts [170]. In 1985 lithium-doped MgO was studied by Ito and Lunsford and found to effectively convert methane to ethane and ethylene at approx. 700°C [11, 12, 171]. It was shown by Myrach *et al.* in 2010 [172] that lithium-doped MgO is not a stable catalyst due to segregation of lithium to the surface. Still, there are experimental indications that *p*-type conductivity and presence of oxygen vacancies are important features for MgO to exhibit catalytic activity for OCM: Dubois and Cameron analyzed the properties of oxide catalysts for OCM and identified *p*-type conductivity as a key factor for good performance [31]. Balint and Aika studied defect sites formed when MgO was doped with lithium or titanium. Pure MgO and lithium-doped MgO always exhibited *p*-type conductivity, whereas titanium-doped MgO was found to be *n*-type conducting. Doping with lithium favored formation of oxygen vacancies, while doping with titanium had the opposite effect [32]. Furthermore, the pristine MgO (100) surface, which is the most stable termination under a wide range of ambient conditions, is chemically inert. In particular, Trevethan *et al.* argue that methane molecules only weakly physisorb on the flat terraces [173]. There is still insufficient knowledge on the stability of oxygen vacancies in MgO under realistic ambient conditions. The only experiment on the stability of the charge-neutral oxygen vacancy in MgO bulk conducted by Kappers *et al.* in 1970 [26] is in disagreement with theoretical work from the 90ies by Kantorovich *et al.*, Scorza *et al.*, Orlando *et al.*, and Pacchioni *et al.* [27, 30, 174, 175]. Due to their electronic structure, also charged oxygen vacancies in MgO are conceivable, but their stability has hardly been studied [112, 176].

In the following, the methodology presented in the first part of this work is applied, aiming at a realistic, accurate description of oxygen vacancies at the MgO (100) surface. In this context also bulk defects are analyzed. The focus is on the global effect of doping on oxygen vacancies, *i.e.*,

doping is considered as means of creating a reservoir for electrons and holes, characterized by a chemical potential (Fermi level). But also lithium as a prototype dopant in MgO is considered, where defect complex formation can be favored due to local interaction between defects and close-by dopants.

6. F centers in bulk MgO

MgO crystallizes in the rock-salt structure, where each atom is six-fold coordinated in the bulk (Fig. 6.1). The experimentally determined lattice constant for MgO is 4.207 Å at $T = 0$ K [177]. When the effects of zero-point vibrations are removed, the lattice constant is 4.186 Å [178]. The bonding type in MgO is strongly ionic, with formal ion charges of magnesium and oxygen 2+ and 2-, respectively. Although the experimental bandgap of MgO is 7.78 eV, as measured by reflectance spectroscopy [179], realistic samples are typically neither clear transparent nor insulating. Defects such as intrinsic point defects, impurities and defect complexes are not only responsible for the color of the samples, but can also give rise to electron or hole conductivity [32, 180, 181].

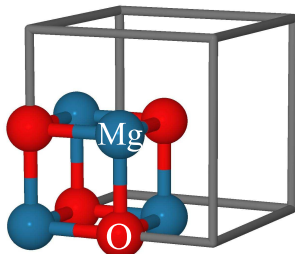


Figure 6.1.: Simple cubic unit cell of MgO.

Oxygen vacancies are typically studied in the context of their influence on the oxide properties. These point defects are also called color centers or F centers, referring to the German word *Farbzentrum*, due to their effect on the optical properties. Despite numerous studies, the actual abundance of oxygen vacancies at realistic conditions remains undetermined. Even for the simplest type of oxygen vacancy, the neutral F^0 center in MgO bulk, the challenge to obtain an accurate estimate for point defect formation energies in experiment and theory becomes evident, since reported experimental and theoretical results disagree severely. In the following, electronic and geometric structure of bulk F centers in MgO are studied, and formation energies as well as electronic levels are tested for their dependence on DFT exchange-correlation treatment. The goal is to find a reliable exchange-correlation functional for the analysis of neutral and charged F centers in MgO.

6.1. Neutral oxygen vacancy in bulk MgO

The formation energy of the neutral oxygen vacancy in bulk MgO was measured by Kappers *et al.* in 1970 [26]. A deviation of 2 eV between theoretical results reported in literature and the experimental value has been a long-standing discrepancy. This issue is approached in the

following paragraphs, using periodic and embedded cluster models and comparing DFT and hybrid DFT results to high level coupled-cluster theory values.

Experimentally measured formation energy

In Kappers' experiment the bulk oxygen vacancies are created by additive coloring [26]. Single crystals of MgO are heated in magnesium vapor at temperatures from 1,870 K to 2,100 K under pressures up to 5.3 atm. The high magnesium chemical potential lowers the formation energy of the bulk F centers (compare Eq. 4.1 and Eq. 4.11) and allows for them to form in detectable concentration. Optical absorption experiments are then performed, and from the maximum intensity u_{\max} and width at half-maximum U of the absorption peak the density of F^0 centers n_{F^0} can be obtained. For this, the Gaussian form of the Smakula formula [182] is used, depending also on oscillator strength f_{os} (a measure of the transition strength) and the index of refraction k :

$$n_{F^0} \propto \frac{k}{(k^2 + 2)^2} \frac{1}{f_{os}} u_{\max} U. \quad (6.1)$$

The ratio between F^0 center density and the density of atoms in the magnesium vapor is shown in Fig. 6.2 (left) for several crystals colored at 2,086 K and 1,885 K. In thermodynamic equilibrium, the increase in free energy if one atom is removed from the magnesium vapor is equal to the increase in free energy if one magnesium atom is added to the crystal and a bulk F center is formed. This relates the ratio of the density of F^0 centers and the magnesium atoms in the vapor to the defect formation enthalpy ΔH_f at $T = 0$ K with respect to cohesive energy of the MgO crystal via

$$n_{F^0}/n_{Mg} = C \cdot e^{-\frac{\Delta H_f}{k_B T}}. \quad (6.2)$$

ΔH_f is the enthalpy change upon removal of a neutral oxygen atom from MgO bulk and placing it into the gas phase. The cohesive energy is defined as the energy cost of separating an MgO crystal into free magnesium and oxygen atoms, per Mg-O pair. The dependence of C on temperature is weak, and is therefore neglected. From the density ratio, measured as a function of temperature, ΔH_f can thus be obtained by a fit to Eq. 6.2, as shown in Fig. 6.2 (right).

The experimental value for the F^0 formation enthalpy estimate at $T = 0$ K is 1.53 eV above the cohesive energy with respect to oxygen atom ($\mu_O = E_O$), and -1.06 eV with respect to O_2 molecule ($\mu_O = 1/2 E_{O_2}$). Adding the experimental cohesive energy of 10.35 eV [183] results in a formation enthalpy of 11.88 eV with respect to oxygen atom, or 9.29 eV with respect to O_2 molecule.

As also mentioned by Kappers [26], it is hard to ensure that thermal equilibrium is reached when the crystals are colored. Additional uncertainty enters through assumptions made to derive Eq. 6.1, which may be problematic for ionic solids, as pointed out by Dexter [182]. Also specifics of the estimate made for the oscillator strength are not documented. Therefore, comparison with different experiments would be desirable.

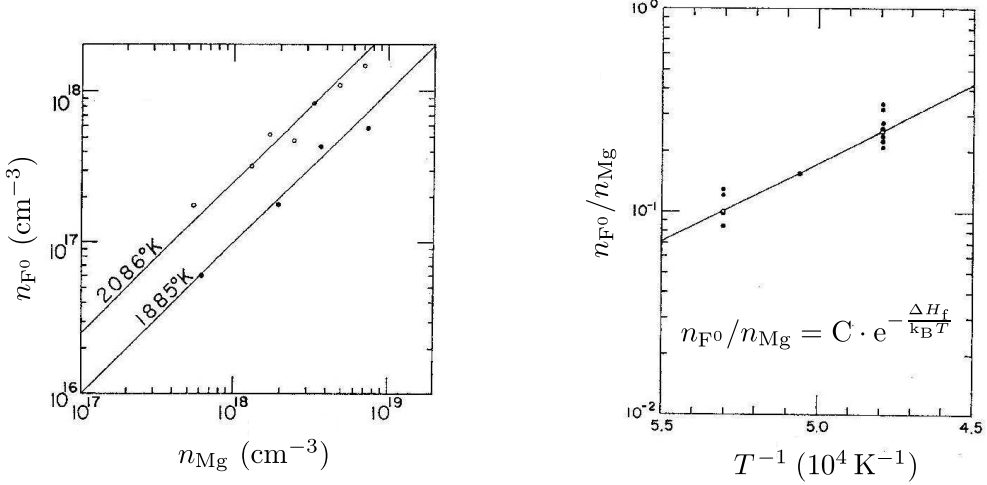


Figure 6.2.: Left: Equilibrium density of F⁰ centers n_{F^0} as a function of the density of atoms in the magnesium vapor n_{Mg} **Right:** Ratio of the density of F⁰ centers to the density of atoms in the vapor as a function of the reciprocal temperature. Each filled point, except for the one measured at an intermediate temperature, corresponds to one data point in the graph on the left. The two open points in the right graph correspond to the two linear fits in the graph on the left. Graphs are taken from Ref. [26], labels have been adjusted to match denotations in the text. (Copyright (1970) by The American Physical Society.)

Theoretical results

The formation energy for the F⁰ center has been calculated and reported in literature using different methods and models [27–30]. Fig. 6.3 summarizes these results, comparing formation energies $G_f^0(T = 0, p^0)$ according to Eq. 4.1 in the oxygen-rich limit ($\mu_{\text{O}} = 1/2 E_{\text{O}_2}^{\text{tot}}$). The zero-point vibrational energy contribution to the formation energy, estimated using the finite-displacement method for a $2 \times 2 \times 2$ MgO bulk unit cell, is -0.12 eV. Vibrational energy contributions are neglected in the following. It becomes evident that the experimental estimate for the F⁰ center formation energy of 9.29 eV is in disagreement with the results reported in literature and with the formation energies calculated within this work (red symbols in Fig. 6.3). Formation energies calculated with LDA are surprisingly closest to the experimental estimate. LDA is known to systematically overestimate the binding between atoms in crystals [184], hence a higher formation energy is obtained than for the other methods used. Compared to the experimental MgO lattice constant of 4.186 Å [177, 178] (extrapolated to $T = 0$ K), the lattice constant optimized with LDA underestimates (4.165 Å), while PBE (4.258 Å), HSE06 (4.218 Å) and PBE0 (4.212 Å) optimized lattice constants overestimate. For details on lattice parameter optimization see appendix A.3. Geometric relaxation effects play a minor role for formation of F⁰ centers. The relaxation energy due to the removal of oxygen is 0.1 eV at PBE level, and therefore only makes up for 1.4% of the formation energy (7.09 eV). Already for a $2 \times 2 \times 2$ supercell, containing 64 atoms, the formation energy of the neutral oxygen vacancy is converged with respect to the supercell size. The two defect electrons remain localized at the vacancy site.

They occupy a defect level in the middle of the bandgap, and are therefore higher in energy than the electrons associated with the regular ionic bonding in the MgO lattice (see also Fig. 6.10).

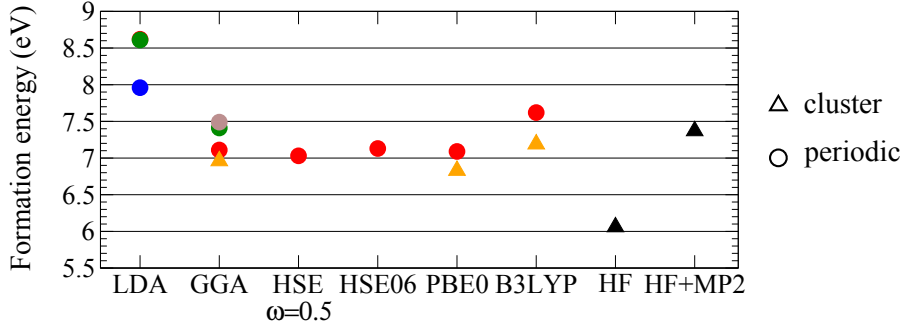


Figure 6.3.: F^0 center formation energy in the oxygen-rich limit ($\mu_O = 1/2 E_{O_2}^{\text{tot}}$). Literature results for $\mu_O = E_O^{\text{tot}}$ were recalculated for $\mu_O = 1/2 E_{O_2}^{\text{tot}}$ using the experimental O_2 binding energy. Different types of exchange-correlation treatment and periodic (circles) or embedded cluster (triangles) models were used. Red circles show results obtained within this work, orange triangles were calculated in a collaboration by S. Sicolo [185]. From literature, periodic DFT calculations at LDA level (blue circle, [27]; green circle [28]) and GGA level (green circle, PBE [28]; gray circle, PW91 [29]), as well as embedded cluster calculations applying HF and HF+MP2 (black triangles [30]) are shown for comparison.

The results calculated with periodic models using the HSE family of functionals, including PBE and PBE0, agree within 0.15 eV, if the O_2 binding energy is corrected, but are ≈ 2 eV lower than the experimental result. The experimental estimate was originally obtained with respect to cohesive energy. Therefore, to compare directly with the measured quantity, G_f^0 is calculated with respect to cohesive energy

$$E_{\text{MgO}}^{\text{coh}} = E_{\text{MgO}}^{\text{bulk}} - E_{\text{Mg}}^{\text{tot}} - 1/2 E_{O_2}^{\text{tot}}, \quad (6.3)$$

where $E_{\text{MgO}}^{\text{bulk}}$ is the total energy of bulk MgO per MgO unit, $E_{\text{Mg}}^{\text{tot}}$ is the total energy of a Mg atom, and the total energy of oxygen $E_{O_2}^{\text{tot}}$ is obtained using the experimental binding energy, as described in Sec. 4.1.2, for different parameter sets (α, ω) (Fig. 6.4). However, the discrepancy between experiment and theory is still mainly due to the formation energy, not the cohesive energy.

It was demonstrated by Ramprasad *et al.* in 2012 that there is a near-linear correlation between the formation energies of neutral point defects in bulk Si, Ge, ZnO, and ZrO_2 and the corresponding valence bandwidth (VBW) of the defect-free parent material, when both are computed as a function of the HSE parameters [186]. The deviations from linearity increase when the bandgap is used instead of the VBW. The bandgap was already pointed out to be an unreliable descriptor for defect formation energies by Lany and Zunger in 2010 [187]. The prescription for finding reliable formation energies for neutral point defects suggested by Ramprasad *et al.* is to find a DFT functional that gives the experimental VBW for the given material – which requires only pristine bulk calculations –, and use the corresponding exchange-correlation functional to compute the accurate defect formation energies.

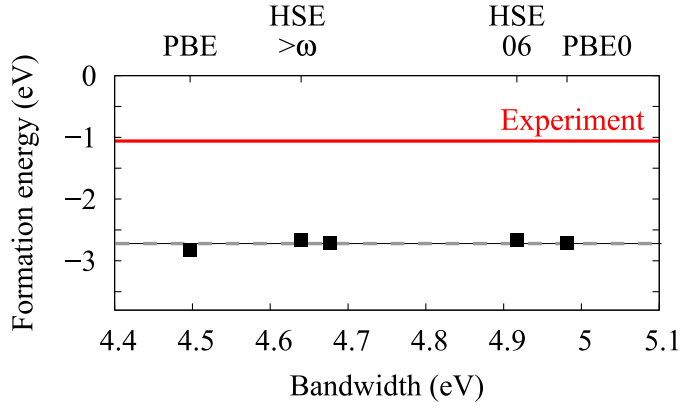


Figure 6.4.: F^0 center formation energy with respect to cohesive energy (Eq. 6.3) in the oxygen-rich limit¹, calculated for different parameter sets (α, ω) of the HSE hybrid-functional family. Formation energies are shown as a function of oxygen 2 p bandwidth, the solid red line indicates the experimental value [26].

For MgO, the bulk neutral F center formation energy G_f^0 only weakly depends on the exchange and screening parameters of HSE. Still, a near-linear correlation with small but finite slope is found for G_f^0 as a function of oxygen 2 p bandwidth (Fig. 6.5). However, the methodology suggested in Ref. [186] cannot be applied to MgO, because of a large uncertainty in experimental oxygen 2 p bandwidth [188–191].

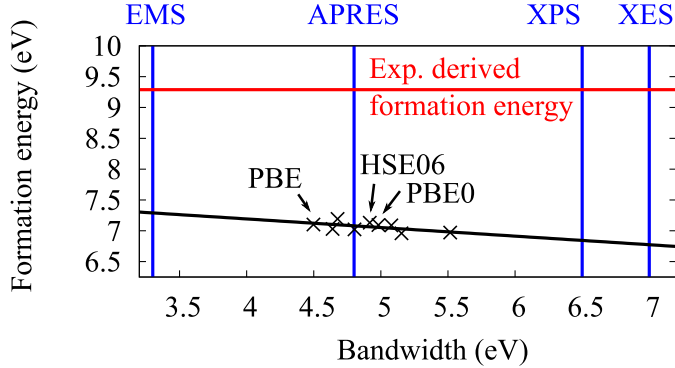


Figure 6.5.: F^0 center formation energy, calculated for different parameter sets of HSE(α, ω) (black symbols), shown as a function of oxygen 2 p bandwidth (black line shows linear fit). The red line indicates the experimentally measured formation energy [26]. The blue lines depict experimental values for the MgO oxygen 2 p bandwidth, measured using electron momentum spectroscopy (EMS) [191], angle-resolved ultraviolet photoelectron spectroscopy (APRES) [190], x-ray photoelectron spectroscopy (XPS) [189] and x-ray emission spectroscopy (XES) [188].

Another approach is to benchmark HSE functionals against higher-level *ab initio* methods,

¹In this work, the oxygen-rich limit is always calculated using the experimental O_2 binding energy as described in Sec. 4.1.2

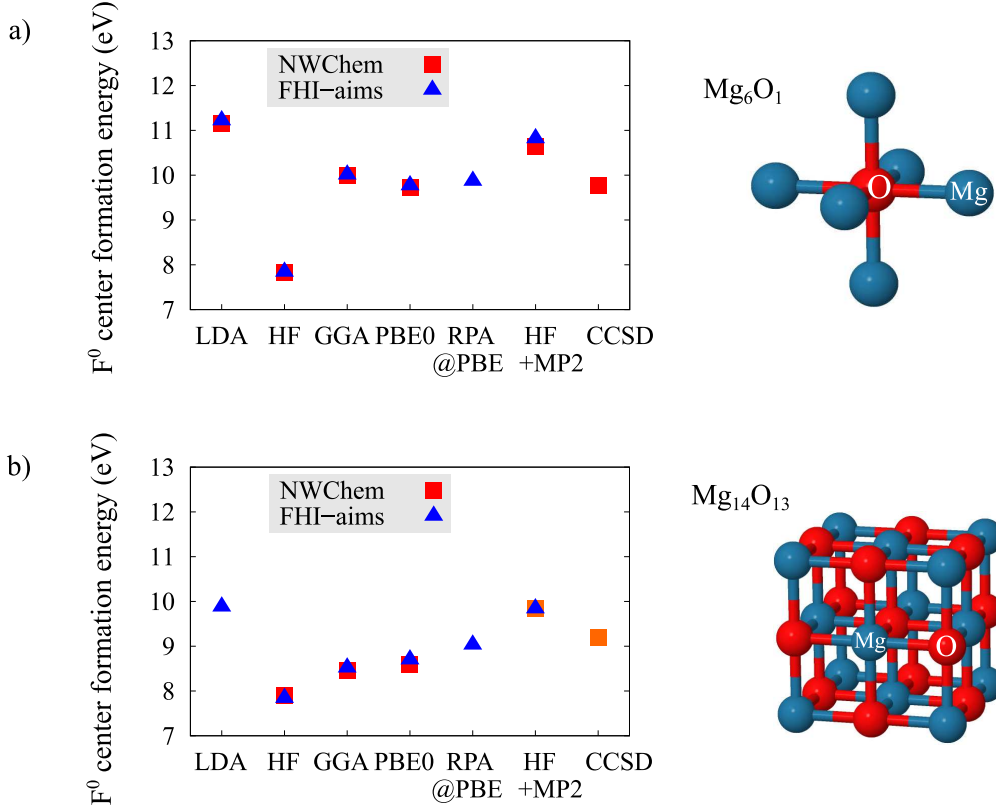


Figure 6.6.: Formation energy of the neutral oxygen vacancy at the center of a) an unembedded Mg₆O₁ (with a charge +10) and b) an unembedded Mg₁₄O₁₃ (with a charge +2) cluster model, calculated at different levels of electronic structure theory using NWChem (red squares) with basis sets up to cc-pVTZ, and FHI-aims (blue triangles) with basis sets up to *tight*, tier 4. Formation energies have been corrected for the basis set superposition error using the counterpoise correction method (see Appendix A.4 for details). In the NWChem calculations for the Mg₁₄O₁₃ cluster, only the cc-pVDZ basis set could be used for the Δ MP2 and Δ CCSD corrections [192–195], since employing a higher-level basis set (cc-pVTZ) using these methods in the available implementation was computationally not feasible due to extremely high memory consumption.

such as coupled-cluster theory with single and double excitations (CCSD), CCSD plus triple excitations by perturbation theory (CCSD(T)), RPA or *GW*. This can be performed efficiently using cluster models. First, two MgO clusters are calculated: a six-coordinated oxygen atom (Mg₆O₁), and a 27-atom MgO cube (Mg₁₄O₁₃) (see Fig. 6.6). The clusters were constructed using the PBE optimized lattice constant of bulk systems. In both clusters there are more magnesium atoms than oxygen atoms. The clusters are therefore charged by removing all magnesium valence electrons that cannot be accommodated by oxygen atoms (counting two electrons per oxygen atom). This corresponds to a charge +10 for Mg₆O₁ and a charge +2 for Mg₁₄O₁₃. The oxygen removal energies for these two (unrelaxed) systems are calculated at different levels

of electronic structure theory, where possible using two different all-electron codes, FHI-aims and NWChem. Since the cluster models are not embedded, the oxygen removal energies are not quantitatively comparable to those of the F^0 center in extended material. However, for each cluster model, the formation energy of the neutral F center calculated with CCSD is close to the results obtained with PBE ($\alpha = 0, \omega = \text{arbitrary}$) and PBE0 ($\alpha = 0.25, \omega = 0$). The formation energies obtained with CCSD are much closer to the HSE results than to the experimental value.

This result has been corroborated in a cooperation with Prof. Sauer's theoretical chemistry group of the Humboldt-Universität zu Berlin. Embedded cluster calculations at PBE, PBE0 and B3LYP level and with the CCSD(T) coupled-cluster method were performed using the TURBOMOLE code [96]. For the DFT TURBOMOLE calculations on embedded clusters, $[5s3p2d1f]/[5s4p3d]$ triple-zeta valence plus polarization basis sets were used [196]. For the CCSD(T) computations also electrons in the magnesium 2 s and 2 p shells were correlated using core-valence correlation consistent basis sets, cc-pCVXZ (X = D, T, Q) for magnesium, whereas on the O^{2-} ions the aug-cc-pVXZ basis sets were used [197]. For consistency between FHI-aims and TURBOMOLE, embedded cluster calculations at PBE, PBE0 and B3LYP level were also performed with FHI-aims using the same cluster models. In both CCSD(T) and DFT calculations, the basis set superposition error (BSSE) was evaluated following the Boys-Bernardi counterpoise correction [198]. The MgO clusters are embedded in a periodic point charge array using the periodic electrostatic embedded cluster model [199] in TURBOMOLE, and a converged finite set of point charges in FHI-aims. To minimize non-physical polarization of peripheral oxygen anions by the embedding point charges, pseudopotentials are added to the first shell of embedding Mg^{2+} cations (all-electron Hay&Wadt effective core potentials (ECPs) [200] in TURBOMOLE, and Troullier-Martins-type norm-conserving non-local pseudopotentials [201, 202] in FHI-aims calculations). The PBE lattice constant is used for the embedded clusters. Apart from the outermost frozen shell of atoms, full relaxation is allowed in the DFT calculations for larger clusters ($Mg_{14}O_{19}$). For the CCSD(T) calculations and respective DFT values obtained for smaller clusters (Mg_6O_9), formation energies of neutral, unrelaxed F centers are compared.

G_f^0 is calculated at very high accuracy with CCSD(T) for the embedded Mg_6O_9 cluster (Fig. 6.7), the largest model that is still computationally feasible, due to high memory consumption. The CCSD(T) value is compared to the formation energies calculated for the same system with various DFT functionals, yielding a correction term $\Delta CCSD(T)$ for each DFT functional. The correction term is finally added to the DFT formation energies calculated for a larger cluster $Mg_{14}O_{19}$ that is converged also with respect to geometric relaxation.

Table 6.1 summarizes the formation energies for a neutral F^0 center in MgO bulk calculated with the Mg_6O_9 model, and formation energies including geometric relaxation as obtained with an $Mg_{14}O_{19}$ embedded cluster. For consistency, formation energies calculated with FHI-aims for the same cluster models using a *tight*, tier 3 basis, and for periodic models using a *tight*, tier 2 basis are also shown. Obviously, the formation energy of the unrelaxed defect is already converged within 0.1 eV with respect to cluster size.

The corrections $\Delta CCSD(T)$ for the DFT formation energies are -0.09 eV for PBE, 0.07 eV for PBE0, and -0.28 eV for B3LYP. Adding these corrections to the DFT formation energies obtained with a converged cluster size $Mg_{14}O_{19}$ (with charge -10), yields DFT+ $\Delta CCSD(T)$ results of 6.85 eV, 6.88 eV, and 6.89 eV, respectively.

From this it is concluded that the formation energies for neutral F centers can be calculated

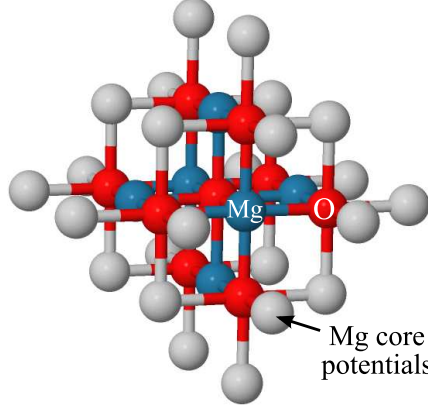


Figure 6.7.: Mg_6O_9 cluster model (with charge -6), embedded by magnesium core potentials. Embedding point charges (see text) are not shown. CCSD(T) calculations were performed using this model at unrelaxed bulk F^0 geometry, where the central oxygen atom in the cluster was removed.

Table 6.1.: Formation energies, G_f^0 , calculated for unrelaxed (unrel.) and relaxed (rel.) atomic coordinates for a bulk F^0 center, as obtained from embedded cluster DFT and CCSD(T) calculations employing FHI-aims (AIMS) and the TURBOMOLE (TURB.) code.

Structure model	PBE	HSE06	PBE0	B3LYP	RPA @PBE	rPT2 @PBE	CCSD	CCSD(T)
Mg_6O_9 (unrel.,TURB.)	7.18	–	7.02	7.37	–	–	7.05	7.09
Mg_6O_9 (unrel.,AIMS)	7.11	7.03	6.99	7.35	7.13	7.45	–	–
$\text{Mg}_{14}\text{O}_{19}$ (unrel.,TURB.)	7.06	–	–	–	–	–	–	–
$\text{Mg}_{14}\text{O}_{19}$ (rel.,TURB.)	6.94	–	6.81	7.17	–	–	–	–
$\text{Mg}_{14}\text{O}_{19}$ (rel.,AIMS)	–	7.05	–	–	–	–	–	–
periodic (rel.,AIMS)	7.09	7.04	7.07	–	–	–	–	–

accurately to within 0.2 eV even at PBE level. In particular, the DFT+ Δ CCSD(T) formation energy values are in good agreement with the HSE06 F^0 formation energies 7.04 eV and 7.05 eV, obtained from the $\text{Mg}_{14}\text{O}_{19}$ embedded cluster and periodic calculations, respectively, using FHI-aims. It is concluded that the experimental value for the bulk F^0 center formation enthalpy in MgO [26] is a significant overestimate. The most likely reason is that thermodynamic equilibrium was not reached in the experiment.

Based on the accurate value of the formation energy, the reasons for the failure of certain electronic structure methods to accurately describe the removal of a neutral oxygen atom from MgO bulk can be deduced (see Fig. 6.3 and Fig. 6.6): using the local density approximation leads to overestimated formation energies, while not including electron correlation yields un-

derestimated formation energies. It is also interesting that the formation energy calculated with the many-body perturbation theory method RPA is in good agreement with the CCSD(T) result, while renormalized second-order perturbation theory rPT2 [72, 203, 204], which goes beyond RPA by including second-order screened exchange (SOSEX) and renormalized single excitations (rSE), rpT2=RPA+SOSEX+rSE, overestimates the F^0 center formation energy (Table 6.1). CCSD, which yields a slightly underestimated formation energy of 7.05 eV, is connected to rPT2 in so far that the Goldstone diagrammatic expression for CCD (where only double, but not single excitations are accounted for) equals that of RPA+SOSEX [204]. RPA+SOSEX yields an overestimated formation energy of 7.40 eV. Obviously, for the considered MgO system, there is no advantageous error cancellation when adding SOSEX and rSE to RPA.

6.2. Charged defects in bulk MgO

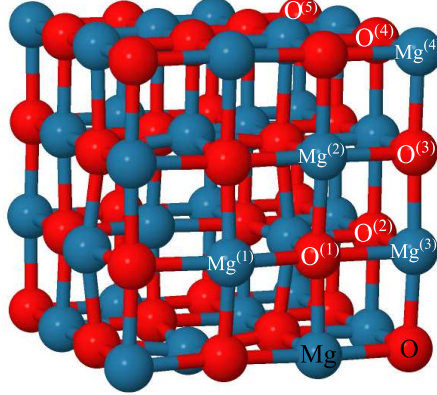
In contrast to the neutral defect discussed above, the calculated energy levels and total energies of charged oxygen vacancies in MgO are found to depend strongly on the employed treatment of exchange and correlation of the many-electron system. A systematic approach is taken to explore this dependence using the whole parameter range of the HSE functional family. An optimal *opt-HSE* functional that correctly describes the charge excitation for the defects is identified by requesting that the ionization potentials obtained with the opt-HSE functional should agree with the results of a G_0W_0 @opt-HSE calculation.

6.2.1. Geometric relaxation

Atomic relaxation, which can make a large contribution to the formation energy, especially for charged defects, is calculated using the semilocal exchange-correlation functional PBE for all periodic models including all atoms in a supercell. HSE calculations are performed at these geometries, since changes in the calculated formation energies when scaled to optimized HSE lattice parameters are found to be negligible. (The absolute error is <0.03 eV for the most severe case, the F^{2+} center, calculated with HSE06 for a bulk defect in a 64-atom supercell and for a surface defect in an 80-atom supercell.)

When an oxygen atom is removed from the MgO lattice, the arrangement of atoms in the vicinity of the defect will adjust to lower the energy of the system. For the neutral F center, where two electrons remain at the defect site, the displacement of atoms is not very pronounced, since the defect electron distribution resembles the electron distribution around an O^{2-} anion. Removing one or both of the defect electrons leads to a more distinct geometric relaxation. The Mg^{2+} ions close to the positively charged oxygen vacancy are repelled, while the O^{2-} lattice ions feel an attraction. For the neutral F^0 center, only the nearest neighboring atoms are involved in the geometric relaxation. For charged defects, also next-nearest neighbors contribute to the geometric relaxation around the oxygen vacancy. There is no symmetry-breaking in either case, which was also tested by starting the relaxation from a geometry with broken symmetry using PBE and HSE06 exchange-correlation functionals. The geometric relaxation for all relevant charge states are quantified in Table 6.2. The equilibrium PBE bulk distances between magnesium and oxygen atoms and the oxygen vacancy site are listed together with the relaxed

distances for the F^0 , F^+ , and F^{2+} center. The relaxations are given in % with respect to the equilibrium bulk distances. There is an outward relaxation of nearest-neighbor magnesium atoms and an inward relaxation of nearest-neighbor oxygen atoms for F^{2+} and F^+ centers, while for the F^0 center a weak outward relaxation of both nearest-neighboring magnesium and oxygen atoms takes place.



Atom	Eq. distance to vacancy site (Å)	Relaxation (%) F^0	Relaxation (%) F^+	Relaxation (%) F^{2+}
Mg (1)	2.129	0.6	5.0	9.3
O (1)	3.011	0.3	-1.1	-2.6
Mg (2)	3.688	0.0	0.1	0.1
O (2)	4.258	0.0	0.5	1.2
Mg (3)	4.761	0.0	0.5	0.9
O (3)	5.215	0.0	-0.2	-0.4
O (4)	6.022	0.0	-0.1	-0.3
Mg (4)	6.388	0.0	0.1	0.1
O (5)	7.375	0.0	-0.1	-0.1

Table 6.2.: Outward (positive) and inward (negative) relaxation in % with respect to the equilibrium bulk distances between close-by atoms and vacancy site. The model shown is a cut out of a periodic 1,000-atom relaxed supercell with an F^{2+} center.

The more distinct the geometric changes due to the defect are, the larger is the supercell size needed to obtain the respective relaxed structure without geometry-related interaction between defects. This is evident from the supercell size dependence of the relaxation energy, which is defined as the total energy difference between the relaxed and unrelaxed system with a defect, shown in Fig. 6.8. In fact, this energy difference also incorporates size-dependent changes in electronic polarizability, which cannot be rigorously separated from the geometric relaxation effects. The converged relaxation energy increases drastically with defect charge, it is < 0.1 eV for the neutral oxygen vacancy, 0.9 eV for the F^+ center, and 3.0 eV for the F^{2+} center. A

$2 \times 2 \times 2$ supercell is sufficient to obtain a relaxation energy converged within 0.01 eV for the neutral oxygen vacancy. However, the defect-defect distance must be $> 12 \text{ \AA}$ for the F^+ center and $> 16 \text{ \AA}$ for the F^{2+} center to reach converged relaxation energies within 0.1 eV.

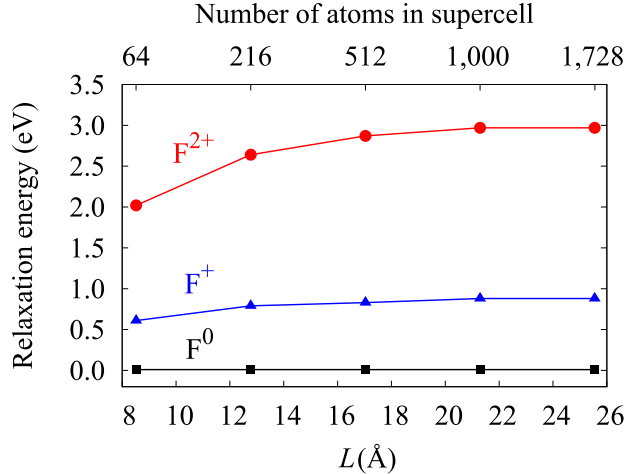


Figure 6.8.: Convergence of relaxation energies with supercell size for the bulk F^0 , F^+ , and F^{2+} centers.² L is the supercell lattice constant. The PBE exchange-correlation functional was used.

6.2.2. Electronic structure

The most prominent feature in the electronic structure of F centers in MgO is a highly localized defect state. For the neutral defect, this state is occupied by two electrons. By removing one or two electrons from the defect level, singly- or doubly-charged oxygen vacancies can be created. As a measure for spatial localization, the spin density for the F^+ center is shown in Fig. 6.9, as calculated with PBE and HSE06. The stronger localization of the defect electrons obtained with HSE06 is due to the reduced self-interaction error. However, in case of F centers in MgO, there is no *qualitative* difference between the PBE and HSE06 results. The strong localization of the *s*-shaped defect wave function is responsible for several unique properties of F centers. The charge density due to the two defect electrons of the F^0 center resemble the missing O^{2-} ion so closely that the crystal lattice is hardly disturbed by the presence of the defect.

The band structures for bulk F centers show the defect level as a flat energy band close to midgap (Fig. 6.10). The absence of dispersion is a consequence of the high degree of defect-state localization. The defect charge has only a weak influence on the position of the defect state with respect to VBM. For the F^+ center, the two spin channels are considered separately, since the two defect spin states are no longer degenerate. Projecting the density of states (DOS) on the basis functions of individual atoms in the system, it is shown that the defect level is mainly due to magnesium 3 *s* states, while the VBM is dominated by oxygen 2 *p* states.

²If not explicitly mentioned, FHI-aims *tight, tier 2* basis settings were used for periodic defect calculations for MgO in this work. (For convergence tests see Appendix A.2.)

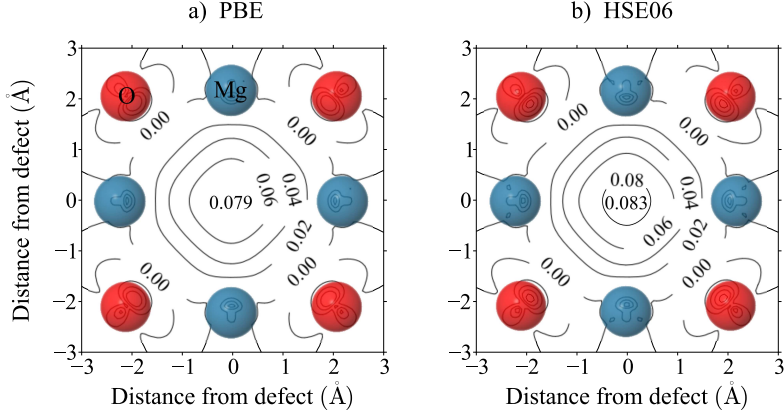


Figure 6.9.: Spin density (in \AA^{-3}) for F^+ , calculated with PBE (a) and HSE06 (b) using a 64-atom supercell. Shown is a cut along the (100) plane with the defect in the center. Contour levels are drawn in steps of 0.02\AA^{-3} .

The positions of defect level and CBm with respect to VBM as a function of supercell size for F centers in different charge states is shown in Fig. 6.11 Again, the supercell size needed to converge the electronic structure increases with defect charge. Geometric relaxation is responsible for a deviation from monotonic behavior for the 64-atom cell. Still, the position of the defect level can be estimated within 0.1 eV from the converged result already for this smallest cell size for all three charge states. The defect level positions with respect to VBM, calculated with HSE06 for a 64-atom supercell are 3.10 eV for F^0 , 2.30 eV for the occupied and 4.52 eV for the unoccupied spin state for F^+ , and 3.77 eV for F^{2+} . The KS bandgap calculated with HSE06 in pristine MgO is 6.5 eV, while the experimental bandgap, measured by reflectance spectroscopy, is 7.78 eV [179].

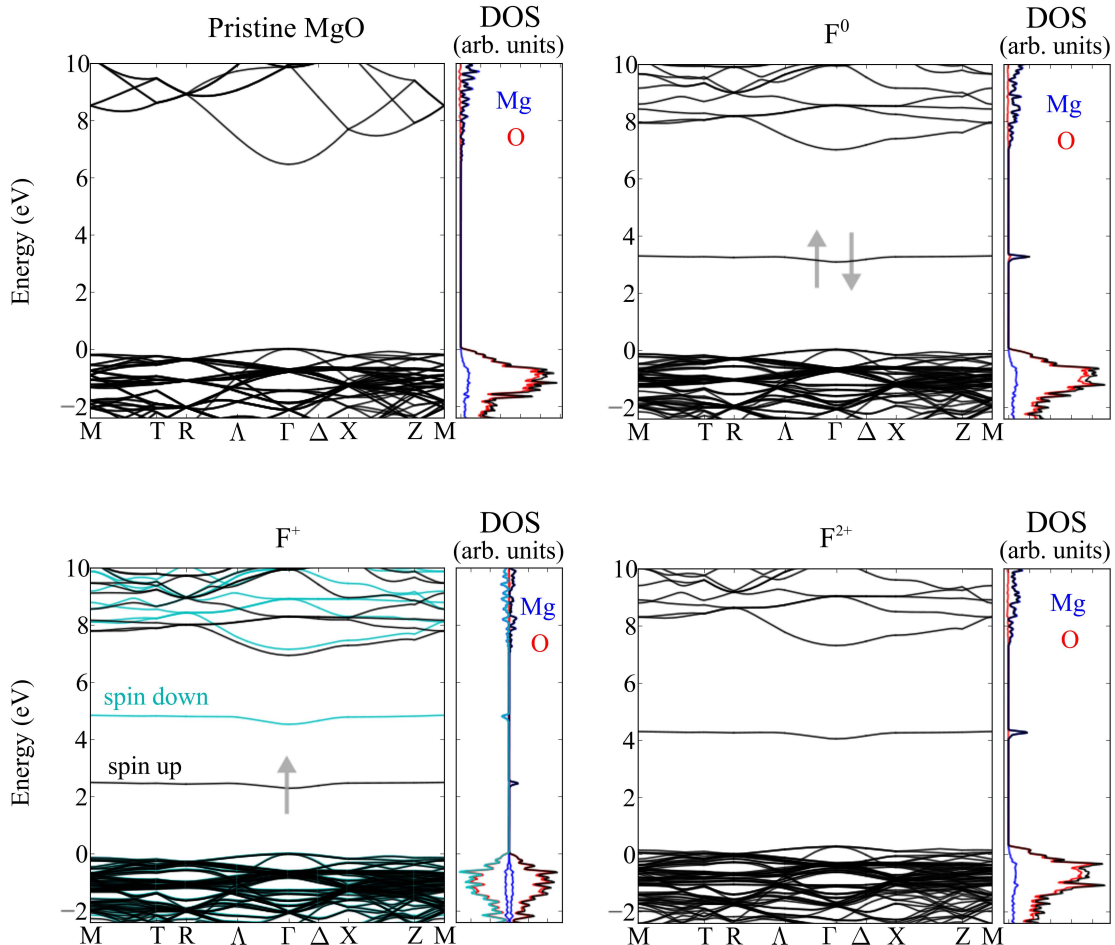


Figure 6.10.: Band structures, total density of states (DOS) (black) and species projected DOS (magnesium blue, oxygen red) for the pristine MgO crystal and the bulk F^0 , F^+ , and F^{2+} centers, calculated for a 64-atom supercell using HSE06. Defect-level occupations are marked by gray arrows.

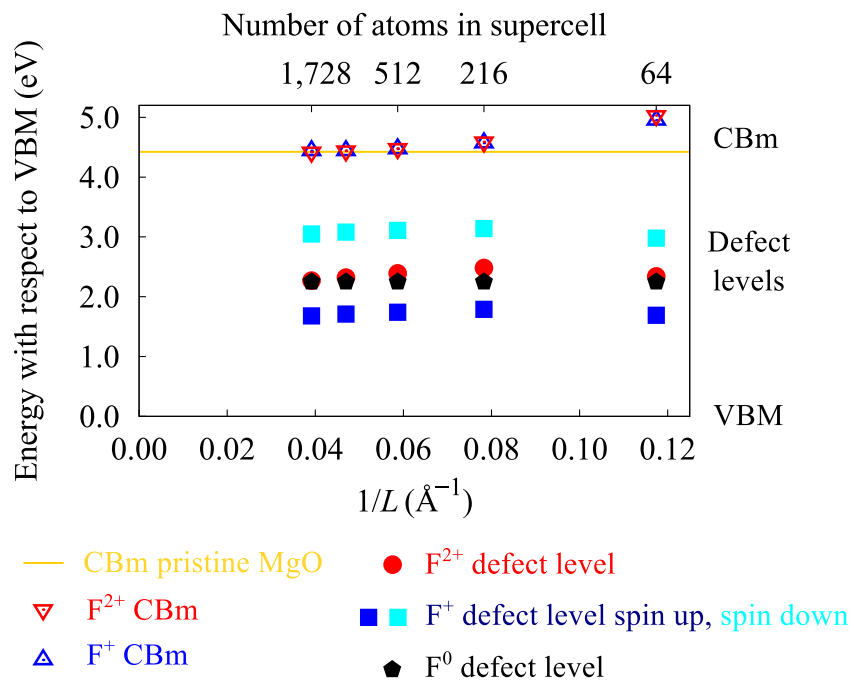


Figure 6.11.: Defect levels and CBm with respect to VBM for increasing supercell size, calculated with PBE. $1/L$ is the reciprocal supercell lattice constant. For each supercell size, the geometry is fully relaxed.

6.2.3. Opt-HSE for charge-transition levels and formation energies

In the following, the dependence of calculated total energies on the exchange-correlation treatment is analyzed by determining the formation energies for the F^0 , F^+ , and F^{2+} centers in the dilute limit (*i.e.*, for isolated defects) for different HSE functionals. To follow the extrapolation procedure outlined in Sec. 4.1.3, formation energies for increasing supercell sizes have to be calculated with each functional. First, the full extrapolation curve for the charged defects is calculated with PBE. For members of the $HSE(\alpha, \omega)$ family that incorporate a fraction of exact exchange, which corresponds to all cases where $\alpha \neq 0$ and ω is finite, this is not a trivial task. Hybrid functional calculations for unit cells of more than 300 atoms are currently unfeasible, since hybrid calculations are far more time-consuming than PBE calculations.

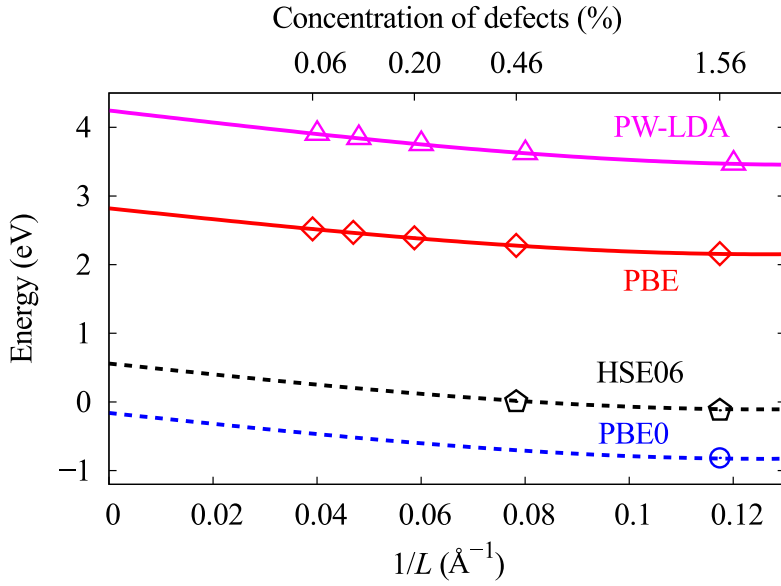


Figure 6.12.: Finite-size scaling for the F^{2+} center formation energy ($\epsilon_F = \text{VBM}$, $\mu_O = 1/2E_{O_2}$). Solid lines show least-squares fits to Eq. 4.28 for LDA and PBE formation energies. Formation energies obtained with HSE06 lie on the shifted PBE curve. Accordingly, PBE coefficients a_1^2 and a_3^2 are used to extrapolate to isolated defects for all members of the $HSE(\alpha, \omega)$ functional family.

However, it is found that the HSE06 formation energies for the two smallest supercells (64- and 216-atom cells), lie on the same fitting curve as the PBE formation energies, but shifted by a constant value, as shown in Fig. 6.12 for the F^{2+} center. Therefore, formation energies for all HSE functionals are calculated for the smallest supercell, and then extrapolated to the dilute limit ($1/L \rightarrow 0$) using a shifted PBE fitting function. The calculated values of the dilute limit $G_f^{\text{bulk},q}(1/L \rightarrow 0)$ and the coefficients a_1^q and a_3^q as obtained by extrapolation, are summarized in Table 6.3. Vibrational contributions to the formation energies are discussed in Sec. 6.2.4.

There is a strong dependence of the formation energies of the charged defects on the parameters of the HSE functional family, when the Fermi level is at the VBM (see Fig. 6.12). The question arises which HSE parameter set (α, ω) should be used to describe the stability of

Table 6.3.: $G_f^{\text{bulk},q}(1/L \rightarrow 0)$ and coefficients a_1^q and a_3^q as obtained with LDA and PBE exchange-correlation (xc) functionals for $\epsilon_F = \text{VBM}$ and $\mu_O = 1/2 E_{O_2}^{\text{tot}}$.

xc functional	q	$G_f^{\text{bulk},q}(1/L \rightarrow 0)$ (eV)	$a_1^q(\text{eV}\text{\AA})$	$a_3^q(\text{eV}\text{\AA}^3)$
LDA	0	8.62	0	0
	1	6.03	-2.17	20.94
	2	4.21	-8.82	162.49
PBE	0	7.09	0	0
	1	4.54	-1.91	20.77
	2	2.82	-7.96	167.27

charged F centers in MgO correctly. To address this issue, the dependence of formation energies and of charge-transition levels on the exchange-correlation treatment is further explored.

The charge-transition level ($q + 1/q$) corresponds to the Fermi level position where point defects in charge states $q + 1$ and q are in thermodynamic equilibrium with each other, so that their formation energies coincide. The charge-transition level between the singly charged and the charge-neutral F centers is therefore given by the equilibrium condition $G_f^1 = G_f^0$, which can be written in terms of total energies and chemical potentials as

$$E_{\text{vac}}^+ - E_{\text{host}}^+ + \mu_O + \epsilon_F = E_{\text{vac}}^0 - E_{\text{host}}^0 + \mu_O. \quad (6.4)$$

The charge-transition level follows as

$$(+/0) = E_{\text{vac}}^0 - E_{\text{host}}^0 - (E_{\text{vac}}^+ - E_{\text{host}}^+). \quad (6.5)$$

In analogy, the charge transition level between the doubly charged and the singly charged F centers is

$$(2 + /+) = E_{\text{vac}}^+ - E_{\text{host}}^+ - (E_{\text{vac}}^{2+} - E_{\text{host}}^{2+}). \quad (6.6)$$

When the neutralizing background method is applied for charge compensation, the host system for both defect states are identically given by the neutral, pristine MgO bulk system and the expression reduces to

$$(+/0) = E_{\text{vac}}^0 - E_{\text{vac}}^+. \quad (6.7)$$

In analogy, the charge-transition level between F^{2+} and F^+ centers can be expressed as

$$(2 + /+) = E_{\text{vac}}^+ - E_{\text{vac}}^{2+}. \quad (6.8)$$

To see how the charge-transition levels and formation energies depend on (α, ω) , the extrapolated formation energies $G_f^{\text{bulk},q}$ for F^0 , F^+ , and F^{2+} centers in the dilute limit are computed for varying HSE parameter sets as a function of Fermi energy. The respective charge-transition levels $(2 + /+)$ and $(+/0)$ can then be obtained at the formation energy intersections, as shown for the example of HSE06 in Fig. 6.13a. Here, oxygen-rich conditions are considered. Changing the oxygen chemical potential results in a constant shift in formation energies (see Eq. 4.1). For

example, at a chemical potential of -0.5 eV below the oxygen-rich limit, all formation energies in Fig. 6.13a are shifted down by -0.5 eV.

Both *p*-type MgO, where the Fermi level is close to VBM, and *n*-type MgO, where the Fermi level is close to CBm, are covered in Fig. 6.13a. In *p*-type MgO, $q = 2$ is the most stable charge state of the bulk F center. In *n*-type MgO, F^0 is the most stable defect, but its formation energy is very high. In the following, the focus is on *p*-type material, because of its intriguing catalytic properties that have been outlined in the introduction (Sec. 1). Only in *p*-type MgO the concentration of oxygen vacancies, namely F^{2+} centers, in thermodynamic equilibrium can be significant.

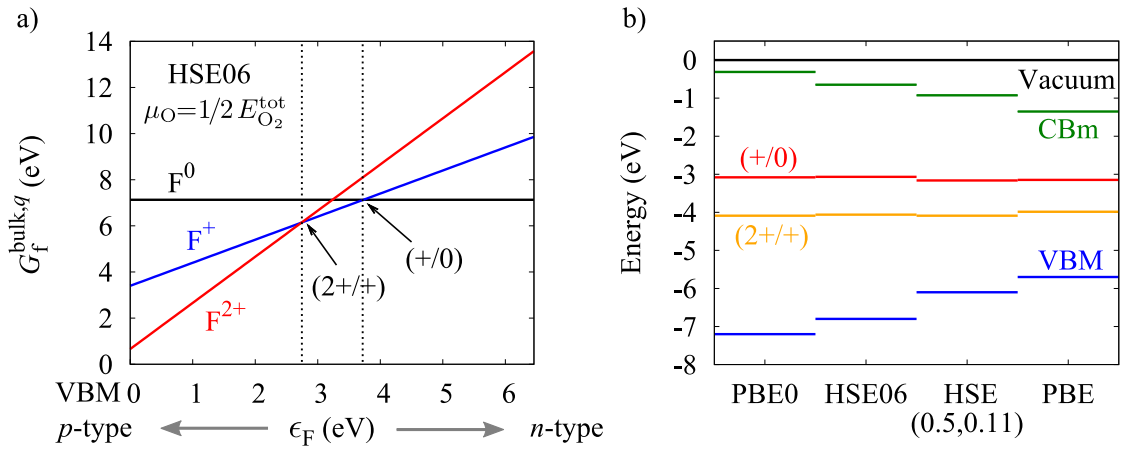


Figure 6.13.: a) Formation energies of oxygen vacancies in bulk MgO, $G_f^{\text{bulk},q}$, in the dilute limit, calculated with HSE06 using (Eq. 4.1) as a function of Fermi energy, in the oxygen-rich limit. The energy zero of ϵ_F is at the VBM. Charge-transition levels (2+/+) and (+/0) are marked by arrows. b) VBM, CBm, and charge-transition levels (Eq. 6.5- 6.6) for different functionals of the HSE family. The energy zero is at the vacuum level.

The fact that, compared to the neutral F center, the formation energies of charged defects depend much stronger on the exchange-correlation functional, hints at a dependence of the VBM energy level (the Fermi level in this system) on exchange-correlation treatment, since only for charged defects the formation energy depends on the Fermi energy (Eq. 4.1, see also Ref. [205]). To investigate the dependence further, the electronic structure, including VBM, CBm, and charge-transition levels, is considered for each functional and aligned at the energy level in vacuum. Setting the energy zero to the vacuum level corresponds to calculating formation energies and charge-transition levels for a situation, where the Fermi level is the vacuum level. This is only considered to gain a better understanding, why for the realistic situation, where $\epsilon_F = \text{VBM}$, the formation energies depend on the exchange-correlation functional. The vacuum level is a well-defined reference energy, which is easily accessible in cluster calculations and can also be determined for a periodic bulk model by performing a calculation for a periodic slab of the pristine MgO (100) surface. A vacuum region of ≈ 200 Å separates repeating 5-layer MgO slabs, where the potential in the middle of this vacuum region is the vacuum level $E_{\text{VAC}}^{\text{Surf}}$ for the surface calculation. To obtain the energy difference between VBM and vacuum level

for the bulk system VBM_{VAC}^{Bulk} , the difference between E_{VAC}^{Surf} and the 1 s core level of magnesium $E_{\text{core}}^{\text{Surf}}$ in the middle, bulk-like layer of the slab is determined. This difference is added to the magnesium 1 s core level in the bulk system $E_{\text{core}}^{\text{Bulk}}$, and the resulting bulk vacuum level is subtracted from the bulk VBM $E_{\text{VBM}}^{\text{Bulk}}$ obtained in the periodic bulk calculation

$$VBM_{VAC}^{\text{Bulk}} = E_{\text{VBM}}^{\text{Bulk}} - \left(E_{\text{core}}^{\text{Bulk}} + (E_{VAC}^{\text{Surf}} - E_{\text{core}}^{\text{Surf}}) \right). \quad (6.9)$$

VBM_{VAC}^{Bulk} is converged with respect to slab separation and slab thickness. The calculated values for VBM_{VAC}^{Bulk} are -5.7 eV for PBE, -6.8 eV for HSE06, and -7.2 eV for PBE0.

Table 6.4.: $G_f^{\text{bulk},q}$, (+/0), and (2++) in eV for F^0 , F^+ , and F^{2+} centers in MgO bulk in the dilute limit, calculated with different exchange-correlation functionals using periodic boundary conditions (pbc), employing FHI-aims. The Fermi level is the vacuum level, the numbers in parentheses correspond to the Fermi level at VBM, μ_0 is $1/2E_{O_2}^{\text{tot}}$. HSE06 provides the best accuracy within the HSE family of functionals for the formation energy of F centers in MgO (discussed below), and the corresponding numbers are therefore highlighted. The calculations in Ref. [30] were performed using embedded clusters (ecm).

Method	F^0	F^+	F^{2+}	(+/0)	(2++)
PBE-pbc	7.09	10.24 (4.54)	14.22 (2.82)	-3.15 (2.55)	-3.98 (1.72)
HSE06-pbc	7.04	10.20 (3.40)	14.16 (0.56)	-3.16 (3.64)	-3.96 (2.84)
PBE0-pbc	7.07	10.15 (2.95)	14.24 (-0.16)	-3.08 (4.12)	-4.09 (3.11)
HF+MP2-ecm [30]	7.35	9.98	13.88	-2.63	-3.90

VBM, CBm, and charge-transition levels are shown in Fig. 6.13b for different functionals of the HSE family, when the Fermi level is the energy level in vacuum. In agreement with related work on ZnO and ZrO_2 by Ramprasad *et al.* [186], the charge-transition levels (2++) and (+/0) for F centers in bulk MgO are almost independent on the exchange-correlation functional within the HSE family, when the Fermi level is the vacuum level. Indeed, in MgO this is even true for the corresponding formation energies $G_f^{\text{bulk},q}$. Bulk F center formation energies and charge-transition levels for ϵ_F at the vacuum energy level and $\epsilon_F = \text{VBM}$ (in parenthesis), calculated with different exchange-correlation functionals, are summarized in Table 6.4.

When ϵ_F is at the vacuum level, formation energies calculated using periodic boundary conditions and the PBE, HSE06, and PBE0 functionals as representative HSE members, agree within 0.05 eV for F^0 , 0.09 eV for F^+ , and 0.08 eV for F^{2+} . The respective deviations for the charge-transition levels are ≤ 0.13 eV.

For the more relevant case, when ϵ_F is at the VBM, the formation energies depend almost linearly on the exchange parameter α , as shown for $\omega = 0.11$ bohr $^{-1}$ and $\omega = 0.3$ bohr $^{-1}$ in Fig. 6.14. This is mainly due to a linear dependence of the VBM with respect to vacuum on the exchange parameter, since the charge-transition levels' positions depend weakly on α when ϵ_F is the energy in vacuum. Accordingly, the near-linear dependence of the formation energy on α is approximately twice as strong for F^{2+} as for F^+ .

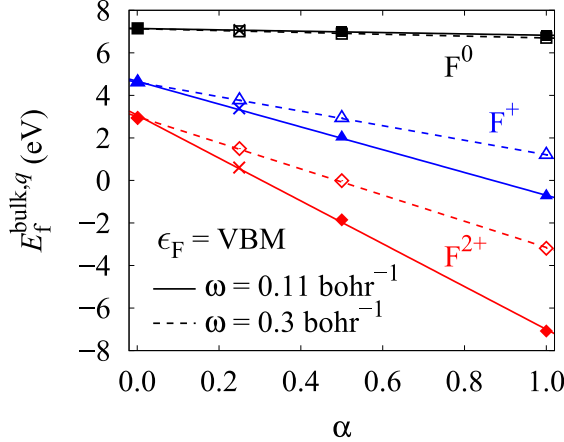


Figure 6.14.: Defect formation energies $G_f^{\text{bulk},q}$ in the dilute limit as a function of HSE exchange parameter α for two choices of the range-separation parameter. Crosses mark the results for HSE06. The Fermi level is at the VBM, and the chemical potential of oxygen $\mu_O = 1/2E_{O_2}$.

Next, an optimal DFT exchange-correlation functional to describe the formation energies of F centers in MgO is identified, according to a condition on DFT ionization energies. The term *ionization energy* originally refers to the energy required to remove an electron from a system and put it to the vacuum. This concept is used in a wider sense, referring to ionization energy as the energy required to remove one electron from the system and put it to the Fermi level. For an F center in charge state q , the ionization energy at fixed geometry describes the charging of the defect $q \rightarrow q + 1$. The charge transition level $(q + 1/q)$, where the energy zero is at the VBM (compare Fig. 6.13) can be interpreted as the *adiabatic* ionization energy, where geometric relaxation due to the change in charge state is accounted for and the removed electron has been brought to the VBM. Since it is found that atomic relaxation around F centers in MgO is described accurately already by the PBE functional, it remains to find HSE parameters that give correct ionization energies at fixed geometry.

The GW approach allows to accurately calculate single-particle excitation energies, which includes the ionization potential. In practice, GW ionization energies are usually calculated as a perturbative correction to the Kohn-Sham levels. To distinguish this approach from the non-perturbative, fully self-consistent GW , it is usually termed $G_0W_0@\text{XCA}$, where XCA denotes the employed exchange-correlation approximation and is replaced by the name of the DFT functional used as an input. The following approach is inspired by the $X\alpha$ concept by Slater [206, 207]: Such parameters of the HSE functional are found that the ΔSCF ionization energy, calculated with the corresponding functional opt-HSE, coincides with the $G_0W_0@\text{opt-HSE}$ ionization energies.

The ionization potential at a fixed defect geometry for a given functional $\text{HSE}(\alpha, \omega)$ is

$$I_{\Delta\text{SCF}}^{q \rightarrow q+1} = E_{\text{vac}}^{q+1} + \epsilon_F - E_{\text{vac}}^q, \quad (6.10)$$

where both E_{vac}^q and E_{vac}^{q+1} are extrapolated to the dilute limit. For $\epsilon_F = \text{VBM}$, $I_{\Delta\text{SCF}}^{q \rightarrow q+1}$ depends

on (α, ω) . The requirement that GW and HSE ionization energies agree defines the opt-HSE functional that correctly describes the charge excitation of the defect

$$I_{G_0W_0}^{q \rightarrow q+1} = \epsilon_F - \epsilon_{\text{HOMO}}^{G_0W_0} \stackrel{!}{=} I_{\Delta\text{SCF}, \text{opt-HSE}}^{q \rightarrow q+1}. \quad (6.11)$$

Here the HOMO level is calculated by G_0W_0 @opt-HSE. An embedded cluster model can be used to efficiently perform this validation step. The ionization energies $I^{0 \rightarrow +}$ and $I^{+ \rightarrow 2+}$ for $\omega = 0.11 \text{ bohr}^{-1}$ as a function of α are calculated for ϵ_F at VBM at F^0 geometry for the embedded Mg_6O_9 cluster model (Fig. 6.7) using FHI-aims. The Fermi level ϵ_F is obtained as $\text{VBM} = E_{\text{host}}^{+1} - E_{\text{host}}$ using HSE functionals, and from the HOMO of the host system in the corresponding G_0W_0 @HSE calculations. The ionization potentials show a near-linear dependence on the exchange parameter α for both ΔSCF and G_0W_0 methods (Fig. 6.15). The starting point dependence of the G_0W_0 ionization energies is weak for this system. The intersection of the linear fits are at $\alpha=0.27$ for $I^{0 \rightarrow +}$ and $\alpha=0.26$ for $I^{+ \rightarrow 2+}$, very close to α in HSE06 ($\alpha=0.25$). The same result is obtained, when the HSE ionization energies are determined from the highest occupied Kohn-Sham level at half occupation [45, 47]. Therefore, HSE06 is used as an opt-HSE functional that correctly describes the charge excitation of the defect. The difference in formation energies with $\alpha=0.25$ instead of $\alpha=0.27$ is negligible for F^0 , less than 0.1 eV for F^+ , and less than 0.2 eV for F^{2+} .

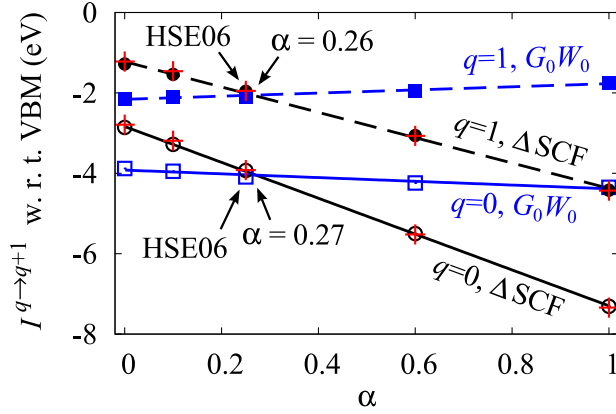


Figure 6.15.: Ionization potentials $I^{q \rightarrow q+1}$ at F^0 geometry calculated for an Mg_6O_9 embedded cluster using the ΔSCF method with HSE functionals (black circles) and from the HOMO of a G_0W_0 @HSE calculation (blue squares). The screening parameter is $\omega = 0.11 \text{ bohr}^{-1}$. Solid and dashed lines show linear fits to $I^{0 \rightarrow +}$ and $I^{+ \rightarrow 2+}$ as a function of exchange parameter α . Red crosses show the Kohn-Sham eigenvalues at half occupation.

Furthermore, it has been found in Sec. 6.1 that DFT+ $\Delta\text{CCSD(T)}$ results of the F^0 formation energy are in good agreement with the HSE06 F^0 formation energy. Thus, HSE06 is the opt-HSE functional in accordance with GW as well as coupled-cluster results, and can be used to accurately calculate F^0 , F^+ , and F^{2+} center formation energies and related properties in MgO.

6.2.4. Changes in lattice vibrations due to defect formation

Vibrational contributions to defect formation energies become important, if there is a considerable change in phonon modes and therefore in the vibrational free energy between host system and system with a defect. The following vibrational free energy estimates are based on DFT calculations of 64-atom bulk cells at PBE level, and were obtained as described in Sec. 4.1.2. In fact, neither for the neutral nor for the charged bulk defects the vibrational energy differs severely from that of the pristine MgO bulk system at technologically relevant temperatures. In Fig. 6.16 the vibrational energy contributions

$$\Delta F_{\text{vib}}(T) = F_{\text{vib}}^{\text{def}} - F_{\text{vib}}^{\text{perf}} \quad (6.12)$$

to the formation energies C_f^q for the F^0 , F^+ , and F^{2+} centers are shown as a function of temperature. For temperatures between 0 and 1,200 K the absolute value of ΔF_{vib} does not exceed 0.13 eV for any of the defects.

Two aspects are important for the change in vibrational energies between the system with and without an oxygen vacancy. On the one hand, one atom is removed, and consequently in the system with a defect there is one nucleus less than in the pristine system that contributes to the phonon energy. This effect dominates in the whole temperature range shown for the neutral oxygen vacancy. On the other hand, for an F^{2+} center at $T \geq 800$ K and for an F^+ center at $T \geq 1,000$ K the gained spatial freedom of the nuclei next to the vacancy becomes important, so that the vibrational energy is actually *higher* than in the pristine system.

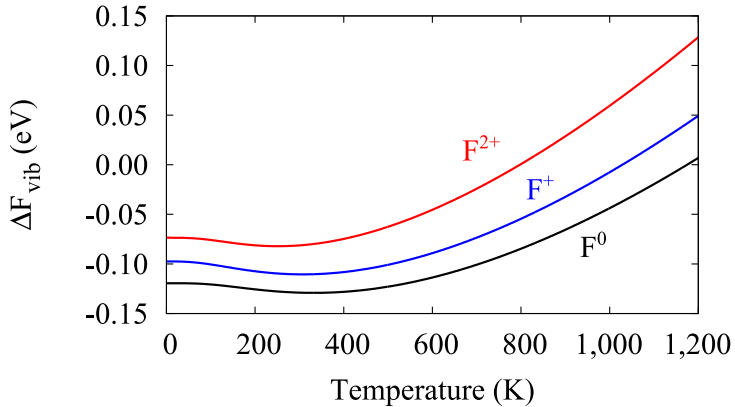


Figure 6.16.: Vibrational free energy contributions to the formation energies of the bulk F^0 , F^+ and F^{2+} centers as a function of temperature (based on PBE).

6.2.5. vdW effects on defect formation energies

HSE exchange-correlation functionals do not comprise non-local correlation. Therefore, the long-range contribution of the van der Waals (dispersion) interaction is not captured by the HSE functional family and has to be computed separately. The two-body van der Waals energy is due

to the electrostatic interaction between fluctuating dipoles. For atoms in a solid, not only short-range effects due to the local environment but also long-range effects play a role. The long-range interactions arise, since fluctuating dipoles interact electrostatically with more distant fluctuating dipoles, creating a correlated, dynamic electric field. This dynamic field in turn has a local influence on the environment of each dipole. Therefore, van der Waals dispersion interactions arise on the one hand due to short-range and on the other hand due to long-range interactions, which both cause local variations in the electron density and influence the polarizability of the atoms in the system.

In pristine MgO the long-range interactions between fluctuating dipoles cancel due to the cubic symmetry of the lattice. However, removal of an oxygen atom breaks the symmetry and leads to a change in van der Waals contribution to the total energy of the system.

The long-range effects that are missing in HSE can be taken into account by solving the self-consistent screening equation of classical electrodynamics as suggested by Tkatchenko *et al.* [208], using TDDFT-based atom-in-solid reference polarizabilities as discussed by Zhang *et al.* [209]. Applying this methodology to F centers in MgO, DFT calculations of 64-atom bulk cells at PBE level are performed, partitioning the electron density using the Hirshfeld partitioning method [114]. The frequency-dependent dielectric constant of MgO, from which the polarizability is obtained, has been calculated In Ref. [209], applying time-dependent DFT using HSE exchange-correlation treatment, coupled with the Nanoquanta non-local exchange-correlation kernel, which includes excitonic effects. The Hirshfeld weights from the PBE DFT calculation are used here to partition this polarizability. Solving the self-consistent screening equation

$$\alpha^{\text{SCS}}(\mathbf{r}, i\omega) = \alpha^{\text{TDDFT}}(\mathbf{r}, i\omega) + \alpha^{\text{SCS}}(\mathbf{r}, i\omega) \int d\mathbf{r}' T(\mathbf{r} - \mathbf{r}') \alpha^{\text{SCS}}(\mathbf{r}', i\omega), \quad (6.13)$$

where $T(\mathbf{r} - \mathbf{r}')$ is the dipole-dipole interaction tensor, results in the atomic screened polarizability tensors $\alpha_{\text{at}}^{\text{SCS}}$. The C_6 coefficient to the pairwise interatomic C_6/r^6 term follows from the Casimir-Polder integral [210, 211]. The van der Waals energy can then be computed according to

$$E_{\text{vdW}} = -\frac{1}{2} \sum_{\text{A,B}} f_d(R_{\text{AB}}, R_{\text{A}}^0, R_{\text{B}}^0) C_6^{\text{AB}} R_{\text{AB}}^{-6}, \quad (6.14)$$

summing over all pairs of atoms A and B. The van der Waals radii R_i^0 were originally defined as half the distance at which the Pauli repulsion balances the London dispersion attraction. In a solid this is defined such that it depends on the corresponding partitioned polarizability [209]. $f_d(R_{\text{AB}}, R_{\text{A}}^0, R_{\text{B}}^0)$ is a damping function that removes the singularity of R_{AB}^{-6} at small distances.

Obviously, the van der Waals contribution to the total energy of the pristine MgO host system and each system with a defect is negative. It is found that the correction is larger for the pristine systems. This results in a positive correction to the formation energy of the defect

$$\Delta E_{\text{vdW}} = E_{\text{total, vdW}}^{\text{D}} - E_{\text{total, vdW}}^{\text{host}}. \quad (6.15)$$

The calculations show that the contribution of the van der Waals interaction tails increases the defect formation energy only slightly for the neutral oxygen vacancy (0.13 eV). However, for the charged defects it becomes more important. It contributes 0.23 eV to the defect formation energy of the singly charged defect, and 0.32 eV for the F^{2+} center. The van der Waals correction to

the formation energy increases with the charge state of the defect. This can be understood qualitatively from the electronic structure of the defects. The electronic configuration for the neutral F center is very similar to that of the pristine system, due to the two defect electrons being localized at the defect site resembling the O^{2-} ion that held this position before. Removing one or two of these defect electrons changes the polarizability of the electronic structure in the vicinity of the defect more drastically. This leads to a larger change in C_6 coefficient and consequently to a larger contribution of van der Waals interaction to the formation energies for the charged defects than for the neutral F center.

6.3. Summary

In this chapter F centers in bulk MgO have been analyzed. It has been shown that formation energies of charged F centers in MgO bulk exhibit a near-linear dependence on the HSE exchange parameter α for a fixed screening parameter ω , due to a variation in VBM with respect to vacuum level with α . To find a reliable exchange-correlation description, it has been requested that the opt-HSE vertical ionization energy, defined as the energy required to remove an electron from the system and put it to a Fermi level, calculated using the Δ -SCF method or Kohn-Sham level at half occupation, should agree with the respective G_0W_0 @ opt-HSE value, obtained from the HOMO of the same system. It is found that HSE06 qualifies as an opt-HSE functional for the description of F centers in MgO. This has been confirmed by CCSD(T) calculations of the neutral F center formation energy. The only available experimental estimate for the formation energy of the F^0 center in MgO [26] is a significant overestimate, most likely since thermodynamic equilibrium was not reached in the experiment.

7. F centers at the MgO (100) surface

Understanding and quantitative characterization of the stability of defects at oxide surfaces is of great value for heterogeneous catalysis. In the first part of this work, an *ab initio* method to calculate interacting defects' concentrations at realistic conditions has been developed. A reliable functional to be used for the respective DFT calculations of F centers in MgO has been identified. In the following, properties of charged F centers at doped MgO surfaces are analyzed applying the VCA to model charged surface systems, using the HSE06 exchange-correlation functional for quantitatively accurate total-energy differences and energy levels, and calculating formation energies and concentrations at realistic ambient conditions, including defect-defect interactions and space-charge effects.

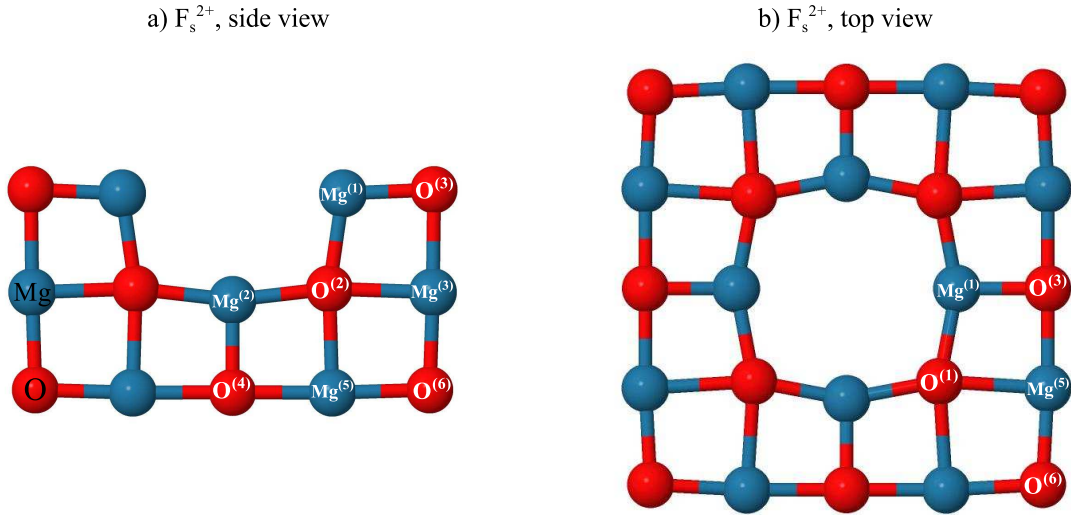
The focus of this chapter and at the same time the highlight of the applications part of this thesis is the analysis of F_s centers in different charge states at the MgO (100) terrace. Electronic and geometric relaxation effects are discussed, and charge-transition levels, formation energies, and defect concentrations are calculated for realistic *p*-type dopant concentrations.

If not stated otherwise, surface systems are calculated using 5-layer slabs separated by a vacuum region of 200 Å. The two lattice vectors along the surface plane are orthogonal and have equal length. The defect is created on one side of the slab. Basis and grid settings are the same as for the bulk calculations (for convergence tests see appendix). Relaxed atomic coordinates for all atoms in the system were calculated using the PBE exchange-correlation functional, and single-point calculations at the relaxed coordinates were performed with HSE functionals.

7.1. Geometric relaxation

First, the pristine MgO surface (without defects) is considered. The (100) termination reduces the coordination of surface atoms with respect to their bulk counterparts. The interatomic distance between a surface oxygen atom and its nearest-neighboring subsurface magnesium atom increases by 1.1 %, while surface magnesium atoms relax inwards by -0.7 %, where relaxed coordinates were obtained using PBE exchange-correlation treatment. This outward/inward relaxation is due to different polarizabilities of the magnesium cations and oxygen anions at the pristine surface and is often referred to as surface rumpling [212, 213]. The displacements of subsurface atoms from bulk positions is below 0.1 %.

Compared to the bulk F centers, the atoms neighboring an F_s center at the surface are less confined. As for the bulk defects, for the surface F_s centers geometric relaxation depends strongly on the charge state of the defect. In Table 7.1 the equilibrium distances between an oxygen atom at the surface and close-by atoms are listed and the change in these distances due to relaxation for an F_s^0 , F_s^+ , and F_s^{2+} center are reported. For the neutral F_s^0 center, all nearest-neighbor atoms relax slightly outward from the vacancy, as for the neutral bulk F^0 center. For the singly- and doubly-charged surface defects, there is a strong outward relaxation of nearest-neighbor mag-



Atom	Eq. distance to vacancy site (Å)	Relaxation (%)		
		F^0	F^+	F^{2+}
Mg (1)	2.130	3.1	7.4	11.8
Mg (2)	2.153	1.4	5.2	10.6
Mg (3)	2.153	0.0	0.6	1.6
O (1)	3.011	0.7	-1.8	-5.9
O (2)	3.034	-0.7	-1.7	-6.7
O (3)	4.258	0.6	1.0	1.9
O (4)	4.288	-0.2	0.2	1.2
Mg (4)	4.761	0.5	1.0	1.8
Mg (5)	4.788	-0.1	0.4	1.3
O (5)	6.022	0.3	-0.2	-0.7
O (6)	6.044	-0.1	-0.3	-1.0

Table 7.1.: Outward (positive) and inward (negative) relaxation in % with respect to the equilibrium distances at the pristine surface between close-by atoms and vacancy site. The model shown in side view (a) and top view (b) is a cut out of a periodic 1,620-atom relaxed MgO (100) surface slab with an F_s^{2+} center. The PBE exchange-correlation functional was used.

nesium and a less pronounced inward relaxation of nearest-neighbor oxygen atoms. Similar to charged F centers in the bulk, removing defect electrons destabilizes the ionic lattice: Relative to the original site there is a net positive charge in the vacancy, so that Mg^{2+} cations are repelled and O^{2-} anions are attracted to the vacancy, and the deformation of the lattice increases with the positive charge of the vacancy from F_s^+ to F_s^{2+} (Tab. 7.1). In Fig. 7.1 the relaxation energies as a function of supercell lattice constant L are shown for the surface defects, calculated using 5 layers in the slab, and for comparison also for the bulk defects. In accordance with the stronger

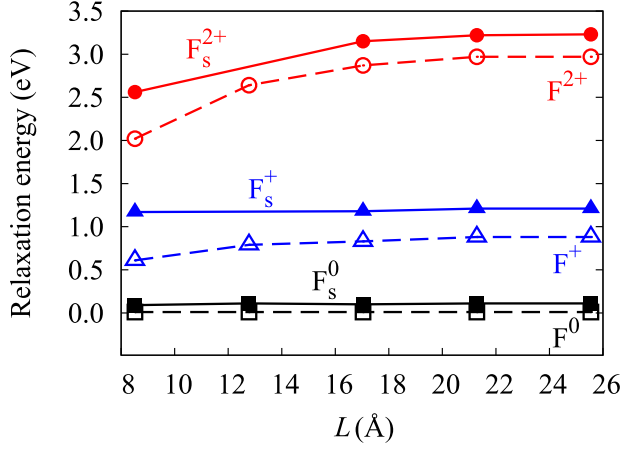


Figure 7.1.: Convergence of relaxation energies with supercell size for the surface F_s^0 , F_s^+ , and F_s^{2+} centers (filled symbols and solid lines) and for the bulk F^0 , F^+ , and F^{2+} centers (open symbols, dashed lines). L is the supercell lattice constant, where $L = L_x = L_y$ parallel to the surface for the surface defects and L_z is kept fixed, so that the extent of the vacuum region is 200 Å. The slab thickness is 5 layers. The PBE exchange-correlation functional was used.

deformation of the crystal lattice around the charged defects for the surface, the relaxation energy is larger for the surface than for the bulk defects. The energy of the system is lowered due to geometric relaxation by 0.11 eV, 1.21 eV, and 3.23 eV for F_s^0 , F_s^+ , and F_s^{2+} , respectively. Supercells with a separation between the point defect and its nearest image of at least 4 lattice constants (for PBE this corresponds to 17.035 Å) have to be used to obtain the relaxation energy, converged within 0.1 eV for F_s^{2+} . At this lateral cell size, 4, 5 and 6 layer slabs yield the same relaxation energy within 0.05 eV (Fig. 7.2).

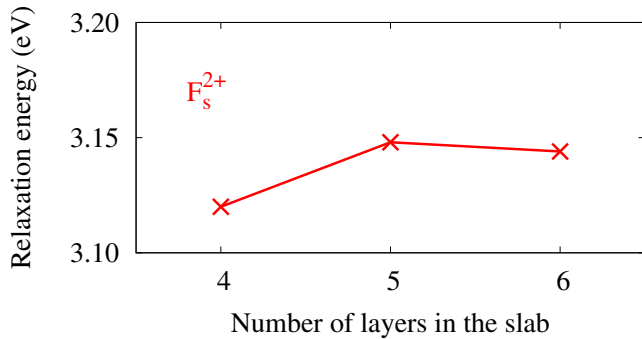


Figure 7.2.: Convergence of relaxation energies, calculated using PBE, for the F_s^{2+} center with the number of MgO layers in the slab. The supercell lattice parameters parallel to the surface are kept fixed to $L_x = L_y = 17.035$ Å.

The results presented here for the F center relaxation energies show that typical sizes of supercells (64 atom bulk cell, $L < 8.5$ Å [214]) and embedded cluster models (≤ 33 atoms in a bulk

and a surface model, embedded with effective core potentials and point charges [30] that have been used in the literature to calculate charged F centers in MgO, are not sufficient to obtain relaxation energies converged within 0.1 eV.

7.2. Electronic structure

Also the electronic relaxation for F_s centers at the surface is less confined than for the bulk defects. As an example, the defect level wave function is shown in Fig. 7.3 for the F_s^{2+} center. Note that the defect level is unoccupied in this case. The defect state spills out only weakly at the surface, it is still clearly localized in an s -orbital shape in the vacancy, with p -shaped contributions mainly on the nearest-neighboring oxygen atoms in the top layer. This is similar to the strongly confined defect states of the bulk oxygen vacancies. The defect state localization at the surface is an important aspect when considering for instance adsorption of molecules like hydrogen or water at surface F centers.

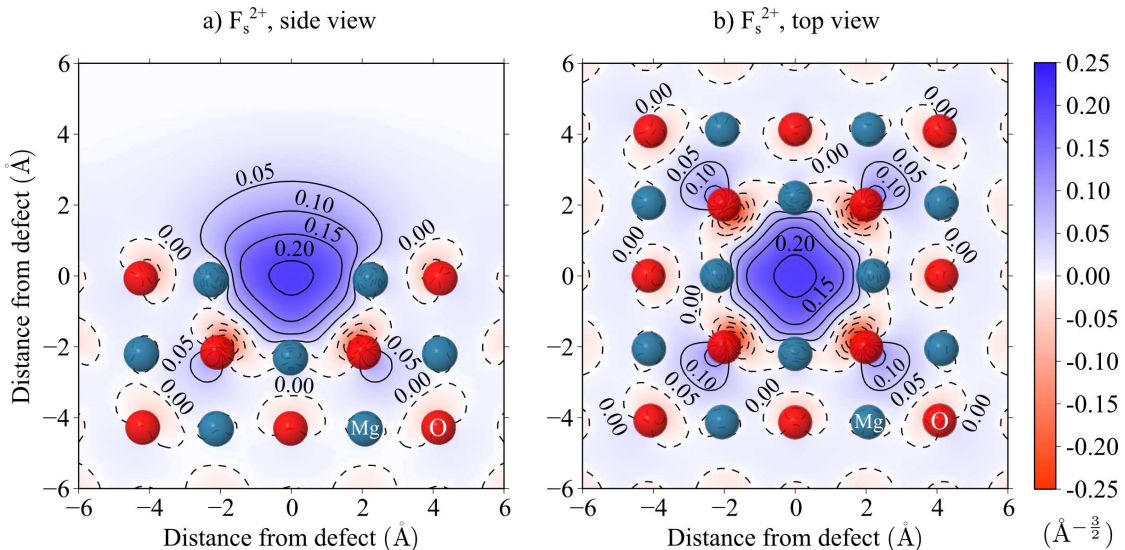


Figure 7.3.: Side view (a) and top view (b) of the defect level wave function (in $\text{\AA}^{-\frac{3}{2}}$) of the MgO (100) surface with an F_s^{2+} center at $(0,0)$, calculated with HSE06 using a $6 \times 6 \times 5$ atom slab. Contour levels are drawn in steps of $0.05 \text{\AA}^{-\frac{3}{2}}$.

The MgO (100) surface introduces surface bands in the bandgap, close to the CBm and at the VBM. Fig. 7.4a shows the surface band structure, computed using a 9-layer slab, and total density of states (DOS) with projected bulk energy bands and DOS. All DOS shown in Fig 7.4 have been normalized by dividing by the number of electrons in each system. The energy zero is at the VBM. The calculations were performed using the HSE06 functional. The projected DOS for the middle layer of the slab agrees well with the DOS obtained from the bulk calculation, when slabs with ≥ 5 layers are used, showing that the atoms in the central layer of the slab have bulk character (Fig. 7.4b). Also for the DOS projected on the surface layer there are only

small quantitative changes when the slab thickness in the calculation is increased from 5 to 9 layers. However, a 3 layer slab is clearly not sufficient to describe the electronic structure of the semi-infinite MgO (100) system.

The HSE06 bandgap for the surface system is smaller than for MgO bulk, since compared to the bulk, the $3s$ states of the magnesium atoms in the surface layer, which determine the CBM, are shifted by 1.2 eV to lower energies (Fig. 7.4a).

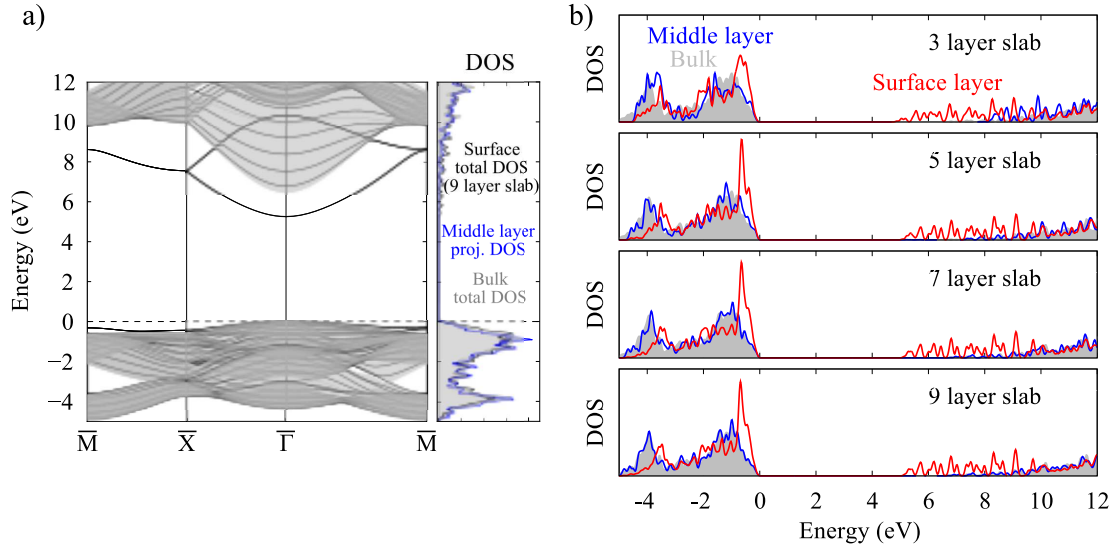


Figure 7.4.: a) Band structure and total density of states (DOS, normalized to DOS per electron) for the pristine MgO (100) surface (black) with the total bulk band structure and normalized DOS projected onto the surface (gray shaded), calculated with HSE06. The primitive simple cubic unit cell (2x2x2 atoms) for the bulk and a 9-layer slab (2x2x9 atoms) for the surface was used. The projected DOS per electron for the atoms in the middle layer of the slab is shown for comparison to the bulk DOS obtained with the bulk model. b) Projected DOS per electron for the middle layer (blue) and the surface layer (red) of 3, 5, 7, and 9 layer slabs, and bulk DOS per electron (gray), calculated with HSE06.

The surface F_s center defect levels are deep in the bandgap – as their bulk counterparts. For an estimate of the charged F_s center defect level positions, slabs of at least 6x6x5 atoms should be used for an accuracy of ≤ 0.2 eV (tested for PBE). Calculated with HSE06, the defect level position for the F_s^{2+} center is 3.4 eV above the VBM, while the bandgap is 5.1 eV.

7.3. Formation energy of the neutral oxygen vacancy at MgO (100)

The published formation energies of the neutral F_s^0 center calculated at different levels of theory are summarized in Fig. 7.5. Vibrational contributions to the formation energy are discussed in Sec. 7.6. For the neutral defect already small cell sizes ($L=8.2$ Å, compare Fig. 7.1) are sufficient to obtain converged, relaxed coordinates. In most of the cluster models used for calcu-

lations shown in Fig. 7.5, only nearest-neighbor atoms were relaxed around the vacancy and the cluster size was not tested with regard to relaxation energy convergence. However, the error in formation energies due to models too small to fully include geometric relaxation, is ≤ 0.11 eV, which corresponds to the converged relaxation energy of the F_s^0 center. The trends observed for the neutral bulk F^0 center are also valid for the surface defect: Using LDA as an approximation to the exchange-correlation energy leads to larger formation energies, while not including electron correlation (HF) yields lower formation energies compared to the results obtained with HSE functionals. Formation energies calculated with PBE, HSE06, and PBE0 agree within 0.1 eV.

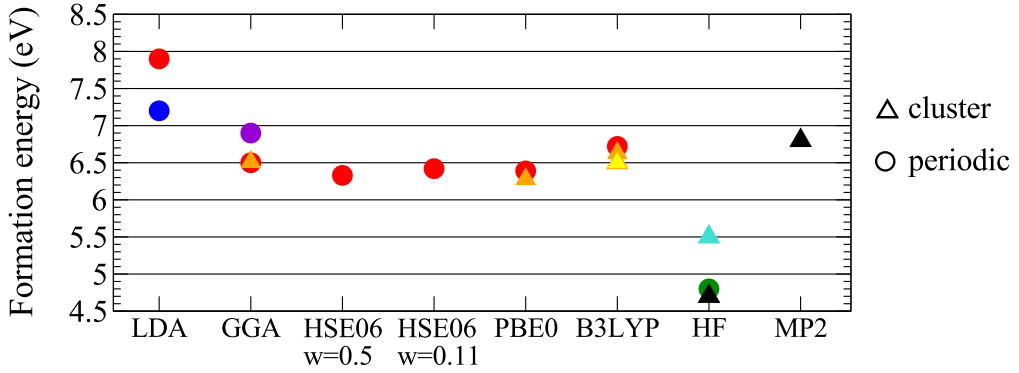


Figure 7.5.: F_s^0 center formation energy for $\mu_O = 1/2 E_{O_2}^{\text{tot}}$ (literature results were recalculated using the experimental O_2 binding energy) for different types of exchange-correlation treatment. Red circles show results obtained within this work, orange triangles were calculated in a collaboration with S. Sicolo and J. Sauer [185]. From literature, periodic DFT calculations at LDA level (blue circle, [27]), GGA level (purple circle, PBE [215]), and using HF (green circle, [174]), as well as embedded cluster calculations applying B3LYP (yellow triangle, [112]), HF (blue triangle [216] and black triangle [30]), and HF+MP2 (black triangle [30]) are shown for comparison.

The formation energy for the F_s^0 center, calculated with an unrelaxed Mg_5O_5 embedded cluster model with the CCSD(T) method, yields corrections $\Delta\text{CCSD}(T)$ for the DFT formation energies of -0.26 eV for PBE, -0.01 eV for PBE0, and -0.28 eV for B3LYP. From the corrected, converged DFT+ $\Delta\text{CCSD}(T)$ and from the embedded cluster and periodic HSE06 results, a formation energy with a reliable error bar of 6.28 ± 0.05 eV is obtained for the F_s^0 center. For comparison, the corresponding bulk defect formation energy is 6.95 ± 0.10 eV. The calculated formation energy values that were used to obtain these results are shown in Table 7.2.

Table 7.2.: Most reliable values of the formation energies G_f^0 in eV for the F^0 center in MgO bulk and for the F_s^0 center at the MgO (100) terrace, calculated using embedded cluster models (ecm) and periodic boundary conditions (pbc). Embedded clusters $Mg_{14}O_{19}$ for the bulk and $Mg_{50}O_{50}$ for the surface were used for the DFT formation energies at relaxed geometric coordinates around the defect. The CCSD(T) corrections for each functional were obtained using bulk Mg_6O_9 and surface Mg_5O_5 embedded clusters. The MgO supercells in the periodic calculations include 64 atoms for the bulk and 80 atoms for the slab, where all coordinates are fully relaxed. The chemical potential of oxygen μ_O $1/2E_{O_2}^{\text{tot}}$. The final results $G_f^0 = 6.95 \pm 0.10$ eV for the F^0 center and $G_f^0 = 6.28 \pm 0.05$ eV for the F_s^0 center are calculated by taking the average of the values listed in this table for the bulk and the surface defect, respectively.

Method	F^0	F_s^0
HSE06-pbc*	7.04	6.34
HSE06-ecm*	7.05	-
PBE $[\Delta\text{CCSD(T)}]$ -ecm [†]	6.94 [-0.09]	6.49 [-0.26]
PBE0 $[\Delta\text{CCSD(T)}]$ -ecm [†]	6.81 [+0.07]	6.26 [-0.01]
B3LYP $[\Delta\text{CCSD(T)}]$ -ecm [†]	7.17 [-0.28]	6.61 [-0.28]

*calculated using FHI-AIMS

[†]calculated using TURBOMOLE in collaboration with Prof. Sauer's Theoretical Chemistry Group, HU Berlin

7.4. Charge-transition levels and formation energies in the dilute limit

The formation energies for the charged surface vacancies are first calculated using the PBE exchange-correlation functional for increasing lateral supercell parameters. As discussed in Sec. 4, the formation energy as a function of defect concentrations can be extrapolated to the dilute limit of a vanishing defect concentration and the coefficients, obtained from fitting the calculated values to Eq. 4.29, can be used to obtain the dependence of the surface defect formation energies on the surface charge. This information is used in the thermodynamic model to describe the concentrations of interacting surface defects (Eq. 4.42). As for the bulk (Fig. 6.12), it is found that the surface F center formation energies calculated using HSE for the two smallest cells ($4 \times 4 \times 5$ and $6 \times 6 \times 6$ atom slabs) lie on the PBE fitting curve, but shifted by a constant value. Therefore, the HSE fitting parameters a_i^q in Eq. 4.29 can safely be approximated by the PBE coefficients, when the formation energy as a function of defect concentration is calculated. It has been shown that HSE06 is the opt-HSE functional to describe F centers in MgO. Still, for completeness, formation energies in the dilute limit (neglecting contributions due to phonons) and charge-transition levels calculated for different exchange-correlation functionals are listed in Table 7.3.

The work function for a pristine MgO slab is the energy at the VBM with respect to the

Table 7.3.: $G_f^{\text{VCA},q}$, (+/0), and (2+/+) in eV for the F_s^0 , F_s^+ , and F_s^{2+} centers at the MgO (100) terrace in the dilute limit, calculated with different exchange-correlation functionals using periodic boundary conditions (pbc) and embedded cluster models (ecm). The Fermi level is the vacuum level. The numbers in parentheses are calculated for the Fermi level at VBM. μ_{O} is $1/2E_{\text{O}_2}^{\text{tot}}$. Values taken from literature have been converted to the molecular oxygen reference using the experimental O_2 binding energy. Formation energies calculated with HSE06 promise the best accuracy within the HSE functionals and are therefore highlighted.

Method	F_s^0	F_s^+	F_s^{2+}	(+/0)	(2+/+)
PBE-pbc*	6.48	9.48 (4.18)	13.28 (2.68)	-3.00 (2.30)	-3.80 (1.50)
HSE06-pbc*	6.34	9.06 (2.76)	13.15 (0.55)	-2.72 (3.58)	-4.09 (2.21)
PBE0-pbc*	6.33	9.26 (2.56)	13.55 (0.12)	-2.93 (3.77)	-4.26 (2.44)
B3LYP-ecm [112]	6.46	8.96	13.46	-2.50	-4.50
HF+MP2-ecm [30]	6.74	8.17	11.46	-1.43	-3.29

* calculated using FHI-AIMS

† calculated using TURBOMOLE in collaboration with Prof. Sauer's Theoretical Chemistry Group, HU Berlin

energy in vacuum VBM_{VAC} . Calculated with PBE, HSE06, and PBE0 VBM_{VAC} is -5.3 eV, -6.3 eV, and -6.7 eV, respectively. The work function corresponds to the ionization energy for the pristine surface that has been estimated as -6.7 eV using the B3LYP functional by Sushko *et al.* [112], and was determined experimentally as -6.7 ± 0.4 eV from metastable impact electron spectra (MIES) on different MgO samples by Kantorovich *et al.* [217]. The reason for the rather large error bar in the experimentally determined value is not explicitly given in Ref. [217]. Most likely it is due to averaging over results obtained with different samples and the peak width in the MIES spectra. Using MIES, excited (metastable) He^* atoms are brought close to the sample surface and interact with the surface atomic layer. In the case of MgO (100), electrons from the $2 p$ states of surface oxygen atoms tunnel into $1 s$ states of the He^* atoms which leads to simultaneous release of $2 s$ electrons from helium. The energy of these released electrons is measured and used to determine the ionization energy for the sample surface. The advantage of using MIES for these measurements is that it is a surface-sensitive technique, where electrons only from the surface top layer can be removed and probed without spurious effects from deeper layers. (For more details see Ref. [112, 217].) The experimental value for the ionization energy of the pristine MgO (100) surface agrees with the B3LYP result reported in Ref. [112], and with the HSE06 and PBE0 periodic calculations in this work.

As for the bulk defects, formation energies and charge-transition levels in the dilute limit agree between different exchange-correlation treatments, if the Fermi level is the vacuum level. If ϵ_F is at the VBM, as in the case of *p*-type MgO, total energy differences and energy levels depend strongly on the functional. For all functionals, the order of stability for the F_s center charge state is $\text{F}_s^{2+} > \text{F}_s^+ > \text{F}_s^0$, as for the bulk defects. The formation energies obtained with the optimal functional, HSE06, differ by more than 2 eV between different charge states. Although this

is still under the assumption of very low defect concentrations, this indicates that F_s^{2+} centers should be the most abundant defects at the (100) surface of *p*-type MgO in thermodynamic equilibrium.

7.5. Concentrations and formation energies of interacting F_s centers

To obtain equilibrium concentrations of interacting defects, the formation energies as a function of surface charge density σ , for a slab thickness d corresponding to 5 MgO layers, are calculated for the F_s^+ and F_s^{2+} centers according to

$$G_f^{\text{VCA},q}(\sigma, d, \epsilon_F, \mu_O) = G_f^{\text{VCA},q}(\sigma \rightarrow 0, \epsilon_F, \mu_O) + a_1^q \left(\frac{\sigma}{qe} \right)^{\frac{1}{2}} + a_2^q(d) \left(\frac{\sigma}{qe} \right) + a_3^q(d) \left(\frac{\sigma}{qe} \right)^{\frac{3}{2}}. \quad (7.1)$$

The extrapolation curve for the F_s^{2+} center, using Eq. 7.1, has already been shown in Fig. 4.5 in Sec. 4.2.2, where the methodology was discussed. The calculated values of the dilute limit $G_f^{\text{VCA},q}(\sigma \rightarrow 0)$ and the coefficients a_i^q , $i = 1-3$, as obtained by extrapolation, are summarized in Table 7.4.

Table 7.4.: $G_f^{\text{VCA},q}(\sigma \rightarrow 0)$ as obtained with the HSE06 functional, and coefficients a_i^q , $i = 1-3$ for a 5-layer surface slab system ($\epsilon_F = \text{VBM}$, $\mu_O = 1/2 E_{\text{O}_2}^{\text{tot}}$).

q	$G_f^{\text{VCA},q}(\sigma \rightarrow 0)$ (eV)	a_1^q (eV \AA)	a_2^q (eV \AA^2)	a_3^q (eV \AA^3)
0	6.34	0	0	0
1	2.76	-4.93	24.76	42.29
2	0.55	-17.49	80.86	258.11

Next, the artificial restriction to the width of the slab is removed by subtracting the energy due to formation of the space-charge region in the slab,

$$qE^{\text{SC}} = \frac{q^2 e}{6\epsilon_r \epsilon_0} \frac{d}{L^2} = \frac{q^2 e d}{6\epsilon_r \epsilon_0} \left(\frac{\sigma}{qe} \right). \quad (7.2)$$

For consistency, the extrapolation is performed again, this time using the analytic expression for the coefficient a_2^q ,

$$a_2^q = \frac{q^2 e}{6\epsilon_r \epsilon_0} d, \quad (7.3)$$

as determined by comparing Eq. 7.2 with Eq. 7.1. The formation energy in the dilute limit and the coefficients a_i^q , $i = 1-3$ as obtained from this second extrapolation procedure are listed in Table 7.5. $G_f^{\text{VCA},q}(\sigma \rightarrow 0)$ and a_1^q agree well with the values obtained only from the DFT data points. a_1^q characterizes the dependence of the electrostatic interaction between surface

charge and compensating charge within the space-charge region z^{SC} . As discussed and shown in Sec. 4.2.2 (see also Fig. 4.5) the coefficient a_3^q only becomes important for small L , corresponding to surface defect concentrations $>10\%$.

Table 7.5.: $G_f^{\text{VCA},q}(\sigma \rightarrow 0)$ as obtained with HSE06 and coefficients a_i^q , $i = 1-3$ for the 5-layer slab ($\epsilon_F = \text{VBM}$, $\mu_O = 1/2 E_{O_2}^{\text{tot}}$), where a_2^q was obtained from Eq. 7.3.

q	$G_f^{\text{VCA},q}(\sigma \rightarrow 0)$ (eV)	a_1^q (eVÅ)	a_2^q (eVÅ ²)	a_3^q (eVÅ ³)
0	6.34	0	0	0
1	2.77	-5.30	30.69	14.35
2	0.60	-20.13	122.78	62.93

Now the formation energy as a function of the surface charge density σ for a uniform distribution of dopants N_D in the semi-infinite crystal is known, according to

$$G_f^{\text{VCA},q}(\sigma) = G_f^{\text{VCA},q}(\sigma, d) - qE^{\text{SC}}(\sigma, d) + qE^{\text{SC}}(\sigma, z^{\text{SC}}), \quad (7.4)$$

where the surface charge density $\sigma = e\eta_1 + 2e\eta_2$ is determined by the concentrations η_1 and η_2 of the charged defects F_s^+ and F_s^{2+} . The formation energy $G_f^{\text{VCA},q}(\sigma)$ can be understood as the energy *per defect* needed to create *at once* a certain defect concentration, corresponding to a surface charge density σ . When defects are not created at once but *one by one*, each of them causes an infinitesimal change in Gibbs free energy of the system. Minimizing the Gibbs free energy of the system using Eq. 4.41 – including electrostatic interaction terms and configurational entropy of the defects – can be interpreted as starting from an initial arbitrary concentration and creating and annihilating defects one by one until this is no more energetically favorable. This results in the equilibrium concentration of oxygen vacancies at the *p*-doped MgO (100) surface and the formation energy $G_f^q(\sigma, T, p_{O_2}, N_D, \epsilon_F)$ (Eq. 4.42) that corresponds to the energy needed to create a surface oxygen vacancy at the given temperature T , oxygen partial pressure p_{O_2} , dopant concentration N_D and equilibrium surface charge density σ .

For oxygen vacancies at the *p*-doped MgO (100) surface the concentrations of F_s^0 and F_s^+ centers are found to be negligible at realistic conditions. The F_s^{2+} concentration η_2 as a function of N_D is shown in Fig. 7.6, *left panel*, for catalytically relevant temperatures and typical pressure ($p_{O_2} = 1$ atm). The corresponding width of the space-charge layer z^{SC} is shown in Fig. 7.6, *right panel*. Although the F_s^{2+} Gibbs free energy of formation at $\sigma \rightarrow 0$ is small or even negative at elevated temperatures, the equilibrium defect concentration does not exceed $\sim 1\%$ at $N_D \leq 10^{18} \text{ cm}^{-3}$. The space-charge layer formation and resulting band-bending effects that limit the surface defect concentration dominate over the electrostatic attraction between defect-induced surface charge and compensating charge. This means that space-charge layer formation can be a mechanism by which wide-bandgap semiconductor surfaces remain stable at high temperatures. The space-charge layer depth is $\sim 10 - 100 \text{ nm}$ for realistic dopant concentrations.

For high dopant concentrations also the vacancy concentration increases and the difference between the defect concentrations at $T = 400 \text{ K}$ and $T = 1,000 \text{ K}$ becomes negligible. The

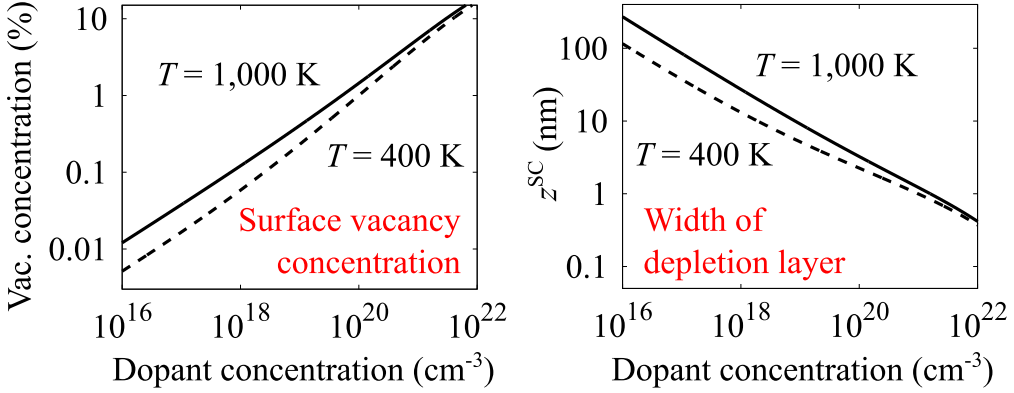


Figure 7.6.: *Left:* F_s^{2+} center concentration as a function of dopant concentration N_D for two different temperatures, oxygen partial pressure of 1 atm, $\epsilon_F = \text{VBM}$, and $\mu_O = 1/2 E_{O_2}^{\text{tot}}$. *Right:* Dependence of the space-charge depth z^{SC} on N_D .

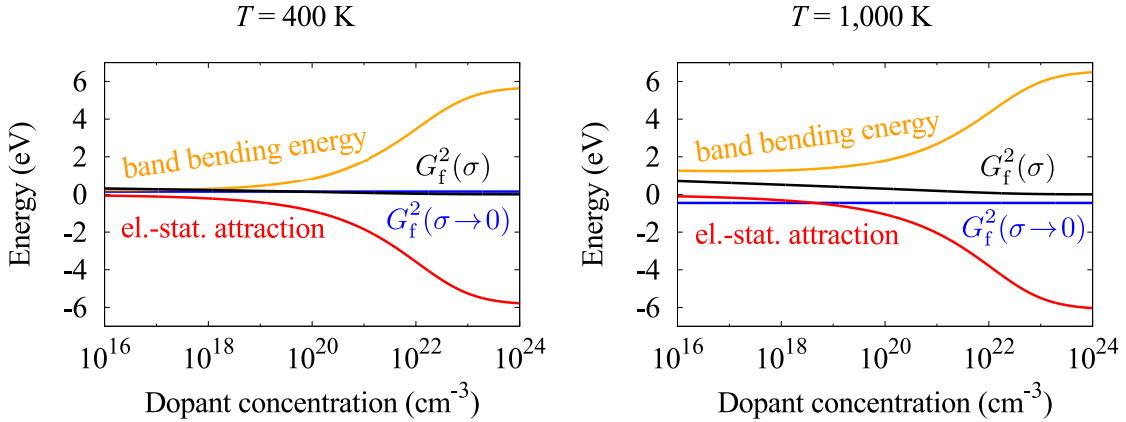


Figure 7.7.: Gibbs free energies of formation of the F_s^{2+} center G_f^2 (black), and the individual energy contributions due to electrostatic attraction between defect-induced surface charge and compensating charge (red) as well as due to band bending (orange) as a function of dopant concentration for the F_s^{2+} center at the p -doped MgO (100) surface for $T = 400 \text{ K}$ (*left*) and $T = 1,000 \text{ K}$ (*right*) at a partial pressure of oxygen $p_{O_2} = 1 \text{ atm}$ and $\epsilon_F = \text{VBM}$. For comparison also the formation energy of the F_s^{2+} center in the dilute limit $\sigma \rightarrow 0$ is shown (blue).

reason for this can be understood by considering the different energy contributions to the formation energy of the F_s^{2+} center. In Fig. 7.7 the formation energy G_f^2 is shown as a function of dopant concentration together with the individual electrostatic terms – due to attraction between surface charge and compensating charge, and due to band bending. It can be seen that these electrostatic terms become dominant at high dopant concentrations, so that temperature effects are suppressed. For comparison also the F_s^{2+} center formation energy in the dilute limit $G_f^2(\sigma \rightarrow 0)$ is shown. For $T = 1,000 \text{ K}$ and a realistic dopant concentration of $N_D = 10^{18} \text{ cm}^{-3}$ the formation energy of the interacting defect is $\approx 1 \text{ eV}$ higher than the formation energy in the

dilute limit. At these conditions the electrostatic attraction term is -0.31 eV and the band bending term is 1.27 eV. The formation energies for the interacting surface F centers in all three charge

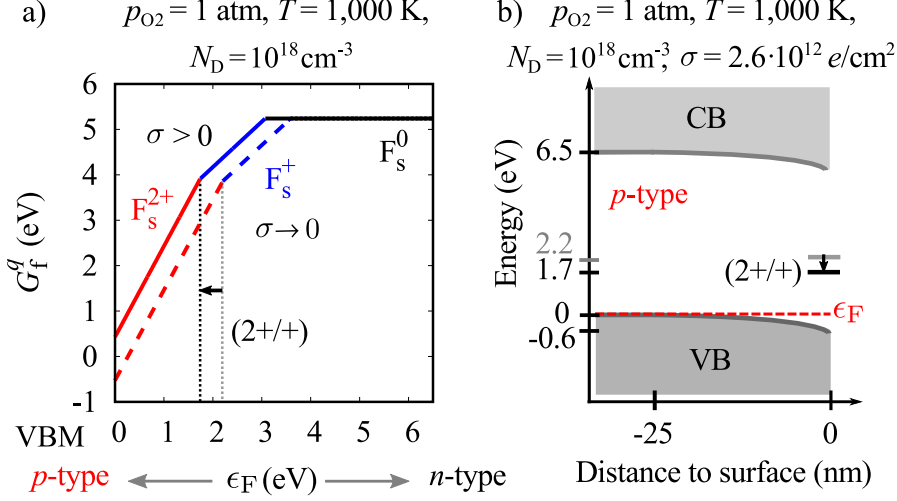


Figure 7.8.: a) Gibbs free energies of formation G_f^q of F centers at the MgO (100) surface for $T = 1,000$ K and partial pressure of oxygen $p_{O_2}=1$ atm, as a function of Fermi energy, ϵ_F , where the energy zero is at the VBM. Realistic dopant concentration $N_D=10^{18} \text{ cm}^{-3}$ and surface charge $\sigma = 2.6 \cdot 10^{12} \frac{e}{\text{cm}^2}$ (solid lines) and the dilute limit $\sigma \rightarrow 0$ (dashed lines) are shown. b) In *p*-type MgO ($\epsilon_F=\text{VBM}$) under realistic conditions, band bending, due to formation of a space-charge region, limits the formation of surface F_s^{2+} centers.

states at these conditions, and the corresponding band bending profile, are shown in Fig. 7.8. Also here it can be seen that the band bending energy dominates over the contribution due to attraction between defects and compensating charge density, raising the formation energies of the charged oxygen vacancies F_s^+ and F_s^{2+} at the surface (Fig. 7.8a). The amount by which the formation energy of the interacting defects is raised in comparison with the formation energies in the dilute limit, is larger for the F_s^{2+} center than for the F_s^+ center. This implies that if two charge states of a defect in a metal oxide are close in stability, comparing formation energies only in the dilute limit can even predict a wrong hierarchy in defect stabilities for the interacting system. For *p*-type MgO, both the dilute-limit estimate and the full treatment of interacting defects yield a stability order of $F_s^{2+} > F_s^+ > F_s^0$, where the concentrations of F_s^+ and F_s^0 centers are negligible. However, the space-charge effects on the defect formation energies are still severe. For the conditions shown in Fig. 7.8a, if the band bending was not taken into account, the (100) surface of *p*-doped MgO would be predicted to be unstable. The band bending profile (Fig. 7.8b) shows that in a realistic situation this does not happen, because the bulk bands bend downwards by 0.6 eV, and the $(2+/+)$ charge-transition level is lowered from 2.2 eV to 1.7 eV above the Fermi level. This makes it energetically less favorable for charged defects to form, and limits their concentrations.

Note, that also in the bulk, the hierarchy of defect stabilities in *p*-type MgO is $F^{2+} > F^+ > F^0$. In fact, for the conditions discussed above for the surface oxygen vacancies, $T = 1,000$ K,

$p_{O_2} = 1$ atm, and $\epsilon_F = VBM$, the formation energy in the dilute limit for the F^{2+} center in MgO bulk is -0.54 eV, implying that F^{2+} centers can readily form in the bulk as far as compensating dopants are available. If all free charge carriers due to p -type dopants transferred to oxygen vacancies, it would mean that the material would no longer exhibit p -type conductivity. However, in experiment it has been shown that MgO , which has been doped with electron acceptors, as for example lithium-doped MgO , is indeed p -type conducting [32]. Reasons for hindered formation of bulk defects can for example be kinetic limitations, where diffusion mechanisms of dopants and vacancies play a role. Furthermore, hydrogen is usually present in experiment and can change the defect properties.

7.6. Lattice-vibration effects on surface-defects energetics

Vibrational energy contributions for the surface defect formation energies can be calculated in the same way as for bulk defects, as described in Sec. 6.2.4, using the PBE exchange-correlation functional and the finite displacement method for a 5-layer slab model containing 80 atoms per unit cell. For the neutral F_s^0 center, the vibrational free energy contribution to the Gibbs free energy of formation is 0.01 eV, and is therefore negligible, while for temperatures ≥ 500 K its contribution is ≥ 0.15 eV.

For charged surface defects charge compensation is provided via the VCA, altering the nuclear charges of the magnesium atoms in the system, and this has consequences for the calculated vibrational energy. Consider the F^{2+} center in the bulk, where the vibrational free energy contribution to the formation energy as a function of temperature can be calculated with both the neutralizing background method (red, solid line in Fig. 7.9) and the VCA (red, dashed-dotted line).

The reference vibrational energy is in both cases that of the pristine system with natural nuclear charges. Applying the VCA and therefore reducing the magnesium nuclear charge by δq leads to a decreased repulsion between the Mg^{2+} cations in the crystal, according to $(q_{Mg}^{VCA})^2 = (2 - \delta q)(2 - \delta q) \approx 4 - 4\delta q$, as well as to a decreased attraction between O^{2-} ions and Mg^{2+} cations, proportional to $q_{Mg}^{VCA} q_O = (2 - \delta q)(-2) = -4 + 2\delta q$. Since the first effect is stronger (by a factor of 2), the potential energy surface becomes stiffer. The phonon frequencies are higher and consequently the vibrational free energy estimate is at a higher energy than that obtained based on the neutralizing background method. By increasing the nuclear mass of atoms in the system, the VCA vibrational energy curve can be adjusted to the background-based result. For F^{2+} in the 64-atom unit cell, changing the nuclear masses of all atoms in the unit cell by 1% makes the VCA curve agree within 0.01 eV with the neutralizing background method (red, dotted line in Fig. 8.3). (Note, that δq and therefore also the scaling factor depend on the size of the supercell.) The correction to nuclear masses derived from the bulk calculations can then be used to determine the corrections for surface defects, to which only the VCA approach is applicable.

Estimates of the vibrational energies of charged surface defects using models of 5-layer slabs with 4×4 or 6×6 atoms per layer or an 11-layer slab with 4×4 atoms per layer with the finite-displacement method show that these supercell sizes are insufficient to yield converged results. To obtain accurate estimates for the vibrational energy contributions to the surface defect for-

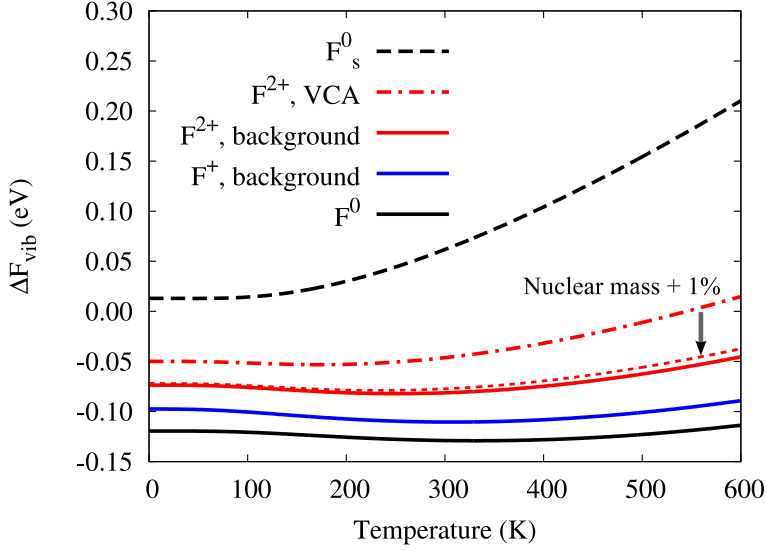


Figure 7.9.: Vibrational free energy contributions to the formation energies of the bulk F^0 , F^+ , and F^{2+} centers, and the F_s^0 center at the (100) terrace

mation energies, an even larger number of layers in the slab is necessary, since localized surface modes may exhibit large vibrational amplitudes. Explicitly including several tens of layers in the finite displacement method and calculating the respective force constants with DFT is computationally too expensive. It has been suggested in literature to apply slab-filling techniques, where force constants of inner layers of a slab are taken for example from less expensive bulk calculations [218, 219]. A crude estimate for the F_s^0 center (see Fig. 7.9, black dashed line), obtained with a 5-layer slab and 6×6 atoms per layer, assuming that the vibrational contributions to the formation energies do not vary severely with the charge state, as is the case for bulk defects, shows that vibrational effects very likely do not change the order of surface vacancy stability, but might slightly lower the surface defect concentrations.

For F centers in MgO bulk the vibrational energy is lower than in the pristine system in the whole temperature range shown here. As discussed in Sec. 6.2.4, for the bulk defects the fact that one nucleus less than in the pristine system contributes to the phonon energy dominates over the gained spatial freedom of the nuclei next to the vacancy. For the estimated vibrational free energy of the surface defect systems the opposite is true. The atoms close to the vacancy at the surface have one more degree of freedom available than their bulk counterparts and increase the vibrational free energy with respect to the system without defect.

7.7. Van der Walls effects on surface defect formation energies

Long-range dispersion interaction contributions on the surface defect formation energies can be determined in analogy with the bulk defects as discussed in Sec. 6.2.5. However, similar to the vibrational contributions, the computed van der Waals energies depend on the applied

charge-compensation method. For the bulk F centers, where both VCA and constant background method are applicable for charged defects, the van der Waals corrections to the formation energies are shown in Fig. 7.10 for both types of charge compensation. The van der Waals contributions to the formation energies

$$\Delta E_{\text{vdW}} = E_{\text{total,vdW}}^{\text{D}} - E_{\text{total,vdW}}^{\text{host}} \quad (7.5)$$

of charged defects are lower when obtained with the VCA than those obtained with the background method. The differences are 0.04 eV for the F^+ center and 0.08 eV for the F^{2+} center. This can be explained by considering the ratio of electronic over nuclear charge for the host system and for the system with a defect and comparing these between VCA and background method. Decreasing the number of electrons in the system leads to a lower polarizability, while decreasing the nuclear charge means that electrons are less strongly bound and the polarizability is increased. In the pristine system without dopants the ratio of electronic over nuclear charge is 1. This is also true for the doped pristine system calculated with the VCA. The difference between the van der Waals corrections $E_{\text{total,vdW}}^{\text{host}}$ for the doped pristine system and the pure host system is ≤ 0.01 . So here the increase in polarizability due to reduced nuclear charge cancels with the decrease in polarizability due to reduction in number of electrons for the virtual crystal. For the systems with charged defects, on the other hand, the ratio of electronic over nuclear charge is 1 when the VCA is used, and <1 when the background approach is applied. The number of electrons is the same in both cases, but using the VCA the nuclear charge is decreased compared to the case where the background method is used. Consequently, the electron density in the virtual crystal is more polarizable and the van der Waals interaction has a more pronounced effect on the total energy of the virtual crystal system than it is the case for the system treated with the constant background method. Taking the difference between the van der Waals energy of the system with a defect and the undisturbed host system thus leads to a van der Waals contribution to the defect formation energy that is lower when the VCA is applied than the one obtained with the background method. The VCA models all have a realistic balance of electronic over nuclear charge, while this is not the case for systems, where the constant background method is applied. For this reason the van der Waals contributions calculated with the VCA, modeling a random distribution of dopants, can be considered more realistic than those obtained with the constant background method.

For the surface, only the van der Waals correction based on the VCA is applicable. From Fig. 7.10 it can be seen that the contribution of van der Waals interaction to G_f^q is smaller by ≈ 0.1 eV for the surface than for the bulk defects. For all surface defect charge states the van der Waals correction to the formation energies is below 0.16 eV. Similar to the bulk defects, the van der Waals correction to the formation energy increases with the charge state also for the surface defects (Fig. 7.10). As mentioned in Sec. 6.2.5, this is because the electronic structure close to a neutral F center is very similar to that of the host system. Increasing the defect charge state by removal of defect electrons introduces more severe changes to the polarizability of the electronic structure in the vicinity of the defect, higher long-range van der Waals energy contributions to the vacancy formation energies for increasing charge states.

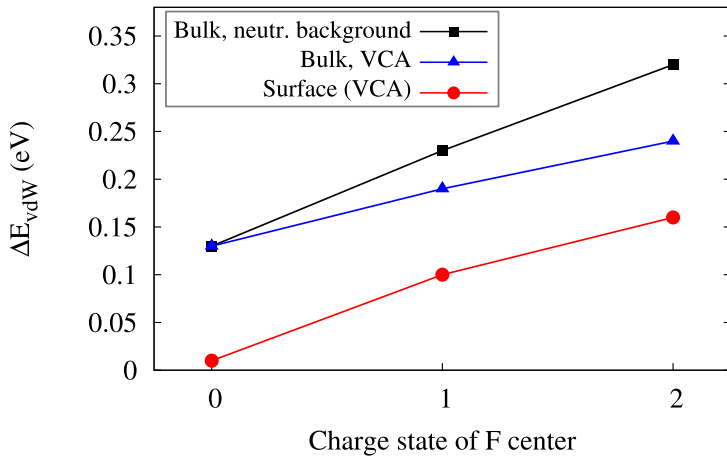


Figure 7.10.: van der Waals corrections to the formation energies of F centers in MgO bulk and at the MgO (100) terrace. For bulk both neutralizing background and VCA charge compensation are shown.

7.8. Summary

The VCA has been used to model charged surface F centers at the MgO (100) surface. To obtain accurate formation energies and equilibrium concentrations for interacting oxygen vacancies the opt-HSE functional for F centers in MgO, HSE06, has been employed. Comparing bulk and surface F centers in MgO reveals many similarities, namely strong localization of the defect level, confined geometric relaxation, and a hierarchy $F_s^{2+} > F_s^+ > F_s^0$ of the stabilities of F centers in different charge states. It has been found that the concentration of surface F_s^{2+} centers can be as high as ~ 1 atomic percent, while F_s^+ and F_s^0 concentrations are negligible, at realistic temperature and pressure conditions relevant for catalytic applications of MgO. For the charged defects space-charge effects play an important role. Electrostatic attraction between surface charge due to charged defects and compensating charge within the space-charge region facilitates surface defect formation, while band bending effects limit the surface defect concentration. For realistic conditions these electrostatic contributions to the formation energy of interacting F_s^{2+} defects are of the order of 1 eV. Downward band bending lowers the charge-transition levels with respect to Fermi level at the surface. This raises the vacancy formation energy by up to 1 eV and, therefore, limits the defect concentration.

8. Defect complexes in lithium-doped MgO

MgO has been studied extensively in heterogeneous catalysis as a catalytically active material and as a catalyst support. Its functionality as an active catalyst can be enhanced when its electronic and morphological properties are modified in a suitable manner, e.g. by inserting electrically active defects or dopants. A prominent example is lithium-doping of MgO, which represents a potential pathway to produce a catalyst material for oxidative coupling of methane. One aspect to explore in this context is the role of the lithium constituents and their interplay with oxygen vacancies in the MgO lattice.

The formation of surface oxygen vacancies in *p*-type MgO, as discussed in Chapter 7, depends on the concentration of mobile holes in the bulk. For simplicity, the concentration of free charge carriers has been referred to as the dopant concentration N_D . Therefore, defect complexes that may be formed in the bulk have not been considered explicitly, since only the remaining *p*-type conductivity was relevant. Lithium dopants in MgO act as monovalent acceptors, and it has been shown in experiment that lithium-doped MgO is indeed *p*-type conducting [32]. However, given the energetically unfavorable nature of lithium defects in MgO [172, 220], the impurity atoms tend to induce compensating defects especially at the high-temperature conditions of a chemical reaction [221]. Myrach *et al.* have demonstrated by *first-principles* calculations that the formation energies for oxygen vacancies in the MgO (100) surface are significantly reduced in the presence of nearby Li [172]. Oxygen vacancies can act as an electron source and can thus annihilate the oxygen 2 *p* hole states and neutralize the effect of the lithium substitutional defect, transferring charge directly to the neighboring dopant. This means that, if lithium is available, the formation of neutral or charged defect complexes constituting one or two Li atoms adjacent to an oxygen vacancy can be favorable. For these defect complexes the global effects of *p*-type doping apply and determine the Fermi level, but also local effects of doping become important: Charge localization, as well as proximity-induced electronic and geometric relaxation effects, influence the formation energy of the dopant-vacancy complex.

Similar to the work of Myrach *et al.* on the influence of lithium close to an oxygen vacancy in MgO [172], the local and also the global effects of various dopant species with variable oxidation states on oxygen-vacancy formation have been studied by Li and Metiu for lanthanum oxide (La_2O_3) in 2010 [124], and by Hu and Metiu for ceria in 2011 [125]. Also in these cases it was shown that local effects of doping can lower the formation energies of oxygen vacancies in the vicinity of dopants substantially.

While in Ref. [124, 125, 172] formation of an oxygen vacancy in doped material is investigated, in the following formation of dopant-vacancy complexes is considered. This means that in the former case a finite concentration of dopants in the bulk is assumed and the doped system is regarded as the host for oxygen defect formation. In the latter case, the formation of defect complexes is considered for varying availability of lithium, determined by its chemical potential, while the host system is pure MgO. The intrinsic material is compared to a situation, where a source of lithium has been provided and lithium has incorporated into MgO, possibly

under formation of lithium-induced (or lithium-mediated) defect complexes. The objective is to understand if and what type of lithium-mediated defect complexes can be present under equilibrium conditions and to explore electronic and structural properties of these complexes. For this, a combination of scanning tunnelling microscopy (STM), optical spectroscopy, and electronic structure calculations performed at the DFT level has been used. The experimental work was performed by F. Stavale and N. Nilius at the FHI Chemical Physics department. Calculated thermodynamic stabilities of defect complexes that can form when lithium dopants are introduced into MgO are compared to scanning tunneling microscopy and cathodo-luminescence spectra revealing experimental signatures for the defects. Simulated Fermi level and (T, p) conditions are chosen in accordance with experimental information. The most relevant experimental observation is a downshift of the fundamental MgO optical mode upon doping, being indicative for new electronic states in the bandgap. As has been explained in previous chapters, oxygen vacancies in MgO generally produce such gap states, but it is not clear *a priori* what charge state and configurations of defect complexes comprising lithium-dopants and an oxygen-vacancy are relevant. Therefore, formation energies in the dilute limit are calculated for a variety of defect complex configurations, in order to identify those with lowest formation energy. For completeness, not only complexes of lithium dopants and oxygen defects but also lithium substitutional and interstitial defects in different charge states without a close-by oxygen vacancy are considered.

8.1. Experimental characterization of lithium-induced defects

The STM and cathodo-luminescence experiments have been performed in ultrahigh vacuum, where the STM was operated at liquid nitrogen temperature. The setup is equipped with an optical readout that enables the collection of photons from the tip-sample junction and their detection with a charge-coupled device unit outside the vacuum chamber. By this means, spatially resolved optical measurements can be carried out in a wavelength window from 200-1,200 nm, using the STM tip as local electron source. For the cathodo-luminescence measurements, the MgO optical modes have been excited by injecting electrons with 100-150 eV energy ($V_s=100$ -150 V) and 5 nA current into a pre-selected sample region [222]. STM topographic images were taken with $V_s=3.5$ V. The MgO films used in the experiments were grown by reactive deposition of magnesium in 5×10^{-7} mbar O₂ onto a sputtered and annealed Mo (001) single crystal [223]. The oxide has been crystallized via annealing to 1,000 K, producing a sharp square pattern in low-energy-electron-diffraction that indicates a (100) termination of rock-salt MgO. STM measurements revealed an atomically flat oxide surface, exposing a network of mainly [100]-oriented dislocation lines (Fig. 8.1a, inset). The line defects develop spontaneously in the film in order to compensate the 5.4 % lattice mismatch with the Mo (001) surface beneath [224].

Lithium-doped MgO samples with a film thickness of 15 ML were prepared in two different ways, embedding lithium into the bulk lattice by simultaneous deposition of magnesium and lithium onto the molybdenum substrate in oxygen atmosphere, and by depositing lithium onto an MgO sample, and subsequent annealing. MgO films with small lithium amounts incorporated into the bulk layers (using the first preparation method) still exhibit the rock salt lattice of the bare oxide [172]. However, the film crystallinity is reduced, i.e. oxide terraces are smaller and

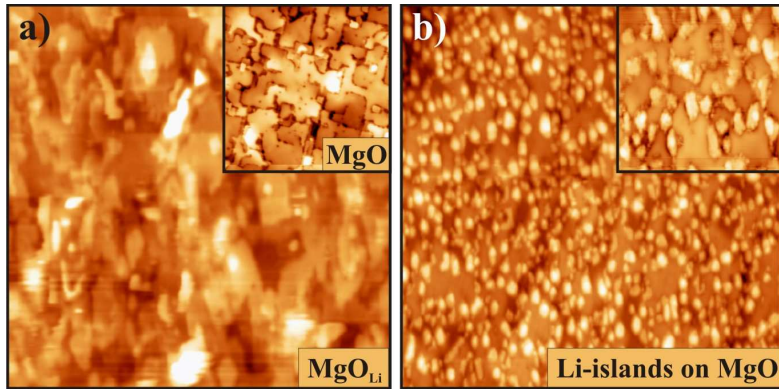


Figure 8.1.: STM topographic images of (a) a 15-monolayer (ML) thick MgO_{Li} mixed film on Mo (001) and (b) a pristine MgO film after exposure to 0.2 ML lithium ($200 \times 200 \text{ nm}^2$). The insets display a bare MgO film (a) and a close up of a lithium-covered film (b). Both insets are $50 \times 50 \text{ nm}^2$ in size. ($V_s = 3.5 \text{ V}$)

defect lines are less straight than in the non-doped case (Fig. 8.1a). This lower film quality can be related to a mixture of kinetic and thermodynamic effects. First, lithium-doped films cannot be annealed as thoroughly as pristine ones, as the alkali impurities tend to leave the oxide at temperatures beyond 800 K. And second, the presence of lithium perturbs the crystallization process of the rock-salt lattice, e.g. by enriching in the dislocation lines, occupying interstitial lattice sites and agglomerating into tiny Li-O units.

Adsorbed lithium deposited at 300 K (using the second preparation method), on the other hand, grows into monolayer islands on the surface (Fig. 8.1b), as discussed in detail in earlier work [172, 225]. The formation of 2D lithium islands is not so much the consequence of the Li-MgO interface interactions, but results from a relatively high barrier for lithium up-step diffusion that impedes the development of 3D particles [226]. Upon annealing above 600 K, the adsorbed lithium structures quickly disappear from the surface. While the majority of lithium simply evaporates into the gas-phase as Li_2O [172], a small amount diffuses into the film.

To take STM topographic images and measure the cathodo-luminescence spectra, the samples were cooled down to liquid nitrogen temperature within ≈ 1 hour. In both preparations – lithium embedding into the bulk lattice and annealing of lithium surface-islands – the presence of lithium defects in the MgO becomes manifest from distinct changes in the optical response of the oxide film (Fig. 8.2). Pristine MgO films of 15-100 ML thickness display a characteristic 400 nm emission peak in cathodo-luminescence spectra performed in the STM setup [223]. This peak can be assigned to the radiative recombination of electron-hole pairs excited by the incoming electrons across the bandgap [227]. These excitonic modes are mobile in the bulk lattice but get trapped at low-coordinated surface sites, in particular at oxygen corner and kink sites, where recombination takes place in a second step [228, 229]. The 400 nm emission peak is therefore representative for exciton recombination at low-coordinated surface sites and can be quenched by dosing small amounts of metals, e.g. gold, onto the oxide film [230].

The characteristic optical signature of the pristine film changes significantly upon lithium

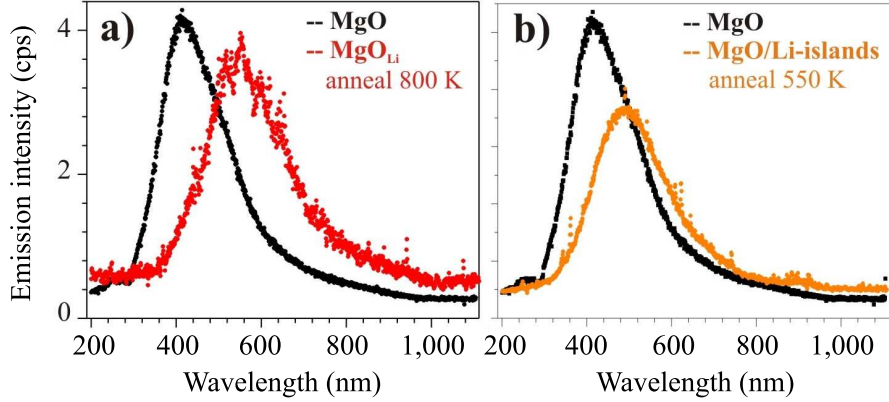


Figure 8.2.: Cathodo-luminescence spectra of (a) bare and mixed MgO_{Li} films of 15 ML thickness and (b) bare and lithium-covered MgO films after annealing to 550 K. All spectra were taken with $V_s = 150$ V, $I = 1$ nA and 60s accumulation time. Note the pronounced red-shift of the main emission peak when lithium is present in the MgO lattice.

incorporation. Most importantly, the emission maximum in the spectrum undergoes a red-shift by 100-150 nm and now peaks at around 550 nm (Fig. 8.2a,b). Additionally, its full-width-half-maximum (FWHM) increases from ≈ 100 nm in the pristine to more than 150 nm in the doped films. (These features in the spectra have also been observed for thicker films with up to 100 layers.) The red-shift suggests the development of new recombination channels for the excitonic modes in the presence of lithium defects, for instance via new localized states in the MgO bandgap. The bulk excitons get trapped and recombine already in deeper layers of the film and do not reach the surface anymore. The possibility that the lithium-induced gap states are surface states is discarded, as the new optical signature and hence the new recombination channel is insensitive against adsorption of rest gas molecules, such as water, CO or hydrogen. Also, surface oxygen defects can disappear via heterolytic water splitting and formation of OH groups, as discussed in the next section. Hence, the low-energy emission signature observed on lithium-doped MgO films may relate to the presence of lithium or oxygen defects or defect complexes in the volume of the film.

8.2. Theoretical analysis of lithium-induced defect complexes

To identify possible bulk defect complex configurations, stabilities of different defect arrangements are calculated using DFT with simple-cubic MgO bulk supercell models including 64, 216, and 512 atoms. Formation energies $G_f^q(T, p)$ for all defect configurations are computed using Eq. 4.1. The dilute limit is obtained by extrapolation to an isolated defect or defect complex in extended material as described in Chapter 4. Formation energies are computed for a temperature of 600 K and an oxygen pressure of 10^{-10} atm, as a set of characteristic conditions for the experiment. Conclusions drawn in the following do not change when ambient conditions are varied within the relevant experimental temperature and pressure range. The oxygen chemical

potential $\Delta\mu_O(600 \text{ K}, 10^{-10} \text{ atm}) = -1.21 \text{ eV}$ with respect to $1/2E_{O_2}$ at the temperature and pressure conditions for which the formation energies are calculated, has been obtained using Eq. 4.10 as described in Sec. 4.1.2. The chemical potential of magnesium is deduced from the condition of thermodynamic stability of bulk MgO. For lithium, different chemical potentials μ_{Li} are considered, ranging between the free energy of the lithium atom and that of lithium in Li_2O . $\Delta\mu_{Li}$ denotes the chemical potential of lithium with respect to that of fully oxidized lithium. The change in volume ΔV of the crystal due to defect complex formation is neglected. (A contribution of 1 meV to the formation energy would correspond to a huge change in crystal volume of $\approx 16 \text{ } \mu\text{m}^3$ for an oxygen pressure of 10^{-10} atm .)

In the following, a notation for defects is used, that is similar to the Kröger-Vink notation, but omits the electronic charge of the species relative to the original site, for simplicity. A defect $(M_S)^q$ describes a species M (for instance M=Li) or a vacancy (M=V) occupying the site of species S (S=Mg, S=O, or S=i for an interstitial). The charge state of the defect, in case of an extra or a removed electron, is specified by q .

The contribution of phonons to the defect complex formation energy is calculated as described in Chapter 4.1 for $3 \times 3 \times 3$ MgO supercells (216 atoms), using the finite displacement method and the PBE exchange-correlation functional. For the most stable defect complexes, the vibrational energy contribution is $\Delta F_{\text{vib}}^q < 0.14 \text{ eV}$ for temperatures below 1300 K (Fig. 8.3). Apparently,

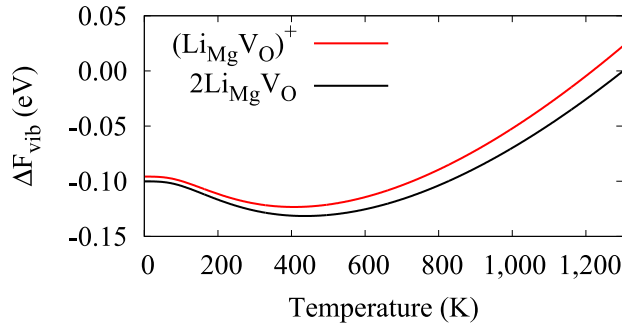


Figure 8.3.: Vibrational free energy contribution ΔF_{vib}^q to the formation energy $G_f^q(T,p)$ for two defect complexes as a function of temperature, calculated using the PBE functional for 216-atom supercells. $\Delta F_{\text{vib}}^q(T)$ is the difference between the vibrational free energy for the MgO system with a defect complex and the vibrational free energy for the pure MgO host system.

the vibrational free energy has no effect on the energy hierarchy of the defects considered here. In the formation energies reported below, the vibrational contribution is therefore neglected.

For all systems fully relaxed atomic coordinates are calculated using the PBE exchange-correlation functional at the respective optimized lattice parameter (4.258 Å). The relaxed geometries for the $2 \times 2 \times 2$ MgO supercell are then scaled to the HSE06 optimized lattice parameter (4.218 Å) and a HSE06 single-point calculation is performed for the scaled, relaxed structures. For neutral defects, convergence tests for increasing cell sizes with fully relaxed coordinates show that interactions between the defect and its image due to geometric and electronic relaxation effects vanish fast with increasing supercell size. The formation energies of these defects are already converged within 50 meV for cubic supercells of 64 atoms (cell length 8.435 Å).

The formation energies for the charged defects are extrapolated to the dilute limit of isolated, non-interacting defects by calculating $G_f^q(L)$ for 64-, 216-, and 512-atom cubic supercells (with $L=8.517$ Å, $L=12.775$ Å and $L=17.034$ Å, respectively), using Eq. 4.28.

For three defect structures, $(\text{Li}_{\text{Mg}}\text{VO})^+$, $2\text{Li}_{\text{Mg}}\text{VO}$, and Li_{Mg} (shown in Fig. 8.6 and discussed in detail below), relaxed atomic coordinates have also been calculated with HSE06. The error made by using the PBE relaxed, scaled to HSE06 lattice constant geometries was found to be <0.03 eV, and the HSE06 relaxed geometries are practically equivalent to those relaxed with PBE. This is in particular interesting for the lithium substitutional defect, where symmetry breaking has been predicted by Lichanot *et al.* in an unrestricted Hartree-Fock study [231]. Using the HF method leads to localization of the lithium valence electron on one nearest-neighbor oxygen atom and as a consequence the distance between the lithium atom and this oxygen atom is elongated with respect to the equilibrium MgO bulk interatomic distance. Indication (but no rigorous proof) for this has also been found in electron paramagnetic resonance spectroscopy (EPR) and electron nuclear double resonance spectroscopy (ENDOR) experiments by Abraham *et al.* [221, 232]. In this work, three different starting geometries have been tested for the HSE06 geometry relaxation: (i) the relaxed symmetric PBE structure, (ii) a structure where the lithium atom has approached one of its nearest-neighbor oxygen atoms, according to the equilibrium structure found in Ref. [231] using HF, and (iii) a structure where the lithium atom is slightly displaced in all three dimensions. In all three cases, calculating the relaxed atomic coordinates using HSE06 resulted in a symmetric structure, as the one obtained with PBE. The total energy difference between the system with starting geometry (ii) and the system with relaxed coordinates, calculated using the HSE06 functional, is <0.2 eV. This shows that the relaxed geometric coordinates correspond to a shallow minimum in the potential energy surface. Therefore, deviations from the relaxed geometric coordinates, which can for example be caused by vibrational effects, will only have a minor effect on the formation energy of the defect.

For the extrapolation, coefficients a_1^q and a_2^q in Eq. 4.28 are determined with PBE and used to extrapolate the formation energy of an isolated defect from the HSE06 calculation of the $2 \times 2 \times 2$ supercell (see also Chapter 6). The FHI-aims electronic structure package [233] is employed for all DFT calculations. The numerical settings are the *tight* predefined settings.

The electronic structure of F centers in MgO is characterized by a defect level deep in the bandgap, which is occupied by 2 electrons in the neutral F^0 center, by 1 electron in the F^+ center and which is empty in the F^{2+} center (see Chapters 6 and 7). Lithium dopants introduce empty states close to the valence band maximum (*p*-type doping), which enables the electrons from the F^0 and F^+ center to lower their energy by transferring into the hole state in the valence band. An F^0 vacancy adjacent to a lithium dopant can transfer one electron to the lithium defect and turns into an F^+ defect, building a defect complex together with the lithium ion. In analogy, an F^0 vacancy adjacent to two lithium substitutional defects evolves to an F^{2+} defect upon electron transfer, within a defect complex that comprises two lithium atoms and an oxygen vacancy. Local geometric and electronic relaxation, which obviously strongly depends on the atomic configuration, can further lower the formation energy of the defect complex.

The frequency shift that is observed in the cathodo-luminescence spectra, when comparing pure MgO to MgO with Li, shows that the preferred decay channel for excitons created in the experiment changes, when Li is present in the sample. As mentioned above, defect complex formation comprising Li dopants and oxygen vacancies can provide electronic levels in the gap

that can open a new exciton decay channel, where electron-hole recombination can happen via a defect level in the bandgap. However, the defect level must be half-filled or empty, so that an excited electron at the CBm can transfer to the defect level and finally to the electron reservoir ϵ_F at the VBM. This means, that defect complexes comprising F^+ or F^{2+} -type defects are possible candidates to be observed in the photon-emission experiments. In contrast, neutral or charged lithium defect configurations without oxygen vacancy, like lithium substitutional defects, interstitials or a combination of both, cannot open new decay channels, because they do not provide suitable gap states. However, in the theoretical analysis also these defects are considered.

Lithium is expected to leave the surface in the form of Li_2O molecules at temperatures above 800 K. However, at lower temperatures the lithium-mediated defect complexes with F^+ - and F^{2+} -type defects can be formed both at the surface and in the bulk. In fact, the free formation energy of all considered defect configurations is lower at the surface in a wide range of conditions in the absence of water. However, in the experiment water is present and can interact with defect complexes at the surface. To test this scenario, the stability of a defect complex comprising an F^{2+} vacancy adjacent to two lithium substitutional defects $2Li_{Mg}V_O$ at the corner of a 2-layer 3 × 3-atom MgO island on a 4-layer MgO (100) surface slab is calculated (Fig. 8.4a). The formation energy of this defect complex is compared to the formation energy of a configura-

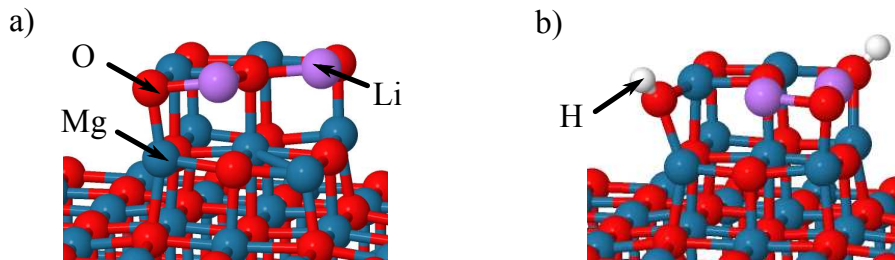


Figure 8.4.: Models for calculating the stability of a defect complex comprising an F^{2+} -type oxygen vacancy adjacent to two lithium substitutional defects at the corner. (a) $2Li_{Mg}V_O$ corner defect complex. (b) Hydrogenatively annihilated defect complex $2Li_{Mg}2H$.

tion $2Li_{Mg}2H$ after hydrogenative annihilation, where two hydrogen atoms of a water molecule have formed OH groups with the surface oxygen atoms nearby the lithium dopants, while the oxygen atom has healed the vacancy Fig. 8.4b). The difference in free formation energy between the two systems is in favor of vacancy healing for temperatures of 600 K and below and water pressures of 10^{-14} atm and above (Fig. 8.5). In principle, vacancy healing is also possible for bulk defect complexes in the presence of water due to diffusion of hydrogen or OH into the bulk (not considered in this study). However, diffusion will be hindered, and the MgO films used in the STM and cathodo-luminescence experiments described above are rather thick (15 ML), so that it is unlikely that all defect complexes in the bulk are hydrogenatively annihilated.

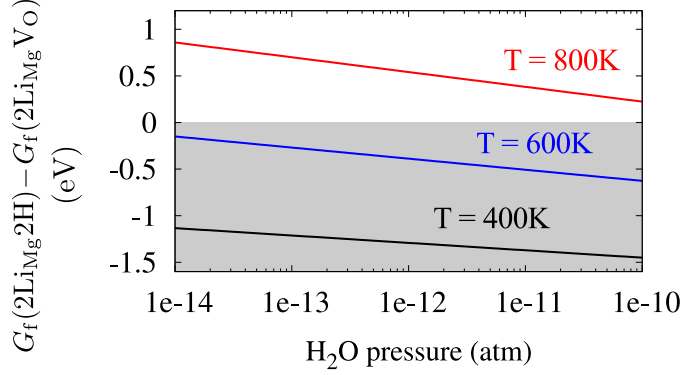


Figure 8.5.: Hydrogenative annihilation of the $2\text{Li}_{\text{Mg}}\text{V}_\text{O}$ corner defect complex. The difference in free energy (calculated with HSE06) between the healed system (Fig. 8.4b) and the system with a $2\text{Li}_{\text{Mg}}\text{V}_\text{O}$ defect complex (Fig. 8.4a) is shown as a function of H_2O pressure for different temperatures. The $2\text{Li}_{\text{Mg}}\text{V}_\text{O}$ defect complex is thermodynamically unstable for temperatures and pressures, where the energy difference is negative (shaded in gray).

8.2.1. Hierarchy of defect stabilities

Ball-and-stick models for all relevant defect configurations are shown in Fig. 8.6. Their relaxed coordinates and charge states are given in Table 8.1. For defect complexes comprising an oxygen vacancy there is an outward relaxation of nearest-neighbor magnesium atoms and an inward relaxation of nearest-neighbor oxygen atoms for F_s^{2+} -type and F_s^+ -type oxygen vacancies, while for F_s^0 -type defects this trend is reversed and less pronounced.

Potential candidates for causing the observed change in the photon emission spectrum are the F^{2+} -type defects within the defect complexes $2\text{Li}_{\text{Mg}}\text{V}_\text{O}$ and $(\text{Li}_{\text{Mg}}\text{V}_\text{O})^+$ (orange lines in Fig. 8.7) and the F^+ -type defects within $(2\text{Li}_{\text{Mg}}\text{V}_\text{O})^-$ and $\text{Li}_{\text{Mg}}\text{V}_\text{O}$ (blue lines), since these defects exhibit an empty or half-filled defect level in the bandgap.

Table 8.1.: Relaxed interatomic distances in Å for defect configurations in different charge states (compare Fig. 8.6). Corresponding distances are also given for pristine MgO for comparison. Distances between adjacent lithium and oxygen atoms $\text{Li}^{(i)}\text{-O}^{(j)}$, where lithium has substituted a magnesium atom in the lattice, can be compared to the distance between nearest neighbor magnesium and oxygen in pure MgO (2.11Å).

103

	pristine MgO	$2\text{Li}_{\text{Mg}}\text{V}_\text{O}$ F ²⁺ -type	$(2\text{Li}_{\text{Mg}}\text{V}_\text{O})^-$ F ⁺ -type	$(2\text{Li}_{\text{Mg}}\text{V}_\text{O})^{2-}$ F ⁰ -type	$(\text{Li}_{\text{Mg}}\text{V}_\text{O})^+$ F ²⁺ -type	$\text{Li}_{\text{Mg}}\text{V}_\text{O}$ F ⁺ -type	$(\text{Li}_{\text{Mg}}\text{V}_\text{O})^-$ F ⁰ -type	Li_{Mg} subst.	Li_{Mg}^- subst.
$\text{O}^{(1)}\text{-Mg}^{(1)}$	2.11	2.09	2.12	2.15	2.09	2.11	2.15	-	-
$\text{Mg}^{(1)}\text{-Mg}^{(2)}$	4.22	4.51	4.33	4.10	4.54	4.37	4.19	4.16	4.15
$\text{O}^{(1)}\text{-O}^{(2)}$	5.97	5.88	5.96	6.03	5.87	5.95	6.03	-	-
$\text{Mg}^{(1)}\text{-O}^{(5)}$	2.11	2.05	2.07	2.09	2.04	2.06	2.09	2.11	2.08
$\text{Li}^{(1)}\text{-O}^{(2)}$	-	2.15	2.15	2.16	2.14	2.15	2.16	2.16	2.17
$\text{Li}^{(1)}\text{-O}^{(3)}$	-	2.20	2.21	2.22	2.14	2.15	2.16	2.16	2.17
$\text{Li}^{(1)}\text{-O}^{(4)}$	-	1.90	1.99	2.09	1.89	1.98	2.07	2.16	2.17
$\text{Li}^{(1)}\text{-O}^{(5)}$	-	2.15	2.15	2.16	2.14	2.15	2.16	2.16	2.17
$\text{Li}^{(1)}\text{-O}^{(6)}$	-	2.09	2.10	2.11	2.14	2.15	2.16	2.16	2.17
$\text{Li}^{(2)}\text{-O}^{(6)}$	-	2.09	2.10	2.11	-	-	-	-	-

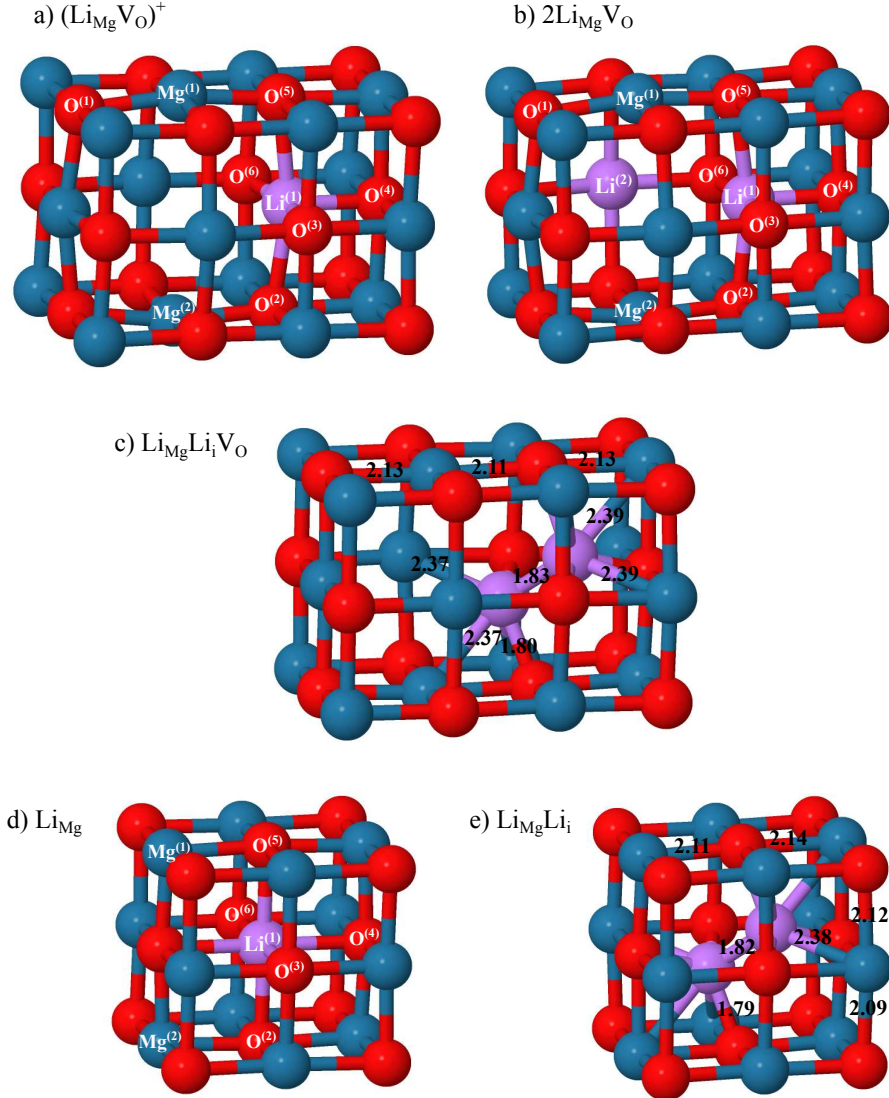


Figure 8.6: Relaxed structures for (a) $(\text{Li}_{\text{Mg}}\text{V}_\text{O})^+$, (b) $2\text{Li}_{\text{Mg}}\text{V}_\text{O}$, (c) $\text{Li}_{\text{Mg}}\text{Li}_\text{i}\text{V}_\text{O}$, (d) Li_{Mg} , and (e) $\text{Li}_{\text{Mg}}\text{Li}_\text{i}$. The shown structures have been cut out from the relaxed coordinates calculated using 216-atom supercells for neutral and 512-atom supercells for charged defect configurations. Relaxed coordinates not given here are listed in Table 8.1

Fig. 8.7a shows the defect formation energies for the Fermi level at the VBM as a function of lithium chemical potential. The Fermi level with respect to the VBM is denoted as $\Delta\epsilon_F$. This situation corresponds to experiments on thicker MgO films (above 10 ML), where electron tunneling from the molybdenum support into the majority of film defects is not possible anymore. In general, free formation energies of lithium-containing defect configurations decrease and, consequently, their concentrations increase with increasing lithium chemical potential. Within

the whole range of lithium chemical potential, the hierarchy of formation energies for defect complexes comprising lithium dopants and oxygen vacancies can be classified in terms of the charge state of the included oxygen vacancy, F^{2+} -type < F^+ -type < F^0 -type. In particular, the defect complexes with F^+ - and F^0 -type defects are so high in formation energy, that their calculated concentrations are negligible. For $\Delta\mu_{Li}$ close to lithium in Li_2O and the Fermi level at the VBM, the order in formation energies for defect complexes comprising F^{2+} - and F^+ -type defects is $(Li_{Mg}V_O)^+ < 2Li_{Mg}V_O$ and $Li_{Mg}V_O < (2Li_{Mg}V_O)^-$, respectively. The lowest formation energy is $G_f((Li_{Mg}V_O)^+) = 1.2$ eV. Thus, $(Li_{Mg}V_O)^+$ will be the most abundant defect complex at an equilibrium temperature of 600 K and an oxygen pressure of 10^{-10} atm.

The order is reversed within each charge state when μ_{Li} approaches the energy of a lithium atom, which would imply that gas phase atoms are the source of lithium during annealing, a condition that is never fulfilled experimentally. The thermodynamic stability of $Li_{Mg}Li_i$, $G_f(Li_{Mg}Li_i) = -3.1$ eV, is then comparable to that of the lowest defect complex $2Li_{Mg}V_O$ containing an F^{2+} -type defect, $G_f(2Li_{Mg}V_O) = -2.6$ eV, for $\Delta\mu_{Li} = 3$ eV and the Fermi level at the VBM.

In Fig. 8.7b the Fermi level is 1.5 eV above the VBM, a situation that is found in ultrathin films (1-5 ML), where ϵ_F is still governed by the Mo (001) support below the film. Again, the formation energies for the different defect configurations are shown as a function of lithium chemical potential. The general trend in formation energies of neutral defect complexes, F^{2+} -type < F^+ -type < F^0 -type in terms of the charge state of the oxygen vacancy in the defect complex, is not affected by the shift in Fermi level. Only defect configurations carrying a net charge $q \neq 0$ depend on ϵ_F . The formation energy of the defect complex $(Li_{Mg}V_O)^+$ (which contains an F^{2+} -type defect), is therefore shifted up by 1.5 eV, while the formation energy of $(2Li_{Mg}V_O)^-$ (comprising an the F^+ -type defect) is shifted down by 1.5 eV with respect to Fig. 8.7a, where $\epsilon_F = VBM$. For $\Delta\mu_{Li} = 0$ eV (oxygen-rich conditions) all defect complexes with oxygen vacancy defects have formation energies higher than 2.5 eV. When lithium is not fully oxidized, its chemical potential is raised and the defect complexes which contain F^{2+} -type defects can form more easily in thermodynamic equilibrium. However, at $\epsilon_F = 1.5$ eV above the VBM, the defect complexes $(Li_{Mg}V_O)^+$ and $(2Li_{Mg}V_O)$, which comprise F^{2+} -type defects, have higher formation energies than Li_{Mg} and $Li_{Mg}Li_i$.

Fig. 8.7 (c) shows the dependence of the formation energies for the different defect configurations on the position of the Fermi level between VBM and CBM. The lithium chemical potential is fixed at the value derived from the stability condition for Li_2O ($\Delta\mu_{Li} = 0$ eV). The lowest transition levels between different defect configurations occur at $\epsilon_F = 4.0$ eV ($2Li_{Mg}V_O/(2Li_{Mg}V_O)^-$, F^{2+} -type to F^+ -type in terms of the contained oxygen vacancies), and at $\epsilon_F = 4.8$ eV ($(2Li_{Mg}V_O)^-/(2Li_{Mg}V_O)^{2-}$, F^+ -type to F^0 -type). Among the defects containing an oxygen vacancy, the structural motif of two lithium substitutional defects adjacent to one oxygen vacancy is favored only when $\epsilon_F > 2.3$ eV, otherwise $(Li_{Mg}V_O)^+$ defects are easier to form. The main conclusion of Fig. 8.7 is that the most abundant bulk defect complexes that may cause the observed shift in the photon-emission peak are those comprising F^{2+} -type defects, namely $(Li_{Mg}V_O)^+$ and $2Li_{Mg}V_O$.

The theoretical analysis enables the following interpretation of the experimental data. For the given film thickness of 15 ML, the metal substrate below the film is an unsuitable electron source, as tunneling into MgO gap states is blocked by a substantial barrier. This situation is

best described by a Fermi level at the VBM. For the lithium chemical potential, as the second variable in Fig. 8.7, lower μ_{Li} can be considered more realistic than higher values, as lithium will be completely surrounded by oxygen species from the MgO matrix after deposition/annealing. The most realistic situation is therefore displayed in Fig. 8.7 (a,c) – left side. Here, $(\text{Li}_{\text{Mg}}\text{V}_\text{O})^+ < 2\text{Li}_{\text{Mg}}\text{V}_\text{O} < \text{Li}_{\text{Mg}}\text{V}_\text{O}$ is the predicted hierarchy of formation energies for defect complexes containing oxygen vacancy defects and lithium impurities. All the defect complexes have characteristic defect states in the MgO bandgap and can thus explain the shift in the optical spectra (see Sec. 8.2.2). Note, that the lithium defects without oxygen vacancy are optically inactive and will therefore diminish the emission response when becoming the dominant species. The visibility of a red-shifted emission peak in lithium-doped MgO therefore proves that the conditions, at which Li_{Mg} and $\text{Li}_{\text{Mg}}\text{Li}_i$ defect complexes become energetically preferred, are not realized in the experiment (high Fermi levels, high lithium chemical potentials). The electronic structure of the defect configurations, which comprise F^{2+} and F^+ defects, is discussed in the following.

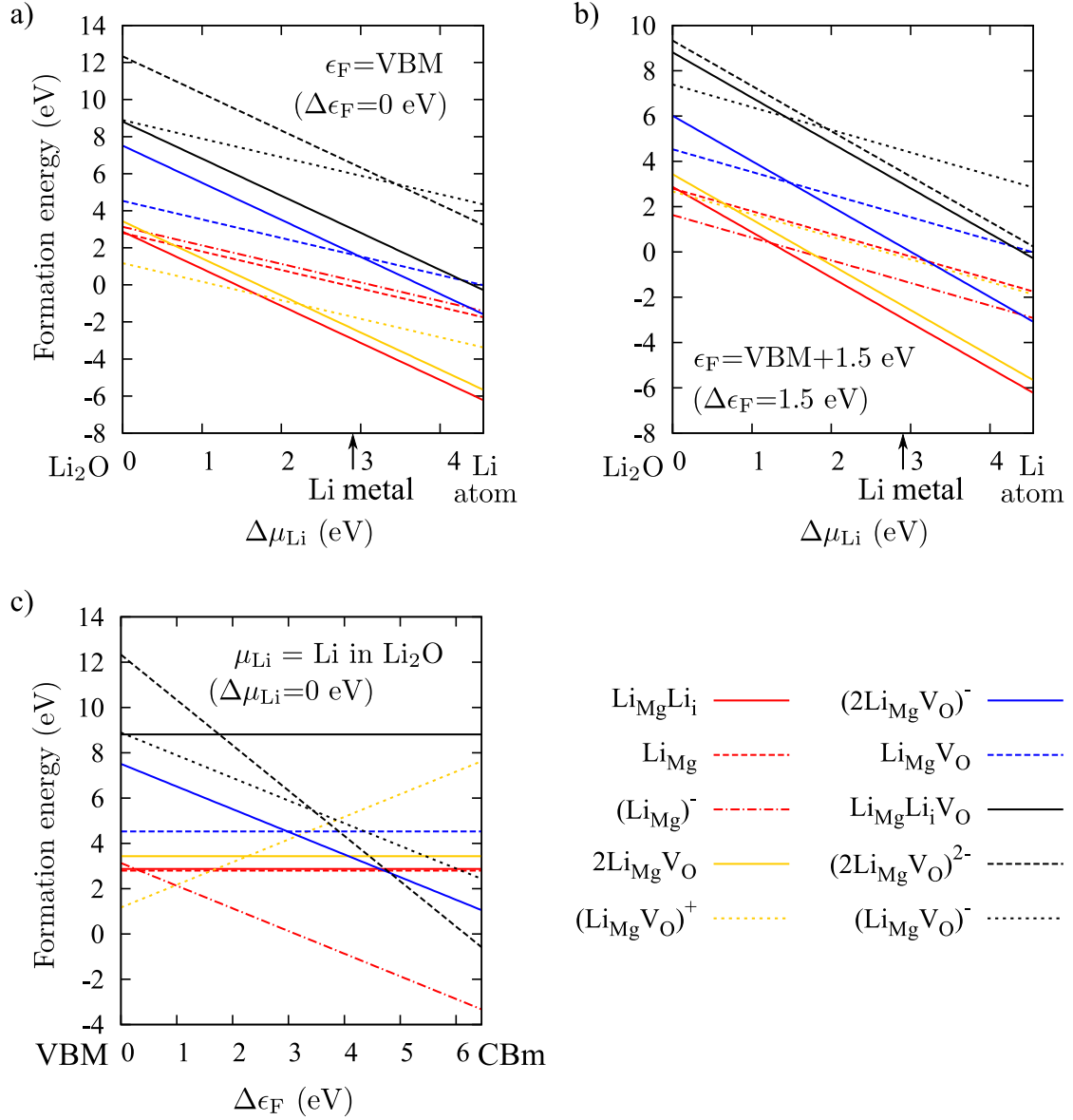


Figure 8.7.: Formation energies of different lithium-mediated defect configurations at a temperature of 600 K and an oxygen partial pressure of 10^{-10} atm. (a) and (b) show the formation energies as a function of the lithium chemical potential, varied between the chemical potential of lithium in Li_2O ($\Delta\mu_{\text{Li}}=0$ eV) and the chemical potential of a lithium atom ($\Delta\mu_{\text{Li}}=4.55$ eV). In (a) the Fermi level is at the valence band maximum ($\Delta\epsilon_{\text{F}}=0$ eV) and in (b) the Fermi level is 1.5 eV above the valence band maximum ($\Delta\epsilon_{\text{F}}=1.5$ eV). In (c) the chemical potential of lithium is fixed to $\Delta\mu_{\text{Li}}=0$ eV and the Fermi level is varied between VBM and CBm. Red lines show lithium substitutional and interstitial defects without oxygen vacancy, while all other defect configurations consist of one or two lithium impurities adjacent to an oxygen vacancy: Black lines show defect complexes comprising F^0 -type defects, blue lines depict defect complexes including F^+ -type defects, and orange lines represent defect complexes which contain F^{2+} -type defects.

8.2.2. Position of defect levels

The HSE06 calculations show that an unoccupied defect level is indeed present deep in the bandgap for the two defect complexes that contain F^{2+} -type defects, $(\text{Li}_{\text{Mg}}\text{V}_\text{O})^+$ and $2\text{Li}_{\text{Mg}}\text{V}_\text{O}$, opening a new channel for recombination of excitons created in the cathodo-luminescence experiment. The total and projected density of states (DOS) for the $(\text{Li}_{\text{Mg}}\text{V}_\text{O})^+$ defect complex is shown in Fig. 8.8. The VBM is due to oxygen 2 p states, while the defect level and the CBm are dominated by magnesium 3 s states (see Chapter 6). The HSE06 Kohn-Sham defect-levels are 4.2 eV above the VBM for $(\text{Li}_{\text{Mg}}\text{V}_\text{O})^+$ and 4.4 eV above the VBM for $2\text{Li}_{\text{Mg}}\text{V}_\text{O}$. For the defect complexes which comprise F^+ -type defects the Kohn-Sham defect levels are 2.7 eV and 2.9 eV above the VBM for $\text{Li}_{\text{Mg}}\text{V}_\text{O}$ and $(2\text{Li}_{\text{Mg}}\text{V}_\text{O})^-$, respectively. The overlap of different recombination channels involving different gap states might be responsible for the substantial peak broadening in emission spectra of lithium-doped MgO.

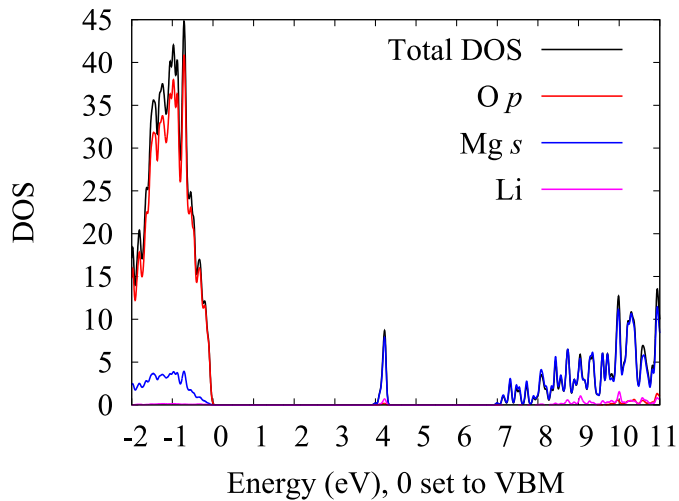


Figure 8.8.: Total and projected density of states for $(\text{Li}_{\text{Mg}}\text{V}_\text{O})^+$, comprising an F^{2+} -type defect, calculated with HSE06. The defect level is unoccupied and allows for additional exciton decay channels.

For the changed optical decay detected in the cathodo-luminescence experiment for lithium-doped MgO compared to pure MgO, in principle two transitions come into consideration. De-excitation of a hot electron in the conduction band involves two steps, one from the CBm to the defect level and the second from the defect level to the VBM. Which transition is dominant for the photon emission depends on the symmetry of the contributing orbitals (Fig. 8.9). For both defect configurations eigenstates at the CBm and in the defect have comparable symmetry, dominated by an s -shaped orbital arising from the magnesium 3 s states. The state at the VBM, on the other hand, shows the distinct symmetry of the oxygen 2 p states. The dipole selection rules for an optical transition can therefore only be fulfilled for the defect \rightarrow VBM transition, where the state symmetry changes according to $\Delta l = \pm 1$, where l is the orbital momentum quantum number. The CBm-defect transition, in contrast, is dipole-forbidden, as the orbital

8.2. Theoretical analysis of lithium-induced defect complexes

symmetry remains constant. A comparison of spatial symmetries of the states therefore suggests, that the peak in the luminescence spectra is mainly due to transitions from the defect levels of defect complexes comprising F^+ - and F^{2+} -type defects to the VBM.

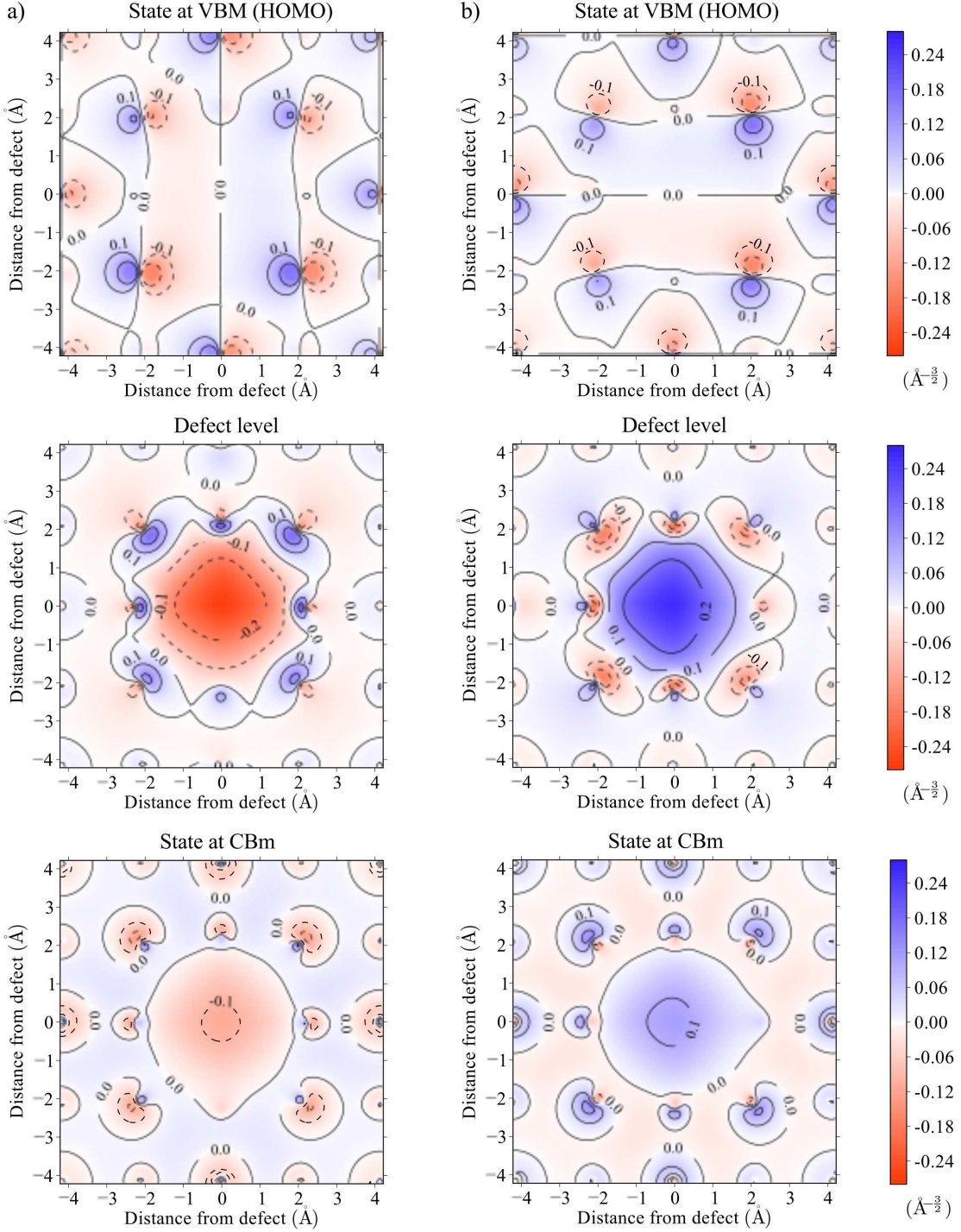


Figure 8.9.: Highest occupied valence state (*top*), defect level (*middle*), and lowest conduction-band state (*bottom*), in $\text{\AA}^{-\frac{3}{2}}$, as a function of spatial coordinates in \AA in the (100) plane for $(\text{LiMgVO})^+$ (a, *left panel*), where LiMg is at $(0, -2.1)$ and V_O at $(0, 0)$ (see Fig. 8.6 (a) for comparison), and 2LiMgV_O (b, *right panel*), where **one** of the two LiMg is at $(2.1, 0)$ and V_O at $(0, 0)$ (see Fig. 8.6b for comparison).

8.3. Summary

In summary, the observed red-shift of the main optical emission band in lithium-doped as compared to pristine MgO films suggests the opening of new recombination channels for electron-hole pairs injected in cathodo-luminescence experiments, which are mediated by new electronic states inside the bandgap of the oxide material. Whereas lithium substitutional defects by themselves do not induce suitable gap states, defect complexes that consist of lithium impurities and compensating oxygen defects are likely candidates to generate the observed emission signature. While defect complexes containing electron-rich F^0 -type oxygen vacancies and lithium dopants can be discarded in this context, as they are unstable, defect configurations comprising electron-poor F^+ - and F^{2+} -type oxygen vacancies that have lost electrons to the lithium-induced hole states in the MgO valence band are compatible with the experimental results. From thermodynamic stability criteria the defect complexes comprising doubly positively charged F^{2+} -type centers are most likely responsible for the red-shifted emission peak at 550 nm, as they imprint a suitable defect state in the MgO bandgap for electrons to decay from the conduction to the valence band. However, also defect complexes that contain F^+ -type defects with a half-filled defect level are potential candidates. Given their higher formation energies with respect to different defect configurations that comprise F^{2+} -type oxygen vacancies, their contribution to the observed optical response of MgO_{Li} films can be considered as small.

It is clearly demonstrated that the majority of lithium-impurities in MgO appears as defect complexes, comprising lithium dopants and oxygen defects, where charge transfer between the oxygen vacancy and one or two lithium atoms annihilates the oxygen $2\ p$ hole states due to lithium and therefore neutralizes the effect of the lithium dopant. (This is one reason, why formation of Li^+O^- pairs, as active centers for methane activation, as suggested by Lunsford in 1985 [234] and widely accepted in the literature, as reviewed by Arndt *et al.* [220] in 2011, is regarded thermodynamically unfeasible.)

9. Concluding remarks

Within the presented work a theoretical methodology was developed and tested that can be used to predict charge states and concentrations of point defects at semiconductor surfaces under realistic conditions from first-principles. The concept has been applied to F centers in MgO, and has led to some important insights on charge state and concentrations of these defects.

One important objective was to find a suitable charge-compensation method for supercell models of charged systems, in particular for surface calculations, where the standard constant-background approach is not applicable. Inspired by early work of Vegard (1921) [126] and Scheffler (1987) [127], a variant of the VCA has successfully been tested and applied to resolve this issue. Within this approach, an adjustable density of states at the Fermi level is introduced by modifying the electron-nuclear interaction potential within the host material, while keeping the system charge-neutral. This simulates the realistic situation of a doped material, where defect states in the bandgap can accommodate charge carriers from shallow dopant levels, providing a natural charge-compensation mechanism. In an all-electron code the idea is easily realized by modifying the nuclear charges of the atoms of the host material by a small fraction. The VCA allows to choose the type of doping (*p*- or *n*-type), and the "dopant" concentration and distribution. The benefits of the VCA for charge compensation are a well-defined Fermi level, applicability to systems of different dimensions (bulk, surface, wire, or cluster), and widely variable dopant concentrations.

To ensure a quantitatively accurate description of formation energies of F centers in MgO, embedded cluster models were employed. For these systems, *GW* and coupled-cluster methods are readily applicable. G_0W_0 @HSE was used to identify HSE06 as an opt-HSE functional that correctly describes the charging of F centers in MgO, in compliance with a condition on the ionization potential. In a collaboration with Prof. Sauer's group from the Humboldt University Berlin, also coupled-cluster calculations of the neutral oxygen vacancy formation energy were performed, confirming that HSE06 provides reliable exchange-correlation treatment for F centers in MgO. Embedded cluster and periodic calculations were carefully tested for consistency. Accurate formation energies with reliable error bars (< 0.15 eV) were calculated for charged and neutral F centers at varying concentrations by combining advantages of both periodic and cluster models. As an important result it has been shown that the only available measurement on the neutral bulk F center formation energy in MgO [26] should be revised, most likely since thermodynamic equilibrium could not be reached in the experiment.

For the last 25 years realistic atomic and electronic chemical potentials, and therefore also realistic temperature and pressure conditions, have been accounted for in theoretical studies of defect stabilities in insulators or semiconductors, using DFT methods by what is now known as *ab initio* atomistic thermodynamics. Defects have been calculated in a relaxed geometry, using an embedded cluster or a supercell of certain size, and from these calculations the formation energy of the defect in the dilute limit, for vanishing defect concentrations was obtained. Indeed, the focus was often on how this dilute limit could be obtained most accurately and efficiently

by extrapolation or correction schemes. However, to address a more realistic situation, finite concentrations of interacting surface vacancies have been considered in this work. As a key result, it has been shown that the formation of charged surface defects in doped materials can be largely determined by formation of a space-charge region with associated band bending and electric field. The contribution of the electric field energy to the defect formation energy can be divided into two parts: the energy need for charging the defects, and the attraction of defects to the compensating charge. The existing approaches to calculating non-interacting defect formation energies and concentrations has been extended to interacting defects. This is achieved by including the interaction energy (the energy of the electric field) into the Gibbs free energy of the system, and then minimizing the free energy with respect to the concentrations of vacancies in all possible charge states. For surface defects, the bulk dopant concentration complements the set of thermodynamic variables (temperature, pressure, and Fermi energy) that the defect stabilities depend on. Also, the configurational entropy of defects in all charge states is accounted for. This framework has been applied to oxygen vacancies in MgO, and the predominant charge state and concentration of these defects under realistic conditions have been predicted.

In MgO, the formation of surface F_s^{2+} centers can reach approx. 1 % at conditions relevant for catalytic applications ($T = 1,000$ K, $p = 1$ atm, $\epsilon_F = \text{VBM}$, $N_D = 10^{18} \text{ cm}^{-3}$). The concentration of F_s^{2+} centers does not exceed 1% due to the build up of the space-charge layer, which raises the defect formation energy by up to 1 eV relative to the isolated defect. In other words, starting from a defect-free surface, first defects are formed spontaneously, but as their concentration grows, each new defect costs more energy. These results are important for future studies of charged defects at semiconductor surfaces, since they show that electrostatic space-charge effects are a type of defect-defect interaction that can not be neglected. The energy of this interaction is sensitive to the distribution of the compensating charge, which can extend over macroscopic length scales. This implies that DFT slab calculations must always be corrected for the limited thickness, as described in this work, when they are used to predict properties of single-crystal surfaces. The same is true for experimental studies, where charged defects at thin films are used to understand properties of single-crystal semiconductor surfaces.

Furthermore, defect complexes in bulk lithium-doped MgO were studied. It has been shown that upon lithium doping, formation of defect complexes incorporating one or two lithium defects and an oxygen vacancy is favored. Also within the complexes with lithium the preferred charge state of the vacancies is 2+. These results are in accordance with an observed red-shift of the main optical emission band in cathodo-luminescence spectra that is observed for lithium-doped MgO when compared to spectra for pristine MgO, measured in Prof. Freund's group of the FHI Chemical Physics department. Interestingly, calculations performed within this work predict that there is a competition between $(\text{Li}_{\text{Mg}}\text{V}_\text{O})^+$ and $(2\text{Li}_{\text{Mg}}\text{V}_\text{O})$ defect complexes. This has not been addressed in literature despite the large amount of work devoted to lithium-doped MgO due to its catalytic properties.

In summary, the goal of this work was to take a step forward on the way to understand defect formation at semiconductor surfaces, motivated in particular by the role of oxygen vacancies in catalysis. This was achieved by providing an understanding of equilibrium F-center concentrations at metal oxide surfaces, in particular at the MgO (100) surface, and introducing a general theoretical framework to calculate charged-defect stabilities.

From here on, using the presented model, theoretical estimates of formation energies and

concentrations of interacting defects can be further improved, for instance by accounting for realistic dopant concentration profiles that can be realized in experiment. Concerning F centers in MgO, also concentrations of defects in different charge states at low-coordinated sites and surface terminations other than MgO (100) are of interest in general, and in catalysis in particular. A brief outlook on some very interesting questions arising for F centers at steps and corners, and at reconstructions of the polar (111) surface of MgO, is given in Chapter 10.

10. Outlook: F centers at low coordinated sites and polar surfaces

Depending on the environment, the most stable surface terminations of a metal oxide can vary. Also, realistic surfaces exhibit steps and corners where defects like oxygen vacancies can appear. It has been shown that while the (100) surface is the most stable termination of pristine MgO, *p*-type doping the material, for example with lithium, can lead to roughening or even to a change in hierarchy of the different surface terminations [172, 235].

Myrach *et al.* have demonstrated in a combined STM and DFT study, that the surface morphology of mixed Li/MgO films changes with temperature such that lithium segregates towards the surface at approximately 700 K in ultra-high vacuum conditions, and Li_{Mg}-rich surface islands are formed. Annealing at higher temperatures leads to the formation of Li_xO clusters at the surface, and their subsequent evaporation, leaving the MgO (100) surface with a characteristic pattern of monolayer-deep rectangular holes in the MgO surface after annealing at approximately 1,050 K [172].

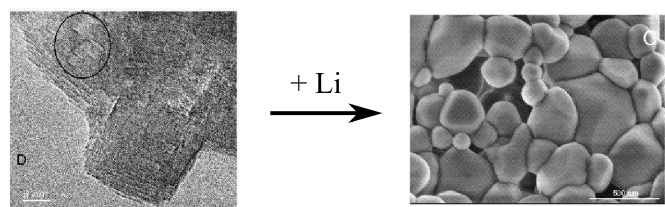


Figure 10.1.: The most stable surface termination of MgO nanocrystals changes from (100) to (111) upon addition of lithium to the precursor [235]. (Figure adapted from Ref. [235], copyright (2011) by John Wiley & Sons, Inc.)

The effect of doping on the surface structure can even be more profound when the morphology is not restricted (as it is in the case of thin films). Zavyalova *et al.* found that adding 1 weight % lithium to the combustion precursor of MgO nanocrystals leads to a morphology change of MgO nanoparticles from on average 8 nm edge length (100) terminated nanocubes to complex nanoparticles with polyhedral surfaces of up to 250 nm in diameter, exposing more and more (111) facets [235] (Fig. 10.1).

No theoretical or experimental studies on F center formation at the MgO (111) surface have been reported so far. One open question is, for example, how bulk lithium dopants influence the composition, stability, and electronic structure of the (111) surface termination. If there are surface states in the bandgap, formation of a space-charge region and associated band bending is possible.

The MgO (111) surface has an interesting feature: it is polar. Stacking of charged atomic

layers (Mg^{2+} and O^{2-}) along the surface normal results in uncompensated charge of the bulk-like surface termination. The surface charge must be compensated to make the polar surface stable. Stabilities of polar oxide surfaces, considering various stabilization mechanisms, such as spontaneous metalization of the surface layers, non-stoichiometry, faceting, or adsorption, have been studied for instance by Noguera [236–240], accounting also for ambient temperature and partial pressures. It would be interesting to see how doping affects composition, stability, and electronic structure of polar oxide surfaces. One possibility is that charged defects, in particular oxygen vacancies, can compensate the surface charge. Consequently, understanding F center formation at these surfaces with regard to charge transfer between surface states, defect states, and Fermi level is desirable.

Concerning the stability of oxygen vacancies at low-coordinated sites, formation energies of neutral defects have been reported already 15 years ago (see for example Ref. [27, 112, 216] for MgO). However, as it was demonstrated above, charged F^{2+} centers in bulk MgO and at the (100) surface are much more stable. Therefore, also charged defects at low-coordinated sites should be considered.

10.1. F centers at MgO (100) steps and corners

In the following, neutral F centers at low-coordinated sites are briefly discussed as a first step towards a full description of these defects, considering all possible charge states.

At structural defects like steps and corners, oxygen atoms are four-fold and three-fold coordinated, respectively. The lower the coordination of the site is, the less confined are geometric and electronic relaxations, and, as a consequence, the formation energy of the neutral oxygen vacancy is reduced with respect to the defect at the terrace. Formation energies G_f^0 for neutral oxygen vacancies at steps and corners have so far only been calculated using embedded cluster models at HF and LDA level of theory [27, 216]. Sushko *et. al.* also reported the formation energy of the corner defect calculated with B3LYP [112]. Embedded cluster models using PBE0 have been calculated in the present work [185].

Periodic models for low-coordinated defects can be constructed in different ways. For the monolayer step, a zig-zag structure and a model with monolayer one-dimensional rail structures on 5-layer (100) surface slabs (see Fig. 10.2a-b) have been calculated and compared at PBE level. Step and rail size, respectively, were increased systematically, until formation energies were converged within 0.04 eV. The formation energies obtained with the two periodic models are in very good agreement (within 0.02 eV). To model the corner site, a $3 \times 3 \times 2$ -atom island of two-layer height on a 4-layer (100) slab has been calculated (see Fig. 10.2c). Structures were relaxed with PBE, and single-point calculations with HSE06 and PBE0 were performed for the relaxed structures, scaled to HSE06 and PBE0 optimized lattice parameters, respectively. The formation energies are listed in Table 10.1. As discussed for F centers in the bulk and at the terrace, the lack of correlation in HF leads to an underestimation of the formation energies, while including only local exchange leads to an overestimated formation energy. It has been demonstrated in Sec. 6 that the formation energy for neutral F centers in MgO only weakly depends on HSE parameters and can be estimated using HSE06 or PBE0. The energies calculated with these functionals are highlighted in the table. The formation of F centers is energetically much more favorable at

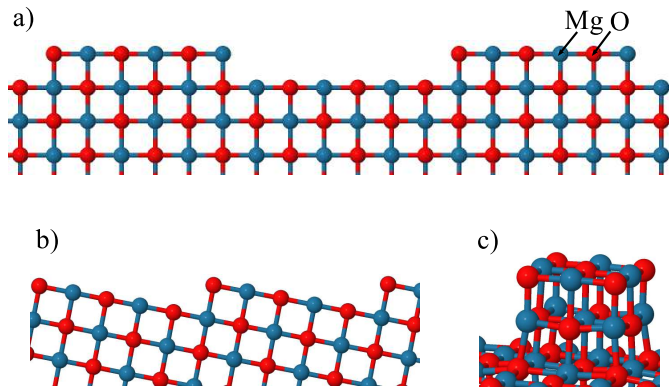


Figure 10.2.: Side view of a) rail and b) zigzag periodic models that were used to calculate an oxygen vacancy at the MgO (100) monolayer step site. c) Island model used to calculate an oxygen vacancy at the corner site.

steps and corners than in the bulk or at the terrace. However, the formation energy of the neutral defect also at these low-coordinated sites is so high that their concentration is still negligible.

The systematic description of the formation energies as a function of defect concentration or surface charge for charged defects at steps and corners is challenging due to the complicated geometry. Periodic models can be used, but the structural models have to be chosen and tested carefully – in particular for the corner models. In addition to F centers also intrinsic interstitials at steps or corners are possible and can be analyzed using the same methodology (for a discussion of neutral oxygen interstitials in bulk MgO see appendix).

Table 10.1.: Formation energies G_f^0 (eV) of the neutral oxygen vacancy at the MgO (100) surface corner and monolayer step, calculated using embedded cluster (ecm) and periodic models (pbc). The chemical potential of oxygen corresponds to the oxygen-rich limit where $\Delta\mu_O = 0$ eV.

Method	Step	Corner
HF-ecm [216]	4.24	3.24
LDA-ecm [27]	6.99	5.45
PBE-ecm [185]	5.68	5.13
PBE0-ecm [185]	5.44	4.89
B3LYP-ecm [185]	5.72	5.07
B3LYP-ecm [112]	-	4.63
PBE-pbc	5.79	5.17
HSE06-pbc	5.61	-
PBE0-pbc	5.61	-

10.2. F centers at the MgO (111) surface

The (111) surface termination of ionic rock-salt metal oxides is polar. Alternating layers of metal and oxygen ions generate an electrostatic dipole field perpendicular to the surface (Fig. 10.3 a)). The calculated surface energy for formally neutral bulk-terminated slabs of increasing thickness diverges. As discussed by Tasker already in 1979, polar surfaces can be stabilized by rearrangement of charge, typically facilitated by substantial surface reconstruction [241]. In some

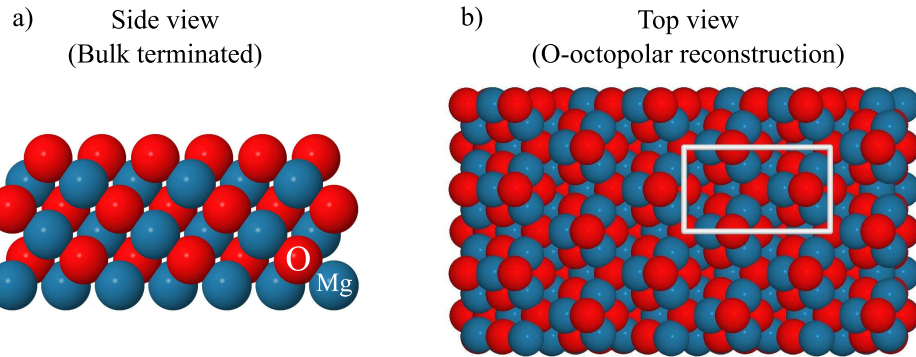


Figure 10.3.: a) Side view of the unstable, bulk-terminated, polar MgO (111) surface. Alternating magnesium cations and oxygen anions lead to an electric dipole perpendicular to the surface. b) Top view of the octopolar O-terminated reconstruction of the MgO (111) surface with the primitive rectangular unit cell (white lines). The structure has been relaxed using PBE.

cases, stabilization can also be achieved merely by electronic charge transfer between layers, as demonstrated by Wander *et al.* for ZnO (0001)-Zn and (000 $\bar{1}$)-O surfaces [242]. The stability, and structural and electronic properties of 12 models of the polar *undoped* MgO (111) surface were studied in 2008 by Zhang and Tang, applying DFT with a GGA functional, and *ab initio* atomistic thermodynamics [243]. In agreement with an earlier study by Finocchi *et. al.* (2004), it was found that under conditions $\Delta\mu_O > -5.6$ eV the O-terminated octopolar structure is the most stable reconstruction of the MgO (111) surface. In the O-terminated octopolar reconstruction, 3/4 of the ions in the outermost layer and 1/4 of the ions in the second layer are missing (Fig. 10.3b). To achieve charge neutrality, half of the negative charge in the surface layer should be removed, which would correspond to removing 50% of the oxygen atoms in the top layer of the slab. Instead, in the octopolar reconstruction 75% of the negative charge is removed from the top layer, but furthermore 25% of the positive charge in the second layer is taken away, so that in total the desired 50% of negative charge at the surface is eliminated and the surface is charge neutral.

There is a fundamental difference between the electronic structure of the MgO (100) and the MgO (111) surface terminations. While the (100) surface bands are at the bulk VBM, the O-octopolar reconstructed (111) surface termination exhibits surface bands in the bandgap, 0.5 eV above the VBM (Fig. 10.4). They are mainly due to oxygen atoms in the top layer of the sur-

face, but there is also a contribution from magnesium atoms in the second layer, as shown by the projected DOS in Fig. 10.4b. Note, that these preliminary calculations have been performed with PBE, and therefore only allow for a qualitative description. For the system without dopants

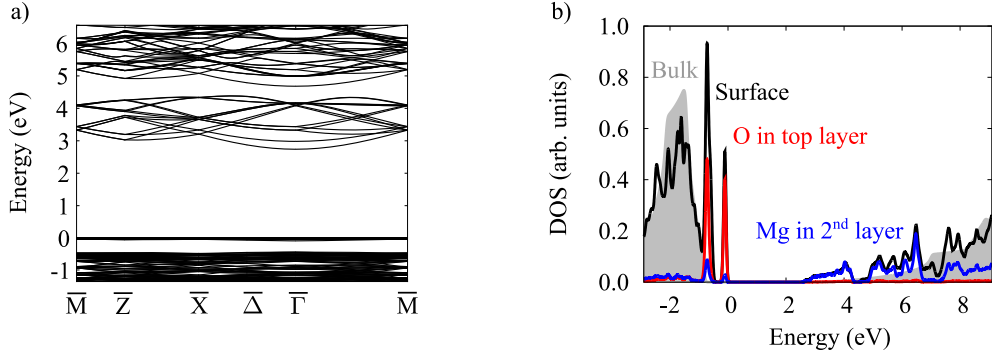


Figure 10.4.: a) Surface band structure of the O-terminated octopolar reconstruction of MgO (111) without defects, calculated for a 288-atom cell with PBE. b) MgO bulk DOS (gray) and surface DOS (black), where both have been normalized by dividing by the number of electrons in the system. The projected DOS for the top-layer oxygen atoms (red) and second-layer magnesium atoms (blue) are also shown (compare surface model in Fig. 10.5).

or defects, the surface bands are fully occupied. Introducing *p*-type dopants in the bulk leads to charge transfer between occupied surface bands and acceptor bands at the bulk VBM. This results in downward band bending and a partial occupation of the surface band. An important step in a study of the doped MgO (111) surface would be to find out how electron transfer and associated space-charge effects influence the surface stoichiometry and reconstruction. In contrast to the (100) surface, band bending at the doped (111) surface will occur without vacancies, and will contribute to the surface energy.

Here, F-center formation at the O-octopolar reconstructed surface is briefly analyzed. The atom that is removed from the surface to create a vacancy is shown in the *left* panel of Fig. 10.5. In this picture also the underlying cubic MgO structure can easily be recognized. The position where the vacancy is created corresponds to the edge of a small $2 \times 2 \times 2$ -atom MgO “cube”. Similar to F centers at MgO (100), geometric relaxation is most pronounced for the $F_{s,111}^{2+}$ center. The next-neighboring atoms below the vacancy try to recover a flat surface. Magnesium atoms move downwards, deeper into the surface, while oxygen atoms are displaced outwards and upwards (Fig. 10.5, *middle* and *right* panel). The surface defects introduce defect levels in the bandgap, above the surface band, similar to F centers in MgO bulk and at the MgO (100) surface. But since here also the surface band is present, the energy gained by electron transfer from a surface defect to an empty surface state – at the VBM of the pristine slab, which is a Fermi level in case it is pinned at the surface of doped MgO – is smaller than for the surface F_s centers at the MgO (100) terrace. Therefore, one more question to be answered is if this effect dominates over differences in electronic and geometric relaxation between (100) and (111) surface oxygen vacancies. Once all aspects mentioned above have been considered, the methodology introduced in this work can be used to calculate concentrations of interacting surface oxygen

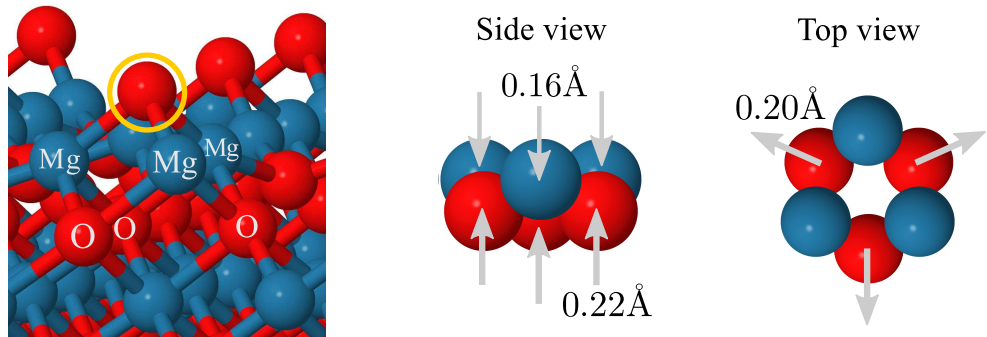


Figure 10.5.: Relaxation due to $F_{s,111}^{2+}$ center. *Left:* O-octopolar reconstruction of the MgO (111) surface. The oxygen atom that is removed to form an F center is marked by a yellow circle. *Middle, right:* Displacement of atoms closest to the $F_{s,111}^{2+}$ center, marked Mg and O, after formation of the defect. Relaxation was calculated with PBE.

vacancies at an MgO (111) surface in analogy with the analysis presented for F centers at the MgO (100) surface.

A. Appendix

A.1. Oxygen interstitials in MgO bulk

Apart from vacancies, self-interstitials are a common type of defect in semiconductors and oxides. Magnesium interstitials are harder to form than oxygen interstitials, because they need more space in the lattice. Here, only the neutral oxygen interstitial will be considered. Since the neutral oxygen vacancy formation energy can accurately be calculated using the PBE exchange-correlation functional, it is safe to assume that this is also valid for the neutral oxygen interstitial.

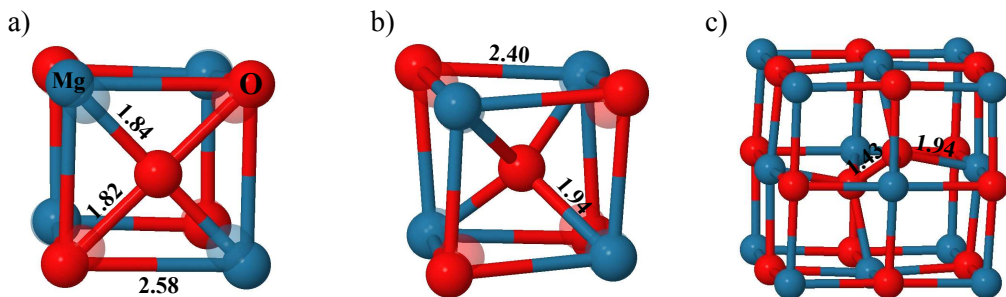


Figure A.1.: Relaxed geometries for three oxygen self-interstitial configurations corresponding to local energy minima: a) face-centered, b) body-centered, and c) dumbbell configuration. Measurements are in Å. The distance between oxygen and magnesium in pristine MgO is 2.13 Å (PBE).

To obtain the most favorable oxygen interstitial geometry, the MgO structure is relaxed starting from different geometric configurations. These are a face-centered, body-centered, and edge, as well as some intermediate positions. The energetically lowest configuration found is a dumbbell configuration, where the interstitial oxygen together with a lattice oxygen atom forms a dumbbell along the [111] direction, centered at the oxygen lattice site. The formation energy for this configuration is 1.93 eV for $\mu_O = 1/2 E_{O_2}^{\text{tot}}$, calculated with PBE. Two local minima are given by the configuration, where the oxygen interstitial is face-centered between two oxygen and two magnesium atoms in the (100) plane as well as by a body-centered configuration. The relaxed structures are shown in Fig. A.1. Most severe changes compared to the pristine MgO lattice are obviously introduced by the dumbbell configuration.

Similar to the oxygen vacancy, the oxygen self-interstitials introduce defect levels in the electronic structure of MgO. Two defect states appear in the bandgap, corresponding to the 2p orbitals of the additional oxygen atom, each of them occupied with two electrons. The face centered oxygen interstitial introduces one defect level deep in the bandgap and the other one close to the VBM. For a body-centered interstitial and a dumbbell formation centered at an oxygen site the levels are almost degenerate and close to the VBM. The bandstructure of pristine MgO

and the bandstructure of the most likely interstitial configuration (dumbbell), both calculated for a 64-atom unit cell with the PBE exchange-correlation functional, are shown in Fig. A.2. The oxygen interstitial defect states are due to oxygen 2p states, mainly of the two oxygen atoms that form the dimer-like interstitial structure.

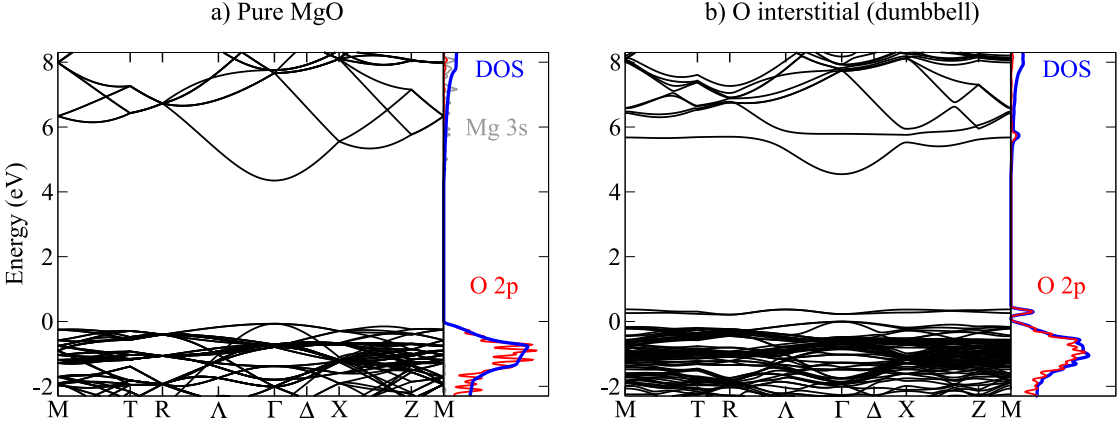


Figure A.2.: Bandstructure and density of states for pristine MgO (a) and the dumbbell interstitial configuration (b), obtained with PBE for a 2x2x2 MgO supercell. The energy zero is set to the VBM. Note the two fully occupied defect levels close to VBM for the dumbbell interstitial configuration.

Fig. A.3 shows the formation energies for the three interstitial configurations and the neutral oxygen vacancy at $T = 600$ K as a function of oxygen chemical potential and oxygen pressure. At this temperature contributions due to phonons are -0.12 eV for F^0 and 0.30 eV for the dumbbell interstitial configuration. Vibrational effects are not taken into account in the following. Referenced to the energetically most favorable dumbbell configuration, the face-centered and body-centered configurations are 1.09 eV and 3.48 eV higher in energy. This is in qualitative agreement with relative energies of 1.45 eV and 3.57 eV, respectively, calculated with a full-potential linear-muffin-tin-orbital method using a 16-atom supercell, where only next neighbors are relaxed [244]. For comparison also the F^0 center formation energy is shown. For increasing oxygen pressure, and therefore for increasing oxygen chemical potential, oxygen interstitials are more easily introduced into the MgO lattice. Under the conditions shown, the formation of a neutral oxygen interstitial is preferred over the formation of a neutral oxygen vacancy.

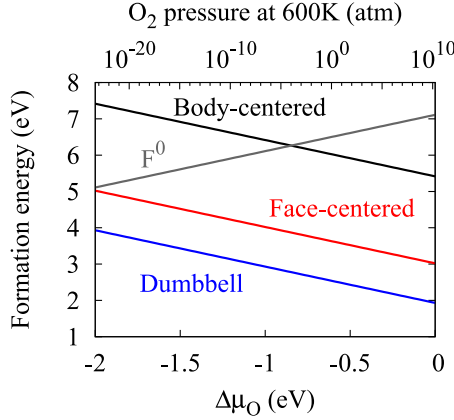


Figure A.3.: Formation energies for interstitials and oxygen vacancy as a function of oxygen chemical potential and O_2 pressure at $T = 600$ K. All defects are charge neutral.

A.2. Convergence tests for periodic systems

Formation energies for oxygen vacancies in periodic bulk and surface systems were calculated in this work with a k -grid of $4 \times 4 \times 4$, *tight* integration grids, a *tier 1* basis for magnesium and *tier 2* for oxygen, where convergence within 0.1 eV is reached for all defect charge states. For the most severe case, the oxygen vacancy in charge state 2+, the convergence tests are shown in Fig. A.4 for the bulk defect. (The convergence behavior for the surface F_s^{2+} center is equivalent.)

Basis functions are constructed in analogy with the following examples.

hydro 2 p 1.8: Hydrogen-like function of 2p type with an effective ionic charge $Z=1.8$.

ionic 3 d auto for Mg: 3d function of the Mg^{2+} ion (always doubly positively charged ion of corresponding element), where the onset radius of the confinement potential is chosen automatically to equal the one specified for the radial function equation.

For each radial function there are corresponding $(2l + 1)$ angular functions.

Basis functions are grouped into tiers, mostly ordered into successive angular momentum shells, based on an iterative basis construction process described in Ref. [99]. Energy convergence with respect to basis set can be achieved by successively adding tiers or single basis functions.

From *light* over *tight* to *safe/really tight* settings, parameters controlling the angular momentum expansion of the atom-centered charge density multipole for the electrostatic potential, the confinement potential for the basis functions, and the grid mesh used for radial and angular integration are altered for increasing accuracy. For details see Ref. [99] and manual that is distributed with the code.

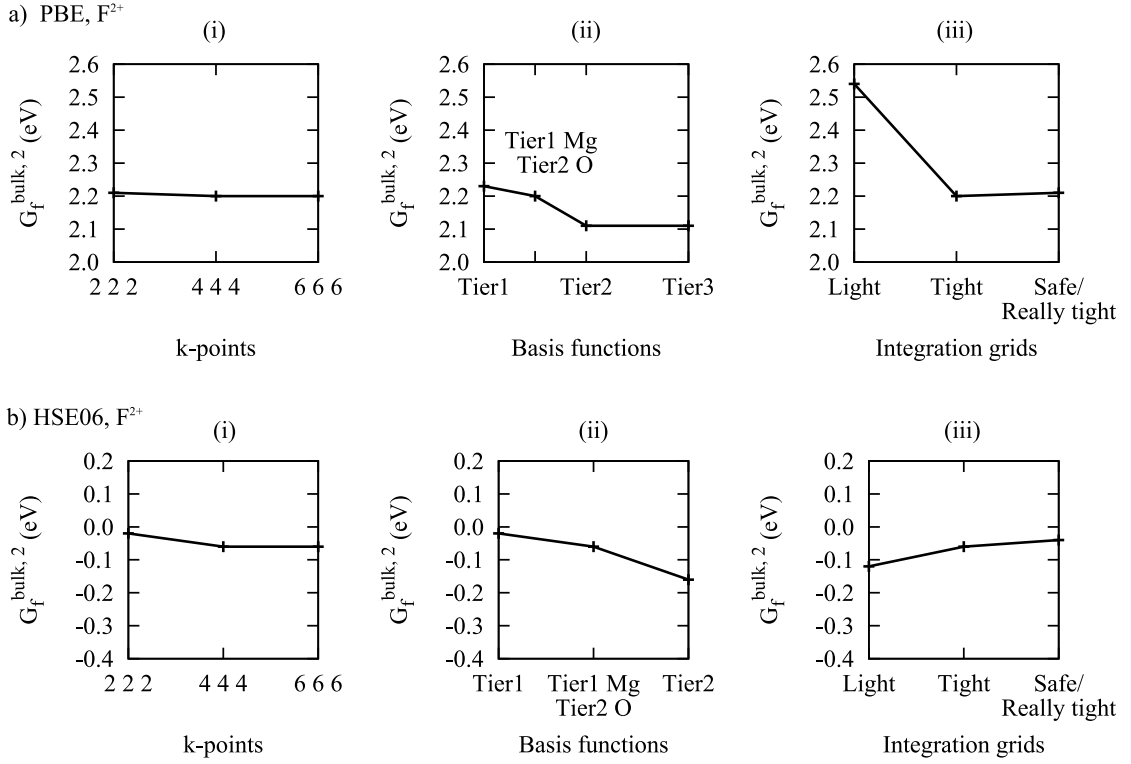


Figure A.4: Convergence of formation energy $G_f^{\text{bulk},2}$ for a bulk F^{2+} center in a 64-atom supercell in the oxygen-rich limit, neglecting vibrational energy contributions, for a) PBE and b) HSE06 exchange-correlation functional, calculated with FHI-aims. The Fermi level is at VBM. (i) Convergence with k-points. *Tight* grids with a *tier 1* basis for magnesium and *tier 2* for oxygen were used. (ii) Convergence with basis sets. *Tight* integration grids and a $4 \times 4 \times 4$ k-point mesh were used. (iii) Convergence with integration grid mesh. A $4 \times 4 \times 4$ k-point mesh and a *tier 1* basis for magnesium and *tier 2* for oxygen were used.

Table A.1.: Standard numerical atom-centered orbital basis for hydrogen, lithium, oxygen, and magnesium, as distributed with FHI-aims [99].

	H	Li	O	Mg
Minimal	1s	[He]2s	[He]2s2p	[Ne] 3s
Tier 1	hydro 2 s 2.1 hydro 2 p 3.5	hydro 2 p 1.6 hydro 2 s 2 hydro 3 d 2.6	hydro 2 p 1.8 hydro 3 d 7.6 hydro 3 s 6.4	hydro 2 p 1.5 ionic 3 d auto hydro 3 s 2.4
Tier 2	hydro 1 s 0.85 hydro 2 p 3.7 hydro 2 s 1.2 hydro 3 d 7	hydro 3 p 4.6 hydro 2 p 1.8 hydro 3 s 6.2 hydro 4 d 4.7	hydro 4 f 11.6 hydro 3 p 6.2 hydro 3 d 5.6 hydro 5 g 17.6	hydro 4 f 4.3 hydro 2 p 3.4 hydro 4 s 11.2 hydro 3 d 6.2
Tier 3	hydro 4 f 11.2 hydro 3 p 4.8 hydro 4 d 9 hydro 3 s 3.2	hydro 4 d 0.95 hydro 3 p 6.2 hydro 3 s 1.7	ionic 2 p auto hydro 4 f 10.8 hydro 4 d 4.7 hydro 2 s 6.8	hydro 2 s 0.6 hydro 3 p 4.8 hydro 4 f 7.4 hydro 5 g 6.6 hydro 2 p 1.6 hydro 3 d 1.8
Tier 4			hydro 3 p 5 hydro 3 s 3.3 hydro 5 g 15.6 hydro 4 f 17.6 hydro 4 d 14	hydro 4 p 0.45 hydro 5 g 10.4 hydro 2 s 12.4 hydro 4 d 1.7

A.3. MgO lattice-parameter optimization

Optimized lattice parameters for different exchange-correlation functionals were obtained calculating the cohesive energy of MgO using simple cubic unitcells (8 atoms) for varying lattice parameters and performing a least-squares fit of the energies versus unit cell volume by the Birch-Murnaghan equation of state [245, 246]. As an example, the fit is shown for HSE06 in Fig. A.5. Optimized lattice constants for different functionals are summarized in table A.2.

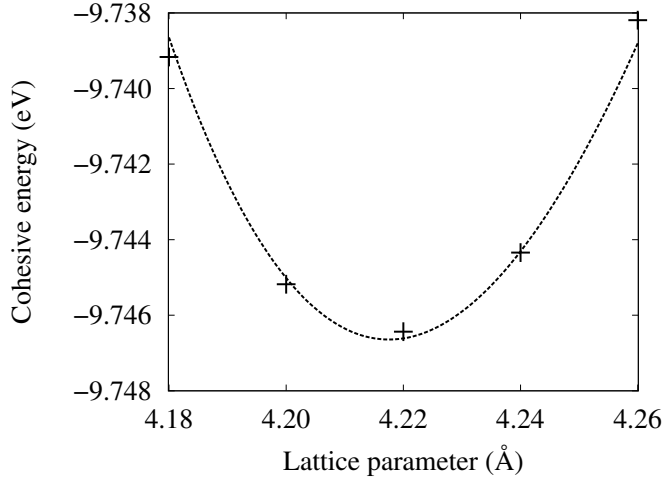


Figure A.5.: Cohesive energy of MgO as a function of lattice constant for HSE06, obtained as a fit by the Birch-Murnaghan equation of state. Total-energy calculations were performed with FHI-aims, using the *tight* predefined grids and basis settings.

Table A.2.: Optimized MgO lattice constants (Å) for different exchange-correlation functionals. Total energy calculations were performed with FHI-aims.

HF	PW-LDA	PBE	HSE06	PBE0	B3LYP
4.185	4.165	4.258	4.217	4.212	4.235

A.4. Convergence tests and BSSE corrections for cluster calculations

An unrelaxed Mg_6O_9 embedded cluster model was used to find the opt-HSE functional for calculating F centers in MgO. Embedding pseudopotentials (compare Fig. 6.7) and point charges were employed. For calculations with FHI-aims a finite set of embedding point charges was used. To insure convergence with respect to embedding conditions, the formation energy of the

neutral F center (formed in the center of the cluster) was calculated for increasing shells of embedding point charges. This was performed for two different embedding geometries, spherical and cubic. Fig. A.6 shows that the formation energy converges fast with respect to the number of embedding shells and that the formation energy does not depend on the embedding geometry. The calculations were performed using PBE exchange-correlation treatment.

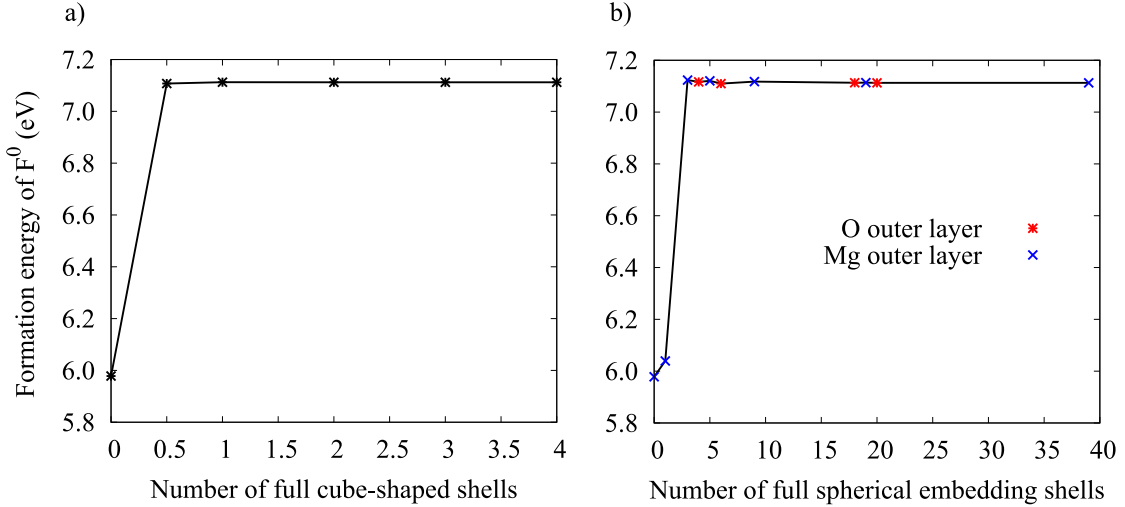


Figure A.6.: Convergence of formation energy G_f^0 for F^0 in eV with respect to number of point charge embedding shells, calculated with PBE, basis set superposition error has been removed. a) cube-shaped embedding , b) spherical embedding

For comparison, the formation energies of the F^0 center, as calculated with different methods using the embedded Mg_6O_9 cluster, are shown in Table A.3. A *tier 3* basis set was used for all atoms in calculations with FHI-aims, where G_f^0 is converged within 0.05 eV for all methods shown. TURBOMOLE calculations were performed by S. Sicolo (Humboldt University Berlin). All formation energies were corrected for the basis set superposition error (BSSE) using the Boys-Bernardi counterpoise correction [198]. The BSSE may arise due to the incompleteness of the atom centered orbital basis sets used in the calculations [99, 103, 198, 247]. Depending on the geometric structure and the basis set used, overlap of basis functions can improve the computed total energy of a system. When energy differences between systems with different numbers of atoms or different atomic arrangements are considered, this may lead to an error, since the superposition of wave functions is not the same for the different atomic configurations. For the defect formation energy G_f^0 three systems are calculated – the cluster without defect, the cluster with defect, and a bare oxygen atom. For example, in the full cluster the atoms adjacent to the central oxygen atom might profit from its basis functions, while this is not the case, when the central oxygen atom is removed in the cluster with a defect. The BSSE corrections as obtained with FHI-aims for the vertical formation energies G_f^0 for an F^0 center, calculated in the embedded Mg_6O_9 cluster, are shown in Table A.4. In general, the BSSE for GGA and hybrid functional ground state energies is small when computed with FHI-aims, due to the construction of numeric atom-centered basis sets, where the total energy of a free non-spinpolarized atom is

already converged at the minimum basis set level [99]. For explicitly correlated methods also unoccupied orbitals are needed (see Sec. 2), so that the BSSE becomes severe [103]. Using the counterpoise correction method, the BSSE can be obtained and corrected for ($G_f^0 \rightarrow G_f^0 + \Delta^{CP}(G_f^0)$) by computing the system fragments, here the cluster with a defect $E_{F^0}^{CP}$ and the bare oxygen atom, $E_{O\text{ atom}}^{CP}$, with the same basis functions that are used in the full system (here the pristine cluster) [198],

$$\Delta^{CP}(G_f^0) = E_{F^0}^{CP} + E_{O\text{ atom}}^{CP} - (E_{F^0} + E_{O\text{ atom}}).$$

Indeed, as shown in Table A.4, the absolute values of the BSSE corrections to the formation energies G_f^0 are negligible (<0.04 eV) for the GGA functional PBE, and the hybrid functionals HSE06, PBE0, and B3LYP, while for the explicitly correlated methods MP2 and RPA they are as large as 1.71 eV and 2.75 eV, respectively. For all cluster calculations in this work, BSSE-corrected energies were used for consistency when comparing different methods and formation energies calculated with different codes. In general, the BSSE also concerns periodic calculations. Since based on the cluster results its absolute value is assumed to be < 0.04 eV for the GGA and hybrid DFT defect formation energy calculations performed in this work, it was neglected in these calculations.

Table A.3.: Vertical formation energies G_f^0 for F^0 in eV, as obtained from embedded Mg_6O_9 cluster calculations (incl. BSSE corrections).

Code	PBE	HSE06	PBE0	B3LYP	MP2	RPA	CCSD(T) @PBE
TURBO-	7.18	–	7.02	7.37	–	–	7.09
MOLE							
FHI-aims	7.11	7.03	6.99	7.35	8.05	7.13	–

Table A.4.: Basis set superposition corrections $\Delta_{G_f^0}^{CP}$ in eV, as obtained from embedded Mg_6O_9 cluster calculations with FHI-aims (see text), using *tier 3* basis sets and *really tight/safe* grid settings.

PBE	HSE06	PBE0	B3LYP	MP2	RPA@PBE
-0.03	-0.03	-0.03	-0.04	-1.71	-2.75

Bibliography

- [1] Z. Zhan, J. Chen, S. Guan, L. Si, and P. Zhang, “Highly sensitive and thermal stable CO gas sensor based on SnO₂ modified by SiO₂,” *J. Nanosci. Nanotechnol.*, vol. 13, no. 2, pp. 1507–1510, 2013. [1](#)
- [2] T. H. Maiman, “Stimulated optical radiation in ruby,” *Nature*, vol. 187, pp. 493–494, 1960. [1](#)
- [3] S. Kumar, N. K. Verma, and M. L. Singla, “Study on reflectivity and photostability of Al-doped TiO₂ nanoparticles and their reflectors,” *J. Mater. Res.*, vol. 28, no. 03, pp. 521–528, 2013. [1](#)
- [4] M. A. El-Gammal, A. M. El-Alfy, and N. M. Mohamed, “Using magnesium oxide wall-board as an alternative building façade cladding material in modern cairo buildings,” *J. Appl. Sci. Res.*, vol. 8, no. 4, pp. 2024–2032, 2012. [1](#)
- [5] M. A. Mitchnick, D. Fairhurst, and S. R. Pinnell, “Microfine zinc oxide (Z-Cote) as a photostable UVA/UVB sunblock agent,” *J. Am. Acad. Dermatol.*, vol. 40, pp. 85–90, 1999. [1](#)
- [6] H. Jiang, J. Ma, and C. Li, “Mesoporous carbon incorporated metal oxide nanomaterials as supercapacitor electrodes,” *Adv. Mater.*, vol. 24, no. 30, p. 4196, 2012. [1](#)
- [7] A. Fujishima and K. Honda, “Electrochemical photolysis of water at a semiconductor electrode,” *Nature*, vol. 238, pp. 37–38, 1972. [1](#)
- [8] A. Fujishima, T. N. Rao, and D. A. Tryk, “Titanium dioxide photocatalysis,” *J. Photochem. Photobiol. C: Photochem. Rev.*, vol. 1, pp. 1–21, 2000. [1](#)
- [9] S. U. M. Khan, M. Al-Shahry, and W. B. Ingler, “Efficient photochemical water splitting by a chemically modified n-TiO₂,” *Science*, vol. 297, pp. 2243–2245, 2002. [1](#)
- [10] M. Ni, M. K. Leung, D. Y. Leung, and K. Sumathy, “A review and recent developments in photocatalytic water-splitting using for hydrogen production,” *Renew. Sust. Energ. Rev.*, vol. 11, pp. 401–425, 2007. [1](#)
- [11] T. Ito and J. H. Lunsford, “Synthesis of ethylene and ethane by partial oxidation of methane over lithium-doped magnesium oxide,” *Nature*, vol. 314, pp. 721–722, 1985. [1, 54](#)
- [12] T. Ito, J. Wang, C. H. Lin, and J. H. Lunsford, “Oxidative dimerization of methane over a lithium-promoted magnesium oxide catalyst,” *J. Am. Chem. Soc.*, vol. 107, pp. 5062–5068, 1985. [1, 54](#)

- [13] E. Iwamatsu, T. Moriyama, N. Takasaki, and K. Aika, “Oxidative coupling of methane over Na^+ - and Rb^+ -doped MgO catalysts,” *J. Catal.*, vol. 113, pp. 25–35, 1988. [1](#)
- [14] V. Sokolovskii, S. Aliev, O. Buyevskaya, and A. Davydov, “Type of hydrocarbon activation and nature of active sites of base catalysts in methane oxidative dehydromerization,” *Catal. Today*, vol. 4, pp. 293–300, 1989. [1](#)
- [15] G. J. Hutchings, M. S. Scurrell, and J. Woodhouse, “Oxidative coupling of methane using Li/MgO catalyst: Re-appraisal of the optimum loading of Li ,” *Catal. Lett.*, vol. 5, pp. 301–308, 1990. [1](#)
- [16] V. R. Choudhary, V. H. Rane, and S. T. Chaudhari, “Influence of various promoters on the basicity and catalytic activity of MgO catalysts in oxidative coupling of methane,” *Catal. Lett.*, vol. 6, pp. 95–98, 1990. [1](#)
- [17] G. Hoogendam, K. Seshan, J. van Ommen, and J. Ross, “Oxidative coupling of methane over doped Li/MgO catalysts,” *Catal. Today*, vol. 21, pp. 333–340, 1994. [1](#)
- [18] R. Nibbelke, J. Scheerova, M. Decroon, and G. Marin, “The oxidative coupling of methane over MgO -based catalysts: A steady-state isotope transient kinetic analysis,” *J. Catal.*, vol. 156, pp. 106–119, 1995. [1](#)
- [19] R. L. P. Goncalves, F. C. Muniz, F. B. Passos, and M. Schmal, “Promoting effect of Ce on the oxidative coupling of methane catalysts,” *Catal. Lett.*, vol. 135, pp. 26–32, 2010. [1](#)
- [20] L. Tang, D. Yamaguchi, L. Wong, N. Burke, and K. Chiang, “The promoting effect of ceria on Li/MgO catalysts for the oxidative coupling of methane,” *Catal. Today*, vol. 178, pp. 172–180, 2011. [1](#)
- [21] K. Langfeld, B. Frank, V. E. Strempel, C. Berger-Karin, G. Weinberg, E. V. Kondratenko, and R. Schomäcker, “Comparison of oxidizing agents for the oxidative coupling of methane over state-of-the-art catalysts,” *Appl. Catal. A*, vol. 417–418, pp. 145–152, 2012. [1](#)
- [22] Q. Wu and R. van de Krol, “Selective photoreduction of nitric oxide to nitrogen by nanosstructured TiO_2 photocatalysts: Role of oxygen vacancies and iron dopant,” *J. Am. Chem. Soc.*, vol. 134, pp. 9369–9375, 2012. [1](#)
- [23] G. Makov and M. C. Payne, “Periodic boundary conditions in ab initio calculations,” *Phys. Rev. B*, vol. 51, pp. 4014–4022, 1995. [2](#), [40](#)
- [24] C. Weinert and M. Scheffler, “Chalcogen and vacancy pairs in silicon: Electronic structure and stabilities,” *Mater. Sci. Forum*, vol. 10–12, pp. 25–30, 1986. [2](#), [37](#)
- [25] J. Rogal and K. Reuter, *Ab Initio Atomistic Thermodynamics for Surfaces: A Primer*. Neuilly-sur-Seine, 2007. [2](#), [37](#)
- [26] L. A. Kappers, R. L. Kroes, and E. B. Hensley, “ F^+ and F' centers in magnesium oxide,” *Phys. Rev. B*, vol. 1, pp. 4151–4157, 1970. [2](#), [51](#), [54](#), [56](#), [57](#), [58](#), [60](#), [63](#), [78](#), [112](#)

- [27] L. Kantorovich, J. Holender, and M. Gillan, “The energetics and electronic structure of defective and irregular surfaces on MgO,” *Surf. Sci.*, vol. 343, pp. 221–239, 1995. [2](#), [54](#), [58](#), [59](#), [84](#), [116](#), [117](#)
- [28] Z. Yang, R. Wu, Q. Zhang, and D. W. Goodman, “Adsorption of Au on an O-deficient MgO(001) surface,” *Phys. Rev. B*, vol. 65, p. 155407, 2002. [2](#), [58](#), [59](#)
- [29] J. Carrasco, N. Lopez, and F. Illas, “First principles analysis of the stability and diffusion of oxygen vacancies in metal oxides,” *Phys. Rev. Lett.*, vol. 93, p. 225502, 2004. [2](#), [58](#), [59](#)
- [30] E. Scorza, U. Birkenheuer, and C. Pisani, “The oxygen vacancy at the surface and in bulk MgO: an embedded-cluster study,” *J. Chem. Phys.*, vol. 107, pp. 9645–9658, 1997. [2](#), [54](#), [58](#), [59](#), [73](#), [82](#), [84](#), [86](#)
- [31] J.-L. Dubois and C. J. Cameron, “Common features of oxidative coupling of methane cofeed catalysts,” *Appl. Catal.*, vol. 67, no. 1, pp. 49–71, 1990. [3](#), [54](#)
- [32] I. Balint and K.-i. Aika, “Specific defect sites creation by doping MgO with lithium and titanium,” *Applied Surf. Sci.*, vol. 173, pp. 296–306, 2001. [3](#), [54](#), [56](#), [91](#), [95](#)
- [33] M. Born and R. Oppenheimer, “Zur Quantentheorie der Moleküle,” *Ann. Phys.*, vol. 389, pp. 457–484, 1927. [6](#)
- [34] H. Hellmann, “Zur Rolle der kinetischen Elektronenenergie für die zwischenatomaren Kräfte,” *Z. Phys. A - Hadron Nucl.*, vol. 85, no. 3, pp. 180–190, 1933. [7](#)
- [35] D. R. Hartree, “The wave mechanics of an atom with a non-Coulomb central field. Part I. Theory and methods,” *Math. Proc. Cambridge Philos. Soc.*, vol. 24, no. 01, pp. 89–110, 1928. [8](#)
- [36] W. Ritz, “Über eine neue Methode zur Lösung gewisser Variationsprobleme der mathematischen Physik.,” *J. reine angew. Math.*, no. 135, pp. 1–61, 1909. [8](#)
- [37] P. Hohenberg and W. Kohn, “Inhomogeneous electron gas,” *Phys. Rev.*, vol. 136, pp. B864–B871, 1964. [9](#)
- [38] L. H. Thomas, “The calculation of atomic fields,” *Math. Proc. Cambridge Philos. Soc.*, vol. 23, no. 05, pp. 542–548, 1927. [9](#)
- [39] E. Fermi, “Eine statistische Methode zur Bestimmung einiger Eigenschaften des Atoms und ihre Anwendung auf die Theorie des periodischen Systems der Elemente,” *Z. Phys.*, vol. 48, pp. 73–79, 1928. [9](#)
- [40] E. K. U. Gross and R. M. Dreizler, *Density Functional Theory*. Springer, 1995. [10](#)
- [41] M. Levy, “Universal variational functionals of electron densities, first-order density matrices, and natural spin-orbitals and solution of the ν -representability problem,” *Proc. Natl. Acad. Sci.*, vol. 76, pp. 6062–6065, 1979. [10](#)

-
- [42] W. Kohn and L. J. Sham, “Self-consistent equations including exchange and correlation effects,” *Phys. Rev.*, vol. 140, pp. A1133–A1138, 1965. [10](#), [12](#)
 - [43] M. Levy, J. P. Perdew, and V. Sahni, “Exact differential equation for the density and ionization energy of a many-particle system,” *Phys. Rev. A*, vol. 30, pp. 2745–2748, 1984. [12](#)
 - [44] C.-O. Almbladh and U. von Barth, “Exact results for the charge and spin densities, exchange-correlation potentials, and density-functional eigenvalues,” *Phys. Rev. B*, vol. 31, pp. 3231–3244, 1985. [12](#)
 - [45] J. F. Janak, “Proof that $\partial E/\partial n_i = \varepsilon$ in density-functional theory,” *Phys. Rev. B*, vol. 18, pp. 7165–7168, 1978. [12](#), [75](#)
 - [46] T. Koopmans, “Über die Zuordnung von Wellenfunktionen und Eigenwerten zu den einzelnen Elektronen eines Atoms,” *Physica*, vol. 1, no. 1–6, pp. 104–113, 1934. [12](#)
 - [47] J. C. Slater, *Quantum Theory of Molecules and Solids Vol. 4: The Self-Consistent Field for Molecules and Solids*. International Series in Pure and Applied Physics, New York: McGraw-Hill, 1 ed., 1974. [12](#), [75](#)
 - [48] P. A. M. Dirac, “Note on exchange phenomena in the Thomas atom,” *Math. Proc. Cambridge*, vol. 26, no. 03, pp. 376–385, 1930. [12](#)
 - [49] D. M. Ceperley and B. J. Alder, “Ground state of the electron gas by a stochastic method,” *Phys. Rev. Lett.*, vol. 45, pp. 566–569, 1980. [12](#)
 - [50] J. P. Perdew and Y. Wang, “Accurate and simple analytic representation of the electron-gas correlation energy,” *Phys. Rev. B*, vol. 45, pp. 13244–13249, 1992. [12](#), [32](#), [38](#)
 - [51] R. O. Jones and O. Gunnarsson, “The density functional formalism, its applications and prospects,” *Rev. Mod. Phys.*, vol. 61, pp. 689–746, 1989. [12](#), [17](#)
 - [52] J. P. Perdew, K. Burke, and M. Ernzerhof, “Generalized gradient approximation made simple,” *Phys. Rev. Lett.*, vol. 77, pp. 3865–3868, 1996. [13](#), [38](#)
 - [53] E. H. Lieb and S. Oxford, “Improved lower bound on the indirect Coulomb energy,” *Int. J. Quantum Chem.*, vol. 19, no. 3, pp. 427–439, 1981. [13](#)
 - [54] V. N. Staroverov, G. E. Scuseria, J. Tao, and J. P. Perdew, “Tests of a ladder of density functionals for bulk solids and surfaces,” *Phys. Rev. B*, vol. 69, p. 075102, 2004. [13](#)
 - [55] F. Tran, R. Laskowski, P. Blaha, and K. Schwarz, “Performance on molecules, surfaces, and solids of the Wu-Cohen GGA exchange-correlation energy functional,” *Phys. Rev. B*, vol. 75, p. 115131, 2007. [13](#)
 - [56] V. N. Staroverov, G. E. Scuseria, J. Tao, and J. P. Perdew, “Erratum: Tests of a ladder of density functionals for bulk solids and surfaces [Phys. Rev. B 69, 075102 (2004)],” *Phys. Rev. B*, vol. 78, p. 239907, 2008. [13](#)

-
- [57] W. Koch and M. C. Holthausen, *A Chemist's Guide to Density Functional Theory*. John Wiley & Sons, 2000. [13](#)
 - [58] A. D. Becke, “A new mixing of Hartree–Fock and local density-functional theories,” *J. Chem. Phys.*, vol. 98, pp. 1372–1377, 1993. [14](#)
 - [59] A. D. Becke, “Density-functional thermochemistry. III. The role of exact exchange,” *J. Chem. Phys.*, vol. 98, pp. 5648–5652, 1993. [14](#)
 - [60] H. J. Monkhorst, “Hartree-Fock density of states for extended systems,” *Phys. Rev. B*, vol. 20, pp. 1504–1513, 1979. [14](#)
 - [61] J. Delhalle and J.-L. Calais, “Direct-space analysis of the Hartree-Fock energy bands and density of states for metallic extended systems,” *Phys. Rev. B*, vol. 35, pp. 9460–9466, 1987. [14](#)
 - [62] J. Paier, M. Marsman, and G. Kresse, “Why does the B3LYP hybrid functional fail for metals?,” *J. Chem. Phys.*, vol. 127, p. 024103, 2007. [14](#)
 - [63] J. Heyd, G. E. Scuseria, and M. Ernzerhof, “Hybrid functionals based on a screened Coulomb potential,” *J. Chem. Phys.*, vol. 118, pp. 8207–8215, 2003. [14](#)
 - [64] J. P. Perdew, M. Ernzerhof, and K. Burke, “Rationale for mixing exact exchange with density functional approximations,” *J. Chem. Phys.*, vol. 105, pp. 9982–9985, 1996. [14](#)
 - [65] A. V. Krukau, O. A. Vydrov, A. F. Izmaylov, and G. E. Scuseria, “Influence of the exchange screening parameter on the performance of screened hybrid functionals,” *J. Chem. Phys.*, vol. 125, p. 224106, 2006. [14](#)
 - [66] K. Kim and K. D. Jordan, “Comparison of density functional and MP2 calculations on the water monomer and dimer,” *J. Phys. Chem.*, vol. 98, pp. 10089–10094, 1994. [15](#)
 - [67] C. Møller and M. S. Plesset, “Note on an approximation treatment for many-electron systems,” *Phys. Rev.*, vol. 46, pp. 618–622, 1934. [16](#)
 - [68] A. Szabo and N. S. Ostlund, *Modern Quantum Chemistry: Introduction to Advanced Electronic Structure Theory*. Courier Dover Publications, 1989. [16](#)
 - [69] D. Bohm and D. Pines, “A collective description of electron interactions. I. Magnetic interactions,” *Phys. Rev.*, vol. 82, pp. 625–634, 1951. [16](#)
 - [70] D. Pines and D. Bohm, “A collective description of electron interactions: II. Collective vs individual particle aspects of the interactions,” *Phys. Rev.*, vol. 85, pp. 338–353, 1952. [16](#)
 - [71] D. Bohm and D. Pines, “A collective description of electron interactions: III. Coulomb interactions in a degenerate electron gas,” *Phys. Rev.*, vol. 92, pp. 609–625, 1953. [16](#)
 - [72] X. Ren, P. Rinke, C. Joas, and M. Scheffler, “Random-phase approximation and its applications in computational chemistry and materials science,” *J. Mater. Sci.*, vol. 47, pp. 7447–7471, 2012. [16, 64](#)

- [73] D. Langreth and J. Perdew, “The exchange-correlation energy of a metallic surface,” *Solid State Commun.*, vol. 17, pp. 1425–1429, 1975. [16](#)
- [74] O. Gunnarsson and B. I. Lundqvist, “Exchange and correlation in atoms, molecules, and solids by the spin-density-functional formalism,” *Phys. Rev. B*, vol. 13, pp. 4274–4298, 1976. [16](#)
- [75] D. C. Langreth and J. P. Perdew, “Exchange-correlation energy of a metallic surface: Wave-vector analysis,” *Phys. Rev. B*, vol. 15, pp. 2884–2901, 1977. [16](#)
- [76] R. Kubo, “The fluctuation-dissipation theorem,” *Rep. Prog. Phys.*, vol. 29, no. 1, pp. 255–284, 1966. [17](#)
- [77] F. Furche, “Molecular tests of the random phase approximation to the exchange-correlation energy functional,” *Phys. Rev. B*, vol. 64, p. 195120, 2001. [17](#)
- [78] J. Harl and G. Kresse, “Accurate bulk properties from approximate many-body techniques,” *Phys. Rev. Lett.*, vol. 103, p. 056401, 2009. [17](#)
- [79] X. Ren, A. Tkatchenko, P. Rinke, and M. Scheffler, “Beyond the random-phase approximation for the electron correlation energy: The importance of single excitations,” *Phys. Rev. Lett.*, vol. 106, p. 153003, 2011. [17](#)
- [80] K. S. Singwi, M. P. Tosi, R. H. Land, and A. Sjölander, “Electron correlations at metallic densities,” *Phys. Rev.*, vol. 176, pp. 589–599, 1968. [17](#)
- [81] A. L. Fetter and J. D. Walecka, *Quantum Theory of Many-Particle Systems*. Courier Dover Publications, 1971. [18](#)
- [82] A. A. Abrikosov and L. P. Gorkov, *Methods of Quantum Field Theory in Statistical Physics*. Courier Dover Publications, 1975. [18](#)
- [83] L. Hedin, “New method for calculating the one-particle Green’s function with application to the electron-gas problem,” *Phys. Rev.*, vol. 139, pp. A796–A823, 1965. [18](#)
- [84] W. G. Aulbur, L. Jönsson, and J. W. Wilkins, “Quasiparticle calculations in solids,” in *Solid State Physics* (Henry Ehrenreich and Frans Spaepen, eds.), vol. 54, pp. 1–218, Academic Press, 1999. [18](#)
- [85] G. Onida, L. Reining, and A. Rubio, “Electronic excitations: Density-functional versus many-body Green’s-function approaches,” *Rev. Mod. Phys.*, vol. 74, pp. 601–659, 2002. [18](#)
- [86] V. Galitskii and A. Migdal, “Application of quantum field theory methods to the many body problem,” *Sov. Phys. JETP*, vol. 7, no. 96, 1958. [18](#)
- [87] J. M. Luttinger and J. C. Ward, “Ground-state energy of a many-fermion system. II,” *Phys. Rev.*, vol. 118, pp. 1417–1427, 1960. [18](#)

-
- [88] A. Klein, “Perturbation theory for an infinite medium of fermions. II,” *Phys. Rev.*, vol. 121, pp. 950–956, 1961. [18](#)
 - [89] F. Fuchs, J. Furthmüller, F. Bechstedt, M. Shishkin, and G. Kresse, “Quasiparticle band structure based on a generalized Kohn–Sham scheme,” *Phys. Rev. B*, vol. 76, p. 115109, 2007. [18](#)
 - [90] T. Körzdörfer and N. Marom, “Strategy for finding a reliable starting point for G_0W_0 demonstrated for molecules,” *Phys. Rev. B*, vol. 86, p. 041110, 2012. [18](#)
 - [91] P. Rinke, A. Qteish, J. Neugebauer, and M. Scheffler, “Exciting prospects for solids: Exact-exchange based functionals meet quasiparticle energy calculations,” *Phys. Status Solidi B*, vol. 245, no. 5, pp. 929–945, 2008. [18](#)
 - [92] I. Shavitt, *Methods of Electronic Structure Theory (Modern theoretical chemistry)*. Springer, 1977. [19](#)
 - [93] F. Coester and H. Kümmel, “Short-range correlations in nuclear wave functions,” *Nucl. Phys.*, vol. 17, pp. 477–485, 1960. [19](#)
 - [94] J. Cizek, “On the correlation problem in atomic and molecular systems. Calculation of wavefunction components in Ursell-type expansion using quantum-field theoretical methods,” *J. Chem. Phys.*, vol. 45, pp. 4256–4266, 1966. [19](#)
 - [95] M. Valiev, E. Bylaska, N. Govind, K. Kowalski, T. Straatsma, H. Van Dam, D. Wang, J. Nieplocha, E. Apra, T. Windus, and W. de Jong, “NWChem: a comprehensive and scalable open-source solution for large scale molecular simulations,” *Comput. Phys. Comm.*, vol. 181, pp. 1477–1489, 2010. [21](#)
 - [96] *TURBOMOLE V6.3 2011, a development of University of Karlsruhe and Forschungszentrum Karlsruhe GmbH, 1989-2007, TURBOMOLE GmbH, since 2007*. [21, 62](#)
 - [97] B. Delley, “An all-electron numerical method for solving the local density functional for polyatomic molecules,” *J. Chem. Phys.*, vol. 92, pp. 508–517, 1990. [21](#)
 - [98] B. Delley, “From molecules to solids with the DMol³ approach,” *J. Chem. Phys.*, vol. 113, pp. 7756–7764, 2000. [21](#)
 - [99] V. Blum, R. Gehrke, F. Hanke, P. Havu, V. Havu, X. Ren, K. Reuter, and M. Scheffler, “Ab initio molecular simulations with numeric atom-centered orbitals,” *Comput. Phys. Commun.*, vol. 180, pp. 2175–2196, 2009. [21, 123, 125, 127, 128](#)
 - [100] V. Lebedev and D. Laikov, “A quadrature formula for the sphere of the 131st algebraic order of accuracy,” *Dokl. Math.*, vol. 59, no. 3, pp. 477–481, 1999. [21](#)
 - [101] P. P. Ewald, “Die Berechnung optischer und elektrostatischer Gitterpotentiale,” *Ann. Phys.*, vol. 369, no. 3, pp. 253–287, 1921. [21, 26](#)

-
- [102] B. Delley, “Fast calculation of electrostatics in crystals and large molecules,” *J. Phys. Chem.*, vol. 100, pp. 6107–6110, 1996. [21](#)
 - [103] X. Ren, P. Rinke, V. Blum, J. Wieferink, A. Tkatchenko, A. Sanfilippo, K. Reuter, and M. Scheffler, “Resolution-of-identity approach to Hartree–Fock, hybrid density functionals, RPA, MP2 and GW with numeric atom-centered orbital basis functions,” *New J. Phys.*, vol. 14, p. 053020, 2012. [22](#), [127](#), [128](#)
 - [104] P. Pulay, “Ab initio calculation of force constants and equilibrium geometries in polyatomic molecules,” *Mol. Phys.*, vol. 18, no. 4, pp. 473–480, 1970. [22](#)
 - [105] R. Gehrke, *First-principles basin-hopping for the structure determination of atomic clusters*. PhD thesis, Freie Universität Berlin, 2009. [22](#)
 - [106] T. Bredow, G. Geudtner, and K. Jug, “Development of the cyclic cluster approach for ionic systems,” *J. Comput. Chem.*, vol. 22, no. 1, pp. 89–101, 2001. [23](#)
 - [107] G. A. Baraff and M. Schlüter, “Self-consistent Green’s-function calculation of the ideal Si vacancy,” *Phys. Rev. Lett.*, vol. 41, pp. 892–895, 1978. [23](#)
 - [108] J. Bernholc, N. O. Lipari, and S. T. Pantelides, “Self-consistent method for point defects in semiconductors: Application to the vacancy in silicon,” *Phys. Rev. Lett.*, vol. 41, pp. 895–899, 1978. [23](#)
 - [109] R. Zeller and P. H. Dederichs, “Electronic structure of impurities in Cu, calculated self-consistently by Korringa-Kohn-Rostoker Green’s-function method,” *Phys. Rev. Lett.*, vol. 42, pp. 1713–1716, 1979. [23](#)
 - [110] F. Beeler, O. K. Andersen, and M. Scheffler, “Theoretical evidence for low-spin ground states of early interstitial and late substitutional 3d transition-metal ions in silicon,” *Phys. Rev. Lett.*, vol. 55, pp. 1498–1501, 1985. [23](#)
 - [111] M. Scheffler, C. Droste, A. Fleszar, F. Máca, G. Wachutka, and G. Barzel, “A self-consistent surface-Green-function (SSGF) method,” *Physica B: Condensed Matter*, vol. 172, pp. 143–153, 1991. [23](#)
 - [112] P. V. Sushko, A. L. Shluger, and C. R. A. Catlow, “Relative energies of surface and defect states: *Ab initio* calculations for the MgO (001) surface,” *Surf. Sci.*, vol. 450, no. 3, pp. 153–170, 2000. [23](#), [54](#), [84](#), [86](#), [116](#), [117](#)
 - [113] R. S. Mulliken, “Electronic population analysis on LCAO MO molecular wave functions. I,” *J. Chem. Phys.*, vol. 23, pp. 1833–1840, 1955. [23](#)
 - [114] F. L. Hirshfeld, “Bonded-atom fragments for describing molecular charge densities,” *Theor. Chim. Acta*, vol. 44, pp. 129–138, 1977. [23](#), [77](#)
 - [115] F. Rittner, R. Fink, B. Boddenberg, and V. Staemmler, “Adsorption of nitrogen on rutile (110): Ab initio cluster calculations,” *Phys. Rev. B*, vol. 57, pp. 4160–4171, 1998. [23](#)

- [116] D. Stolt and C. Hättig, “Embedded cluster density functional and second-order Møller-Plesset perturbation theory study on the adsorption of N₂ on the rutile (110) surface,” *J. Chem. Phys.*, vol. 137, no. 11, p. 114705, 2012. [23](#)
- [117] M. J. Puska, S. Pöykkö, M. Pesola, and R. M. Nieminen, “Convergence of supercell calculations for point defects in semiconductors: Vacancy in silicon,” *Phys. Rev. B*, vol. 58, pp. 1318–1325, 1998. [25](#)
- [118] H.-P. Komsa and A. Pasquarello, “Finite-size supercell correction for charged defects at surfaces and interfaces,” *Phys. Rev. Lett.*, vol. 110, p. 095505, 2013. [26](#)
- [119] S. Lany and A. Zunger, “Accurate prediction of defect properties in density functional supercell calculations,” *Modell. Simul. Mater. Sci. Eng.*, vol. 17, no. 8, p. 084002, 2009. [27, 40](#)
- [120] A. Garcia and J. E. Northrup, “Compensation of p-type doping in ZnSe: the role of impurity-native defect complexes,” *Phys. Rev. Lett.*, vol. 74, p. 1131, 1995. [27](#)
- [121] S. B. Zhang and J. E. Northrup, “Chemical potential dependence of defect formation energies in GaAs: Application to Ga self-diffusion,” *Phys. Rev. Lett.*, vol. 67, p. 2339, 1991. [27](#)
- [122] J. Shim, E. Lee, Y. J. Lee, and R. M. Nieminen, “Density-functional calculations of defect formation energies using supercell methods: Defects in diamond,” *Phys. Rev. B*, vol. 71, p. 035206, 2005. [27, 40, 42](#)
- [123] A. Zywiertz, J. Furthmüller, and F. Bechstedt, “Vacancies in SiC: influence of Jahn-Teller distortions, spin effects, and crystal structure,” *Phys. Rev. B*, vol. 59, p. 15166, 1999. [27](#)
- [124] B. Li and H. Metiu, “DFT studies of oxygen vacancies on undoped and doped La₂O₃ surfaces,” *J. Phys. Chem. C*, vol. 114, pp. 12234–12244, 2010. [27, 95](#)
- [125] Z. Hu and H. Metiu, “Effect of dopants on the energy of oxygen-vacancy formation at the surface of ceria: Local or global?,” *J. Phys. Chem. C*, vol. 115, no. 36, pp. 17898–17909, 2011. [27, 95](#)
- [126] L. Vegard, “Die Konstitution der Mischkristalle und die Raumfüllung der Atome,” *Z. Phys.*, vol. 5, no. 1, pp. 17–26, 1921. [29, 112](#)
- [127] M. Scheffler, “Lattice relaxations at substitutional impurities in semiconductors,” *Physica B+C*, vol. 146, pp. 176–186, 1987. [29, 112](#)
- [128] N. J. Ramer and A. M. Rappe, “Application of a new virtual crystal approach for the study of disordered perovskites,” *J. Phys. Chem. Solids*, vol. 61, pp. 315–320, 2000. [29](#)
- [129] L. Bellaiche and D. Vanderbilt, “Virtual crystal approximation revisited: Application to dielectric and piezoelectric properties of perovskites,” *Phys. Rev. B*, vol. 61, p. 7877, 2000. [29](#)

-
- [130] D. Fritsch, H. Schmidt, and M. Grundmann, “Pseudopotential band structures of rocksalt MgO, ZnO, and $Mg_{1-x}Zn_xO$,” *Appl. Phys. Lett.*, vol. 88, no. 13, p. 134104, 2006. [29](#)
 - [131] M. Casarin, C. Maccato, and A. Vittadini, “Electronic structure of Nb impurities in and on TiO_2 ,” *Phys. Chem. Chem. Phys.*, vol. 1, pp. 3793–3799, 1999. [29](#)
 - [132] J. Sauer and M. Sierka, “Combining quantum mechanics and interatomic potential functions in ab initio studies of extended systems,” *J. Comput. Chem.*, vol. 21, no. 16, pp. 1470–1493, 2000. [29](#)
 - [133] E. Kaxiras, Y. Bar-Yam, J. D. Joannopoulos, and K. C. Pandey, “Ab initio theory of polar semiconductor surfaces. I. Methodology and the (2×2) reconstructions of GaAs(111),” *Phys. Rev. B*, vol. 35, no. 18, pp. 9625–9635, 1987. [37](#)
 - [134] M. Scheffler, “Thermodynamic aspects of bulk and surface defects,” *Stud. Surf. Sci. Catal.*, vol. 40, pp. 115–122, 1988. [37](#)
 - [135] K. Reuter, C. Stampfl, and M. Scheffler, “Ab initio thermodynamics and statistical mechanics of surface properties and functions,” in *Handbook of Materials Modeling, Part A. Methods* (S. Yip, ed.), Springer, 2005. [37](#)
 - [136] D. A. Mc Quarrie, *Statistical Mechanics*. Harper and Row, New York, 1976. [37](#)
 - [137] M. Ernzerhof, J. P. Perdew, and K. Burke, “Coupling-constant dependence of atomization energies,” *Int. J. Quantum Chem.*, vol. 64, no. 3, pp. 285–295, 1997. [38](#)
 - [138] A. Gross, *Theoretical Surface Science: A Microscopic Perspective*. Springer, 2009. [38](#)
 - [139] D. Feller and K. A. Peterson, “Re-examination of atomization energies for the Gaussian-2 set of molecules,” *J. Chem. Phys.*, vol. 110, no. 17, pp. 8384–8396, 1999. [38](#)
 - [140] D. Stull and P. H., *JANAF Thermochemical Tables, 2nd edn.* U.S. National Bureau of Standards, Washington, D.C., 1971. [38](#)
 - [141] N. W. Ashcroft and N. D. Mermin, *Solid State Physics*. CBS Publishing, Tokyo, 1981. [39](#)
 - [142] A. Togo, F. Oba, and I. Tanaka, “First-principles calculations of the ferroelastic transition between rutile-type and $CaCl_2$ -type SiO_2 at high pressures,” *Phys. Rev. B*, vol. 78, p. 134106, 2008. [39](#)
 - [143] M. Leslie and N. J. Gillan, “The energy and elastic dipole tensor of defects in ionic crystals calculated by the supercell method,” *J. Phys. C*, vol. 18, pp. 973–982, 1985. [40](#)
 - [144] J. Lento, J. Mozos, and R. Nieminen, “Charged point defects in semiconductors and the supercell approximation,” *J. Phys.: Condens. Mat.*, vol. 14, no. 10, pp. 2637–2645, 2002. [40](#)
 - [145] D. Segev and S. Wei, “Design of shallow donor levels in diamond by isovalent-donor coupling,” *Phys. Rev. Lett.*, vol. 91, no. 12, p. 126406, 2003. [40, 42](#)

- [146] C. G. Van de Walle, "First-principles calculations for defects and impurities: Applications to III-nitrides," *J. Appl. Phys.*, vol. 95, no. 8, p. 3851, 2004. [40](#)
- [147] P. A. Schultz, "Theory of defect levels and the "Band gap problem" in silicon," *Phys. Rev. Lett.*, vol. 96, p. 246401, 2006. [40](#)
- [148] C. W. M. Castleton, A. Höglund, and S. Mirbt, "Managing the supercell approximation for charged defects in semiconductors: Finite-size scaling, charge correction factors, the band-gap problem, and the ab initio dielectric constant," *Phys. Rev. B*, vol. 73, p. 035215, 2006. [40](#)
- [149] A. Janotti and C. Van de Walle, "Native point defects in ZnO," *Phys. Rev. B*, vol. 76, no. 16, p. 165202, 2007. [40](#)
- [150] C. Freysoldt, J. Neugebauer, and C. G. Van de Walle, "Fully ab initio finite-size corrections for charged-defect supercell calculations," *Phys. Rev. Lett.*, vol. 102, p. 016402, 2009. [40](#)
- [151] C. Freysoldt, J. Neugebauer, and C. G. Van de Walle, "Electrostatic interactions between charged defects in supercells," *Phys. Status Solidi B*, vol. 248, pp. 1067–1076, 2011. [40](#)
- [152] C. W. M. Castleton and S. Mirbt, "Finite-size scaling as a cure for supercell approximation errors in calculations of neutral native defects in InP," *Phys. Rev. B*, vol. 70, p. 195202, 2004. [42](#)
- [153] A. F. Wright and N. A. Modine, "Comparison of two methods for circumventing the Coulomb divergence in supercell calculations for charged point defects," *Phys. Rev. B*, vol. 74, p. 235209, 2006. [42](#)
- [154] S. Lany and A. Zunger, "Assessment of correction methods for the band-gap problem and for finite-size effects in supercell defect calculations: Case studies for ZnO and GaAs," *Phys. Rev. B*, vol. 78, p. 235104, 2008. [42](#)
- [155] S. B. Zhang, S. Wei, and A. Zunger, "Intrinsic n-type versus p-type doping asymmetry and the defect physics of ZnO," *Phys. Rev. B*, vol. 63, p. 075205, 2001. [42](#)
- [156] T. R. Paudel and W. R. L. Lambrecht, "First-principles calculation of the O vacancy in ZnO: A self-consistent gap-corrected approach," *Phys. Rev. B*, vol. 77, p. 205202, 2008. [42](#)
- [157] S. Limpijumnong, S. B. Zhang, S. Wei, and C. H. Park, "Doping by large-size-mismatched impurities: The microscopic origin of arsenic- or antimony-doped p-type zinc oxide," *Phys. Rev. Lett.*, vol. 92, p. 155504, 2004. [42](#)
- [158] J. Robertson, P. W. Peacock, M. D. Towler, and R. Needs, "Electronic structure of p-type conducting transparent oxides," *Thin Solid Films*, vol. 411, pp. 96–100, 2002. [42](#)
- [159] A. E. Huges and B. Henderson, *Point Defects in Solids*, vol. 1. Plenum Press, New York-London, 1972. [43](#)

- [160] J. R. Jasperse, A. Kahan, J. N. Plendl, and S. S. Mitra, “Temperature dependence of infrared dispersion in ionic crystals LiF and MgO,” *Phys. Rev.*, vol. 146, no. 2, pp. 526–542, 1966. [43](#)
- [161] R. O. Simmons and R. W. Balluffi, “Measurements of equilibrium vacancy concentrations in aluminum,” *Phys. Rev.*, vol. 117, pp. 52–61, 1960. [50](#)
- [162] G. Fiquet, P. Richet, and G. Montagnac, “High-temperature thermal expansion of lime, periclase, corundum and spinel,” *Phys. Chem. Miner.*, vol. 27, pp. 103–111, 1999. [51](#)
- [163] A. Seeger, “Investigation of point defects in equilibrium concentrations with particular reference to positron annihilation techniques,” *J. Phys. F*, vol. 3, pp. 248–294, 1973. [51](#)
- [164] I. K. MacKenzie, T. L. Khoo, A. B. McDonald, and B. T. A. McKee, “Temperature dependence of positron mean lives in metals,” *Physical Review Letters*, vol. 19, pp. 946–948, 1967. [51](#)
- [165] S. Nanao, K. Kurabayashi, S. Tanigawa, M. Mori, and M. Doyama, “The measurement of the formation energy of a vacancy in Cu by positron annihilation,” *J. Phys. F*, vol. 3, pp. L5–L8, 1973. [51](#)
- [166] S. Dannefaer, P. Mascher, and D. Kerr, “Monovacancy formation enthalpy in silicon,” *Phys. Rev. Lett.*, vol. 56, pp. 2195–2198, 1986. [51](#)
- [167] M. Mizuno, Y. Inoue, K. Sugita, H. Araki, Y. Shirai, T. Mizoguchi, I. Tanaka, and H. Adachi, “Positron annihilation study of formation of Mg vacancy in MgO,” *Mater. Sci. Forum*, vol. 445-446, pp. 153–155, 2004. [51](#)
- [168] R. Pareja, R. M. D. L. Cruz, R. Gonzalez, and Y. Chen, “Positron annihilation spectroscopy of vacancy aggregates in neutron-irradiated MgO crystals,” *Philos. Mag. A*, vol. 66, no. 4, pp. 597–607, 1992. [51](#)
- [169] S. Bonanni, K. Aït-Mansour, W. Harbich, and H. Brune, “Effect of the TiO₂ reduction state on the catalytic CO oxidation on deposited size-selected Pt clusters,” *J. Am. Chem. Soc.*, vol. 134, pp. 3445–3450, 2012. [51](#)
- [170] G. Keller and M. Bhasin, “Synthesis of ethylene via oxidative coupling of methane: I. Determination of active catalysts,” *J. Catal.*, vol. 73, pp. 9–19, 1982. [54](#)
- [171] D. J. Driscoll, W. Martir, J. X. Wang, and J. H. Lunsford, “Formation of gas-phase methyl radicals over magnesium oxide,” *J. Am. Chem. Soc.*, vol. 107, pp. 58–63, 1985. [54](#)
- [172] P. Myrach, N. Nilius, S. V. Levchenko, A. Gonchar, T. Risse, K. Dinse, L. A. Boatner, W. Frandsen, R. Horn, H. Freund, R. Schlögl, and M. Scheffler, “Temperature-dependent morphology, magnetic and optical properties of Li-doped MgO,” *ChemCatChem*, vol. 2, pp. 854–862, 2010. [54, 95, 96, 97, 115](#)

- [173] T. Trevethan and A. L. Shluger, “Building blocks for molecular devices: Organic molecules on the MgO (001) surface,” *J. Phys. Chem. C*, vol. 111, no. 42, pp. 15375–15381, 2007. [54](#)
- [174] R. Orlando, R. Millini, G. Perego, and R. Dovesi, “Catalytic properties of F-centres at the magnesium oxide surface: Hydrogen abstraction from methane,” *J. Mol. Catal. A: Chem.*, vol. 119, pp. 253–262, 1997. [54](#), [84](#)
- [175] G. Pacchioni, “Ab initio theory of point defects in oxide materials: Structure, properties, chemical reactivity,” *Solid State Sci.*, vol. 2, pp. 161–179, 2000. [54](#)
- [176] S. Lany, J. Osorio-Guillén, and A. Zunger, “Origins of the doping asymmetry in oxides: Hole doping in NiO versus electron doping in ZnO,” *Phys. Rev. B*, vol. 75, p. 241203, 2007. [54](#)
- [177] K.-H. Hellwege, ed., *Landolt-Börnstein, New Series, Group III*, vol. 7b. Springer, Berlin, 1966. [56](#), [58](#)
- [178] P. Haas, F. Tran, and P. Blaha, “Calculation of the lattice constant of solids with semilocal functionals,” *Phys. Rev. B*, vol. 79, p. 085104, 2009. [56](#), [58](#)
- [179] R. C. Whited and W. C. Walker, “Exciton spectra of CaO and MgO,” *Phys. Rev. Lett.*, vol. 22, no. 26, pp. 1428–1430, 1969. [56](#), [67](#)
- [180] S. P. Mitoff, “Electrical conductivity of single crystals of MgO,” *J. Chem. Phys.*, vol. 31, no. 5, pp. 1261–1269, 1959. [56](#)
- [181] N. I. Hadi, “Electrical conductivity of rocks and dominant charge carriers: The paradox of thermally activated positive holes,” *J. Earth Sci. Clim. Change*, vol. 03, no. 03, p. 128, 2012. [56](#)
- [182] D. L. Dexter, “Absorption of light by atoms in solids,” *Phys. Rev.*, vol. 101, pp. 48–55, 1956. [57](#)
- [183] Weast, *CRC Handbook of Chemistry and Physics*. CRC Press, 61st edition ed., 1980. [57](#)
- [184] S. Kurth, J. P. Perdew, and P. Blaha, “Molecular and solid-state tests of density functional approximations: LSD, GGAs, and meta-GGAs,” *Int. J. Quantum Chem.*, vol. 75, no. 4–5, pp. 889–909, 1999. [58](#)
- [185] N. A. Richter, S. Sicolo, S. V. Levchenko, J. Sauer, and M. Scheffler, “Concentration of vacancies at metal oxide surfaces: Case study of MgO (100),” *Phys. Rev. Lett.*, vol. 111, no. 4, p. 045502, 2013. [59](#), [84](#), [116](#), [117](#)
- [186] R. Ramprasad, H. Zhu, P. Rinke, and M. Scheffler, “New perspective on formation energies and energy levels of point defects in nonmetals,” *Phys. Rev. Lett.*, vol. 108, no. 6, p. 066404, 2012. [59](#), [60](#), [73](#)

- [187] S. Lany and A. Zunger, “Many-body GW calculation of the oxygen vacancy in ZnO,” *Phys. Rev. B*, vol. 81, p. 113201, 2010. [59](#)
- [188] D. W. Fischer, “Chemical bonding and valence state – nonmetals,” in *Adv. X-Ray Anal.* (B. L. Henke, J. B. Newkirk, and G. R. Mallett, eds.), pp. 159–181, Springer US, 1970. [60](#)
- [189] S. Kowalczyk, F. McFeely, L. Ley, V. Gritsyna, and D. Shirley, “The electronic structure of SrTiO₃ and some simple related oxides (MgO, Al₂O₃, SrO, TiO₂),” *Solid State Commun.*, vol. 23, pp. 161–169, 1977. [60](#)
- [190] L. Tjeng, A. Vos, and G. Sawatzky, “Electronic structure of MgO studied by angle-resolved ultraviolet photoelectron spectroscopy,” *Surf. Sci.*, vol. 235, pp. 269–279, 1990. [60](#)
- [191] V. A. Sashin, H. E. Dorsett, M. A. Bolorizadeh, and M. J. Ford, “The valence band structures of BeO, MgO, and CaO,” *J. Chem. Phys.*, vol. 113, pp. 8175–8182, 2000. [60](#)
- [192] C. Tuma and J. Sauer, “A hybrid MP2/planewave-DFT scheme for large chemical systems: proton jumps in zeolites,” *Chem. Phys. Lett.*, vol. 387, pp. 388–394, 2004. [61](#)
- [193] C. Tuma and J. Sauer, “Treating dispersion effects in extended systems by hybrid MP2:DFT calculations – protonation of isobutene in zeolite ferrierite,” *Phys. Chem. Chem. Phys.*, vol. 8, pp. 3955–3965, 2006. [61](#)
- [194] Q.-M. Hu, K. Reuter, and M. Scheffler, “Towards an exact treatment of exchange and correlation in materials: Application to the “CO adsorption puzzle” and other systems,” *Phys. Rev. Lett.*, vol. 98, p. 176103, 2007. [61](#)
- [195] Q.-M. Hu, K. Reuter, and M. Scheffler, “Erratum: Towards an exact treatment of exchange and correlation in materials: Application to the “CO adsorption puzzle” and other systems [Phys. Rev. Lett. 98, 176103 (2007)],” *Phys. Rev. Lett.*, vol. 99, p. 169903, 2007. [61](#)
- [196] F. Weigend and R. Ahlrichs, “Balanced basis sets of split valence, triple zeta valence and quadruple zeta valence quality for H to Rn: Design and assessment of accuracy,” *Phys. Chem. Chem. Phys.*, vol. 7, no. 18, pp. 3297–3305, 2005. [62](#)
- [197] T. H. Dunning, “Gaussian basis sets for use in correlated molecular calculations. I. The atoms boron through neon and hydrogen,” *J. Chem. Phys.*, vol. 90, pp. 1007–1023, 1989. [62](#)
- [198] S. Boys and F. Bernardi, “The calculation of small molecular interactions by the differences of separate total energies. Some procedures with reduced errors,” *Mol. Phys.*, vol. 19, no. 4, pp. 553–566, 1970. [62, 127, 128](#)
- [199] A. M. Burow, M. Sierka, J. Döbler, and J. Sauer, “Point defects in CaF₂ and CeO₂ investigated by the periodic electrostatic embedded cluster method,” *J. Chem. Phys.*, vol. 130, p. 174710, 2009. [62](#)

- [200] P. J. Hay and W. R. Wadt, “Ab initio effective core potentials for molecular calculations. Potentials for the transition metal atoms Sc to Hg,” *J. Chem. Phys.*, vol. 82, pp. 270–283, 1985. [62](#)
- [201] L. Kleinman and D. M. Bylander, “Efficacious form for model pseudopotentials,” *Phys. Rev. Lett.*, vol. 48, no. 20, pp. 1425–1428, 1982. [62](#)
- [202] M. Fuchs and M. Scheffler, “Ab initio pseudopotentials for electronic structure calculations of poly-atomic systems using density-functional theory,” *Comput. Phys. Commun.*, vol. 119, no. 1, pp. 67–98, 1999. [62](#)
- [203] J. Paier, X. Ren, P. Rinke, G. E. Scuseria, A. Grüneis, G. Kresse, and M. Scheffler, “Assessment of correlation energies based on the random-phase approximation,” *New J. Phys.*, vol. 14, p. 043002, 2012. [64](#)
- [204] X. Ren, P. Rinke, G. E. Scuseria, and M. Scheffler, “Renormalized second-order perturbation theory for the electron correlation energy: Concept, implementation, and benchmarks,” *Phys. Rev. B*, vol. 88, p. 035120, 2013. [64](#)
- [205] D. West, Y. Y. Sun, and S. B. Zhang, “Importance of the correct Fermi energy on the calculation of defect formation energies in semiconductors,” *Appl. Phys. Lett.*, vol. 101, p. 082105, 2012. [72](#)
- [206] J. C. Slater and J. H. Wood, “Statistical exchange and the total energy of a crystal,” *Int. J. Quantum Chem.*, vol. 5, no. S4, pp. 3–34, 1970. [74](#)
- [207] J. C. Slater, “Statistical exchange-correlation in the self-consistent field,” in *Adv. Quantum Chem.* (Per-Olov Löwdin, ed.), vol. 6, pp. 1–92, Academic Press, 1972. [74](#)
- [208] A. Tkatchenko, R. A. DiStasio, R. Car, and M. Scheffler, “Accurate and efficient method for many-body van der Waals interactions,” *Phys. Rev. Lett.*, vol. 108, p. 236402, 2012. [77](#)
- [209] G.-X. Zhang, A. Tkatchenko, J. Paier, H. Appel, and M. Scheffler, “van der Waals interactions in ionic and semiconductor solids,” *Phys. Rev. Lett.*, vol. 107, p. 245501, 2011. [77](#)
- [210] Casimir, H. B. G., “On the attraction between two perfectly conducting plates,” *Proc. K. Ned. Akad. Wet.*, vol. B 51, pp. 793–795, 1948. [77](#)
- [211] H. B. G. Casimir and D. Polder, “The influence of retardation on the London-van der Waals forces,” *Phys. Rev.*, vol. 73, pp. 360–372, 1948. [77](#)
- [212] M. Welton-Cook and M. Prutton, “A simple shell model calculation of differential ionic relaxations at the (100) surfaces of NaCl structure alkali halides,” *Surf. Sci.*, vol. 64, pp. 633–640, 1977. [79](#)
- [213] M. Welton-Cook and M. Prutton, “A simple shell model calculation of the differential ionic relaxation of the MgO(100) surface,” *Surf. Sci.*, vol. 74, pp. 276–284, 1978. [79](#)

- [214] P. Rinke, A. Schleife, E. Kioupakis, A. Janotti, C. Rödl, F. Bechstedt, M. Scheffler, and C. G. Van de Walle, “First-Principles optical spectra for F centers in MgO,” *Phys. Rev. Lett.*, vol. 108, no. 12, p. 126404, 2012. [81](#)
- [215] L. Giordano, U. Martinez, G. Pacchioni, M. Watkins, and A. L. Shluger, “F and F⁺ centers on MgO/Ag(100) or MgO/Mo(100) ultrathin films: Are they stable?,” *J. Phys. Chem. C*, vol. 112, pp. 3857–3865, 2008. [84](#)
- [216] G. Pacchioni and P. Pescarmona, “Structure and stability of oxygen vacancies on sub-surface, terraces, and low-coordinated surface sites of MgO: An *ab initio* study,” *Surf. Sci.*, vol. 412–413, pp. 657–671, 1998. [84, 116, 117](#)
- [217] L. N. Kantorovich, A. L. Shluger, P. V. Sushko, J. Günster, P. Stracke, D. W. Goodman, and V. Kempter, “Mg clusters on MgO surfaces: Study of the nucleation mechanism with MIES and ab initio calculations,” *Faraday Discuss.*, vol. 114, pp. 173–194, 1999. [86](#)
- [218] J. Fritsch and U. Schröder, “Density functional calculation of semiconductor surface phonons,” *Phys. Rep.*, vol. 309, pp. 209–331, 1999. [92](#)
- [219] J. Meyer, *Ab initio Modeling of Energy Dissipation during Chemical Reactions at Transition Metal Surfaces*. PhD thesis, Freie Universität Berlin, 2012. [92](#)
- [220] S. Arndt, G. Laugel, S. Levchenko, R. Horn, M. Baerns, M. Scheffler, R. Schlögl, and R. Schomäcker, “A critical assessment of Li/MgO-Based catalysts for the oxidative coupling of methane,” *Cat. Rev.*, vol. 53, no. 4, pp. 424–514, 2011. [95, 111](#)
- [221] M. Abraham, Y. Chen, L. Boatner, and R. Reynolds, “Stable [Li]⁰ defects in MgO single crystals,” *Phys. Rev. Lett.*, vol. 37, pp. 849–852, 1976. [95, 100](#)
- [222] H.-M. Benia, P. Myrach, and N. Nilius, “Photon emission spectroscopy of thin MgO films with the STM: From a tip-mediated to an intrinsic emission characteristic,” *New J. Phys.*, vol. 10, no. 1, p. 013010, 2008. [96](#)
- [223] S. Benedetti, H. Benia, N. Nilius, S. Valeri, and H. Freund, “Morphology and optical properties of MgO thin films on Mo(001),” *Chem. Phys. Lett.*, vol. 430, no. 4–6, pp. 330–335, 2006. [96, 97](#)
- [224] S. Benedetti, P. Torelli, S. Valeri, H. M. Benia, N. Nilius, and G. Renaud, “Structure and morphology of thin MgO films on Mo(001),” *Phys. Rev. B*, vol. 78, no. 19, p. 195411, 2008. [96](#)
- [225] J. A. Farmer, N. Ruzycki, J. F. Zhu, and C. T. Campbell, “Lithium adsorption on MgO(100) and its defects: Charge transfer, structure, and energetics,” *Phys. Rev. B*, vol. 80, no. 3, p. 035418, 2009. [97](#)
- [226] L. Xu and G. Henkelman, “Calculations of Li adsorption and diffusion on MgO(100) in comparison to Ca,” *Phys. Rev. B*, vol. 82, no. 11, p. 115407, 2010. [97](#)

- [227] S. Stankic, M. Müller, O. Diwald, M. Sterrer, E. Knözinger, and J. Bernardi, “Size-dependent optical properties of MgO nanocubes,” *Angew. Chem., Int. Ed.*, vol. 44, no. 31, pp. 4917–4920, 2005. [97](#)
- [228] M. Anpo, Y. Yamada, Y. Kubokawa, S. Coluccia, A. Zecchina, and M. Che, “Photoluminescence properties of MgO powders with coordinatively unsaturated surface ions,” *J. Chem. Soc., Faraday Trans. 1*, vol. 84, no. 3, pp. 751–764, 1988. [97](#)
- [229] A. L. Shluger, P. V. Sushko, and L. N. Kantorovich, “Spectroscopy of low-coordinated surface sites: Theoretical study of MgO,” *Phys. Rev. B*, vol. 59, no. 3, pp. 2417–2430, 1999. [97](#)
- [230] H. M. Benia, X. Lin, H.-J. Gao, N. Nilius, and H.-J. Freund, “Nucleation and growth of gold on MgO thin films: A combined STM and luminescence study,” *J. Phys. Chem. C*, vol. 111, no. 28, pp. 10528–10533, 2007. [97](#)
- [231] A. Lichanot, C. Larrieu, R. Orlando, and R. Dovesi, “Lithium trapped-hole centre in magnesium oxide. An ab initio supercell study,” *J. Phys. Chem. Solids*, vol. 59, pp. 7–12, 1998. [100](#)
- [232] M. M. Abraham, W. P. Unruh, and Y. Chen, “Electron-nuclear-double-resonance investigations of $[\text{Li}]^0$ and $[\text{Na}]^0$ centers in MgO, CaO, and SrO,” *Phys. Rev. B*, vol. 10, pp. 3540–3545, 1974. [100](#)
- [233] V. Blum, R. Gehrke, F. Hanke, P. Havu, V. Havu, X. Ren, K. Reuter, and M. Scheffler, “Ab initio molecular simulations with numeric atom-centered orbitals,” *Comput. Phys. Commun.*, vol. 180, no. 11, pp. 2175–2196, 2009. [100](#)
- [234] T. Ito and J. H. Lunsford, “Synthesis of ethylene and ethane by partial oxidation of methane over lithium-doped magnesium oxide,” *Nature*, vol. 314, pp. 721–722, 1985. [111](#)
- [235] U. Zavyalova, G. Weinberg, W. Frandsen, F. Girgsdies, T. Risse, K. P. Dinse, R. Schloegl, and R. Horn, “Lithium as a modifier for morphology and defect structure of porous magnesium oxide materials prepared by gel combustion synthesis,” *ChemCatChem*, vol. 3, no. 11, pp. 1779–1788, 2011. [115](#)
- [236] A. Pojani, F. Finocchi, J. Goniakowski, and C. Noguera, “A theoretical study of the stability and electronic structure of the polar 111 face of MgO,” *Surf. Sci.*, vol. 387, pp. 354–370, 1997. [116](#)
- [237] C. Noguera, “Polar oxide surfaces,” *J. Phys.: Condens. Matter*, vol. 12, p. R367, 2000. [116](#)
- [238] F. Bottin, F. Finocchi, and C. Noguera, “Stability and electronic structure of the (1×1) SrTiO_3 (110) polar surfaces by first-principles calculations,” *Phys. Rev. B*, vol. 68, p. 035418, 2003. [116](#)

- [239] F. Finocchi, A. Barbier, J. Jupille, and C. Noguera, “Stability of rocksalt (111) polar surfaces: Beyond the octopole,” *Phys. Rev. Lett.*, vol. 92, p. 136101, 2004. [116](#)
- [240] J. Goniakowski, C. Noguera, and L. Giordano, “Using polarity for engineering oxide nanostructures: Structural phase diagram in free and supported MgO(111) ultrathin films,” *Phys. Rev. Lett.*, vol. 93, p. 215702, 2004. [116](#)
- [241] P. W. Tasker, “The stability of ionic crystal surfaces,” *J. Phys. C*, vol. 12, p. 4977, 1979. [118](#)
- [242] A. Wander, F. Schedin, P. Steadman, A. Norris, R. McGrath, T. S. Turner, G. Thornton, and N. M. Harrison, “Stability of polar oxide surfaces,” *Phys. Rev. Lett.*, vol. 86, pp. 3811–3814, 2001. [118](#)
- [243] W.-B. Zhang and B.-Y. Tang, “Stability of MgO(111) polar surface: Effect of the environment,” *J. Phys. Chem. C*, vol. 112, pp. 3327–3333, 2008. [118](#)
- [244] T. Brudevoll, E. A. Kotomin, and N. E. Christensen, “Interstitial-oxygen-atom diffusion in MgO,” *Phys. Rev. B*, vol. 53, pp. 7731–7735, 1996. [122](#)
- [245] F. D. Murnaghan, “The compressibility of media under extreme pressures,” *Proc. Nat. Acad. Sci.*, vol. 30, pp. 244–247, 1944. [126](#)
- [246] F. Birch, “Finite elastic strain of cubic crystals,” *Phys. Rev.*, vol. 71, pp. 809–824, 1947. [126](#)
- [247] H. Jansen and P. Ros, “Non-empirical molecular orbital calculations on the protonation of carbon monoxide,” *Chem. Phys. Lett.*, vol. 3, pp. 140–143, 1969. [127](#)

Acknowledgements

I would like to thank Matthias Scheffler for giving me the opportunity to be a PhD student at the FHI, where I could work on a challenging, extremely interesting project in a very active, motivated group with exceptional computational facilities and many opportunities to discuss with well-known experts in the field. Thank you for sharing your experience and expertise by providing helpful advice and guidance for my PhD project. Also your help on improving my presentation and scientific writing skills was much appreciated.

Then, a huge thanks goes to Sergey Levchenko. Working with you made my PhD project an interesting, rewarding, and enjoyable experience for me. I am very thankful that you never got tired of enthusiastically discussing all aspects of defects in MgO with me, that you taught me a lot about the possibilities of electronic structure theory, and that you supervised my research always being open to my ideas and interested in the latest progress. I am very grateful that I could always rely on thoughtful feedback, suggestions, and support from you. Thank you!

Further, I would like to thank Andreas Knorr for accepting to be a referee for this work and I thank Mario Dähne for agreeing to chair my PhD defense.

Many discussions and advice from former and present members of the theory department helped me a lot to bring my project forward. Thanks to all of you, especially to the catalysis group, for the committed and communicative atmosphere.

For fruitful discussions during our collaborations I thank Sabrina Sicolo and Joachim Sauer from the Humboldt University Berlin and Fernando Stavale and Niklas Nilius from the FHI CP department.

I would also like to acknowledge the IMPRS "Complex Surfaces in Materials Science" for funding and its coordinators and my fellow student members for many inspiring discussion meetings and the great experience to organize our own conference meeting.

I was very lucky to have exceptionally likable office mates throughout my PhD time. Many thanks to you for all the interesting every day discussions on science and the good spirit in T 1.07. In specific, thanks to Jelena for making me feel welcome at FHI from the start, to Claudi for sharing her chemist's point of view on science and being a great friend throughout, to Falko for enjoying many burger lunch breaks together, to Mark for some interesting insights on programming and life in general, and to Robin for cheering me up during the latest busy weeks.

Guoxu and Franzi, many, many thanks for your friendship and great times spent together. I will never forget our girls team at FHI.

For an open ear to research related questions, but also for friendship and support I thank Luca (also for the music, of course!), Sabrina, Vivek, and Anthony.

Finally, I would like to say thank you to my friends outside FHI and to my family, especially to my parents Edith and Matthias, and to my brothers Lennart and Lasse. Thank you for your encouragement, support, and most of all for your understanding.

And to Torben, thank you so much.